The University Of Sheffield.

Characterisation and Simulation of Linear and Geiger Mode Avalanche Photodiodes

Jonathan Derek Taylor-Mew

A thesis submitted in partial fulfilment of the requirements for the degree of Doctor of Philosophy

The University of Sheffield
Faculty of Engineering
Department of Electrical and Electronic Engineering

Submission Date

23rd September 2022

HUMAN BEINGS MAKE LIFE SO INTERESTING. DO YOU KNOW, THAT IN A UNIVERSE SO FULL OF WONDERS, THEY HAVE MANAGED TO INVENT BOREDOM.

Death, Hogfather

Terry Pratchett

Contents

Abstract

$Al_{0.85}Ga_{0.15}As_{0.56}Sb_{0.44}$ is a wide bandgap material latticed matched to InP. Narrow devices from the literature show a very low excess noise factor, suggesting a wide disparity between the impact ionisation coefficients. In this work, a 600 nm pin is experimentally characterised for electron-initiated avalanche multiplication and excess noise factor. Using these results and those from the literature, a Simple Monte Carlo parameter set was validated, and the impact ionisation coefficients were extracted for an electric field range of 400 – 1200 $kV.cm^{-1}$.

A Random Path Length model is a simplistic Monte Carlo model with a short simulation runtime compared to the more complex Simple Monte Carlo Model. The RPL has previously been used to model breakdown probability but could not accurately model the time to breakdown due to the limitations imposed by the saturation velocity assumption. In this work, an enhanced velocity for Si, InP and $Al_{0.85}Ga_{0.15}As_{0.56}Sb_{0.44}$ was proposed. The enhanced velocity of these materials was validated against the Simple Monte Carlo model with good agreement over a wide range of simulated devices.

Finally, a Simple Monte Carlo model parameter set was validated for $In_{0.53}Ga_{0.47}As$, and the impact ionisation coefficients were extracted over an electric field range of 80 – 340 $kV.cm^{-1}$. $In_{0.53}Ga_{0.47}As$ is a common absorption material for III-V based SAM APDs. $In_{0.53}Ga_{0.47}As$ has previously been characterised to have an abnormally low electric field election initiated avalanche multiplication due to the large energy offset between E_Γ and the indirect energy valleys. Careful attention was made to ensure the avalanche multiplication simulations followed both the low and high electric field trends.

Acknowledgements

I would like to thank my supervisor Prof. Jo Shien Ng for giving me the opportunity to pursue my PhD. Your guidance, insight and patience have been invaluable over the duration of my research and during the Covid-19 pandemic. I would also thank Prof. Chee Hing Tan and Prof John David for your insight, discussions and advice through out.

I would like the thank past and current members of the Impact Ionisation Group: Dr. Jon Petticrew, Dr. Vladimir Shulyak, Dr. Simon Dimler, Dr. Lizzy Stark, Tarick Blain, Dr. Yuting Ji, Dr. Leh Woon Lim, Dr. Ben White, Guanwei Huang, Jonty Veitch, and Ye Cao.

I am grateful for the financial support from the ESPRC, without which I would not of been able to pursue this Ph.D

I also thank my parents, Rosemary and Derek, my twin, Matthew for your support though out. In particular, I would like to thank Ellie, for your support during the hardest times and nodding along while I try and explain the latest puzzle to be solved.

Publications

Journal Papers:

J. Taylor-Mew, V. Shulyak, B. White, C. H. Tan, and J. S. Ng, 'Low Excess Noise of $Al_{0.85}Ga_{0.15}As_{0.56}Sb_{0.44}$ Avalanche Photodiode From Pure Electron Injection', *IEEE Photon. Technol. Lett.*, vol. 33, no. 20, pp. 1155–1158, Oct. 2021, doi: 10.1109/LPT.2021.3110123.

J. D. Taylor-Mew, J. D. Petticrew, C. H. Tan, and J. S. Ng, 'Simulation of $Al_{0.85}Ga_{0.15}As_{0.56}Sb_{0.44}$ avalanche photodiodes', *Opt. Express*, vol. 30, no. 11, p. 17946, May 2022, doi: 10.1364/OE.458922.

Y. Cao, T. Blain, **J. D. Taylor-Mew**, L. Li, J. S. Ng, and C. H. Tan, 'Extremely low excess noise avalanche photodiode with GaAsSb absorption region and AlGaAsSb avalanche region', *Applied Physics Letters*, 2023, doi: 10.1063/5.0139495.

Conferences:

X. Collins, B. White, Y. Cao, T. Osman, **J. Taylor-Mew**, J. S. Ng, C. H. Tan ., 'Low-noise AlGaAsSb avalanche photodiodes for 1550nm light detection', in *Optical Components and Materials XIX*, San Francisco, United States, Mar. 2022, p. 16. doi: 10.1117/12.2608842.

J. D. Taylor-Mew, J. D. Petticrew, B. S. White, C. H. Tan, and J. S. Ng, 'Excess Noise Characteristics and Simulation Model of $Al_{0.85}Ga_{0.15}As_{0.56}Sb_{0.44}$ Avalanche Photodiodes', presented at the UK Semiconductors, Sheffield, UK, Jul. 2022.

Abbreviations

ABMC	Analytical Band Monte Carlo
APD	Avalanche Photodiodes
APD	Avalanche Photodiode
CMOS	Complementary Metal Oxide Semiconductor
CPS	Counts per second
CQC	Capacitive Quenching Circuit
DCR	Dark Count Rate
e-APD	Electron only Avalanche Photodiode
ENBW	Effective Noise Bandwidth
eVOA	Electronically controlled Variable Optical Attenuator
FBMC	Full Band Monte Carlo
FLIM	Fluorescence lifetime Imaging Microscopy
FWHM	Full Width Half Maximum
HPMTs	Hybrid photomultiplier tubes
LIA	Lock-in Amplifier
LiDAR	Light Detection and Ranging
MBE	Molecular Beam Epitaxy
MCA	MultiChannel Analyser
MOVPE	Metalorganic vapour-phase epitaxy
PDE	Probability of Detection Efficiency
PDF	Probability density Function
PMTs	Photomultiplier Tubes
QKD	Quantum Key Distribution
QSS	Quantum secret sharing
RMS	Root Mean Square
RPL	Random Path Length
SAM APD	Separate Absorber-Multiplication Avalanche Photodiode
SIMS	Secondary Ion Mass Spectrometry
SMC	Simple Monte Carlo
SNSPDs	Superconducting nanowire Single-Photon Detectors
SPAD	Single Photon Avalanche Photodiode

SPDE	Single Photon Detection Efficiency
TAC	Time to Amplitude Converter
TCSPC	Time-Correlated Single Photon Counting
TEC	Thermoelectric cooler
TES	Transmission Edge Sensor
TIA	Transimpedance Amplifier
TLM	Transmission Line Measurement

Symbols

$\bar{n}$	Average number of photons
B_{eff}	Effective Bandwidth
c	Speed of light
C	Capacitance
C_{bd}	Thermal coefficient of Avalanche breakdown
C_{ii}	Prefactor of impact ionisation rate
$d_e : d_h$	Deadspace of electrons (holes)
E_c	Energy of carrier
E_g	Bandgap energy
E_{th}	Threshold energy (SMC)
E_{the}	Threshold energy of electrons (RPL)
E_{thh}	Threshold energy of holes (RPL)
$E_\Gamma : E_x : E_L$	Energy of $\Gamma : x : L$ Valley
F	Excess Noise Factor
h	Plank's Constant
$h_e(x) : h_h(x)$	Impact ionisation path lengths for electrons (holes)
$\hbar\omega$	Phonon energy
I_0	Reverse Saturation current
i_{br}	Avalanche breakdown current
I_f	Forward bias current
I_{ph}	Photocurrent
I_{pri}	Primary unmultiplied photocurrent
I_{tun}	Tunnelling Current
J_d	Current density
k	Impact ionisation coefficient ratio
k_b	Boltzmann constant
k_{pr}	Shot noise fitting gradient
l	Random path length
L_d	Minority carrier diffusion length
M	Avalanche Multiplication
m^*	Effective mass
m_i	Instantaneous Avalanche Multiplication
M_{od}	Overdrive multiplier

n	Ideality factor
n_{br}	Number of carriers for a breakdown event
p, i, n	Doping type: positive, intrinsic and negative
P_b	Breakdown Probability
q	Electron charge
r	A random number between 0 and 1
R_{ab}	Rate of phonon absorption scattering
R_{alloy}	Rate of alloy scattering
R_{em}	Rate of phonon emission scattering
R_{ii}	Rate of impact ionisation scattering
R_p	Reptation rate
R_s	Series resistance
t_b	Time to breakdown
T_{on}	On time
v	Velocity
V_{br}	Breakdown Voltage
v_{en}	Enhanced Velocity
v_{sat}	Saturation velocity
w	Depletion width
W_0	Lambert-W function 0^{th} term
w_{tun}	The distance that a carrier can tunnel
$\alpha(*)$	Electron (Effective) Impact Ionisation Coefficient
$\beta(*)$	Hole (Effective) Impact Ionisation Coefficient
γ	Softness factor
δ	Duty cycle
Δt	Change in time
ΔT	Change in temperature
ε_0	The permittivity of free space
ε_r	The relative permittivity of a material
η	External quantum efficiency
λ	Mean free path
λ_i	The wavelength of the injected light
ξ	Electric Field Strength
σ_{tun}	Tunnelling current fitting parameter

List of Figures

List of Tables

Chapter 1

Introduction

1.1) Applications of optical detectors

Optical detectors are sensors designed to convert an optical signal to an electrical signal. Semiconductor optical detectors rely on the photoelectric effect (first explained by Einstien in 1905 [1]), in which light can be thought of as particles. These particles of light are called photons. If a photon's energy is sufficiently high, absorption of a photon in a semiconductor material can generate a free electron-hole pair. Movements of the newly generated electron-hole pair yield an electrical current, which can be detected by subsequent circuitry. Applications utilising optical detectors are wide-ranging, and notable examples include Light Detection and Ranging (LiDAR), Time-Correlated Single Photon Counting (TCSPC) and Quantum Key Distribution.

1.1.1) LiDAR

LiDAR has seen an increase in popularity and research activities with the advancement of driverless and driver-assisted cars. LiDAR systems are now also applied in industries such as construction, site surveying [2] and agriculture [3]–[5]. A LiDAR system uses an optical emitter to send out optical pulses to the target and an optical detector to sense the reflections of those optical pulses. By measuring the time interval between the output of the optical emitter and the return signal from the optical detector, a distance is given by $\frac{\Delta t\, c}{2}$, where c is the speed of light. The optical detector employed for LiDAR typically has high gain because the returning optical signal is weak (following scatterings in the path from the target back to the system). Variation in Δt is called timing jitter and can arise from several sources, including the optical pulse source, the detector and the receiver circuit. Jitter from the optical source may be due to variations in the driver circuit and current build-up. The detector's jitter may be due to differences in where the photon is absorbed in the absorption medium and the build-up of the electrical signal to a detectable level. The timing jitter of a system is typically quantified by the Full-Width-at-Half-Maximum (FWHM) of the timing response and is a key performance metric for LiDAR as it dictates the accuracy of the system overall.

1.1.2) TCSPC

TCSPC is becoming increasingly prominent, especially when used in combination with LiDAR [6], [7], with the advances in low jitter single photon detectors. TCSPC relies upon detectors capable of repeatably detecting and responding to optical levels down to a single photon, such as PhotoMultiplier Tubes (PMT) and

Single Photon Avalanche Photodiodes (SPADs). For TCSPC measurements to be successful, a detector must have a low timing jitter, high detection probability and low error (dark) count rate.

Fluorescence Lifetime Imaging Microscopy (FLIM) operates by exciting a fluorescent dye with an optical pulse and recording the time when a photon is emitted when the fluorescent dye relaxes [8]. The TCSPC needs to reliably detect single photons and accurately record the time delay between the optical pulse and the detected signal. The wavelength of the photon emitted by the dye varies, but they are typically in the visible wavelength spectrum [9], in order to utilise PMTs or Si CMOS SPADs [10]. A study on DNA for FLIM measurements of Nucleus and chromocenters had an timing jitter of 26 ps [11]. Another TCSPC application is Raman spectroscopy. This is a method of identifying material by the Raman scattering of light, which is a scattering process between optical phonons and electrons first reported in 1928 [12]. It has found use in non-invasive medical diagnosis and chemical analysis [13].

1.1.3) QKD

Quantum Key Distribution (QKD) is a communication principle relying upon detecting a single photon [14] to create a secure communication channel. Although there are different schemes for implementation of a QKD system, they all rely on the fact that, when each bit of the signal is made up of a single photon (or its absence), then the communication may not be intercepted without the knowledge of the sender or the receiver. It is impossible to replicate a quantum state [15], hence if an eavesdropper intercepts the single photon, they cannot replicate the photon without introducing detectable errors. These will reveal the presence of the eavesdropper [16]. QKD-based communications rely upon detectors such as PMTs and SPADs due to the inherent reliance on a single photon for communication.

QKD systems are based on a 2 party system. For more than two parties, Quantum secret sharing (QSS) is used [17]. One QKD protocol (Twin-field QKD) has been demonstrated to have a practical operating distance of up to 500 km [18] using ultra lower fibre without a repeater. Twin-field QKD uses an optical signal generated by two sources that are phase-randomised and encoded to obscure the nature of the signal [19].

1.2) Types of optical detectors

1.2.1) PMTs

Photomultiplier tubes (PMTs) were first reported in 1935 [20]. In a PMT, the incoming photons strike a photocathode, releasing electrons, which are then focused using high voltage electrodes onto a set of high voltage dynodes. As the electrons strike each dynode, further secondary electrons are released, increasing the system gain—the more dynodes in the tube, the high the gain of the PMT. The electrons are finally focused on an anode for electrical detection. PMT typically operate at high voltages, with dynodes operating in the

kV's region as standard. PMTs were the first detector technology capable of detection down to single photon levels and were used predominately for all low light level detection while APDs and SPADs were in their infancy [21].

As APD and SPADs have matured, PMTs have been phased out of all but the most specialised use cases. This is partly due to the high operating voltages and the fragility of the glass tubes, which means that the failure of a single PMT could cause all the other PMTs in a detector array to fail too, which was the fate of the Super-Kamiokande I detector array in 2001 [22]. Other significant drawbacks are their low Quantum Efficiency (QE) and slow response in the Near-Infrared band, e.g. QE of 0.04% at 1060 nm [23] and 2% at 1.55 μm wavelength with a response time of 23 ns [24]. These are significantly worse than available Near-Infrared (NIR) SPADs. They are, however, still commercially available for both NIR and visible detection [25]. PMTs find use in specialised roles requiring a dark count rate < 1000 [24], for example, in the Super-Kamiokande neutrino detector [22].

A variation on the PMT has been developed, such as the hybrid PMTs (HPMTs), where the dynode has been replaced with an avalanche diode [26] [27]. HPMTs have a better temporal response compared to PMTs. The rise and fall times are in the order of 100's ps and jitter of 50-130 ps [28]. Microchannel Plates PMTs (MCP – PMT) [29] is another variation in which the 'air' gap between the cathode and anode is made up of many capillaries coated in a photoemissive material. This allows the detector to still achieve a high gain (300k) and dark count (2000 s^{-1}) with a significantly lower time response and jitter [30]. They, however, still operate at several kV and suffer from a low active area to volume ratio compared to SPADs.

1.2.2) Photodiodes (p-i-n)

The simplest form of detector operates under the photoelectric effect principle. Photodiodes operate with unity gain, so a single electron-hole pair is generated for every photon absorbed. Photodiodes also have a lower output noise than Avalanche Photodiodes for the same output current. The photodiode's primary noise source is shot noise, which is linearly proportional to current. In contrast, an APD has the same shot noise and excess noise, which is associated with fluctuations of the APD gain. Hence, a photodiode has a lower total noise for very strong optical power. However, in many important applications, the optical power is low, so an external circuit, such as a trans-impedance amplifier, is required to amplify the photodiode's signal. The TIA will introduce noise; hence, a photodiode – TIA circuit can exhibit a higher noise than an equivalent APD-based circuit. At very high optical powers, a photodiode can suffer from a space charge effect where many photogenerated electrons generate an electric field opposing the bias applied to the diode.

1.2.3) Avalanche Photodiodes

In the simplest form, Avalanche photodiodes are a p-n junction diode with a higher applied bias so that avalanche breakdown may occur. Impact ionisation, a process noted by Hippel [31] 1931, was used by Zener to define the relationship between electric field and breakdown [32]. Later, breakdown current was observed in a Ge p-n junction by McFee [33]. Avalanche breakdown and impact ionisation coefficient were first reported in Si by McKay [34] in 1954. McKay noted pulse-type noise associated with the breakdown point, which would fluctuate at the breakdown but would not be observed below or above the breakdown. Also, the noise pulses were proportional to temperature. In 1965, Haitz [35] investigated these noise pulses further and found three contributing factors: 1) thermal carriers from the generation sites, 2) re-emission of trapped carriers, and 3) carrier generation due to band-to-band tunnelling (trap-assisted tunnelling). Haitz suggested that mechanisms 2) and 3) could be reduced by driving the diode into the secondary breakdown. Effectively driving the diode to self-anneal due to the junction temperature, reducing the overall defect site in the crystal, which the two mechanisms required. McKay [34] also noted that breakdown did not occur at a single electric field as previously assumed by scaling with device width. In the same year, Chynoweth parameterised Si electron ionisation rates in a uniform Si p-n junction [36]. Photon emission was observed in a Si device in breakdown for both grown and diffused junctions in 1956 [37]. The photon emission was observed to be randomly spaced across the whole junction. The number of light spots increases with current, with the photon being emitted by recombination at the light spot sites.

A detailed study into the effect of avalanche multiplication on the Silicon p-n junction was carried out [38]. It was found that the inverse avalanche multiplication versus voltage did not follow a linear trend as previously expected. This was attributed to the space-charge effect and the pulsing noise mechanism. Si APDs with a gain of 1000 was reported in 1964 [39] for a planar device with a nominal i-region of 20 μm. The noise power transfer function was derived as a function of gain. Soon after, Johnson produced a high-speed Si APD with a signal-to-noise ratio of 45 dB for both a mesa and planar device [40].

As APD quality improved, models were sought after to explain the experimental observations. McIntyre established equations to calculate the probability of a breakdown event [41] and the multiplication noise in an APD [42]. The latter is now called the local model for excess noise and used extensively for experimental comparisons nowadays. A theory on impact ionisation coefficients was proposed by Okuto *et al.* [43], building on the work by Wolff [44] for high electric fields and Shockley for low electric fields [45]. Okuto *et al.* presented impact ionisation coefficients considering a non-localised concept for Si, Ge, GaAs, and GaP [46]. Oldham e*t al.* built on the model theorems to produce coupled differential equations to describe the breakdown probability for electron and hole initialisation, which could be used for any material where the impact ionisation coefficients were known [47]. McIntyre [48], using the experimental results from Conradi [49], sought to simplify the equation from Oldham e*t al.* and produce a model for avalanche gain, excess noise

factor, and determine the probability of detection, so by calculating the minimum number of photons a device required to guarantee detections and hence the suitability of an APD in such an application.

Many of the early APD structures were simple p-n or p-i-n junction diodes made of a single homogeneous material. This material is required to both absorb the photon and generate the internal gain through impact ionisation. For infrared detection, a narrow bandgap material is required, such as $In_{0.53}Ga_{0.75}As$, which can absorb light up to 1.7 μm or 0.75 eV. However, narrow bandgap materials are susceptible to band-to-band tunnelling at high electric fields, which are required for high avalanche multiplication. To avoid band-to-band tunnelling, a wide bandgap material is required for generating avalanche gains. Hence there exists a tradeoff in material choice for infrared APDs.

In the late 1970s Nishida *et al.* [50] demonstrated a SAM APD (Separate-Absorption-Multiplication Avalanche Photodiode), containing an InGaAsP absorber and an InP avalanche region. The APD exhibited a gain > 1,000 for 1.25 μm optical injection. The 1.25 μm wavelength photon passes through the wide-bandgap InP layer but are then absorbed in the InGaAsP layer generating electron-hole pairs. The photo-generated carriers then travel under the electric field and impact ionise in the InP layer. The design was improved by adding grading layers between the absorber and the avalanche material [51]. They have intermediary bandgaps to smooth out the band offsets between the two regions and reduce the charge buildup, increasing the APD's bandwidth.

Capasso *et al.* improved upon this by ensuring that the absorber would have a lower electric field than the avalanche region [52]. This was achieved by adding a highly doped region between the absorber and the avalanche regions. Changing the charge sheet's doping density and/or thickness determines difference of electric fields in the avalanche region and the absorber. A study by Ng *et al.* investigated the effects of a high electric field in an InGaAs absorber on the avalanche gain and excess noise factor of a SAM APD [53]. SAM APDs are now commonplace for 1.3 and 1.55 μm detection utilising grading layers and a charge sheet. If grown on InP substrates, SAM APDs will utilise InGaAs as an absorber material, and then any wide bandgap material as an avalanche region lattice matched to InP, such as InP, $In_{0.52}Al_{0.48}As$, $AlAs_{0.56}Sb_{0.44}$, and $Al_{0.85}Ga_{0.15}As_{0.56}Sb_{0.44}$. These avalanche materials will be discussed later in this chapter.

1.2.4) Single Photon Avalanche Photodiodes

Single Photon Avalanche Photodiodes (SPADs) are diodes capable of responding to a single photon input. The reverse bias applied to SPADs and APDs differs. When operated above the breakdown, the APD is operated in the Geiger mode, making it a SPAD. When operated below the breakdown, the APD is operated in the linear mode.

Early Si SPADs consisted of p-n junctions [35] and were found to have exceptional timing resolution [54] compared to the main alternative at the time, PMTs. Si SPAD has since become the dominant detector for

the visible wavelength. This is partly due to Si SPAD being formed as a custom SPAD device or taking advantage of the Complementary Metal-Oxide Semiconductor (CMOS) design and fabrication. Custom Si SPADs design allows for complete control over the doping profile, type of doping (implant or growth) and processes such as annealing, which reduces dark counts by reducing defects such as those caused by implantation. A relatively thin custom Si SPAD had been reported with an SPDE of 48% at 550 nm [55], with a dark count rate of 200 s^{-1} while cooled. Recently a Si SPAD with an SPDE of 69 % at 633 nm at room temperature [56] has been reported with a nominal breakdown voltage of 30 V. To achieve higher SPDE at a longer wavelength, the SPADs have very thick i-regions, but they require high breakdown voltages in the several 100's V [57]. Red-enhanced SPADs, such as those reported in [58] and [56], utilise a pseudo-SAM structure electric field profile. They have a high electric field region that is relatively narrow to ensure a low breakdown voltage and good temporal characteristics. Another thick, low electric field region is included to maximise the SPAD's photon absorption efficiency. Such SPADs, however, require a high degree of control over the doping profiles compared to a simple thick SPAD.

CMOS design allows the SPAD to be fabricated in conjunctions with biasing, quenching and read-out circuits on the same substrate. The advantage is a reduction in parasitic due to bond wires and cabling, the potential for higher operating frequencies and a reduction in external circuity requirements. However, the disadvantage is that CMOS SPADs tend to be relatively thin, limiting the maximum responsivity and the lack of high-temperature annealing processes, which results in a higher dark count rate than a custom SPAD of comparable specifications.

Ge has been used as a homogeneous infrared SPAD [59] and had a timing resolution of < 1 ns [60]. The devices however suffered from a high band-to-band tunnelling current and require cryogenic cooling. A Ge on Si SPAD was reported with an SPDE of 4% and a DCR of 6 Ms^{-1} at 10 % overbias while cooled at 100 K. While this SAM structure represents an improvement on a homogeneous Ge SPAD, the high dark count was attributed to surface leakage and lattice mismatch between Si and Ge and limited the device to 100 K or lower operation. Lu *et al.* [61]reported a Ge-on-Si SPAD with a DCR between 100 Ms^{-1} and 250 Ms^{-1} at 200 K. They reported an SPDE of 14 %; however, it was obtained using a relatively high optical power of 1 photon per pulse on average. Also, the work calculated SPDE assuming multiple events may be detected simultaneously, which is not valid for a Geiger mode SPAD [56]. Hence the reported SPDE value is likely to be an overestimate of practical values.

For III-V infrared detection, SAM structures are the most commonly used. InGaAs-InP SAM SPADs were extensively characterised by Levine *et al.* [62]–[66]. The first InGaAs-InP SPAD operated at 10 MHz at 253 K (-20 °C) with an SPDE of 12 %. Pellegrini *et al.*[67] obtained an SPDE of 10 % with an FWHM of 470 ps. Comandar *et al.* [68] more recently obtained an SPDE of 55% while operating at 500 MHz at room

temperature. Afterpulsing at this frequency was calculated to be 10%. This represents one of the highest SPDE achieved at 1550 nm for an InGaAs-InP SPAD. A commercially available InGaAs-InP SPAD detector module [69] has been used for 3D imagining objects up to 10 km away [70]. The InP in the multiplication layer can be replaced with an InAlAs. Since InAlAs has a more desirable impact ionisation coefficient ratio and has been predicted to have a lower theoretical dark count rate than InP [71]. Meng *et al.* characterised an InGaAs-InAlAs SPAD and obtained an SPDE of 26 % and a DCR of 300 Ms^{-1} while cooled at 210 K. The DCR, in this case, was reportedly due to poor quality InGaAs resulting in a higher than expected dark current. As InGaAs-InAlAs SAM growth and fabrication technique mature, the SPDE is expected to increase.

1.2.5) Single photon detectors (cryogenic cooling)

Superconduction is where a device has zero resistance and occurs when the difference in electron states is less than the phonon energy [72], [73]. At near 0 K, the electrical resistance of metal becomes undetectable. This property has been utilised in two types of single photon detectors, as described below.

Superconducting nanowire single-photon detectors (SNSPDs) operate in a temperature range between 1.5 and 4 K. The nanowire is biased below its critical current. When a photon strikes it, the wire becomes resistive, inducing a voltage which can be measured [74]. The detectors consist of a long thin wire that meanders to increase the detection area of the SNSPDs [75]. Niobium nitride (NbN) is a commonly used material for SNSPDs due to the relatively high transition temperature of 16.11 K [76], although the typical operating temperature is 2-4 K. An SNSPDs has been reported with an SPDE of 57 % at 1550 nm, an FWHM of 41 ps [77], and significantly higher SPDE than previously reported at 17 % [78]. SNSPDs based on Tungsten Silicon achieved an SPDE of 90 % at 1550 nm, one of the highest reported [79]. Although not superconducting recently, an InGaAs-GaAs SAM nanowire was reported with single photon capability operating at 77 K [80]

In a Transmission Edge Sensor (TES), the location of photon absorption sees an increased resistance due to an absorbed photon [81]. The change in resistance is detected as a change in current flow through the voltage-biased device. They can have one of the highest SPDE reported of any detector system, at 95 % at 1556 nm [82] and 98 % at 850 nm [83]. The reset time between photon events can be as long as a couple of µs. A high-speed TES reported with a decay time of 100 ns [84]. While TES have the highest SPDEs available, they have limited bandwidth and require cooling to 300 mK to obtain such a high SPDE.

1.3) III-V Avalanche materials latticed matched to InP

InP is a III-V material which is commercially available as both a device and a substrate for the growth of other materials. InP has a lattice constant of 5.87 Å [85]. The primary use case of III-V detectors over Si is that InP-based detectors can operate at short wave Infrared with materials such as $In_{0.53}Ga_{0.47}As$ acting as an absorption material. This allows alloys optimised for infrared detection and avalanche multiplication to be

growth latticed matched to InP and hence grown on InP substrates to achieve good crystal quality with low defects due to lattice mismatch.

For alloys used for avalanche multiplication, the desirable characteristics are: 1) wide bandgap to minimise band-to-band tunnelling, which is especially important for thin structures where high electric fields are present; 2) dissimilar α and β to minimise excess noise factors for linear mode operation or maximise breakdown probability for Geiger mode operation; 3) a small thermal coefficient of avalanche breakdown (C_{bd}). The smaller the C_{bd} of the device, the less sensitive the breakdown voltage to temperature. This allows for simplistic biasing and thermal stabilising solutions to be viable for the detector system, reducing cost and complexity.

1.3.1) InP

InP is one of the most prominent III-V materials used in APDs, partly due to it being a wide-bandgap material; wafer substrates may be formed from it and materials being latticed matched to it to allow for infrared detection used by the telecommunication industry. InP has a band gap of 1.34 eV [85], resulting in a cut-off wavelength ~ 930 nm. InP has been experimentally characterised for gain and excess noise for both electron [86] and hole injection [87]. For few and single photon detection, InP has been used as the avalanche material for over 5 decades [88] [67]. The impact ionisation coefficients at a temperature of 300 to 150 K for an electric field range of 400 and 800 kV.cm^{-1} were reported [89]. InP is a hole preference material with a beta alpha difference of ×2.3 at 400 kV.cm^{-1}. The temperature-dependent breakdown for InP has been characterised as $\frac{\Delta V_{br}}{\Delta T} = 42.5 \times w + 0.5$[90], which has allowed temperature-based impact ionisation modelling to be verified for both a Simple Monte Carlo model and effective ionisation coefficieints used for simpler models [89].

1.3.2) $In_{0.52}Al_{0.48}As$

$In_{0.52}Al_{0.48}As$ (InAlAs) is a III-V ternary alloy latticed matched to InP. It has a bandgap of 1.45 eV, corresponding to a cut-off wavelength of 860 nm. InAlAs have been extensively characterised for avalanche multiplication, and excess noise [91], and the impact ionisation coefficients, have been reported [91]–[94]. InAlAs was investigated as a potential replacement of InP as the avalanche region of SAM APDs. Its larger ionisation coefficient ratio resulted in a lower excess noise characteristic compared to InP. At low electric fields (350 kV.cm^{-1}), the ratio between α and β is ×12. Additionally, the wider bandgap results in the material being less suspectable to band-to-band tunnelling, allowing for a theoretically lower DCR for narrower SPAD devices than InP.

Additionally, models such as the Simple Monte Carlo model [92] and the Full Band Monte Carlo model [95] have been verified. A theoretical comparison for Geiger mode APD of InAlAs and InP suggests that InP has an advantage over InAlAs for timing response due to the smaller impact ionisation ratio but a lower dark count

rate because of the ratio [71]. InAlAs have also been used for single photon detection work, achieving a PDP of 60 % [96]. InAlAs's $C_d = \frac{\Delta V_{br}}{\Delta T} = 15.3 \times w + 1$[90], for *w* of 0.1-1 µm, which is 1.9-2.7 times smaller C_{bd} than InP for a given *w*.

$In_{0.52}As_{0.48}As$ can be grown as a random alloy and as a digital alloy. A digital alloy is formed by the growing ratio of the monolayers of the two binary materials, InAs and AlAs, to form the full ternary alloy. A digital alloy 600 nm pin device was characterised for excess noise [97] and was found to have a significantly lower excess noise factor than a random alloy pin with a comparable structure [91]. Growth by digital alloy can have an improved growth quality over random alloy by avoiding phase separation. Additionally, the alloy can be designed to suppress hole impact ionisation [93].

1.3.3) $AlAs_{0.56}Sb_{0.44}$

$AlAs_{0.56}Sb_{0.44}$ is a wide indirect bandgap material which has become of much interest in recent years as an alternative to InP and $In_{0.52}Al_{0.48}As$. AlAsSb has a direct bandgap (E_Γ) of 1.96 eV and an indirect bandgap (E_x) of 1.65 eV [98]. Thin AlAsSb devices have shown insignificant band-to-band tunnelling [99] compared to InP and InAlAs due to the wide bandgap. The temperature dependant coefficient of breakdown for the thin devices was found to be 0.95 $mV.K^{-1}$ for *w* = 80 nm [99] and 1.93 $mV.K^{-1}$ for *w* = 230 nm [100]. The C_{bd} due to *w* was calculated to be 8.5 $mV.K^{-1}.\mu m^{-1}$ [101]. An InGaAs/AlAsSb SAM diode was experimentally shown to have a temperature-dependent coefficient of the breakdown of 8 $mV.K^{-1}$ [102] significantly smaller than equivalent InP and $In_{0.52}Al_{0.48}As$ SAM devices. AlAsSb has been characterised for excess noise factor over a wide electric field range [103], [104]. The impact ionisation coefficient for AlAsSb has been parameterised using a local model by Yi *et al.* [105] for an electric field range of 250 – 1250 $kV.cm^{-1}$ and 360 – 1250 $kV.cm^{-1}$ for α and β, respectively. This work was then expanded on to yield temperature-dependent impact ionisation coefficients [101]. Theoretical AlAsSb SPADs has been simulated for *w* between 100 and 2000 nm [106].

1.3.4) $Al_{0.85}Ga_{0.15}As_{0.56}Sb_{0.44}$

$Al_{0.85}Ga_{0.15}As_{0.56}Sb_{0.44}$ (AlGaAsSb) is a quaternary alloy based on $AlAs_{0.56}Sb_{0.44}$, popularised in recent years as an alternative to AlAsAb, which the alloy is based upon. Gallium was added to the structure to help suppress the high surface leakage seen in AlAsSb [107]. As the gallium content increases in the alloy, the surface leakage becomes less dominant; however, the E_g also starts to decrease [98]. $Al_{0.85}Ga_{0.15}As_{0.56}Sb_{0.44}$, like AlAsSb, is an indirect bandgap material, Zhou *et al.* [98] estimated the direct and lowest indirect band gap from extramental photoresponse. The direct bandgap (E_Γ) was determined to be 1.77 eV, and the indirect bandgap (E_x) of 1.56 eV. $Al_{0.85}Ga_{0.15}As_{0.56}Sb_{0.44}$ has grown as a digital alloy, primarily to avoid phase separation at the wafer growth temperature. The bandgap (E_x) was determined in this case to be 1.52 eV [108]. In this

case, Lee *et al.* determined the indirect bandgap from PL measurements of the sample rather than from optical absorption spectrum measurements.

Thin $Al_{0.85}Ga_{0.15}As_{0.56}Sb_{0.44}$ was used to determine the temperature dependant coefficient of breakdown, 1.6 $mV.K^{-1}$ [109], between 24 and 80 °C. Zhou *et al.* calculated the temperature dependant coefficient of breakdown, from phase-sensitive avalanche multiplication, for $Al_{1-x}Ga_xAs_{0.56}Sb_{0.44}$, where x = 0, 0.05, 0.1, and 0.15 for a thin 100 nm p-i-n sample to be 1.07-1.08, 1.03-1.05, 0.95-0.96, and 0.86-0.91 $mV.K^{-1}$ for a temperature range between 77 K and 297 K. Recently, thick AlGaAsSb temperature dependent coefficient of breakdown was determined from the photocurrent of 4.22±0.08 and 5.92 ± 0.36 $mV.K^{-1}$ for a digital and random alloy respectively [110]. It has been suggested that the small temperature of AlGaAsSb is due to significant alloy scattering, which arises due to the differences between As and Sb atom covalent radii [109], indicating a high alloy scattering potential, which is insensitive to temperature [99]. It should also be noted that temperature dependence of breakdown is also affected by the device's width; the narrower the width, the smaller the dependence. Ong *et al.* [111] suggest this is due to the higher electric field in thin devices. At higher electric fields, the average impact ionisation path lengths are reduced, resulting in fewer phonon scattering events. Phonon scattering events are highly dependent on the phonon occupancy factor.

The thin AlGaAsSb has been characterised for avalanche multiplication and excess noise factor [112]. Pinel *et al* experimentally characterised a pair of p-i-n and n-i-p samples with a nominal *w* of 100 and 200 nm for pure injection and two mixed injection profiles. These results confirmed that $\alpha >> \beta$ and that the thin devices exhibited a very strong dead-space effect since the excess noise factor – Avalanche Multiplication did not follow McIntyre local noise model [42]. The optical injection profiles for this work were determined from linear interpolation of the binary alloys [85], [113], [114]. Recently, Guo *et al.* [115] experimentally characterised a 1 µm digital alloy pin to determine the optical absorption coefficient of AlGaAsSb. Lee *et al.* experimentally characterised a digital alloy [108] and random alloy [116] AlGaAsSb pin for close to pure and pure electron injection, respectively. Lee's results show that the excess noise factor of the digital and random alloy both had a McIntyre k value of 0.01, with a breakdown voltage of 53 and 56 V, respectively. Guo *et al.* have then used avalanche multiplication presented previously in the literature [108], [112], [116], including those presented in Chapter 4 of this work [117], to determine the local impact ionisation coefficients using a random path length model [118].

1.3.5) Comparison

A comparison between the impact ionisation coefficient ratio of InP, InAlAs, AlAsb and AlGaAsSb is in Fig. 1.1. InP shows that over a wide electric field range, the ratio between the ionisation coefficients is around 2 times. The InP exhibited the highest $F(M)$ of the compared materials. At 800 $kV.cm^{-1}$ InAlAs exhibit a comparable ionisation ratio to InP. However, as the electric field decreases, the coefficients start to diverge, resulting in a lower $F(M)$ overall. AlAsSb and AlGaAsSb both show a substantial difference in the ionisation coefficient, which has been attributed to low hole impact ionisation in the materials. AlAsSb and AlGaAsSb

are expected to be comparable due to the AlGaAsSb being based on AlAsSb. However, limited studies have been made on the effect Ga has on the impact of ionisation coefficients to date. A study by Lewis *et al.* [119] has, however, indicated a decrease in the coefficient ratio for $Al_{0.75}Ga_{0.25}As_{0.56}Sb_{0.44}$ compared to $Al_{0.85}Ga_{0.15}As_{0.56}Sb_{0.44}$.

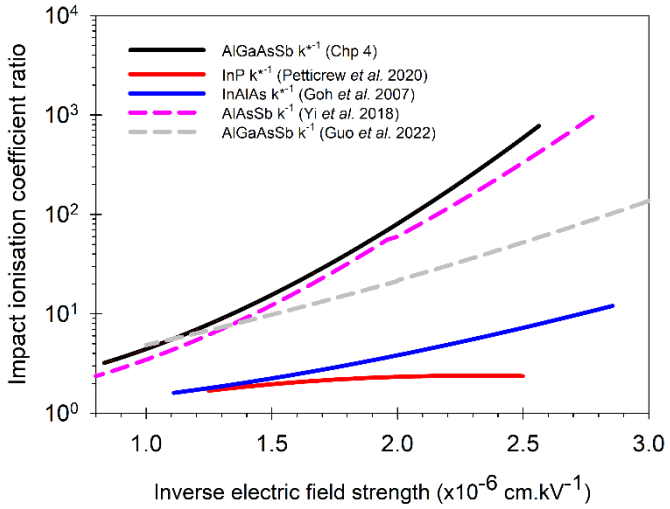

Fig. 1.1 Comparison between impact ionisation coefficient ratio for avalanching multiplication material latticed matched to InP. InP [89] InAlAs [91] AlAsSb [105], and AlGaAsSb [118]

A comparison of experimental excess noise factor at an avalanche multiplication of 10 with respect to the i-region width for some III-V materials is presented in Fig. 1.2. InP, as shown in Fig. 1.1, has an impact ionisation coefficient ratio peak of ~2.3, resulting in a relatively high excess noise at an avalanche multiplication of 10. As the width of the InP high field region increases, so too does the excess noise, tending toward F~5, indicating narrow InP *F(M)* benefits from deadspace. InAlAs, show a similar trend to InP, with an initial low F increasing with increased width up to F~4. Around 1 μm the F(10) starts to decrease. AlAsSb F(10) shows a different trend than InP and InAlAs. The trend seen in InP and InAlAs is also observed in GaAs and AlGaAs.

Narrow AlAsSb exhibited the highest F(10) and decreased with an increase of i-region width. From Fig. 1.1, AlAsSb has a very large impact ionisation coefficient ratio compared to both InP and InAlAs, resulting in a lower F(10). The trend exhibited by AlAsSb in Fig. 1.2 indicates that the increase in impact ionisation coefficient ratio is more significant than the decrease in deadspace to width ratio. AlGaAsSb, similar to AlAsSb, also exhibits a higher F(10) for narrow devices, with thicker devices [108], [116] exhibiting slightly lower F(10) than AlAsSb. The sample characterised in Chp 4, and later, shows exceptionally low F(10), lower than that of InP, InAlAs and AlAsSb.

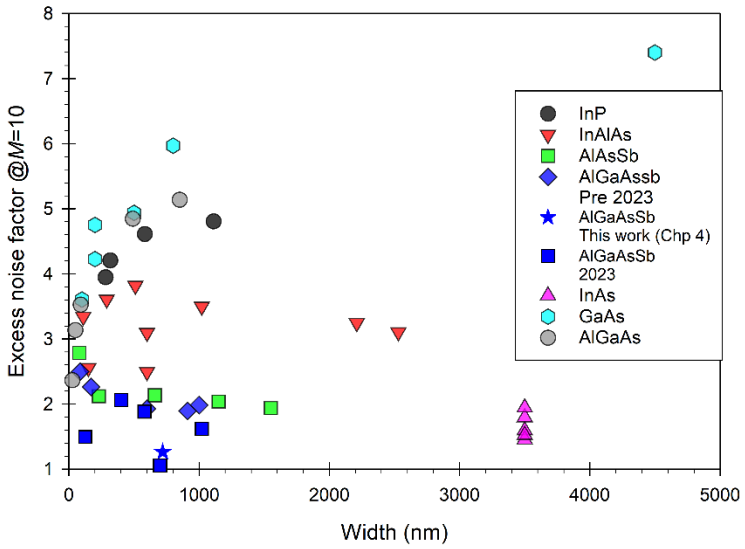

Fig. 1.2 Comparison between Excess noise factor at an avalanche multiplication of 10 for III-V materials. InP[120]–[122] ,$In_{0.52}Al_{0.48}As$ [91], [93], [94], [123], $AlAs_{0.56}Sb_{0.44}$[103], [104], $Al_{0.85}Ga_{0.15}As_{0.56}Sb_{0.44}$ [108], [112], [116], [117], [124]–[127], InAs [128], [129], GaAs [86], [130], [131], $Al_{0.6}Ga_{0.4}As$[132].

1.3.6) $In_{0.53}Ga_{0.47}As$

$In_{0.53}Ga_{0.47}As$ (InGaAs) is a narrow bandgap material that is latticed and matched to InP. InGaAs has a bandgap of 0.75 eV and can detect wavelengths up to 1.7 µm [133]. InGaAs is commonly used as the optical absorption material for telecommunication applications. Due to the narrow bandgap, band-to-band tunnelling current can become the dominant current leakage mechanism at an electric field strength of 200 $kV.cm^{-1}$ and higher [134]. Hence, for a SAM APD design, the absorber's electric field is intentionally low. However, due to tolerances in the doping, higher than expected fields may occur in the practical device, which can have a detrimental effect on the excess noise factor of the device [53]. The avalanche multiplication [134], [135] and excess noise factor [136] have been experimentally measured for high electric fields. Ng *et al.* showed that InGaAs could have non-negligible electron impact ionisation at low electric fields and parameterised the ionisation coefficients [137]. It was determined that impact ionisation could occur in the E_Γ at low energies as well as following the three-valley approximation at higher energies. Electron impact ionisation was also determined to have a positive temperature dependence at low fields. However, at high fields, the ionisation coefficients temperature dependences were negative. Holes, however, exhibited a negative temperature dependence for all electric fields measured [138]. Tan *et al.* developed an ABMC model to simulate the electron impact ionisation rate with regard to temperature Tan *el al.* [139] and Choo *et al.* [140], [141].

1.4) Thesis outline

Chapter 2 gives the background theory for impact ionisation, which yields avalanche multiplication and excess noise in linear mode operated devices and breakdown events in Geiger mode operated devices. Additionally, several models capable of simulating linear and Geiger mode performance are discussed, along with a comparison of III-V latticed materials matched to InP. The experimental methods used to measure a device's performance are discussed in chapter 3, along with simulation models used in this work.

A novel $Al_{0.85}Ga_{0.15}As_{0.56}Sb_{0.44}$ is characterised in chapter 4 for avalanche multiplication and excess noise factor for pure electron injection. A Simple Monte Carlo model parameter set is then verified using these results and those found in the literature. The model is then used to extract the effective ionisation coefficient of the material system between 400 and 1200 $kV.cm^{-1}$.

A theoretical comparison is made between the Simple Monte Carlo and Random Path Length models in chapter 5 for breakdown probability, time to breakdown and jitter. The RPL model represents a significant reduction in simulation runtime compared to the SMC model. However, the RPL is simplistic and can not accurately replicate the SMC's temporal results. In this work, the saturation velocity of the carriers assumed in the RPL model is scaled with the electric field to allow the RPL to replicate the SMC results. Three materials are verified in this work: Si, InP and $Al_{0.85}Ga_{0.15}As_{0.56}Sb_{0.44}$ for a range of devices for w = 100 to 1500 nm.

Chapter 6 verifies a Simple Monte Carlo model parameter set for $In_{0.53}Ga_{0.47}As$ for gain and excess noise factor. The SMC model was modified to capture the low and high electric field impact ionisation seen in the literature.

1.5) References

[1] A. Einstein, 'Über einen die Erzeugung und Verwandlung des Lichtes betreffenden heuristischen Gesichtspunkt', *Ann. Phys.*, vol. 322, no. 6, pp. 132–148, 1905, doi: 10.1002/andp.19053220607.

[2] K. V. S. Badarinath, S. Kumar Kharol, and A. Rani Sharma, 'Long-range transport of aerosols from agriculture crop residue burning in Indo-Gangetic Plains—A study using LIDAR, ground measurements and satellite data', *J. Atmospheric Sol.-Terr. Phys.*, vol. 71, no. 1, pp. 112–120, Jan. 2009, doi: 10.1016/j.jastp.2008.09.035.

[3] M. Hämmerle and B. Höfle, 'Effects of Reduced Terrestrial LiDAR Point Density on High-Resolution Grain Crop Surface Models in Precision Agriculture', *Sensors*, vol. 14, no. 12, pp. 24212–24230, Dec. 2014, doi: 10.3390/s141224212.

[4] J. Estrada, H. Sánchez, L. Hernanz, M. Checa, and D. Roman, 'Enabling the Use of Sentinel-2 and LiDAR Data for Common Agriculture Policy Funds Assignment', *ISPRS Int. J. Geo-Inf.*, vol. 6, no. 8, p. 255, Aug. 2017, doi: 10.3390/ijgi6080255.

[5] V. V. Kirsanov *et al.*, 'Laser Fluorescence and Extinction Methods for Measuring the Flow and Composition of Milk in a Milking Machine', *Photonics*, vol. 8, no. 9, p. 390, Sep. 2021, doi: 10.3390/photonics8090390.

[6] 'The SPLICE Objectives', *QLM Technology Ltd.* https://qlmtec.com/the-splice-objectives/ (accessed Aug. 24, 2022).

[7] S. K. Poultney, 'Single Photon Detection and Timing in the Lunar Laser Ranging Experiment', *IEEE Trans. Nucl. Sci.*, vol. 19, no. 3, pp. 12–17, Jun. 1972, doi: 10.1109/TNS.1972.4326697.

[8] K. König, Ed., *Multiphoton Microscopy and Fluorescence Lifetime Imaging: Applications in Biology and Medicine*. De Gruyter, 2018. doi: 10.1515/9783110429985.

[9] L. Klein, A. S. Kristoffersen, J. Touš, and K. Žídek, 'Versatile compressive microscope for hyperspectral transmission and fluorescence lifetime imaging', *Opt. Express*, vol. 30, no. 9, p. 15708, Apr. 2022, doi: 10.1364/OE.455049.
[10] A. T. Erdogan *et al.*, 'A CMOS SPAD Line Sensor With Per-Pixel Histogramming TDC for Time-Resolved Multispectral Imaging', *IEEE J. Solid-State Circuits*, vol. 54, no. 6, pp. 1705–1719, Jun. 2019, doi: 10.1109/JSSC.2019.2894355.
[11] E. Abdollahi, G. Taucher-Scholz, and B. Jakob, 'Application of fluorescence lifetime imaging microscopy of DNA binding dyes to assess radiation-induced chromatin compaction changes', *Int. J. Mol. Sci.*, vol. 19, no. 8, p. 2399, Aug. 2018, doi: 10.3390/ijms19082399.
[12] C. V. RAMAN and K. S. KRISHNAN, 'A New Type of Secondary Radiation', *Nature*, vol. 121, no. 3048, pp. 501–502, Mar. 1928, doi: 10.1038/121501c0.
[13] F. Ceccarelli, G. Acconcia, A. Gulinatti, M. Ghioni, I. Rech, and R. Osellame, 'Recent Advances and Future Perspectives of Single-Photon Avalanche Diodes for Quantum Photonics Applications', *Adv. Quantum Technol.*, p. 2000102, Dec. 2020, doi: 10.1002/qute.202000102.
[14] N. Gisin, G. Ribordy, W. Tittel, and H. Zbinden, 'Quantum cryptography', *Rev. Mod. Phys.*, vol. 74, no. 1, p. 145, 2002.
[15] W. K. Wootters and W. H. Zurek, 'A single quantum cannot be cloned', *Nature*, vol. 299, no. 5886, p. 802, Oct. 1982, doi: 10.1038/299802a0.
[16] M. Hillery, V. Bužek, and A. Berthiaume, 'Quantum secret sharing', *Phys. Rev. A*, vol. 59, no. 3, pp. 1829–1834, Mar. 1999, doi: 10.1103/PhysRevA.59.1829.
[17] W. P. Grice *et al.*, 'Two-Party secret key distribution via a modified quantum secret sharing protocol', *Opt. Express*, vol. 23, no. 6, p. 7300, Mar. 2015, doi: 10.1364/OE.23.007300.
[18] M. Minder *et al.*, 'Experimental quantum key distribution beyond the repeaterless secret key capacity', *Nat. Photonics*, vol. 13, no. 5, pp. 334–338, May 2019, doi: 10.1038/s41566-019-0377-7.
[19] M. Lucamarini, Z. L. Yuan, J. F. Dynes, and A. J. Shields, 'Overcoming the rate–distance limit of quantum key distribution without quantum repeaters', *Nature*, vol. 557, no. 7705, pp. 400–403, May 2018, doi: 10.1038/s41586-018-0066-6.
[20] H. Iams and B. Salzberg, 'The Secondary Emission Phototube', *Proc. Inst. Radio Eng.*, vol. 23, no. 1, pp. 55–64, Jan. 1935, doi: 10.1109/JRPROC.1935.227243.
[21] S. Cova, M. Bertolaccini, and C. Bussolati, 'The measurement of luminescence waveforms by single-photon techniques', *Phys. Status Solidi A*, vol. 18, no. 1, pp. 11–62, Jul. 1973, doi: 10.1002/pssa.2210180102.
[22] S. Fukuda *et al.*, 'The Super-Kamiokande detector', *Nucl. Instrum. Methods Phys. Res. Sect. Accel. Spectrometers Detect. Assoc. Equip.*, vol. 501, no. 2–3, pp. 418–462, Apr. 2003, doi: 10.1016/S0168-9002(03)00425-X.
[23] 'R5108_TPMS1012E.pdf', *Hamamatsu Photomultiplier tube R5108*. https://www.hamamatsu.com/eu/en/product/optical-sensors/pmt/pmt_tube-alone/side-on-type/R5108.html (accessed Sep. 08, 2022).
[24] 'R5509-43_-73_TPMH1360E.pdf'. Accessed: Aug. 27, 2022. [Online]. Available: https://www.hamamatsu.com/content/dam/hamamatsu-photonics/sites/documents/99_SALES_LIBRARY/etd/R5509-43_-73_TPMH1360E.pdf
[25] 'Photomultiplier tube | Hamamatsu Photonics'. https://www.hamamatsu.com/eu/en/product/optical-sensors/pmt/pmt_tube-alone.html (accessed Aug. 27, 2022).
[26] Hamamatsu, 'Hybrid Photo Detector'.
[27] L. K. van Geest and K. W. J. Stoop, 'Hybrid phototube with Si target', *Nucl. Instrum. Methods Phys. Res. Sect. Accel. Spectrometers Detect. Assoc. Equip.*, vol. 310, no. 1–2, pp. 261–266, Dec. 1991, doi: 10.1016/0168-9002(91)91040-3.
[28] 'HPD_TPMH1361E.pdf'. https://www.hamamatsu.com/resources/pdf/etd/HPD_TPMH1361E.pdf (accessed Aug. 01, 2019).

[29] 'Microchannel plate PMTs (MCP-PMT) | Hamamatsu Photonics'. https://www.hamamatsu.com/eu/en/product/optical-sensors/pmt/pmt_tube-alone/mcp-pmt.html (accessed Aug. 27, 2022).
[30] Hamamatsu, 'R3809U-50_TPMH1067E.pdf'. https://www.hamamatsu.com/content/dam/hamamatsu-photonics/sites/documents/99_SALES_LIBRARY/etd/R3809U-50_TPMH1067E.pdf (accessed Aug. 01, 2019).
[31] A. v. Hippel, 'Der Mechanismus des "elektrischen" Durchschlages in festen Isolatoren. I', *Z. Für Phys.*, vol. 67, no. 11–12, pp. 707–724, Nov. 1931, doi: 10.1007/BF01390754.
[32] C. Zener, 'A theory of the electrical breakdown of solid dielectrics', *Proc. R. Soc. A*, vol. 145, no. 885, p. 7, Mar. 1934, doi: 10.1098/rspa.1934.0116.
[33] K. B. McAfee, E. J. Ryder, W. Shockley, and M. Sparks, 'Observations of Zener Current in Germanium p − n Junctions', *Phys. Rev.*, vol. 83, no. 3, pp. 650–651, Aug. 1951, doi: 10.1103/PhysRev.83.650.
[34] K. G. McKay, 'Avalanche Breakdown in Silicon', *Phys. Rev.*, vol. 94, no. 4, pp. 877–884, May 1954, doi: 10.1103/PhysRev.94.877.
[35] R. H. Haitz, 'Mechanisms Contributing to the Noise Pulse Rate of Avalanche Diodes', *J. Appl. Phys.*, vol. 36, no. 10, pp. 3123–3131, Oct. 1965, doi: 10.1063/1.1702936.
[36] A. G. Chynoweth, 'Uniform Silicon p-n Junctions. II. Ionization Rates for Electrons', *J. Appl. Phys.*, vol. 31, no. 7, pp. 1161–1165, Jul. 1960, doi: 10.1063/1.1735795.
[37] A. G. Chynoweth and K. G. McKay, 'Photon Emission from Avalanche Breakdown in Silicon', *Phys. Rev.*, vol. 102, no. 2, pp. 369–376, Apr. 1956, doi: 10.1103/PhysRev.102.369.
[38] R. H. Haitz, A. Goetzberger, R. M. Scarlett, and W. Shockley, 'Avalanche Effects in Silicon *p—n* Junctions. I. Localized Photomultiplication Studies on Microplasmas', *J. Appl. Phys.*, vol. 34, no. 6, pp. 1581–1590, Jun. 1963, doi: 10.1063/1.1702639.
[39] K. Johnson, 'Photodiode signal enhancement effect at avalanche breakdown voltage', in *1964 IEEE International Solid-State Circuits Conference. Digest of Technical Papers*, Philadelphia, PA, USA: IEEE, 1964, pp. 64–65. doi: 10.1109/ISSCC.1964.1157526.
[40] K. M. Johnson, 'High-speed photodiode signal enhancement at avalanche breakdown voltage', *IEEE Trans. Electron Devices*, vol. 12, no. 2, pp. 55–63, Feb. 1965, doi: 10.1109/T-ED.1965.15453.
[41] R. J. McIntyre, 'Theory of Microplasma Instability in Silicon', *J. Appl. Phys.*, vol. 32, no. 6, pp. 983–995, Jun. 1961, doi: 10.1063/1.1736199.
[42] R. J. McIntyre, 'Multiplication noise in uniform avalanche diodes', *IEEE Trans. Electron Devices*, vol. ED-13, no. 1, pp. 164–168, Jan. 1966, doi: 10.1109/T-ED.1966.15651.
[43] Y. Okuto and C. R. Crowell, 'Energy-Conservation Considerations in the Characterization of Impact Ionization in Semiconductors', *Phys. Rev. B*, vol. 6, no. 8, pp. 3076–3081, Oct. 1972, doi: 10.1103/PhysRevB.6.3076.
[44] P. A. Wolff, 'Theory of Electron Multiplication in Silicon and Germanium', *Phys. Rev.*, vol. 95, no. 6, pp. 1415–1420, Sep. 1954, doi: 10.1103/PhysRev.95.1415.
[45] W. Shockley, 'Problems related to p-n junctions in silicon', *Solid-State Electron.*, vol. 2, no. 1, pp. 35–67, Jan. 1961, doi: 10.1016/0038-1101(61)90054-5.
[46] Y. Okuto and C. R. Crowell, 'Ionization coefficients in semiconductors: A nonlocalized property', *Phys. Rev. B*, vol. 10, no. 10, pp. 4284–4296, Nov. 1974, doi: 10.1103/PhysRevB.10.4284.
[47] W. G. Oldham, R. R. Samuelson, and P. Antognetti, 'Triggering phenomena in avalanche diodes', *IEEE Trans. Electron Devices*, vol. 19, no. 9, p. 5, Sep. 1972.
[48] R. J. McIntyre, 'The distribution of gains in uniformly multiplying avalanche photodiodes: Theory', *IEEE Trans. Electron Devices*, vol. 19, no. 6, pp. 703–713, Jun. 1972, doi: 10.1109/T-ED.1972.17485.
[49] J. Conradi, 'The distribution of gains in uniformly multiplying avalanche photodiodes: Experimental', *IEEE Trans. Electron Devices*, vol. 19, no. 6, p. 6, Jun. 1972.
[50] K. Nishida, K. Taguchi, and Y. Matsumoto, 'InGaAsP heterostructure avalanche photodiodes with high avalanche gain', *Appl. Phys. Lett.*, vol. 35, no. 3, pp. 251–253, Aug. 1979, doi: 10.1063/1.91089.

[51] J. C. Campbell, A. G. Dentai, W. S. Holden, and B. L. Kasper, 'High-performance avalanche photodiode with separate absorption "grading" and multiplication regions', *Electron. Lett.*, vol. 19, no. 20, p. 818, 1983, doi: 10.1049/el:19830558.
[52] F. Capasso, A. Y. Cho, and P. W. Foy, 'Low dark current low voltage 1.3-1.6 um Avalanche Photodiode with high-low electric field profile and separate absorption and multiplication regions by molecular beam epitaxy', *Electron. Lett.*, vol. 20, no. 15, pp. 635–637, 1984, doi: 10.1049/el:19840437.
[53] J. S. Ng, C. H. Tan, J. P. R. David, and G. J. Rees, 'Effect of impact ionization in the InGaAs absorber on excess noise of avalanche photodiodes', *IEEE J. Quantum Electron.*, vol. 41, no. 8, pp. 1092–1096, Aug. 2005, doi: 10.1109/JQE.2005.850700.
[54] S. Cova, A. Longoni, and A. Andreoni, 'Towards picosecond resolution with single-photon avalanche diodes', *Rev. Sci. Instrum.*, vol. 52, no. 3, pp. 408–412, Mar. 1981, doi: 10.1063/1.1136594.
[55] A. Giudice *et al.*, 'High-rate photon counting and picosecond timing with silicon-SPAD based compact detector modules', *J. Mod. Opt.*, vol. 54, no. 2–3, pp. 225–237, Jan. 2007, doi: 10.1080/09500340600763698.
[56] J. D. Petticrew, 'Design and Device fabrication of Silicon Single Photon Avalanche Diodes', PhD Thesis, The University of Sheffield, Department of Electronic and Electrical Engineering, 2020. [Online]. Available: uk.bl.ethos.815542
[57] 'Excelitas Technologies, C30921SH datasheet'.
[58] A. Gulinatti *et al.*, 'New silicon SPAD technology for enhanced red-sensitivity, high-resolution timing and system integration', *J. Mod. Opt.*, vol. 59, no. 17, pp. 1489–1499, Oct. 2012, doi: 10.1080/09500340.2012.701340.
[59] W. Haecker, O. Groezinger, and M. H. Pilkuhn, 'Infrared Photon Counting by Ge Avalanche Diodes', *Appl. Phys. Lett.*, vol. 19, no. 4, pp. 113–115, Aug. 1971, doi: 10.1063/1.1653834.
[60] W. Fichtner and W. Häcker, 'Time resolution of Ge avalanche photodiodes operating as photon counters in delayed coincidence', *Rev. Sci. Instrum.*, vol. 47, no. 3, pp. 374–377, Mar. 1976, doi: 10.1063/1.1134628.
[61] Z. Lu, Y. Kang, C. Hu, Q. Zhou, H.-D. Liu, and J. C. Campbell, 'Geiger-Mode Operation of Ge-on-Si Avalanche Photodiodes', *IEEE J. Quantum Electron.*, vol. 47, no. 5, pp. 731–735, May 2011, doi: 10.1109/JQE.2011.2110637.
[62] B. F. Levine and C. G. Bethea, '10-MHz single photon counting at 1.3 μm', *Appl. Phys. Lett.*, vol. 44, no. 6, pp. 581–582, Mar. 1984, doi: 10.1063/1.94847.
[63] B. F. Levine and C. G. Bethea, 'Detection of single 1.3 μm photons at 45 Mbit/s', *Electron. Lett.*, vol. 20, no. 6, pp. 269–271, Mar. 1984, doi: 10.1049/el:19840180.
[64] B. F. Levine and C. G. Bethea, 'Error rate measurement for single photon detection at 1.3 μm', *Appl. Phys. Lett.*, vol. 44, no. 7, pp. 649–650, Apr. 1984, doi: 10.1063/1.94864.
[65] B. F. Levine and C. G. Bethea, 'Single photon detection at 1.3 μm using a gated avalanche photodiode', *Appl. Phys. Lett.*, vol. 44, no. 5, pp. 553–555, Mar. 1984, doi: 10.1063/1.94800.
[66] B. F. Levine, C. G. Bethea, and J. C. Campbell, 'Near room temperature 1.3 μm single photon counting with a InGaAs avalanche photodiode', *Electron. Lett.*, vol. 20, no. 14, pp. 596–598, Jul. 1984, doi: 10.1049/el:19840411.
[67] S. Pellegrini *et al.*, 'Design and performance of an InGaAs-InP single-photon avalanche diode detector', *IEEE J. Quantum Electron.*, vol. 42, no. 4, pp. 397–403, Apr. 2006, doi: 10.1109/JQE.2006.871067.
[68] L. C. Comandar *et al.*, 'Gigahertz-gated InGaAs/InP single-photon detector with detection efficiency exceeding 55% at 1550 nm', *J. Appl. Phys.*, vol. 117, no. 8, p. 083109, Feb. 2015, doi: 10.1063/1.4913527.
[69] A. Tosi, A. Della Frera, A. Bahgat Shehata, and C. Scarcella, 'Fully programmable single-photon detection module for InGaAs/InP single-photon avalanche diodes with clean and sub-nanosecond gating transitions', *Rev. Sci. Instrum.*, vol. 83, no. 1, p. 013104, Jan. 2012, doi: 10.1063/1.3675579.
[70] A. M. Pawlikowska, A. Halimi, R. A. Lamb, and G. S. Buller, 'Single-photon three-dimensional imaging at up to 10 kilometers range', *Opt. Express*, vol. 25, no. 10, p. 11919, May 2017, doi: 10.1364/OE.25.011919.

[71] S. C. Liew Tat Mun *et al.*, 'A Theoretical Comparison of the Breakdown Behavior of $In_{0.52}Al_{0.48}As$ and InP Near-Infrared Single-Photon Avalanche Photodiodes', *IEEE J. Quantum Electron.*, vol. 45, no. 5, pp. 566–571, May 2009, doi: 10.1109/JQE.2009.2013094.
[72] J. Bardeen, L. N. Cooper, and J. R. Schrieffer, 'Theory of Superconductivity', *Phys. Rev.*, vol. 108, no. 5, pp. 1175–1204, Dec. 1957, doi: 10.1103/PhysRev.108.1175.
[73] H. K. Onnes, 'On the sudden change in the rate at which the resistance of mercury disapears', in *Proceedings of the Koninklijke Akademie van Wetenschappen te Amsterdam*, 1911.
[74] R. H. Hadfield, 'Single-photon detectors for optical quantum information applications', *Nat Photon*, vol. 3, no. 12, pp. 696–705, Dec. 2009, doi: 10.1038/nphoton.2009.230.
[75] A. J. Annunziata *et al.*, 'Reset dynamics and latching in niobium superconducting nanowire single-photon detectors', *J. Appl. Phys.*, vol. 108, no. 8, p. 084507, Oct. 2010, doi: 10.1063/1.3498809.
[76] S. P. Chockalingam, M. Chand, J. Jesudasan, V. Tripathi, and P. Raychaudhuri, 'Superconducting properties and Hall effect of epitaxial NbN thin films', *Phys. Rev. B*, vol. 77, no. 21, p. 214503, Jun. 2008, doi: 10.1103/PhysRevB.77.214503.
[77] K. M. Rosfjord *et al.*, 'Nanowire single-photon detector with an integrated optical cavity and anti-reflection coating', *Opt. Express*, vol. 14, no. 2, p. 527, 2006, doi: 10.1364/OPEX.14.000527.
[78] A. Korneev *et al.*, 'Quantum Efficiency and Noise Equivalent Power of Nanostructured, NbN, Single-Photon Detectors in the Wavelength Range From Visible to Infrared', *IEEE Trans. Appiled Supercond.*, vol. 15, no. 2, pp. 571–574, Jun. 2005, doi: 10.1109/TASC.2005.849923.
[79] F. Marsili *et al.*, 'Detecting single infrared photons with 93% system efficiency', *Nat. Photonics*, vol. 7, no. 3, pp. 210–214, Mar. 2013, doi: 10.1038/nphoton.2013.13.
[80] A. C. Farrell *et al.*, 'InGaAs–GaAs Nanowire Avalanche Photodiodes Toward Single-Photon Detection in Free-Running Mode', *Nano Lett.*, vol. 19, no. 1, pp. 582–590, Jan. 2019, doi: 10.1021/acs.nanolett.8b04643.
[81] K. D. Irwin, 'An application of electrothermal feedback for high resolution cryogenic particle detection', *Appl. Phys. Lett.*, vol. 66, no. 15, pp. 1998–2000, Apr. 1995, doi: 10.1063/1.113674.
[82] A. E. Lita, A. J. Miller, and S. W. Nam, 'Counting near-infrared single-photons with 95% efficiency', *Opt. Express*, vol. 16, no. 5, p. 3032, 2008, doi: 10.1364/OE.16.003032.
[83] D. Fukuda *et al.*, 'Titanium-based transition-edge photon number resolving detector with 98% detection efficiency with index-matched small-gap fiber coupling', *Opt. Express*, vol. 19, no. 2, p. 870, Jan. 2011, doi: 10.1364/OE.19.000870.
[84] D. Fukuda *et al.*, 'Titanium TES based photon number resolving dectors with 1 MHZ counting rate and 65% quantum eficiency.txt', in *The International society for optics and photonics*, 2009.
[85] S. Adachi, *Properties of semiconductor alloys: group-IV, III-V and II-VI semiconductors*. in Wiley series in materials for electronic & optoelectronic applications. Chichester, U.K: Wiley, 2009.
[86] K. F. Li, 'Avalanche Noise in Submicron GaAs and InP Structures', PhD Thesis, University of Sheffield, Department of Electronic and Electrical Engineering, 1999.
[87] L. J. J. Tan, J. S. Ng, C. H. Tan, and J. P. R. David, 'Avalanche Noise Characteristics in Submicron InP Diodes', *IEEE J. Quantum Electron.*, vol. 44, no. 4, pp. 378–382, Apr. 2008, doi: 10.1109/JQE.2007.914771.
[88] B. F. Levine, C. G. Bethea, and J. C. Campbell, 'Room-temperature 1.3-µm optical time domain reflectometer using a photon counting InGaAs/InP avalanche detector', *Appl. Phys. Lett.*, vol. 46, no. 4, pp. 333–335, Feb. 1985, doi: 10.1063/1.95622.
[89] J. D. Petticrew, S. J. Dimler, C. H. Tan, and J. S. Ng, 'Modeling Temperature-Dependent Avalanche Characteristics of InP', *J. Light. Technol.*, vol. 38, no. 4, pp. 961–965, Feb. 2020, doi: 10.1109/JLT.2019.2948072.
[90] L. J. J. Tan *et al.*, 'Temperature Dependence of Avalanche Breakdown in InP and InAlAs', *IEEE J. Quantum Electron.*, vol. 46, no. 8, pp. 1153–1157, Aug. 2010, doi: 10.1109/JQE.2010.2044370.
[91] Y. L. Goh *et al.*, 'Excess Avalanche Noise in $In_{0.52}Al_{0.48}As$', *IEEE J. Quantum Electron.*, vol. 43, no. 6, pp. 503–507, Jun. 2007, doi: 10.1109/JQE.2007.897900.

[92] S. C. Liew Tat Mun, C. H. Tan, Y. L. Goh, A. R. J. Marshall, and J. P. R. David, 'Modeling of avalanche multiplication and excess noise factor in $In_{0.52}Al_{0.48}As$ avalanche photodiodes using a simple Monte Carlo model', *J Appl Phys*, vol. 104, p. 7, 2008, doi: 10.1063/1.2952003.
[93] W. Wang *et al.*, 'Characteristics of thin InAlAs digital alloy avalanche photodiodes', *Opt. Lett.*, vol. 46, no. 16, p. 3841, Aug. 2021, doi: 10.1364/OL.435025.
[94] Y. Yuan *et al.*, 'Temperature dependence of the ionization coefficients of InAlAs and AlGaAs digital alloys', *Photonics Res.*, vol. 6, no. 8, p. 794, Aug. 2018, doi: 10.1364/PRJ.6.000794.
[95] D. Dolgos, H. Meier, A. Schenk, and B. Witzigmann, 'Full-band Monte Carlo simulation of high-energy carrier transport in single photon avalanche diodes with multiplication layers made of InP, InAlAs, and GaAs', *J. Appl. Phys.*, vol. 111, no. 10, p. 104508, May 2012, doi: 10.1063/1.4717729.
[96] X. Meng *et al.*, 'InGaAs/InAlAs single photon avalanche diode for 1550 nm photons', *R. Soc. Open Sci.*, vol. 3, no. 3, p. 150584, Mar. 2016, doi: 10.1098/rsos.150584.
[97] J. Zheng *et al.*, 'Digital Alloy InAlAs Avalanche Photodiodes', *J. Light. Technol.*, vol. 36, no. 17, pp. 3580–3585, Sep. 2018, doi: 10.1109/JLT.2018.2844114.
[98] X. Zhou, S. Zhang, J. P. R. David, J. S. Ng, and C. H. Tan, 'Avalanche Breakdown Characteristics of $Al_{1-x}Ga_xAs_{0.56}Sb_{0.44}$ Quaternary Alloys', *IEEE Photonics Technol. Lett.*, vol. 28, no. 22, pp. 2495–2498, Nov. 2016, doi: 10.1109/LPT.2016.2601651.
[99] S. Xie and C. H. Tan, 'AlAsSb Avalanche Photodiodes With a Sub-mV/K Temperature Coefficient of Breakdown Voltage', *IEEE J. Quantum Electron.*, vol. 47, no. 11, pp. 1391–1395, Nov. 2011, doi: 10.1109/JQE.2011.2165051.
[100] I. C. Sandall, S. Xie, J. Xie, and C. H. Tan, 'High temperature and wavelength dependence of avalanche gain of AlAsSb avalanche photodiodes', *Opt. Lett.*, vol. 36, no. 21, p. 4287, Nov. 2011, doi: 10.1364/OL.36.004287.
[101] X. Jin *et al.*, 'Temperature Dependence of the Impact Ionization Coefficients in AlAsSb Lattice Matched to InP', *IEEE J. Sel. Top. Quantum Electron.*, vol. 28, no. 2: Optical Detectors, pp. 1–8, Mar. 2022, doi: 10.1109/JSTQE.2021.3099912.
[102] Jingjing Xie, Jo Shien Ng, and Chee Hing Tan, 'An InGaAs/AlAsSb Avalanche Photodiode With a Small Temperature Coefficient of Breakdown', *IEEE Photonics J.*, vol. 5, no. 4, pp. 6800706–6800706, Aug. 2013, doi: 10.1109/JPHOT.2013.2272776.
[103] J. Xie, S. Xie, R. C. Tozer, and C. H. Tan, 'Excess Noise Characteristics of Thin AlAsSb APDs', *IEEE Trans. Electron Devices*, vol. 59, no. 5, pp. 1475–1479, May 2012, doi: 10.1109/TED.2012.2187211.
[104] X. Yi *et al.*, 'Extremely low excess noise and high sensitivity $AlAs_{0.56}Sb_{0.44}$ avalanche photodiodes', *Nat. Photonics*, vol. 13, no. 10, pp. 683–686, Oct. 2019, doi: 10.1038/s41566-019-0477-4.
[105] X. Yi *et al.*, 'Demonstration of large ionization coefficient ratio in AlAs0.56Sb0.44 lattice matched to InP', *Sci. Rep.*, vol. 8, no. 1, p. 9107, Dec. 2018, doi: 10.1038/s41598-018-27507-w.
[106] J. Ahmed *et al.*, 'Theoretical Analysis of $AlAs_{0.56}Sb_{0.44}$ Single Photon Avalanche Diodes With High Breakdown Probability', *IEEE J. Quantum Electron.*, vol. 57, no. 2, pp. 1–6, Apr. 2021, doi: 10.1109/JQE.2021.3058356.
[107] X. Zhou, L. L. Pinel, S. J. Dimler, S. Zhang, J. S. Ng, and C. H. Tan, 'Thin Al1-xGaxAs0.56Sb0.44 Diodes With Low Excess Noise', *IEEE J. Sel. Top. Quantum Electron.*, vol. 24, no. 2, pp. 1–5, 2018.
[108] S. Lee *et al.*, 'Low noise $Al_{0.85}Ga_{0.15}As_{0.56}Sb_{0.44}$ avalanche photodiodes on InP substrates', *Appl. Phys. Lett.*, vol. 118, no. 8, p. 081106, Feb. 2021, doi: 10.1063/5.0035571.
[109] S. Abdullah, C. H. Tan, X. Zhou, S. Zhang, L. Pinel, and J. S. Ng, 'Investigation of temperature and temporal stability of AlGaAsSb avalanche photodiodes', *Opt. Express*, vol. 25, no. 26, pp. 33610–33616, Dec. 2017, doi: 10.1364/OE.25.033610.
[110] B. Guo *et al.*, 'Temperature dependence of avalanche breakdown of AlGaAsSb and AlInAsSb avalanche photodiodes', *J. Light. Technol.*, pp. 1–9, 2022, doi: 10.1109/JLT.2022.3185417.
[111] J. S. Ong, J. S. Ng, A. B. Krysa, and J. P. David, 'Temperature dependence of avalanche multiplication and breakdown voltage in Al0. 52In0. 48P', *J. Appl. Phys.*, vol. 115, no. 6, p. 064507, 2014.
[112] L. L. G. Pinel *et al.*, 'Effects of carrier injection profile on low noise thin $Al_{0.85}Ga_{0.15}As_{0.56}Sb_{0.44}$ avalanche photodiodes', *Opt. Express*, vol. 26, no. 3, p. 3568, Feb. 2018, doi: 10.1364/OE.26.003568.

[113] S. Adachi, 'Optical dispersion relations for GaP, GaAs, GaSb, InP, InAs, InSb, $Al_xGa_{1-x}As$, and $In_{1-x}Ga_xAs_yP_{1-y}$', *J. Appl. Phys.*, vol. 66, no. 12, pp. 6030–6040, Dec. 1989, doi: 10.1063/1.343580.

[114] S. Zollner, C. Lin, E. Schönherr, A. Böhringer, and M. Cardona, 'The dielectric function of AlSb from 1.4 to 5.8 eV determined by spectroscopic ellipsometry', *J. Appl. Phys.*, vol. 66, no. 1, pp. 383–387, Jul. 1989, doi: 10.1063/1.343888.

[115] B. Guo *et al.*, 'Optical constants of $Al_{0.85}Ga_{0.15}As_{0.56}Sb_{0.44}$ and $Al_{0.79}In_{0.21}As_{0.74}Sb_{0.26}$', *Appl. Phys. Lett.*, vol. 119, no. 17, p. 171109, Oct. 2021, doi: 10.1063/5.0062035.

[116] S. Lee *et al.*, 'Random alloy thick AlGaAsSb avalanche photodiodes on InP substrates', *Appl. Phys. Lett.*, vol. 120, no. 7, p. 071101, Feb. 2022, doi: 10.1063/5.0067408.

[117] J. Taylor-Mew, V. Shulyak, B. White, C. H. Tan, and J. S. Ng, 'Low Excess Noise of $Al_{0.85}Ga_{0.15}As_{0.56}Sb_{0.44}$ Avalanche Photodiode From Pure Electron Injection', *IEEE Photonics Technol. Lett.*, vol. 33, no. 20, pp. 1155–1158, Oct. 2021, doi: 10.1109/LPT.2021.3110123.

[118] B. Guo *et al.*, 'Impact ionization coefficients of digital alloy and random alloy Al0.85Ga0.15As0.56Sb0.44 in a wide electric field range', *Light. Technol.*, p. 8, doi: 10.1109/JLT.2022.3169008.

[119] H. I. J. Lewis *et al.*, 'Variation in Impact Ionization Coefficients with Alloy Composition in Aluminium-Gallium Containing III-V Compounds', presented at the UK Semiconductors, Sheffield, Jul. 2022.

[120] P. Yuan *et al.*, 'Impact ionization characteristics of III-V semiconductors for a wide range of multiplication region thicknesses', *IEEE J. Quantum Electron.*, vol. 36, no. 2, pp. 198–204, Feb. 2000, doi: 10.1109/3.823466.

[121] R. Wang, Y. Tian, Q. Li, and Y. Zhao, 'High gain and low excess noise InGaAs/InP avalanche photodiode with lateral impact ionization', *Appl. Opt.*, vol. 59, no. 7, p. 1980, Mar. 2020, doi: 10.1364/AO.382001.

[122] Y. Takanashi and Y. Horikoshi, 'Temperature Dependence of Ionization Coefficients for InP and 1.3 μm InGaAsP Avalanche Photodiodes', *Jpn. J. Appl. Phys.*, vol. 20, no. 10, p. 1907, Oct. 1981, doi: 10.1143/JJAP.20.1907.

[123] N. Li *et al.*, 'InGaAs/InAlAs avalanche photodiode with undepleted absorber', *Appl. Phys. Lett.*, vol. 82, no. 13, pp. 2175–2177, Mar. 2003, doi: 10.1063/1.1559437.

[124] X. Collins *et al.*, 'Low-noise AlGaAsSb avalanche photodiodes for 1550nm light detection', in *Optical Components and Materials XIX*, M. J. Digonnet and S. Jiang, Eds., San Francisco, United States: SPIE, Mar. 2022, p. 16. doi: 10.1117/12.2608842.

[125] X. Collins *et al.*, 'Low-noise AlGaAsSb avalanche photodiodes for 1550 nm light detection', in *Optical Components and Materials XX*, M. J. Digonnet and S. Jiang, Eds., San Francisco, United States: SPIE, Mar. 2023, p. 24. doi: 10.1117/12.2651669.

[126] S. Lee *et al.*, 'High gain, low noise 1550 nm GaAsSb/AlGaAsSb avalanche photodiodes', *Optica*, vol. 10, no. 2, p. 147, Feb. 2023, doi: 10.1364/OPTICA.476963.

[127] Y. Cao, T. Blain, and J. D. Taylor-Mew, 'Extremely low excess noise avalanche photodiode with GaAsSb absorption region and AlGaAsSb avalanche region', *Appl. Phys. Lett.*, 2023, doi: 10.1063/5.0139495.

[128] A. R. J. Marshall, C. H. Tan, M. J. Steer, and J. P. R. David, 'Extremely Low Excess Noise in InAs Electron Avalanche Photodiodes', *IEEE Photonics Technol. Lett.*, vol. 21, no. 13, pp. 866–868, Jul. 2009, doi: 10.1109/LPT.2009.2019625.

[129] P. J. Ker, J. P. R. David, and C. H. Tan, 'Temperature dependence of gain and excess noise in InAs electron avalanche photodiodes', *Opt. Express*, vol. 20, no. 28, p. 29568, Dec. 2012, doi: 10.1364/OE.20.029568.

[130] G. E. Bulman, V. M. Robbins, and G. E. Stillman, 'The determination of impact ionization coefficients in (100) gallium arsenide using avalanche noise and photocurrent multiplication measurements', *IEEE Trans. Electron Devices*, vol. 32, no. 11, pp. 2454–2466, Nov. 1985, doi: 10.1109/T-ED.1985.22295.

[131] C. Hu, K. A. Anselm, B. G. Streetman, and J. C. Campbell, 'Excess noise in GaAs avalanche photodiodes with thin multiplication regions', *IEEE J. Quantum Electron.*, vol. 33, no. 7, pp. 1089–1093, Jul. 1997, doi: 10.1109/3.594870.

[132] Chee Hing Tan, J. P. R. David, S. A. Plimmer, G. J. Rees, R. C. Tozer, and R. Grey, 'Low multiplication noise thin $Al_{0.6}Ga_{0.4}As$ avalanche photodiodes', *IEEE Trans. Electron Devices*, vol. 48, no. 7, pp. 1310–1317, Jul. 2001, doi: 10.1109/16.930644.

[133] D. A. Humphreys, R. J. King, D. Jenkins, and A. J. Moseley, 'Measurement of absorption coefficients of $Ga_{0.47}In_{0.53}As$ over the wavelength range 1.0–1.7 μm', *Electron. Lett.*, vol. 21, no. 25–26, p. 1187, 1985, doi: 10.1049/el:19850839.

[134] J. S. Ng, 'Impact ionisation measurement and modelling of long wavelength avalanche photodiodes', Ph.D dissertation, University of Sheffield, Department of Electronic and Electrical Engineering, 2003.

[135] Y. L. Goh, 'Impact Ionisation in InGaAs, InAlAs and InGaAs/GaAsSb Superlattices for Near Infrared Avalanche Photodetectors', Ph.D dissertation, University of Sheffield, Department of Electronic and Electrical Engineering, 2008.

[136] Yu Ling Goh, Jo Shien Ng, Chee Hing Tan, W. K. Ng, and J. P. R. David, 'Excess noise measurement in $In_{0.53}$ Ga $_{0.47}As$', *IEEE Photonics Technol. Lett.*, vol. 17, no. 11, pp. 2412–2414, Nov. 2005, doi: 10.1109/LPT.2005.857239.

[137] J. S. Ng, C. H. Tan, J. P. R. David, G. Hill, and G. J. Rees, 'Field dependence of impact ionization coefficients in $In_{0.53}$ Ga $_{0.47}As$', *IEEE Trans. Electron Devices*, vol. 50, no. 4, pp. 901–905, Apr. 2003, doi: 10.1109/TED.2003.812492.

[138] W. K. Ng, C. H. Tan, J. P. R. David, P. A. Houston, M. Yee, and J. S. Ng, 'Temperature dependent low-field electron multiplication in $In_{0.53}$ Ga $_{0.47}As$', *Appl. Phys. Lett.*, vol. 83, no. 14, pp. 2820--2822, 2003, doi: 10.1063/1.1615684.

[139] C. H. Tan, G. J. Rees, P. A. Houston, J. S. Ng, W. K. Ng, and J. P. R. David, 'Temperature dependence of electron impact ionization in $In0._{0.53}Ga_{0.47}As$', *Appl. Phys. Lett.*, vol. 84, no. 13, p. 2322, 2004, doi: 10.1063/1.1691192.

[140] K. Y. Choo and D. S. Ong, 'Analytical band Monte Carlo simulation of electron impact ionization in $In0._{0.53}Ga_{0.47}As$', *J. Appl. Phys.*, vol. 96, no. 10, pp. 5649–5653, Nov. 2004, doi: 10.1063/1.1803930.

[141] K. Y. Choo and D. S. Ong, 'Positive and negative temperature dependences of electron-impact ionization in $In0._{0.53}Ga_{0.47}As$', *J. Appl. Phys.*, vol. 98, no. 2, p. 023714, Jul. 2005, doi: 10.1063/1.1993755.

Chapter 2

Background Theory

2.1) Impact ionisation

Impact ionisation is the process of an electron-hole pair being generated by the loss of energy of another free carrier. The energy loss occurs when a carrier with sufficiently high energy strikes the material lattice to promote the electron-hole pair. An electron-hole pair is not generated if the initial carrier does not impart enough energy to exceed the energy band gap.

2.1.1) Avalanche Multiplication

Avalanche Multiplication (*M*), also known as gain, is a current amplification process where a free carrier gains sufficient energy under an electric field (ξ) to create a secondary (daughter) electron-hole pair by impacting the lattice. The original carrier energy is reduced by the process, with the energy being transferred to the daughter electron-hole pair. The process is repeated for all free carriers and will continue until it leaves the area under the electric field called the depletion width. This is often referred to as the linear mode of operation of the device. The average number of impact ionisation events per initial carrier is known as Avalanche Multiplication. An example of an energy band diagram with impact ionisation is presented in Fig. 2.1

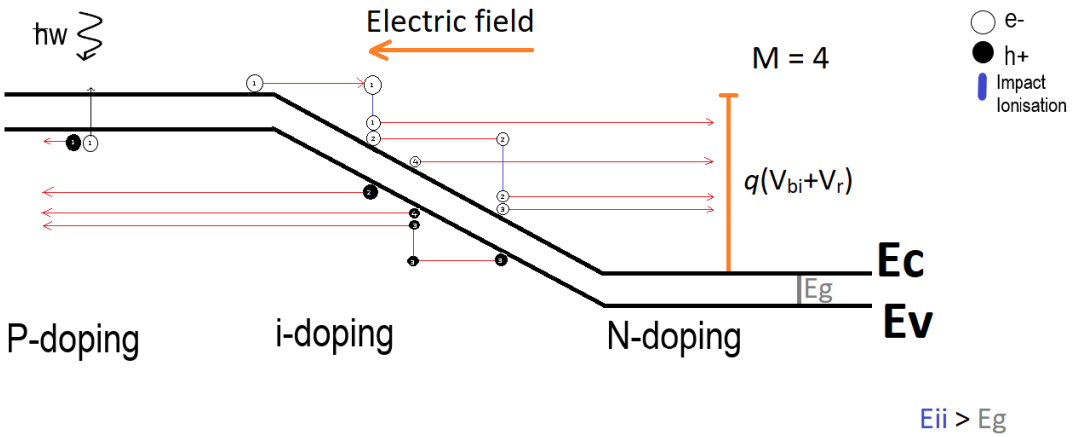

Fig. 2.1. Example of Impact ionisation for a linear mode p-i-n diode

The rate of impact ionisation events per unit distance is called the impact ionisation coefficient, with symbols α and β for electrons and holes, respectively. α and β are dependent on the applied electric field and is typically expressed as

$$\alpha(\xi) = \mathrm{A}\exp\left[-\left(\frac{\mathrm{B}}{\xi}\right)^{\mathrm{c}}\right] \mathrm{cm}^{-1}, \tag{2.1}$$

where A, B, and C are fitting parameters for a given material.

In a practical device, a carrier will deviate from this average distance depending on the instantaneous energy of the carrier, which gives rise to an excess noise factor. This distribution of impact ionisation as a function of ionisation path lengths is characterised by the probability density function (PDF), $h_e(x)$ and $h_h(x)$ for electrons and holes.

The distribution of impact ionisation is also affected by the carrier's history, giving rise to the term dead space. Dead space is used to describe the minimum distance a carrier may travel through an electric field until it gains sufficient energy to undergo impact ionisation. If a carrier has recently undergone impact ionisation, it must gain sufficient energy before it can impact ionise again, giving rise to the name deadspace. For ease, a hard dead space approximation is commonly used, and $h_{e(h)}(x)$is described by [1]

$$h_e(x) = \begin{cases} 0, & x \le d_e \\ \alpha^* exp[-\alpha^*(x - d_e)], & x > d_e \end{cases} \tag{2.2a}$$

$$h_h(x) = \begin{cases} 0, & x \le d_h \\ \beta^* exp[-\beta^*(x - d_h)], & x > d_h \end{cases} \tag{2.2b}$$

An example of $h_e(x)$, Fig. 2.2, illustrates the effect hard deadspace has on the impact ionisation path length PDF. α assumes no deadspace is present, and α* assumes a hard deadspace value.

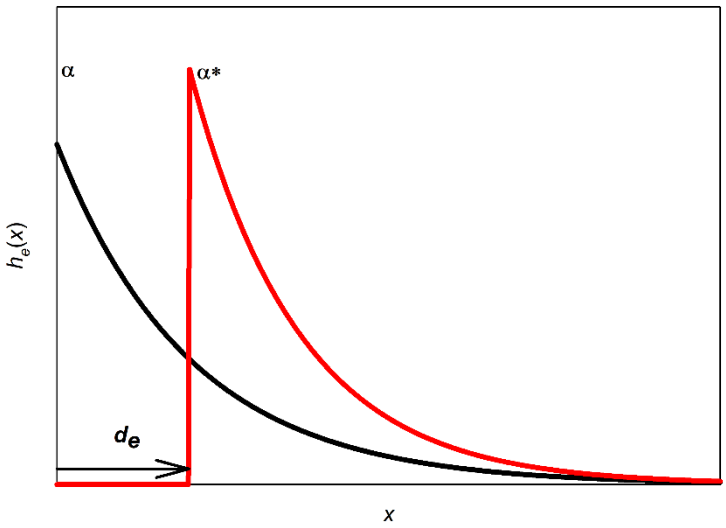

Fig. 2.2. Example of $h_{e(h)}(x)$ with (α) and without (α) deadspace*

α^* (β^*) denotes the effective impact ionisation coefficients of electrons (holes), where dead space has been extracted or separated from the coefficient. The effective impact ionisation coefficients can be calculated from impact ionisation coefficients by

$$\alpha^*(\xi) = \frac{1}{\frac{1}{\alpha(\xi)} - d_e(\xi)}, \tag{2.3}$$

The dead space value is material specific and inversely proportional to the applied electric field. Since dead space is related to a carrier gaining sufficient energy as it travels along the electric field, carriers may initiate impact ionisation with different carrier's energy and hence *x*. An example ionisation path length PDF in Appendix C (Fig. C1) illustrates this distribution of *x*. In practice, dead space is related to a carrier's energy, and if a carrier gains sufficient energy, it may impact ionise before this distance, giving rise to the concept of soft dead space. Soft dead space more accurately describes the impact ionisation path length; however, parameterising it is non-trivial.

The excess noise factor (*F*) describes the electrical noise generated by the randomness in the impact ionisation process. Because impact ionisation is a stochastic process, each photogenerated carrier will yield a different number of impact ionisation events. It is this randomness which gives rise to excess noise given by

$$F = \frac{\langle m_i{}^2 \rangle}{\langle m_i \rangle^2} = \frac{\langle m_i{}^2 \rangle}{M^2} \tag{2.4}$$

The brackets indicate an average where m_i is the avalanche multiplication achieved in a single trial.

2.2) Geiger devices

Geiger mode is an operating region of an APD where the applied voltage causes the electric field to be above the critical breakdown point. By doing this, a single injected carrier may, upon impact ionisation, causes an avalanche cascade where the current increases indefinitely and is self-sustaining, whereas in linear mode devices, shown previously, the current will eventually stop. The onset of the self-sustaining avalanche current defines the Breakdown Voltage (V_{br}). The current in the device does not decay but instead increases indefinitely, giving an avalanche multiplication of infinite. Practically the current is limited either by contact resistance or thermally. The temperature coefficient of breakdown voltage (C_{bd}) described how the breakdown voltage varies with temperature. C_{bd} is material, and device structure dependent and is desired to be as low as possible to allow for predictable response. Therefore as the current increases, so too does the device's temperature; hence V_{br} increases. Avalanche breakdown does not occur in e-APD material such as InAs as the holes do not practically impact ionise. Hence no build-up in avalanche current is possible.

Geiger mode devices are typically used for single and low photon detection because of this cascade avalanche effect.

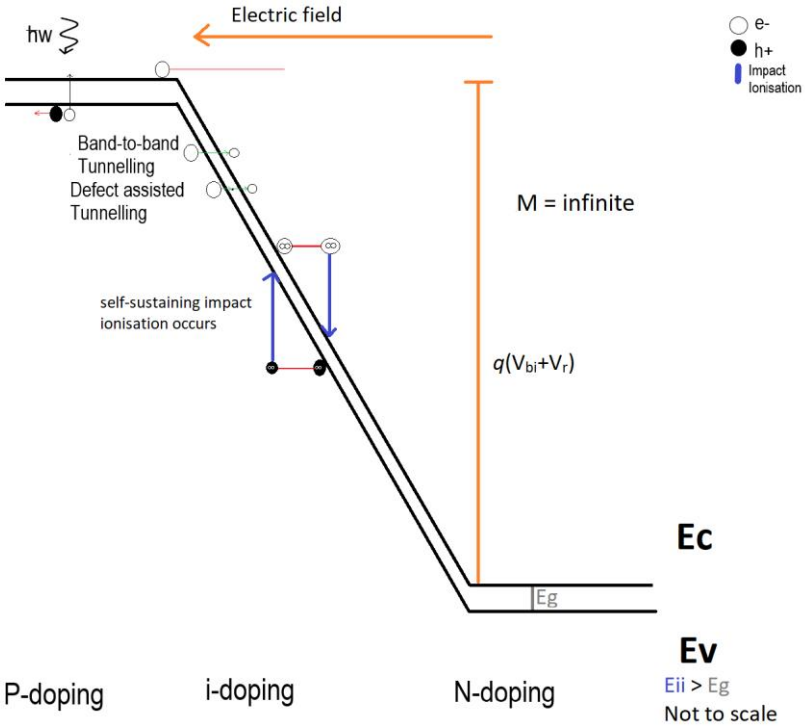

Fig. 2.3 Example of the energy band structure of a p-i-n device operating in the Geiger region

2.2.1) Dark Count Rate

A dark (false) count occurs when a SPAD undergoes a self-starting avalanche breakdown event without a photogenerated free carrier. Hence a dark count gives rise to a false event count; hence DCR is an error parameter for determining the quality of a SPAD. The mechanisms that can give rise to dark count generation include band-to-band tunnelling, trap-assisted tunnelling, thermal excitation and after-pulsing [2].

Band-to-band tunnelling occurs when the electrons in the valence band can tunnel through the forbidden region to the conduction band [3]. The forbidden region is between the valence band's highest energy and the conduction band's lowest energy state, also referred to as the bandgap energy (E_g). The forbidden region is devoid of available energy states, so a carrier would have to have enough energy to go from the valance band to the conduction band. The distance a carrier would need to tunnel between the two bands (w_{tun}) is described by [4]

$$w_{tun} = \frac{E_g}{qE}, \tag{2.5}$$

and is dependent upon both the energy bandgap of the material and the applied electric field. Band-to-band tunnelling can be reduced through the choice of avalanche material, device structure and control of the electric field profile.

Trap-assisted tunnelling occurs when defects in the material cause an energy state to occur in the forbidden region. This effectively adds an energy level in the forbidden region, allowing valance band electrons to require lower energy to rise up to the conduction band. This, combined with thermal excitation, will cause a significant increase in dark counts. Trap-assisted tunnelling typically occurs due to issues that arise through wafer growth and processing. Hence it can be unpredictable for III-V alloy devices.

After-pulsing can occur when a carrier falls into a trap and is released when the device is active, creating a breakdown event [5]. After-pulsing can also occur due to a failed quench [6]. The trapped carrier may have originated from a previously absorbed photon or from a previous breakdown event. A trap may be formed from defects similar to trap-assisted tunnelling. A hold-off time is introduced to limit the after-pulsing effect of a device. Hold-off or dead time is when the device is inactive and allows the trapped carriers to recombine without causing an event. The hold-off time can vary between nanoseconds and microseconds, limiting the device's maximum operating frequency.

Thermal excitation is where the carriers can gain enough thermal energy to promote themselves. For electrons, this is the valence band to the conduction band and the inverse for holes. This can significantly increase dark counts for devices with narrow bandgaps. It has been reported that the absorber in an InGaAs/InP SPAD exhibited significant amounts of thermal excitation [7]. Dark counts from thermal excitation can be reduced by cooling the devices with cryogenics or thermoelectric cooling (TEC).

2.2.2) Probability of detection efficiency

The probability of detection efficiency is the probability that a photon-initiated event is achieved. Typically Single Photon Detection Efficient (SPDE) is used when referring to Geiger mode APDs. A SPAD's PDE is given by

$$PDE = \eta \times P_b \tag{2.6}$$

Where η is external quantum efficiency and P_b is breakdown probability. The external quantum efficiency is the product of the probability that the photon is absorbed (P_a), generates an electron-hole pair and the probability that the carrier will transition (P_t) into the avalanche region of the diode before recombination in the case of a Separate Absorption Multiplication (SAM) APD. Breakdown probability is the probability that an injected electron-hole pair will result in an avalanche breakdown event. An avalanche breakdown event occurs when a SPAD generates a self-sustaining avalanche current that an external circuit must quench. In this work, 100 µA is used to define when a breakdown event occurs. For high-speed switching applications, source-load impedance matching is used, with 50 Ω being the standard. For 100 µA, a 5 mV pulse will be induced, which is reliably detectable experimentally [8]. Breakdown probability increases as the applied bias increases

above breakdown, which is termed overbias. For an array of SPADs, the PDE will include a fill factor to account for a portion of the optical opening of the device that is not optically active.

2.2.3) Jitter

Jitter is the variation in time between a photon's absorption and the avalanche current being detected. Jitter is a important metric for time-correlated applications, such as time of flight used in distance measuring. For time-of-flight measurements, every picosecond of jitter results in an error of 150 µm in the calculated distance. Typically jitter of a device is in the order of 100's ps, or ~1.5 cm of uncertainty. The jitter of a device is affected by the device structure and the materials used for absorption and avalanche. The location of where a photon is absorbed and the shape of the electric field profile will impact the time taken to build up the avalanche current [9].

2.2.4) Linear mode SPADs

High avalanche multiplication linear mode APDs can detect a single photon level of light. While this is possible for Geiger mode-capable devices to operate like this [10], this approach is far more common for e-APD materials such as InAs. InAs is an unusual material as only electrons can practically impact ionisation [11] at operating electric fields. Typically InAs APDs are operated at low electric fields (<70 $kV.cm^{-1}$) to limit tunnelling current due to the bandgap of 0.34 eV [12]. InAs can not operate in Geiger mode due to no hole impact ionisation at these low electric fields. Hence no self-sustaining avalanche can take place. InAs, however, can detect few single photons due to high multiplication [13] and low non-rising excess noise. The advantage InAs has over Geiger-mode APDs is the speed of response; all carriers will leave the device within two transience periods. An advantage of linear mode SPAD, in general, is that no additional quenching circuitry is required as the impulse current is finite.

Additionally, it is possible to determine the number of photon-initiated events by analysing the device's instantaneous current, as each event will change the output pulse. With Geiger mode APDs the output has only two states, high and low, as the first event will mask any other photon-initiated events. The disadvantage is that additional circuitry is required for detection as the instantaneous current from a single event decays quickly.

2.3) Quenching Circuits

In Geiger mode operation, when a SPAD has a breakdown event, the current must be quenched to reset the SPAD so it can continue to detect. The SPAD can only detect a single event at a time; whether it is dark or photon initiated, the user can not tell. During breakdown, the SPAD is blind and can not detect another event until the current is quenched and the SPAD operating bias reset. To quench the breakdown current

additional external circuitry is required to reduce the bias across the SPAD to below the breakdown voltage. Many different quenching circuits are possible, which can be generalised into three basic groups: Passive, Gated, and Active [14] [15].

2.3.1) Passive quenching

Passive quenching is the simplest quenching mechanism consisting of a high valve ballast resistor, typically in the order of 100's kΩ. The ballast resistor is placed in series with the SPAD between a static voltage bias supply and the ground. An example of the quenching mechanism circuit is presented in Fig. 2.4. When the SPAD breakdown, the current through the series connection increases; hence a voltage is induced across the ballast resistor. Since the bias supply is held at a static voltage, the voltage across the SPAD reduces and continues to reduce until the voltage across the SPAD is at or just below the breakdown voltage, placing the SPAD in the linear mode operation. Hence the SPAD breakdown current is quenched. The advantage of this quenching method is the ease with which it may be set up and incorporated, requiring only a resistor. The disadvantage of this method is that the SPAD will be partially quenched as the current build to the detectable level, which could lead to non-detectable events being quenched or a longer build-up time is required.

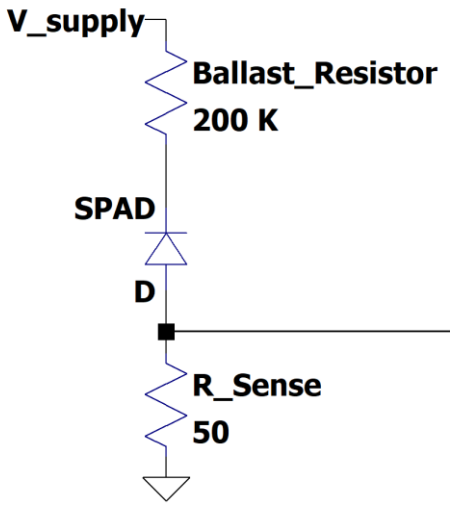

Fig. 2.4 An example of a passive Quenching circuit

2.3.2) Gated quenching

Gated quenching works by utilising two bias sources, one static (sometimes termed Dc) and one pulsed (sometimes termed Ac). The two sources are combined, using a bias tee, with the static bias source being set to slightly below breakdown. A simplified circuit is shown in Fig. 2.5. When the pulsed source is high, the total applied bias is greater than the breakdown voltage, and when the pulsed source is low, the SPAD is biased out of the Geiger region, and hence the SPAD is quenched. Commonly the pulsed source is a square wave, but any waveform can be used, with sinusoidal gating also being used [16], [17]. For the characterisation of novel

materials, the square waveform is optimal for accurate knowledge of the applied voltage for P_b calculations. The advantage of this quenching method is that it allows for easy time correlation of the events. However, due to the capacitive nature of the diode, transience effects are seen on the rising and falling edge of the pulse signal, with the rising edge overshooting resulting in a higher probability of a dark count occurring. The overshoot will exhibit a ringing decay to the intended bias level.

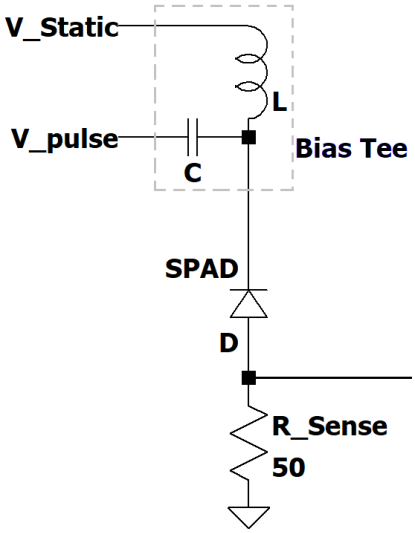

Fig. 2.5 An example of a gated quenching circuit

For a well-behaved SPAD under a constant bias, the dark count occurs at a random time. Using a gated or active quenching method, described later, recording when the dark count occurs is possible to ensure this behaviour holds [18]. Using this method, it is also possible to determine the shape of the over bias pulse from the pulse bias source that the SPAD has seen. Since dark events occur randomly over a long measurement period, the events should show no trend. If a trend is seen in the distribution, it is indicative of a change in applied bias, which changes the P_b, such as the rise and fall time of the gated signal and transience [19]. This method can be used to examine the after-pulse effect of the pile-up of the dark counts early in the over bias period.

One variation of gated quenching highlighted here is Capacitive quenching [20]. Capacitate quenching uses the capacitor on the bias tee as a charge storage device. The capacitor is charged on the rising edge of the pulse bias, and on the falling edge, the capacitor is discharged. On the rising and falling edge of the square pulse, there is no voltage drop across the capacitor, as the voltage change is instantaneous, so the SPAD sees the pulse voltage for biasing. However, once (dis)charged, the same capacitor blocks the pulse voltage as the bias is in a steady state. When the SPAD breakdown, the current through the SPAD increases, causing the capacitor to discharge. As the capacitor discharges, the bias applied to the SPAD starts to drop, $i = C\frac{\Delta V}{\Delta t}$. Since the pulse bias is now in steady-state the capacitor discharges, and does not recharge due to the steady-state. Once the capacitor is fully discharged, the bias applied to the SPAD is only due to the static bias source. Hence,

the SPAD is quenched and can not break down until the capacitor is recharged on the rising pulse edge. The advantage of this method is the SPAD is quenched as soon as it breakdown rather than waiting for the gate period to end. This helps reduce the heating effect of the SPAD and protects the SPAD from unnecessary long periods of high current flows.

2.3.3) Active quenching

The SPAD is biased above the breakdown voltage in active quenching until a breakdown event is detected. When the event is detected, the circuitry drops the bias seen by the SPAD for a predetermined period, after which the SPAD is rebiased [15]. This is one of the most complex quenching mechanisms due to the high-frequency detection and switching required. Active quenching is preferable to gated as the device is always active, like passive quenching, making the method more versatile as the incident photon does not need to be injected at a specific time. Making this method preferable for applications such as LiDAR.

2.4) Impact ionisation models

Several models exist for simulations of impact ionisation characteristics, including avalanche multiplication, excess noise factor, breakdown probability, and time to breakdown. Five models commonly used for this are described below in increasing order of complexity: Local, Recurrence, Random Path Length, Simple Monte Carlo, and Full / Analytical Band Monte Carlo models. The simulation model selection depends on the complexity of the desired results and the simulation runtime. In general, the more complex the model, the longer the simulation runtime.

2.4.1) Local model

The local model, popularised by McIntyre [21], uses impact ionisation coefficients to model a device of width, *w*. The model assumes all impact ionisation events are dependent on the local electric field, and the history of the impacting carrier does not influence the probability of impact ionisation. Due to the latter assumption, the local model is generally considered to be valid for devices with a large avalanche multiplication width. This assumption holds for avalanche multiplication; however, some deviation can be seen with $F(M)$, especially for low-noise materials.

In the local model avalanche multiplication is calculated as,

$$M(x) = \frac{\exp\left[-\int_0^x (\alpha(x') - \beta(x'))d_{x'}\right]}{1 - \int_0^w \alpha(x') \exp\left[-\int_0^{x'} (\alpha(x'') - \beta(x''))d_{x''}\right]} \tag{2.7}$$

where x defines the starting position of the initial electron-hole pair. The electrons move from 0 to x and holes move in the opposite direction. For an ideal p-i-n where the electric field in the i-region is constant, the equation may be simplified to

$$M(x) = \frac{(\alpha - \beta)\exp[-(\alpha - \beta)x]}{\alpha\, exp[-(\alpha - \beta)w] - \beta} \tag{2.8}$$

This can be simplified further for the pure electron (M_e) and hole (M_h) avalanche multiplication. For M_e the initial injection condition is $x = 0$. For M_h the initial condition is $x = w$. These result in

$$M_e = \frac{\alpha - \beta}{\alpha\, exp[-(\alpha - \beta)w] - \beta} \tag{2.9}$$

and

$$M_h = \frac{(\alpha - \beta)\exp[-(\alpha - \beta)w]}{\alpha\, exp[-(\alpha - \beta)w] - \beta} \tag{2.10}$$

Since the local model only requires α and β, we can extract these from thick experimental devices with a well-defined high electric field region by rearranging eq. (2.9) and eq. (2.10). With experimental values of $M_e(\xi)$ and $M_h(\xi)$, α and β are calculated using

$$\alpha(\xi) = \frac{1}{w}\left(\frac{M_e(\xi) - 1}{M_e(\xi) - M_h(\xi)}\right)\ln\left(\frac{M_e(\xi)}{M_h(\xi)}\right) \tag{2.11}$$

and

$$\beta(\xi) = \frac{1}{w}\left(\frac{M_h(\xi) - 1}{M_h(\xi) - M_e(\xi)}\right)\ln\left(\frac{M_h(\xi)}{M_e(\xi)}\right) \tag{2.12}$$

For excess noise factor (F), the local model may also be used to determine the pure electron excess noise factor (F_e) and pure hole (F_h) as follows.

$$F_e(M_e) = kM_e + \left(2 - \frac{1}{M_e}\right)(1 - k) \tag{2.13}$$

and

$$F_h(M_h) = \frac{k}{M_h} - \left(2 - \frac{1}{M_h}\right)\left(1 - \frac{1}{k}\right) \tag{2.14}$$

Where k is the ratio between the secondary ionisation coefficient and primary coefficient. For example, for InAlAs, $k = \beta/\alpha$ and InP, $k = \alpha/\beta$. This k referred to McIntyre k-line is often quoted as a figure of merit for devices. Using the local model, the lowest F will occur at a $k = 0$ and will result in $F(M)$ tending toward 2 at a high gain. Experimentally we see an $F(M)$ increases as w decreases, which the local model follows. However, for small values of w, the $F(M)$ starts to decrease due to the dead space effect, which the local model can not follow due to the initial assumptions. Hence the local model is invalid for thin devices and high electric field modelling, such as Geiger mode. Where the local model stops being valid is dependent on the specific material.

2.4.2) Recurrence model

The recurrence equations for avalanche gain were developed in [1] and use probability densities of the impact ionisation path lengths for electrons $h_e(x)$ and holes $h_h(x)$, eq (2.2). The recurrence model uses coupled integral equations that, when solved, will yield $M(V)$ and $F(M)$ in the following example,

$$M(x) = \frac{\big(Z(x') + Y(x')\big)}{2} \tag{2.15}$$

and

$$F = \frac{Z_2(x') + 2Z(x')Y(x') + Y_2(x')}{\big(Z(x') + Y(x')\big)^2} \tag{2.16}$$

Where x' is the primary carrier's initial position, $Z(x')$ is the number of generated electrons, and $Y(x')$ is the number of generated holes.

$$Z(x') = 1 - (w - x')\int_{-\infty}^{x'} h_e(x)dx + \int_{x'}^{w} \langle 2Z(x) + Y(x)\rangle h_e(x - x')dx \tag{2.17}$$

$$Y(x') = 1 - \int_{-\infty}^{x'} h_h(x)\,dx + \int_{0}^{x'} \langle 2Y(x) + Z(x)\rangle h_h(x' - x)dx \tag{2.18}$$

Where the first half of the term represents if the carrier does not impact ionise and the second half of the term is if the carrier does impact ionise. $h_e(x)$ and $h_h(x)$ were previously defined in equation (2.2). $Z_2(x')$ and $Y_2(x')$ are the mean squared values of $Z(x')$ and $Y(x')$.

$$Z(x') = 1 - (w - x')\int_{-\infty}^{x'} h_e(x)dx + \int_{x'}^{w} \big(2Z_2(x) + Y_2(x) + 4Z(x)Y(x) + 2Z_2(x)\big)h_e(x - x')dx \tag{2.19}$$

and

$$Y(x') = 1 - \int_{-\infty}^{x'} h_h(x)dx + \int_{x'}^{w} \big(2Y(x) + Z_2(x) + 4Z(x)Y(x) + 2Y_2(x)\big)h_h(x' - x)dx \tag{2.20}$$

The recurrence model utilises the hard dead space approximation allowing it to more accurately model excess noise factor and thin devices compared to the local model. The recurrence equations have also been developed to calculate stable APD impulse currents [22], [23] and breakdown probability in Geiger mode APDs [24].

2.4.3) Random Path Length model

The Random Path Length (RPL) [25] model is one of the simplest Monte Carlo-based models. The RPL model uses the effective impact ionisation coefficients and hard dead space. The effective impact ionisation coefficients exist for several materials, such as Si [26], InP [27], [28], $In_{0.52}Al_{0.53}As$ [29], [30], $Al_xGa_{1-x}As$ (x = 0, 0.15, 0.3, 0.6) [31], $Al_{0.8}Ga_{0.2}As$ [32], $Al_{0.52}In_{0.48}P$ [33], $Ga_{0.52}In_{0.48}P$ [34], 4H-SiC [35], and InAs [36]. The parametrised ionisation coefficient is extracted from fitting [1] probability density functions to simulate the impact ionisation path lengths.

The random path lengths, l, are calculated by[25]

$$l_{e(h)} = d_{e(h)} - \frac{\ln(r)}{\alpha^*(\beta^*)} \tag{2.21}$$

Where r is a random number between 0 and 1, this process works by injecting an initial carrier between distance (x) of 0 and w, where $x = 0$ is for electron injection, $x = w$ is for hole injection and $0 < x < w$ is for mixed injection. Therefore, electrons travel in a positive direction and holes in a negative direction. The initial carrier then travels l, length. In the case of electrons, if $x_{initial} + l_e < w$, then the carrier has an impact ionised, and the model generates a daughter electron-hole pair at this location. This process is repeated until all carriers, initial and generated via impact ionisation, have left the depletion width. The total number of impact ionisation events is recorded, and this is m_i for that trial. The trial is then repeated a statistically significant number of times (20 k) to generate avalanche multiplication and excess noise factor. Using the saturation velocity for the material and Ramo's theory [37], the instantaneous current may be calculated. The RPL model simulates Geiger mode for breakdown probability and temporal results. By comparing when the instantaneous current exceeds a predetermined value, typically 100 µA.

The RPL model is commonly favoured for designing novel APDs due to the higher degree of accuracy than the local model, especially for thin devices, without a significant time penalty for linear mode APD design and simplistic implementation. For Geiger mode APDs the RPL is typically considered too simplistic, due to the saturation velocity assumption, to model temporal results such as time to breakdown and jitter [26]. It has been suggested that the saturation velocity is a poor assumption for a free carrier which will impact ionise shortly after dead space length has been achieved [38], such as narrow and Geiger mode operated APDs. In a Geiger mode, APD, the carrier has a significantly higher probability of impact ionising than linear mode. Hence for a trial that will yield a breakdown event, the carrier could be travelling at an enhanced velocity, higher than the saturation velocity. Using simulation data from a more complex model such as the Simple Monte Carlo model, a fitting may be applied to the saturation velocity to account for the expected change and hence allow the RPL to replicate the temporal results of a more complex model with a significant reduction in time.

2.4.4) Simple Monte Carlo model

The Simple Monte Carlo (SMC) model, originally developed by Plimmer [39] to model GaAs, is more complex than the previous model. The SMC model uses energy dependant scattering rates to model impact ionisation results to approximate a single parabolic band rather than a band structure. The model was expanded to model InP [28], $In_{0.52}Al_{0.48}As$ [40], $In_{0.48}Ga_{0.52}P$ [41], $Al_xGa_{x-1}As$ [42] [43], Si [44] [26], $Al_{0.85}Ga_{0.15}As_{0.56}Sb_{0.44}$ [45] and, $In_{0.53}Ga_{0.47}As$. A compilation of SMC model parameters is presented in Appendix H. The SMC calculates and models three scattering rates, with the fourth being an optional and material dependant: Intervalley phonon emission (R_{em}), Intervalley phonon absorption (R_{ab}), Impact ionisation scattering (R_{ii}) and Alloy scattering (R_{alloy}), where applicable. Where the rates are calculated from the following equations,

$$R_{em} = \frac{N(T)+1}{\lambda\,(2N(T)+1)}\sqrt{\frac{2(E_c-\hbar\omega)}{m^*}}, \tag{2.22}$$

and

$$R_{ab} = \frac{N(T)}{\lambda\,(2N(T)+1)}\sqrt{\frac{2(E_c+\hbar\omega)}{m^*}}, \tag{2.23}$$

$\hbar\omega$ is phonon energy, m^* is the effective mass of the free carrier, E_c is the carrier's energy, λ is the mean free path, T is temperature, and $N(T)$ is the temperature-dependent phonon occupation factor. $N(T)$ is given by

$$N(T) = \left(\exp\left(\frac{\hbar\omega}{k_bT}\right)-1\right)^{-1}, \tag{2.24}$$

where k is Boltzmann's constant. R_{ii} is calculated using the Keldysh equation [46]

$$R_{ii} = C_{ii}\left(\frac{E_c - E_{th}}{E_{th}}\right)^{\gamma}, \tag{2.25}$$

where C_{ii} is the prefactor of impact ionisation rate, E_{th} is the SMC model's threshold energy for impact ionisation, and γ is the softness factor. The threshold energy for impact ionisation, E_{th} is calculated from the weighted average three valley approximation [47],

$$E_{th} = \frac{E_\Gamma + 3E_x + 4E_L}{8} \tag{2.26}$$

Where E_Γ, E_x and E_L are the three valleys for the material

Alloy scattering rate (R_{alloy}) [40], [48] is given by

$$R_{alloy} = C_{alloy} (m^*)^{\frac{3}{2}} \sqrt{E_c}, \tag{2.27}$$

where C_{alloy} is an alloy constant. For each carrier type (electron and hole), a probability table is generated for the scattering mechanisms, weighted by the magnitude of the rates. A random number generator is used to determine which scattering mechanism is chosen for the intended carrier.

The SMC has been used to model both avalanche multiplication and excess noise factor by fitting the rate equations to the available literature. Individual parameters may be found in literature, such as E_{th} and $\hbar\omega$, but some are specific to the model, such as m^* and λ, so they have to be modified for the SMC to model results from the literature. The SMC has also been shown to model breakdown probability and temporal results. However, due to the lack of experimental results for validation, it is validated against other models.

2.4.5) Analytical and Full Band Monte Carlo model

Full Band Monte Carlo (FBMC) is a complex model that simulates the materials' full band structure, which can then be used to model the parameters of a material, such as drift velocity. FBMC exist for materials such as Si [49], GaAs [50], InP [51], InAlAs [52] and recently AlInAsSb [53] as a digital alloy. Analytical Band Monte Carlo (ABMC) models are computationally less intense than FBMC by using analytical models to describe the band structures. AMBC are commonly used to model carrier transport. Models exist for $In_{0.53}Ga_{0.47}As$ [54], InAs, AlAs, AlGaAs [55], GaAs, GaSb [56]. Occasionally FBMC and AMBC are used for modelling impact ionisation simulations for linear and Geiger modes [57].

References: Chapter 2

[1] M. M. Hayat, B. E. A. Saleh, and M. C. Teich, 'Effect of dead space on gain and noise of double-carrier-multiplication avalanche photodiodes', *IEEE Trans. Electron Devices*, vol. 39, no. 3, pp. 546–552, Mar. 1992, doi: 10.1109/16.123476.

[2] F. Zappa, S. Tisa, A. Tosi, and S. Cova, 'Principles and features of single-photon avalanche diode arrays', *Sens. Actuators Phys.*, vol. 140, no. 1, pp. 103–112, Oct. 2007, doi: 10.1016/j.sna.2007.06.021.

[3] G. A. M. Hurkx, D. B. M. Klaassen, and M. P. G. Knuvers, 'A new recombination model for device simulation including tunneling', *IEEE Trans. Electron Devices*, vol. 39, no. 2, pp. 331–338, Feb. 1992, doi: 10.1109/16.121690.
[4] W. J. Kindt, 'Geiger Mode Avalanche Photodiode Arrays: For spatially resolved single photon counting', Delft University, Electrical Engineering, Mathematics and Computer Science, 1999.
[5] S. Cova, A. Lacaita, and G. Ripamonti, 'Trapping phenomena in avalanche photodiodes on nanosecond scale', *IEEE Electron Device Lett.*, vol. 12, no. 12, pp. 685–687, Dec. 1991, doi: 10.1109/55.116955.
[6] M. Stipčević, 'Active quenching circuit for single-photon detection with Geiger mode avalanche photodiodes', *Opt. Soc. Am.*, vol. 48, no. 9, p. 1705, 2009, doi: 10.1364/AO.48.001705.
[7] M. A. Itzler *et al.*, 'Single photon avalanche diodes (SPADs) for 1.5 µm photon counting applications', *J. Mod. Opt.*, vol. 54, no. 2–3, pp. 283–304, Jan. 2007, doi: 10.1080/09500340600792291.
[8] I. Rech, D. Resnati, A. Gulinatti, M. Ghioni, and S. Cova, 'Self-suppression of reset induced triggering in picosecond SPAD timing circuits', *Rev. Sci. Instrum.*, vol. 78, no. 8, p. 086112, Aug. 2007, doi: 10.1063/1.2772779.
[9] A. Spinelli and A. L. Lacaita, 'Physics and numerical simulation of single photon avalanche diodes', *IEEE Trans. Electron Devices*, vol. 44, no. 11, pp. 1931–1943, Nov. 1997, doi: 10.1109/16.641363.
[10] B. F. Levine, C. G. Bethea, and J. C. Campbell, 'Near room temperature 1.3 µm single photon counting with a InGaAs avalanche photodiode', *Electron. Lett.*, vol. 20, no. 14, pp. 596–598, Jul. 1984, doi: 10.1049/el:19840411.
[11] A. R. J. Marshall, J. P. R. David, and C. H. Tan, 'Impact Ionisation in InAs Electron Avalanche Photodiodes', *IEEE Trans. Electron Devices*, vol. 57, no. 10, pp. 2631–2638, Oct. 2010, doi: 10.1109/TED.2010.2058330.
[12] T. Osman, L. W. Lim, J. S. Ng, and C. H. Tan, 'Fabrication of infrared linear arrays of InAs planar avalanche photodiodes', *Opt. Express*, vol. 30, no. 12, p. 21758, Jun. 2022, doi: 10.1364/OE.460017.
[13] C. H. Tan, A. Velichko, L. W. Lim, and J. S. Ng, 'Few-photon detection using InAs avalanche photodiodes', *Opt. Express*, vol. 27, no. 4, p. 5835, Feb. 2019, doi: 10.1364/OE.27.005835.
[14] S. Cova, M. Ghioni, A. Lacaita, C. Samori, and F. Zappa, 'Avalanche photodiodes and quenching circuits for single-photon detection', *Appl. Opt.*, vol. 35, no. 12, p. 1956, Apr. 1996, doi: 10.1364/AO.35.001956.
[15] A. Gallivanoni, I. Rech, and M. Ghioni, 'Progress in Quenching Circuits for Single Photon Avalanche Diodes', *IEEE Trans. Nucl. Sci.*, p. 5658087, Dec. 2010, doi: 10.1109/TNS.2010.2074213.
[16] C. Scarcella, G. Boso, F. Acerbi, A. Ruggeri, A. D. Frera, and A. Tosi, '100 Mcount/s InGaAs/InP single-photon detector', in *Quantum Sensing and Nanophotonic Devices XI*, Jan. 2014, vol. 8993, p. 89932F. doi: 10.1117/12.2040189.
[17] C. Scarcella, G. Boso, A. Ruggeri, and A. Tosi, 'InGaAs/InP Single-Photon Detector Gated at 1.3 GHz With 1.5% Afterpulsing', *IEEE J. Sel. Top. Quantum Electron.*, vol. 21, no. 3, pp. 17–22, May 2015, doi: 10.1109/JSTQE.2014.2361790.
[18] S. J. Dimler, 'A capacitive quenching characterisation system for Single Photon Avalanche Diodes and Avalanche Photodiodes', PhD Thesis, University of Sheffield, Department of Electronic and Electrical Engineering, 2015.
[19] A. Cominelli, G. Acconcia, I. Labanca, M. Ghioni, and I. Rech, 'Accurate non-invasive measurement of the turn-on transition of fast gated single photon avalanche diodes', *Rev. Sci. Instrum.*, vol. 90, no. 3, p. 033102, Mar. 2019, doi: 10.1063/1.5056222.
[20] S. J. Dimler, J. S. Ng, R. C. Tozer, G. J. Rees, and J. P. R. David, 'Capacitive Quenching Measurement Circuit for Geiger-Mode Avalanche Photodiodes', *Sel. Top. Quantum Electron. IEEE J. Of*, vol. 13, no. 4, pp. 919–925, Aug. 2007, doi: 10.1109/JSTQE.2007.903595.
[21] R. J. McIntyre, 'Multiplication noise in uniform avalanche diodes', *IEEE Trans. Electron Devices*, vol. ED-13, no. 1, pp. 164–168, Jan. 1966, doi: 10.1109/T-ED.1966.15651.
[22] M. M. Hayat and B. E. A. Saleh, 'Statistical properties of the impulse response function of double-carrier multiplication avalanche photodiodes including the effect of dead space', *J. Light. Technol.*, vol. 10, no. 10, pp. 1415–1425, Oct. 1992, doi: 10.1109/50.166785.

[23] M. M. Hayat and D. A. Ramirez, 'Multiplication theory for dynamically biased avalanche photodiodes: new limits for gain bandwidth product', *Opt. Express*, vol. 20, no. 7, p. 8024, Mar. 2012, doi: 10.1364/OE.20.008024.
[24] R. J. McIntyre, 'A new look at impact ionisation-part I: A theory of gain, noise, breakdown probability, and frequency response', *IEEE Trans. Electron Devices*, vol. 46, no. 8, pp. 1623–1631, Aug. 1999, doi: 10.1109/16.777150.
[25] D. S. Ong, K. F. Li, G. J. Rees, J. P. R. David, and P. N. Robson, 'A simple model to determine multiplication and noise in avalanche photodiodes', *J. Appl. Phys.*, vol. 83, no. 6, pp. 3426–3428, 1998, doi: 10.1063/1.367111.
[26] J. D. Petticrew, S. J. Dimler, X. Zhou, A. P. Morrison, C. H. Tan, and J. S. Ng, 'Avalanche Breakdown Timing Statistics for Silicon Single Photon Avalanche Diodes', *IEEE J. Sel. Top. Quantum Electron.*, vol. 24, no. 2, 2018, doi: 10.1109/JSTQE.2017.2779834.
[27] L. J. J. Tan, J. S. Ng, C. H. Tan, and J. P. R. David, 'Avalanche Noise Characteristics in Submicron InP Diodes', *IEEE J. Quantum Electron.*, vol. 44, no. 4, pp. 378–382, Apr. 2008, doi: 10.1109/JQE.2007.914771.
[28] J. D. Petticrew, S. J. Dimler, C. H. Tan, and J. S. Ng, 'Modeling Temperature-Dependent Avalanche Characteristics of InP', *J. Light. Technol.*, vol. 38, no. 4, pp. 961–965, Feb. 2020, doi: 10.1109/JLT.2019.2948072.
[29] Y. L. Goh *et al.*, 'Excess Avalanche Noise in $In_{0.52}Al_{0.48}As$', *IEEE J. Quantum Electron.*, vol. 43, no. 6, pp. 503–507, Jun. 2007, doi: 10.1109/JQE.2007.897900.
[30] S.-C. L. T. Mun, 'Characterisation of quantum dot infrared photodetectors and modelling of $In_{0.52}Al_{0.48}As$ linear and Geiger mode avalanche photodiodes', PhD Thesis, University of Sheffield, Department of Electronic and Electrical Engineering, 2008.
[31] S. A. Plimmer, J. P. R. David, G. J. Rees, and P. N. Robson, 'Ionisation coefficients in $Al_x Ga_{1-x} As$ (x = 0 - 0.60)', *Semicond. Sci. Technol.*, vol. 15, no. 7, pp. 692–699, Jul. 2000, doi: 10.1088/0268-1242/15/7/307.
[32] B. K. Ng *et al.*, 'Avalanche multiplication characteristics of $Al_{0.8}Ga_{0.2}As$ diodes', *IEEE Trans. Electron Devices*, vol. 48, no. 10, pp. 2198–2204, Oct. 2001, doi: 10.1109/16.954454.
[33] J. S. L. Ong, J. S. Ng, A. B. Krysa, and J. P. R. David, 'Impact Ionization Coefficients in $Al_{0.52}In_{0.48}P$', *IEEE Electron Device Lett.*, vol. 32, no. 11, pp. 1528–1530, Nov. 2011, doi: 10.1109/LED.2011.2165520.
[34] R. Ghin *et al.*, 'Avalanche multiplication and breakdown in $Ga_{0.52}In_{0.48}P$ diodes', *IEEE Trans. Electron Devices*, vol. 45, no. 10, pp. 2096–2101, Oct. 1998, doi: 10.1109/16.725241.
[35] W. S. Loh *et al.*, 'Impact Ionization Coefficients in 4H-SiC', *IEEE Trans. Electron Devices*, vol. 55, no. 8, pp. 1984–1990, Aug. 2008, doi: 10.1109/TED.2008.926679.
[36] A. R. J. Marshall, P. Vines, P. J. Ker, J. P. R. David, and C. H. Tan, 'Avalanche Multiplication and Excess Noise in InAs Electron Avalanche Photodiodes at 77 K', *IEEE J. Quantum Electron.*, vol. 47, no. 6, pp. 858–864, Jun. 2011, doi: 10.1109/JQE.2011.2128299.
[37] S. Ramo, 'Currents Induced by Electron Motion', *Proc. IRE*, vol. 27, no. 9, pp. 584–585, Sep. 1939, doi: 10.1109/JRPROC.1939.228757.
[38] P. J. Hambleton, J. P. R. David, and G. J. Rees, 'Enhanced carrier velocity to early impact ionisation', *J. Appl. Phys.*, vol. 95, no. 7, pp. 3561–3564, Apr. 2004, doi: 10.1063/1.1646434.
[39] S. A. Plimmer, J. P. R. David, D. S. Ong, and K. F. Li, 'A simple model for avalanche multiplication including deadspace effects', *IEEE Trans. Electron Devices*, vol. 46, no. 4, pp. 769–775, Apr. 1999, doi: 10.1109/16.753712.
[40] S. C. Liew Tat Mun, C. H. Tan, Y. L. Goh, A. R. J. Marshall, and J. P. R. David, 'Modeling of avalanche multiplication and excess noise factor in $In_{0.52}Al_{0.48}As$ avalanche photodiodes using a simple Monte Carlo model', *J Appl Phys*, vol. 104, p. 7, 2008, doi: 10.1063/1.2952003.
[41] C. H. Tan, R. Ghin, J. P. R. David, G. J. Rees, and M. Hopkinson, 'The effect of dead space on gain and excess noise in $In_{0.48} Ga_{0.52} P$ p in diodes', *Semicond. Sci. Technol.*, vol. 18, no. 8, pp. 803–806, Aug. 2003, doi: 10.1088/0268-1242/18/8/314.

[42] S. A. Plimmer, 'Avalanche multiplication in $Al_xGa_{1-x}As$', Ph.D dissertation, University of Sheffield, Department of Electronic and Electrical Engineering, 1997.
[43] C. K. Chia and G. K. Dalapati, 'Monte Carlo Simulation of Hot Carrier Transport in Heterogeneous Ge/Al_xGa_{1-x} As (0<x<0.8) Multilayer Avalanche Photodiodes', *IEEE Trans. Electron Devices*, vol. 60, no. 10, pp. 3435–3441, Oct. 2013, doi: 10.1109/TED.2013.2275970.
[44] X. Zhou, J. S. Ng, and C. H. Tan, 'A simple Monte Carlo model for prediction of avalanche multiplication process in Silicon', *J. Instrum.*, vol. 7, no. 08, p. P08006, 2012, doi: 10.1088/1748-0221/7/08/P08006.
[45] J. D. Taylor-Mew, J. D. Petticrew, C. H. Tan, and J. S. Ng, 'Simulation of $Al_{0.85}Ga_{0.15}As_{0.56}Sb_{0.44}$ avalanche photodiodes', *Opt. Express*, vol. 30, no. 11, p. 17946, May 2022, doi: 10.1364/OE.458922.
[46] L. V. Keldysh, 'Kinetic theory of impact ionisation in semiconductors', *Sov Phys JETP*, vol. 37, no. 10, pp. 509–518, 1960.
[47] J. Allam, '"Universal" Dependence of Avalanche Breakdown on Bandstructure: Choosing Materials for High-Power Devices', *Jpn. J. Appl. Phys.*, vol. 36, no. Part 1, No. 3B, pp. 1529–1542, Mar. 1997, doi: 10.1143/JJAP.36.1529.
[48] M. A. Littlejohn, J. R. Hauser, T. H. Glisson, D. K. Ferry, and J. W. Harrison, 'Alloy scattering and high field transport in ternary and quaternary III–V semiconductors', *Solid-state Electronics*, vol. 21, no. 1, pp. 107–114, 1978, doi: 10.1016/0038-1101(78)90123-5.
[49] T. Kunikiyo *et al.*, 'A Monte Carlo simulation of anisotropic electron transport in silicon including full band structure and anisotropic impact-ionisation model', *J. Appl. Phys.*, vol. 75, no. 1, p. 297, 1994, doi: 10.1063/1.355849.
[50] J. Požela and A. Reklaitis, 'Electron transport properties in GaAs at high electric fields', *Solid-State Electron.*, vol. 23, no. 9, pp. 927–933, Sep. 1980, doi: 10.1016/0038-1101(80)90057-X.
[51] K. Brennan and K. Hess, 'Theory of high-field transport of holes in GaAs and InP', *Phys. Rev. B*, vol. 29, no. 10, pp. 5581–5590, May 1984, doi: 10.1103/PhysRevB.29.5581.
[52] D. Dolgos, H. Meier, A. Schenk, and B. Witzigmann, 'Full-band Monte Carlo simulation of high-energy carrier transport in single photon avalanche diodes with multiplication layers made of InP, InAlAs, and GaAs', *J. Appl. Phys.*, vol. 111, no. 10, p. 104508, May 2012, doi: 10.1063/1.4717729.
[53] J. Zheng *et al.*, 'Full band Monte Carlo simulation of AlInAsSb digital alloys', *InfoMat*, vol. 2, no. 6, pp. 1236–1240, Nov. 2020, doi: 10.1002/inf2.12112.
[54] C. H. Tan, G. J. Rees, P. A. Houston, J. S. Ng, W. K. Ng, and J. P. R. David, 'Temperature dependence of electron impact ionisation in $In0._{0.53}Ga_{0.47}As$', *Appl. Phys. Lett.*, vol. 84, no. 13, p. 2322, 2004, doi: 10.1063/1.1691192.
[55] H. Arabshahi, M. R. Khalvati, and M. R. Rokn-Abadi, 'Temperature and doping dependencies of electron mobility in InAs, AlAs and AlGaAs at high electric field application', *Braz. J. Phys.*, vol. 38, no. 3a, Sep. 2008, doi: 10.1590/S0103-97332008000300001.
[56] H. Arabshahi, 'Calculation of High Field Electron Transport Properties in GaSb and GaAs', *Int. J. Sci. Adv. Technol.*, vol. 1, no. 4, Jun. 2009.
[57] D. Dolgos, H. Meier, A. Schenk, and B. Witzigmann, 'Full-band Monte Carlo simulation of single photon avalanche diodes', in *2013 IEEE Photonics Conference*, Bellevue, WA, USA, Sep. 2013, pp. 360–361. doi: 10.1109/IPCon.2013.6656586.

Chapter 3

Experimental Procedures and Simulation Models

3.1 Current-Voltage

Current-Voltage (I-V) measurements are typically the first form of electrical characterisation an APD or SPAD will undergo to determine device performance and uniformity. They are performed using a Source-Measure-Unit (SMU), which can simultaneously supply a voltage and measure the resultant current. There are many types of information that could be obtained from I-V data. Typical uses include (i) assessing the significance of contact resistance, (ii) quickly establishing if the device exhibits diode-like characteristics, (iii) providing an indicative breakdown voltage, (iv) identifying the dominant leakage mechanism(s), and (v) assess the uniformity of devices across the sample. All of these are important for further photodiode/APD characterisation.

The I-V measurements used either an HP4140B Picoammeter or a Keithley 236 SMU. Alternative SMUs (Keithley 237, 238 or Agilent B1505A) may be used if a higher supply voltage (> 110 V) or currents (>100 mA) is required. These are connected to a pair of probe positioners for the anode and cathode connections.

3.1.1 Forward Bias I-V measurement

Forward bias I-V can be used to estimate the series resistance (R_s) of the diode. In an ideal diode under forwarding bias, the diode's dark current is given by

$$I_f(V) = I_0 \left[\exp\left(\frac{qV}{nk_bT}\right) - 1\right], \tag{3.1}$$

where I_0 is the forward saturation current at 0 V, n is the ideality factor of the diode ($1 < n < 2$), k_b is Boltzmann's constant, and T is the temperature (in Kelvin). The ideal forward I-V characteristics with n = 1 or 2 are compared in Fig. 3.1. The gradient of the characteristics in this log-linear plot is $^{q}/_{nk_bT}$.

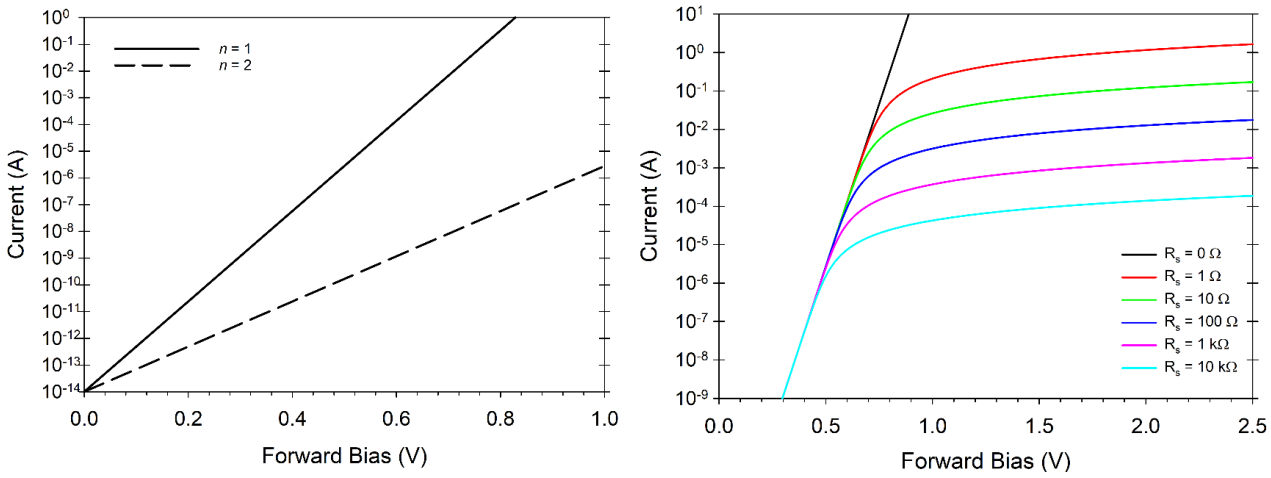

Fig. 3.1 Calculated forward Current-Voltage characteristics of diodes with I_0 = 10 fA and ideality factor of 1 or 2 (L). Calculated forward Current-Voltage of diodes with I_0 = 10 fA and ideality factor of 1 for R_s = 0 to 10 kΩ. (R).

In a practical diode, the presence of series resistance (R_s) modifies Eqn. (3.1) into

$$I_f(V) = I_0\left[\exp\left(\frac{q(V-I_fR_s}{nk_bT}\right)-1\right]. \tag{3.2}$$

Two methods of solving Eqn (3.2) for R_s and n are described here. In the first method, Eqn. (3.2) is rearranged to [1]

$$V = \frac{nk_bT}{q}\ln(I_f) - \frac{nk_bT}{q}\ln(I_0) + I_fR_s. \tag{3.3}$$

Differentiating Eqn. (3.3) with respect to I_f yields

$$\frac{dV}{dI_f} = \frac{nk_bT + R_sqI_f}{qI_f}. \tag{3.4}$$

By plotting $I_f\frac{dV_f}{dI_f}$ against I_f, values of R_s and n can be determined from the gradient and the y-intercept, respectively. In practice, however, uncertainty in experimental results may produce non-linear characteristics of $I_f\frac{dV_f}{dI_f}$ against I_f, preventing reliable extraction of R_s.

The second method [2] first rearranges Eqn. (3.2) and then makes use of the Lambert W function, which yields

$$I_f(V) = \frac{nk_bT}{qR_s}W_0\left[\frac{qk_bR_s}{nk_bT}exp\left(\frac{q}{nk_bT}[I_0R_s+V]\right)\right] - I_0, \tag{3.5}$$

where W_0[] is the zeroth solution of the Lambert W function, other solution sets are complex and hence are not applicable. Assuming n = 1 and I_0 of 10 fA at room temperature, forward *I-V* characteristics were calculated using Eqn. (3.2) with R_s ranging from 0 to 10 kΩ are compared in Fig. 3.1 (R).

3.1.2 Reverse Bias I-V measurements

Performing I-V measurements between +1 V to -1V will reveal if the diode exhibits rectifying behaviour, i.e. asymmetrical I-V in the forward bias and the reverse bias regions. Focusing on the reverse bias region and increasing the voltage range yields reverse bias I-V characteristics. An indicative breakdown voltage corresponds to voltages with a sudden increase in current (several orders of magnitude). More detailed reverse bias I-V measurements are carried out to assess the uniformity of devices across the sample and identify the dominant leakage mechanism(s).

The uniformity of the devices across the sample can be assessed by comparing reverse I-V characteristics obtained from multiple devices of the same radius across the sample. In addition, the avalanche breakdown of diodes should be unaffected by the diode's diameter. Hence the variation in breakdown voltage values from experimental reverse I-V characteristics could imply edge breakdown, which is undesirable. Edge breakdown in mesa devices occurs when electric fields on the diode's sidewalls are higher than those in the bulk of the diode. In this case, a localised hotspot occurs, causing the diode to exhibit premature breakdown.

Multiple devices of different radii are measured to identify the dominant leakage mechanism(s). Data of reverse current from a given device is then divided by the device area and perimeter to produce current density (J_d) and current/perimeter, respectively. The dominance of bulk or surface leakage mechanisms can be observed from these plots. Surface leakage refers to the current that flows along with the diode's peripherals, which could arise from the mesa sidewalls for mesa diodes or edges of the Zn-diffusion regions for planar diodes.

Example characteristics of current, current density, and current/perimeter versus reverse bias are shown in Fig. 3.2(a), (b), and (c), respectively. These indicate that the surface leakage mechanism(s) dominate the measured dark current since the current scales with the perimeter.

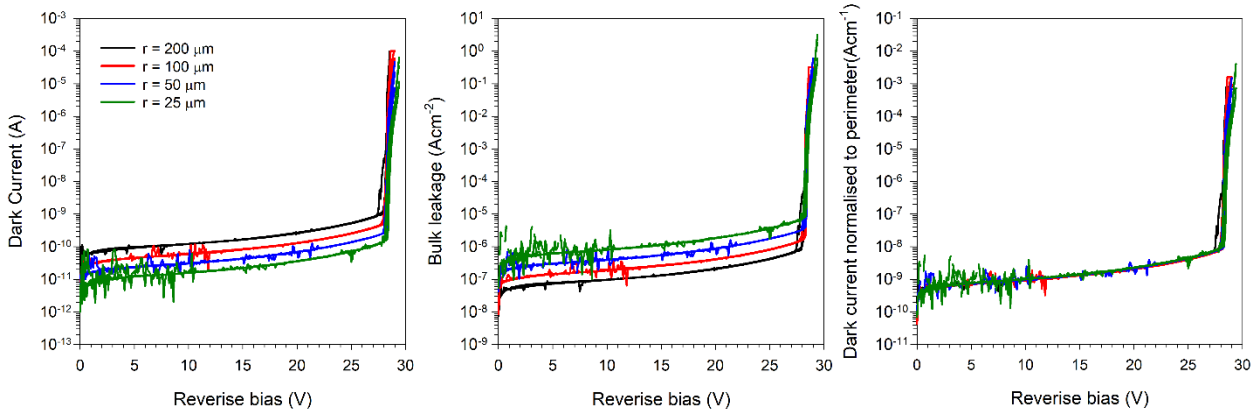

Fig. 3.2. Example of experimental dark I-V (L) after normalisation to device area (M) and device perimeter (R).

Typical bulk dark current mechanisms include diffusion current and generation-recombination current. A third bulk current mechanism important for APDs is band-to-band tunnelling current, which is given by

$$I_{tun}(V) = \frac{(2m_e^*)^{0.5} q^3 \xi V A}{h^2 E_g^{0.5}} \exp\left(-\frac{2\pi\sigma_{tun} {m^*}_e^{0.5} E_g^{1.5}}{qh\xi}\right), \tag{3.6}$$

where m^*_e is the electron's effective mass, ξ is the electric field strength, V is the applied voltage, A is the area of the diode, h is Plank's constant, E_g is the bandgap, and σ_{tun} is the tunnelling current fitting parameter. Band-to-band tunnelling occurs when the energy bands have been deformed significantly by the applied electric field that the electrons in the valence band may tunnel into the conduction band without a photon being absorbed. Appendix G shows the tunnelling current fitting parameters and validation data for $Al_{0.85}Ga_{0.15}As_{0.56}Sb_{0.44}$.

3.1.3 Transmission Line Measurement (TLM)

These measurements are used to determine the contact resistance between the metal contact and the semiconductor material. TLM measurements are typically done when forward I-V data suggest high series resistance. A suitable TLM sample usually consists of metal contact pads deposited on the semiconductor contact layer. There should be an increased separation between each adjacent pair of metal contact pads, and a range of separation should be covered. The TLM samples used are illustrated schematically in Fig. 3.3 (top). Each set has six rectangular pads with dimensions of 100 × 50 µm and is separated by 5 µm to 25 µm. For each pair of the pads, the total resistance ($R_{measured}$) is a sum of the two contact resistances ($R_{contact}$), semiconductor resistance (R_{gap}), and measurement system resistance (R_{system}). This can be expressed as

$$R_{measured}(w) = 2R_{contact} + R_{gap}(w) + R_{system}.$$

For accurate TLM data, the measurement system resistance must be accounted for. The system resistance is obtained by short-circuiting the two probes and extracting the resistance from the linear I-V characteristics. Then, each pair of adjacent pads are probed, and an I-V characteristic is obtained. A voltage range of -1 V to +1 V is usually sufficient, and the linear I-V characteristics yield a resistance value. Some samples may produce non-linear I-V characteristics (possibly due to Schottky contacts) for which TLM is not applicable. The resistance values are plotted against w in a linear-linear plot. Using a linear regression fitting through the data points and extrapolating the fitting to the vertical axis produces $R_{contact}$, as shown in Fig. 3.3 (bottom).

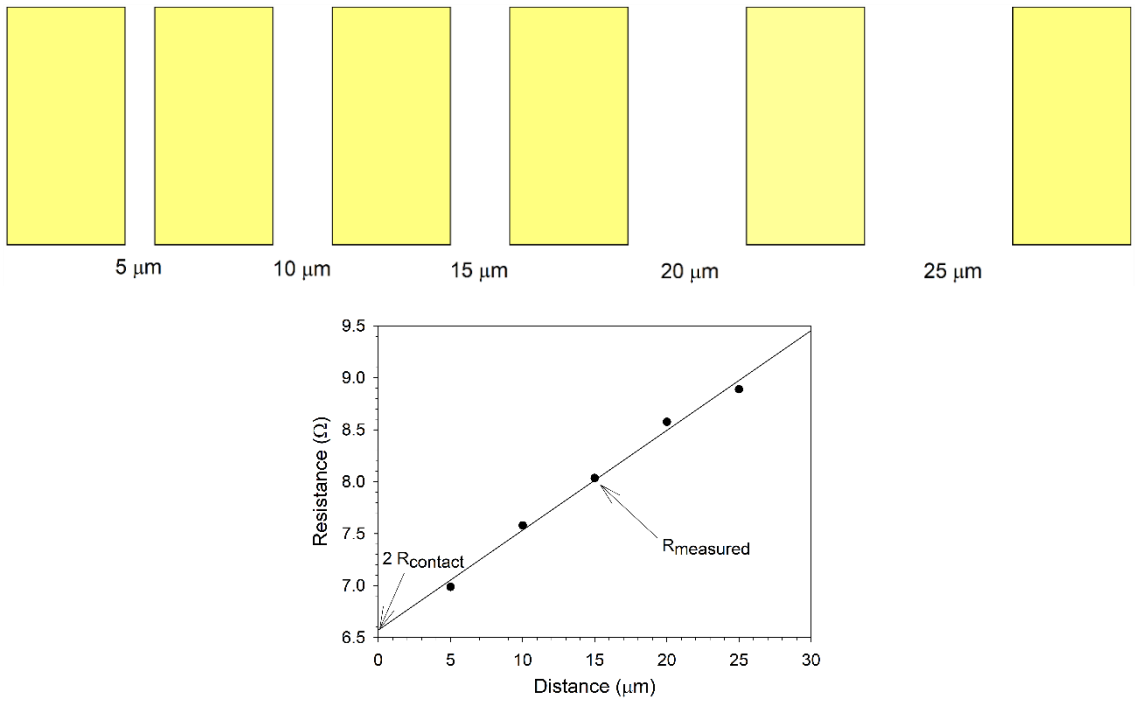

Fig. 3.3. Example of TLM pad arrangement (top). Measured resistance versus separation and the linear regression fitting (bottom).

3.2) Capacitance-Voltage measurements

Capacitance-Voltage (C-V) measurements are used to calculate the doping profile and depletion width of a device. C-V is measured using an LCR meter, which applies a DC bias to reverse bias the device; a small signal, a high-frequency AC signal, is superimposed onto the DC bias. The resultant voltage, current magnitude, and phase shift are recorded to calculate the device's impedance. The capacitance is calculated by assuming a parallel resistor-capacitor circuit, representing the diode's leakage current and junction capacitance.

The C-V measurements were carried out using an HP 4275A LCR meter connected to four matched lengths of BNC cable and two probe positioners. The LCR meter has four outputs: high voltage, high current, low voltage, and low current. The two high outputs are connected using a three-way BNC adaptor, the same for the two low connections. These combined 'high' and 'low' terminals are connected to the probe positioners.

Typical settings for the LCR meter are the AC signal magnitude of 50 mV_{rms} and frequency of 1 MHz. The AC magnitude must be high enough to produce impedance measurements without significantly affecting the overall (DC) bias. Since a typical diode used in this work has a capacitance between 1 and 10 pF, using an AC signal frequency of 1 MHz is within the recommended range from the equipment manual. Although the LCR meter is specified to measure capacitance down to 10 fF, the setup can only produce reliable measurements for values above 500 - 700 fF. This limit is possibly due to the long wires needed for the probe positioners.

3.2.1) Radius reduction

Many of the research-grade devices used in this work were fabricated using wet chemical etching. Typically, mesa devices are etched with a range of different radii to measure uniformity, as shown in the reverse I-V section. During device fabrication, the isotropic nature of wet chemical etching produces mesa diodes with radii slightly less than the intended values. Hence the mesa diodes are not usually cylindrical but slightly tapered. For measurements such as $M(V)$ and $F(M)$, a slightly reduced radius (typically < 2 µm) does not affect the measurement accuracy. The reduction in the effective radius will create uncertainty in any analysis, such as depletion width and doping profile. Therefore, C-V analyses begin with radius correction, which involves applying a fixed reduction to all radii until the C/A characteristics from different-sized devices agree.

The need for area correction is illustrated by considering an InAlAs p-i-n diode with a 100 nm thick i-layer. The doping densities of the p-layer and n-layer are 2×10^{18} cm$^{-3,}$ while the i-region doping density is 1×10^{15} cm^{-3}. Fig. 3.4(a) shows the calculated C-V for a range of radii, where the dashed and solid lines are for a radius with and without a 2 µm radial reduction, respectively. Fig. 3.4(b) shows the percentage difference between the two calculated C-V. For the devices with a larger radius, the error is relatively low and comparable to the repeatability of the setup. As the device radius reduces, the 2 µm reduction becomes more significant, leading to noticeable error in the smallest devices. These errors, in turn, cause uncertainty in subsequent C-V analyses.

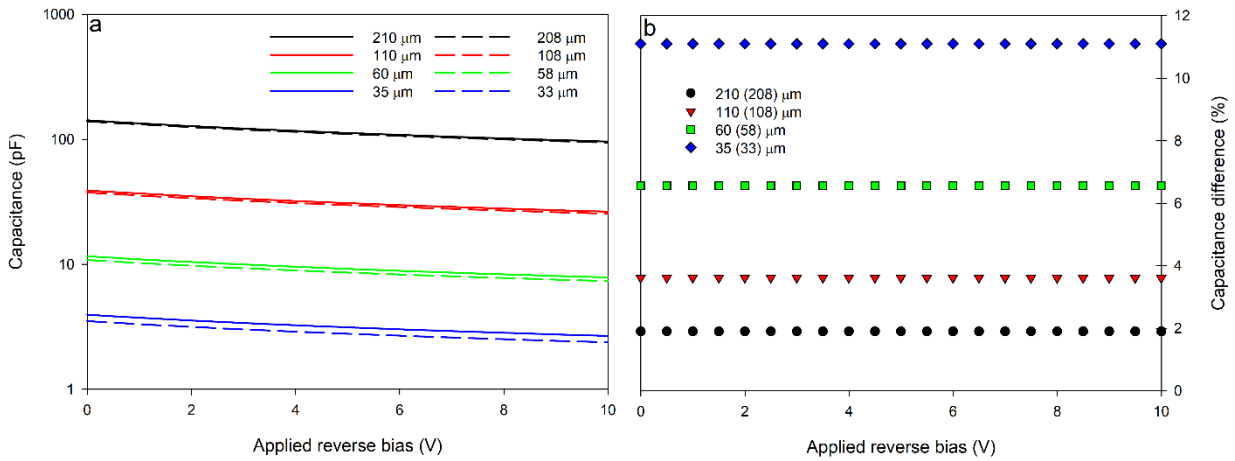

Fig. 3.4. Calculated Capacitance-Voltage of a 100 nm InAlAs p-i-n diode for a range of radii (a) and capacitance difference associated with a 2 µm reduction (b).

3.2.2) Depletion width

In the parallel plate capacitance equation, the device's depletion width can be deduced from

$$W(V) = \frac{\varepsilon_0 \varepsilon_r A}{C(V)}, \tag{3.7}$$

where ε_0 and ε_r are the permittivity of free space and relative permittivity of the material, A is the area of the DUT using the effective radius. For example, data of depletion width versus reverse bias (from the InAlAs pin diode used in Fig. 3.5), is shown in Fig. 3.5. The dash lines represent a diode with a 2 µm radial reduction which has been ignored when calculating the depletion width from the capacitance and mesa area. The dash lines used a radius of 210 (black), 110 (red), 60 (green) and 35 µm (blue) whereas the solid lines used a radius of 208 (black), 108 (red), 58 (green), and 33 µm (blue). As the device radius decreases, the error in the capacitance increases, which causes the depletion width calculated to increase as the device radius decreases. Using the corrected radial radius, the depletion width for all radii agrees.

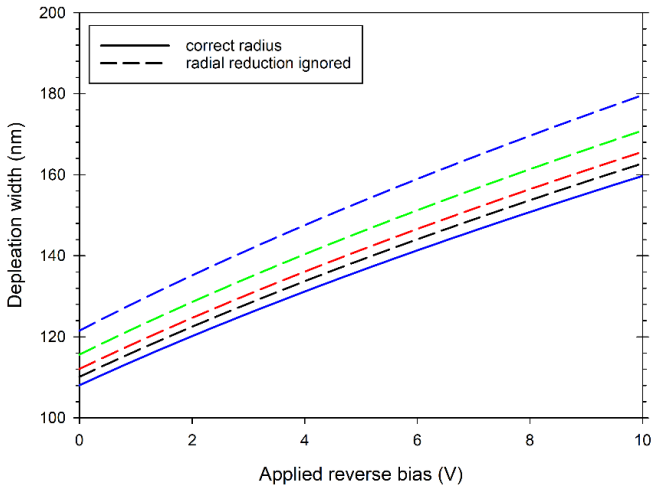

Fig. 3.5. Calculated depletion width of a 100 nm InAlAs p-i-n diode where the radial reduction of 2µm is ignored (dash) and included (solid)

It is possible to infer the relative doping concentrations and i-layer thickness from the C-V and depletion width. If there is a significant change in depletion width at low bias, the i-region is being depleted. This may be due to a high background doping in the i-layer or a thick i-layer. For a p-i-n diode, the depletion width is not expected to change significantly at high reverse bias.

3.2.3) Doping Profile fitting

Using a 1D Poisson's equation solver, the doping concentration and layer structure can be determined for an experimental device. Poisson's equation solver will calculate the electric field profile and depletion width for a given doping profile. The calculated C-V is compared to experimental C-V data, and the doping profile is modified until the C-V agree. This allows Eqn. (3.7) to be solved for a given structure.

Typically, a three-layer approximation is used for p-i-n structures or five layers for SAM structures. This approximation requires a constant doping approximation in each region and abrupt junctions. This approximation can yield an unsatisfactory fitting for devices with highly diffused dopants. Such devices may require Secondary Ion Mass Spectrometry (SIMS) analysis to deduce their doping profiles. When using SIMS

data in C-V fitting, the raw SIMS data may need to be scaled downwards because SIMS data include electrically active and electrically inactive dopant atoms.

3.3) Phase-sensitive measurements

Phase-sensitive measurements are used for low photocurrent measurements, such as Avalanche Multiplication, Responsivity and Excess Noise Factor. A Lock-in Amplifier (LIA) allows an AC signal to be distinguished from other signals at other frequencies. This is applied to ensure the photocurrent is measured independently from dark current and currents due to other unintended optical sources. The AC light source is obtained by either placing a mechanical chopper in the light path of a DC light source or driving the light source with AC pulses. The frequency used by the mechanical chopper or the AC pulse driver is fed to the reference input of the LIA. The LIA will yield a magnitude and phase readings for the signal at the reference frequency, where the output is the product of the input signal and the LIA-generated reference signal. The LIA will vary the phase of the LIA-generated signal until it agrees with the input signal, so the phase component effect is removed, and the signal can be measured.

3.3.1) Avalanche Multiplication and responsivity

In phase-sensitive $M(V)$ measurements, readings of photocurrent are obtained using the phase-sensitive method. In the setup, a mechanically chopped light source provides AC light signal to the device under reverse bias. An SMU provides reverse bias to the device via a series resistor. An LIA (model SR830) measures the photovoltage induced across the series resistor. By varying the reverse bias, the photocurrent is measured as a function of reverse bias.

$M(V)$ is given by the ratio of the measured photocurrent to the primary current, I_{pri} (V). The latter is defined as the unmultiplied photocurrent. It is determined experimentally using either a single $M(V) = 1$ point or baseline correction. The first method is used primarily for SAM APD characterisation, in which a single photocurrent point after punch-through is selected as the $M(V) = 1$ point. This is appropriate for a SAM APD because depletion width increase is negligible after punch-through.

For other devices, the primary current often has a stronger dependence on voltage due to an increase in carrier collection efficiency as depletion edges approach the light absorption regions (usually near the top surface). Assuming that all the light is absorbed for a single point, the primary photocurrent is described by

$$I_{pri}(V) = \frac{I_{pri}(0)}{\cosh\left(\frac{L(V)}{L_d}\right)}, \tag{3.8}$$

where $I_{pri}(0)$ is the primary current at 0 V, L(V) is the distance between where the majority of the light is absorbed and the depletion edge, and L_d is the minority carrier diffusion length. L_d is often unknown for novel III-V materials. Experimentally the primary photocurrent may be extracted with a linear fit of the low bias photocurrent and extrapolation to higher biases. An experimental 800 nm InAlAs *p-i-n* photocurrent versus

reverse bias is shown in Fig. 3.6. In Region 1, there is a non-linear increase in photocurrent; this is due to a rapid increase in the depletion region through the i-region, which leads to an increase in carrier collection efficiency. In Region 2, photocurrent increases linearly as the depletion region starts to cover parts of the *p* and *n* regions. In Region 3, the photocurrent increases faster than linear, indicating the onset of avalanche gain. I_{pri} can be extracted from a linear fit of the region 2 results.

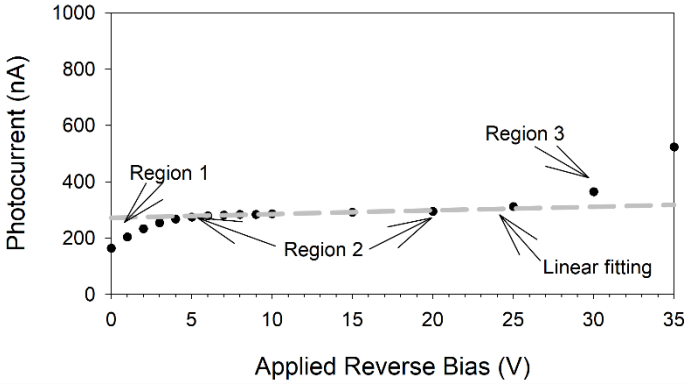

Fig. 3.6. Example of experimental 800 nm InAlAs p-i-n photocurrent. Region 1: depletion through i-region, Region 2: depletion into P and N region, and Region 3: start of non-negligible impact ionisation for this device

M(*V*) may also be obtained from a pair of illuminated I-V and dark I-V measurements. The photocurrent is extracted by subtracting the dark current from the total current. This can then be used to calculate *M*(*V*) using either M = 1 data point or primary photocurrent.

Three experimental Si diodes were tested under the same condition, phases sensitive measurement (symbols) and the illuminated I-V (lines). A comparison between the phase-sensitive calculated avalanche multiplication and the I-V method is shown in Fig. 3.7. The illuminated I-V method shows an increased *M*(*V*) compared to the phase-sensitive method. Typically, the I-V method requires around two to three orders of magnitude difference to be accurate, which is lost near breakdown. This method can be unsuitable for determining the avalanche multiplication for devices with high avalanche gain, high dark current, or low photocurrent devices due to poor responsivity.

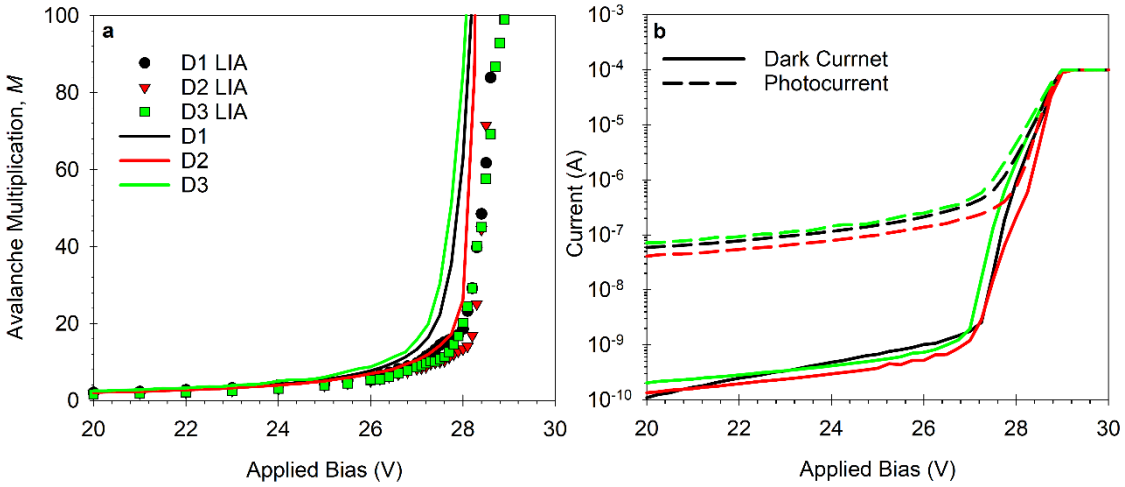

Fig. 3.7. Example of experimental Si p-i-n gain using a phase-sensitive measurement (symbols) and illuminated I-V method (lines) (a). Dark current and photocurrent of the devices (b)

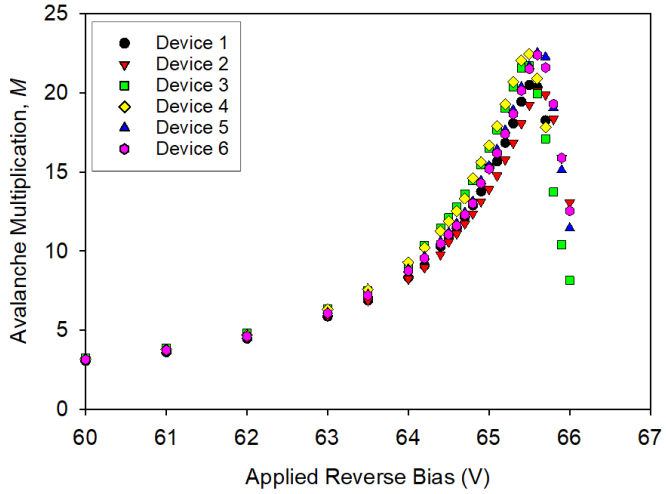

Fig. 3.8. Effect of high series resistance on avalanche multiplication characterisation

The effect of high series resistance on the measured avalanche multiplication can be observed in Fig. 3.8. The SMU supplies a total voltage split between the three effective loads as $V_{SMU} = V_{device} + V_{R_{sense}} + V_{R_s}$. As the current increases the voltage drops across the sense resistor, and the series resistor increases, reducing the voltage across the device and hence the avalanche multiplication.

Responsivity is measured using the same procedure as the phase-sensitive avalanche multiplication characterisation, and the continuous wave (CW) optical power is measured. The responsivity is then calculated as the photocurrent verse optical power

$$\text{Responsivity } \left({}^{A}/_{W}\right) = \frac{\left[\frac{LIA(V)}{R_{sense} \times 0.45}\right]}{optical\ power\ (W)'} \tag{3.9}$$

where LIA(*V*) is the recorded voltage across the sense resistor, and 0.45 is the factor for converting the RMS voltage of a square wave to a peak-to-peak value.

3.3.2) Excess noise factor

The excess noise factor is noise which arises due to the stochastic nature of the impact ionisation process. It is a key performance parameter for both comparing different avalanche materials and device design(s). Both photodiodes and APDs exhibit shot noise, but only APDs exhibit excess noise. The excess noise factor is calculated by measuring the total noise of a DUT and comparing it to a reference shot noise value.

The setup uses a phase-sensitive technique for both the photocurrent and the noise power equivalent voltage. The diode is illuminated with a pulsed light source at 180 Hz, and the noise is measured using a bandpass filter at 10 MHz. The noise power is measured using a power meter which yields an equivalent voltage for a given power.

As shown in Fig. 3.9, the excess noise setup consists of a trans-impedance amplifier (TIA) followed by a series of amplifiers, an attenuator, a bandpass filter and a power meter. The DUT's cathode is connected to a 47 nF capacitor (C2) and a bias supply (SMU). The capacitor C2 provides a low impedance path for any transience that occurs between the SMU and the diode by the cable. The DUT's anode is connected to the input of the TIA and two RF diodes (D1 and D2). Should the DUT fails, these diodes protect the TIA input from the bias supply by sinking the bias current to the ground and limiting the potential at TIA's input to ±0.7 V.

The TIA consists of an AD9631an op-amp with a feedback loop, a trans-impedance gain of 66.8 dB, and a cut-off frequency of 21.9 MHz. The output of the TIA is split into three paths: two buffer amplifiers and a 50 Ω impedance match output. The top buffer amplifier is connected to an LIA for measurement of the photocurrent, whereas the bottom one is connected to an oscilloscope for signal monitoring during the measurement session. Using two buffer amplifiers instead of a BNC three-way splitter ensures consistency in signal magnitudes in the three paths, irrespective of connections in any of the three paths.

In the 50 Ω impedance match path, the magnitude of the noise signal is scaled by a combination of a wide bandwidth amplifier (Mini-Circuits ZFL-1000LN+) with a fixed gain of 20 dB and a variable attenuator (Agilent 4875A) to prevent saturating the following components (especially the power meter). The noise signal is then filtered by a bandpass filter centred at 10.2 MHz with a bandwidth of 4.4 MHz (Mini-Circuits SBP-10.2), followed by a second amplifier (Mini-Circuits ZFL-1000LN+) and the power meter circuit. The power meter uses an AD835-based circuit which provides an output voltage proportional to the noise signal power. The power meter's output is then measured by a second LIA, with a duplicate fed to an oscilloscope for monitoring. The DUT's junction capacitance must be < 30 pF to avoid the system self-oscillating. Also, the DUT current must be < 1.8 mA since the maximum output of the op-amp is 3.9 V, to avoid saturation. This is

particularly important for narrow bandgap materials such as $In_{0.53}Ga_{0.47}As$ where tunnelling current can dominate, causing the TIA or noise circuit to saturate. This can lead to the $F(M)$ to artificially plateau, leading to a lower excess noise being recorded.

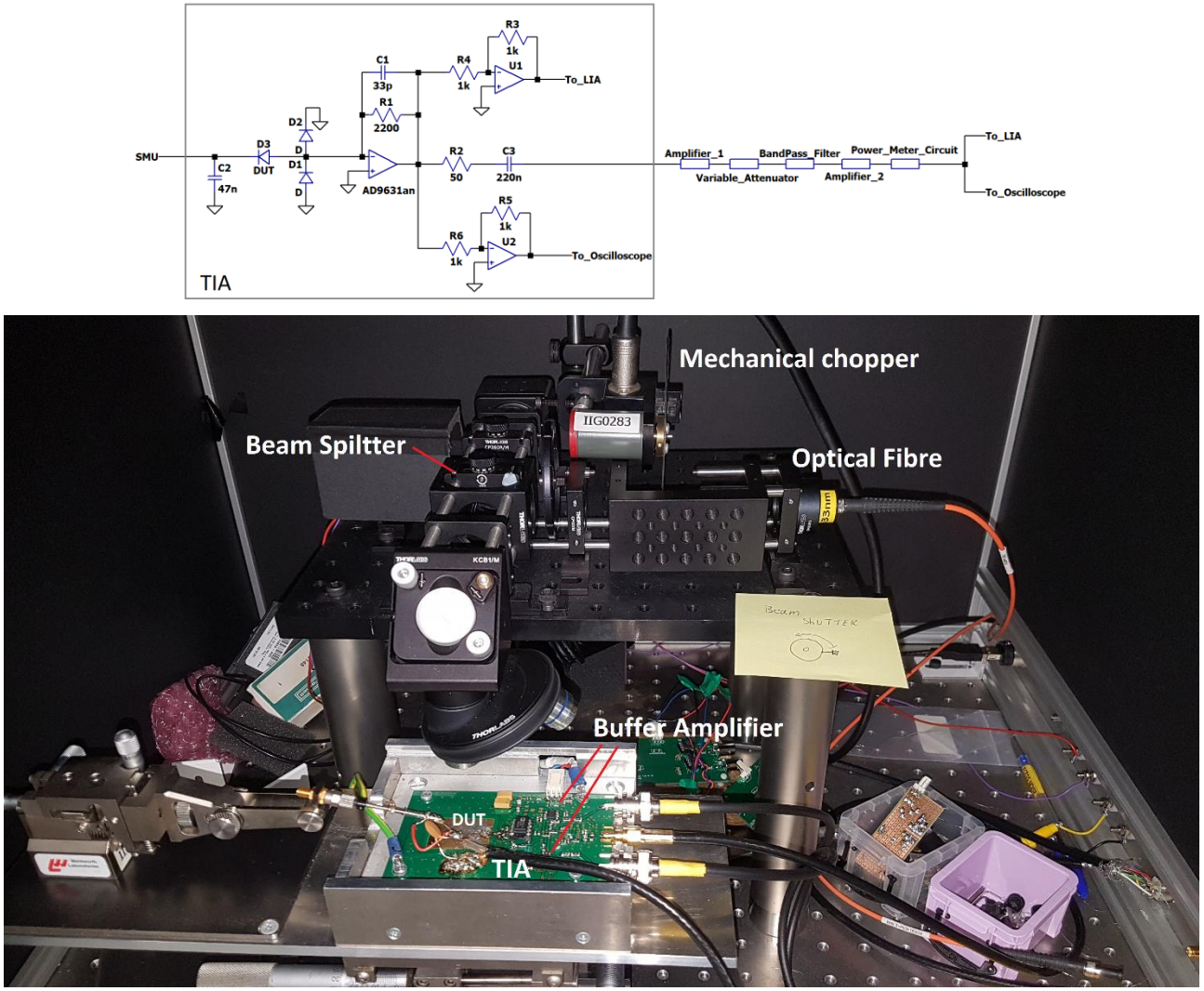

Fig. 3.9. Simplified diagram of the Excess noise setup (top) Excess noise TIA and optical setup (bottom)

Accurate excess noise measurements require two calibrations: shot noise calibration and effective noise bandwidth (ENBW) calibration. The shot noise calibration is used to determine the shot noise and offset expected for a non-avalanching device and is required to calculate the excess noise factor. The ENBW calibration is required to compensate for the change in system gain due to front-end capacitance changes, which arise due to the change in depletion width for the DUT. These calibrations are described in detail in the appendix.

The process for obtaining excess noise factor using the calibrated setup is detailed below. Shot noise is given by

$$N_{shot} = 2qI_{ph}B_{eff}, \tag{3.10}$$

where q is the electron charge, I_{ph} is the measured photocurrent, and B_{eff} is the effective bandwidth of the measurement. The noise of an APD is given by

$$N_{APD} = 2qI_{pr}\bar{M}^2FB_{eff}, \tag{3.11}$$

where I_{pr} is the primary photocurrent. Combining the two equations gives

$$N_{APD} = N_{shot}\bar{M}^2F. \tag{3.12}$$

From (3.10), the shot noise is linearly proportional with photocurrent (primary current in an APD) as all other factors are assumed constant. Linear regression is fitted to the experimentally measured shot noise power equivalent voltage

$$Shot\ noise\ power\ equivalent\ voltage\ = k_{pr}I + C, \tag{3.13}$$

where K_{pr} is the gradient and C is the y-intercept. These two constants are the shot noise calibration. This using (3.12) yields

$$N_{APD} = k_{pr}I_{pr}\bar{M}^2F + (c). \tag{3.14}$$

Eqn. (3.14) can be rearranged into

$$F = \frac{N_{APD}}{k_{pr}I_{pr}\bar{M}^2 + c}. \tag{3.15}$$

Eqn. (3.15) is then modified for use with the setup to account for the dependence of bandwidth on device capacitance (ENBW) and variable attenuator

$$F = \frac{N_{LIA}10^{\frac{Attenuator\ (dB)}{10}}}{k_{pr}V_{pr}\bar{M}^2 + c}\frac{ENBW_{C_{cal}}}{ENBW_{C_{DUT}}}. \tag{3.16}$$

An example of the shot noise fitting values is shown in Table 3.1 for a range of light sources. The shot noise for 420 – 633 nm was calibrated using a BPX65 Si photodiode, and the 940 and 1520 nm wavelength was calibrated with an FGA015 InGaAs photodiode.

Table 3.1 Shot noise fitting

Wavelength of light source (nm)	Fitting		Device capacitance (pF)	Light source type
	K_{pr}	C		
420	38.55	2.7	4.7	LED
543	39.43	1.61	4.7	Laser: HeNe
633	39.37	4.84	4.7	Laser: HeNe
940	40.8	7.77	1.5	LED
1520	42.1	0.8	1.5	Laser: HeNe

The ENBW is fitted to the equation $xc_j^2 + yc_j + z$, where c_j is in pF., the fittings are shown in Table 3.2. The effect of the ENBW ratio has on the noise signal is shown in Fig. 3.10 for both reference photodiodes. The measured noise is scaled up or down depending on the DUT capacitance. The DUT capacitance ideally will be comparable to the reference device to minimise uncertainties introduced by the correction.

Table 3.2. Selected Effective Noise Bandwidth calibrations

Date	x	y	z	notes
1999	460	77000	4240000	K.Li [3]
Dec 2018	562.31	73833	4309280	
Mar 2020	428.1	82610	4429000	

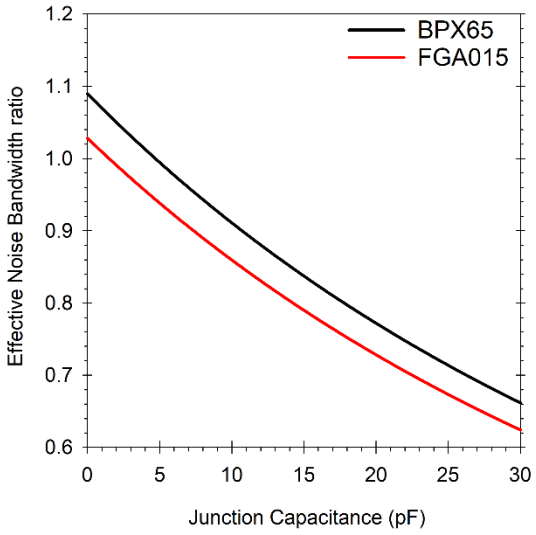

Fig. 3.10 Effective Noise Bandwidth correction ratio

3.4) Single Photon Avalanche Photodiode characterisation

Single Photon Avalanche Photodiodes (SPADs) are devices capable of responding to a single photon input. Typically, this is achieved by operating the device in the Geiger region so that a single carrier may cause a self-sustain avalanche current. High gain linear mode APDs are capable of detecting single-photon events.

Linear mode SPADs used for single and few photons injection can be experimentally characterised in the same way described previously. They are typically, used for single-carrier impact ionisation materials, such as InAs. A thicker i-region is required to facilitate a large enough $M(V)$ to respond to a single photon. Since this event does not create a self-sustaining current, the device will naturally quench, so no additional consideration for the circuitry is required compared to an APD, which is advantageous. Another advantage is that the device can detect multiple events concurrently, so a distinction can be made between a single photon

and multiple photons. The devices, however, typically have to be very thick compared to APDs, which increases the chance of poor device quality.

For Geiger mode SPADs, the device is biased above breakdown, and a self-sustaining avalanche current is produced when an "event" occurs. An event occurs when each electron-hole pair generates at least one additional electron-hole pair before leaving the device, creating a self-sustaining current. An event occurs when the diode generates an avalanche current. This may be initiated by either a photogenerated electron(hole) or a dark carrier, a generalised term for any event that occurred by non-photo initialised means such as the band-to-band tunnelling, trap-assisted tunnelling, thermal excitation and after-pulsing. In a Geiger mode SPAD, only a single event may be detected at a time. Hence no distinction can be made between dark events, single-photon injection events or multiple photon injection events. Due to the self-sustaining avalanche current, additional circuit considerations is required to allow the current to be quenched and the device reset. The devices, however, are of comparable width compared to APDs, where a typical avalanche region is ≤ 1 μm.

Two setups are used for characterising SPADs, with the preferred method requiring a packaged device and a gated Capacitive Quenching Circuit (CQC) [4]. The setup, however, has a small temperature range of 18 to 25°C. This setup is hereafter known as the SPAD setup. Temperate stability is achieved by placing the SPAD in a copper holder connected to a Peltier element (controlled by a Keithley 2510 TEC source meter). The second method uses unpackaged devices, but the quenching mechanism is limited to either passive or gated. The advantage of the second method is that a cryogenic probe station may be used for temperature-dependent measurement.

The SPAD setup and the gated measurements in the cryogenic probe station have some common pieces of equipment. The DUT is reverse biased via a bias-tee by two sources: a DC voltage source (Keithley 6487 Picoammeter to provide a voltage at just below the breakdown voltage) and an AC voltage source (TTi TGP3152 to provide overbias pulses). The device is over biased only when the AC pulse is on. Thus when the AC pulse is off, any avalanche current in the preceding on-period could be quenched.

The AC pulse is split between the bias tee and a dummy load capacitor. The dummy load capacitor replicates the capacitive transients caused by the device's capacitance. The output of the diode and the dummy load is connected to a differential amplifier, which aims to remove the capacitive transients and provide a cleaner signal for the detection of avalanche breakdown events.

The SPAD setup uses the CQC board, which incorporates a bias tee, dummy load and differential amplifier on a printed circuit board, shown in Fig. 3.11(top). The CQC board also incorporates an active probe to monitor the ac bias applied to the SPAD. The bias tee, dummy load, and differential amplifier are discrete components when using the cryogenic probe station. The bias tee used is Picosecond Pulse Labs, and the dummy load is a single value capacitor soldered to a simple PCB with 50 Ω terminals.

The breakdown events are detected using a discriminator, which uses a front-end comparator with one input from the device and the other from a tunable threshold voltage. When the signal from the device exceeds

the set threshold level, a breakdown event has occurred. The threshold level is required to be higher than the transients due to the ac pulse or other noise sources so that the counts recorded are accurate. The dummy load and differential amplifier reduce the transience seen on the input of the discriminator, which allows for the detection of smaller breakdown events. The output of the comparator is converted to a Nuclear Instrumentation Module (NIM) pulse for counting. The NIM pulse is defined as -16 mA into 50 Ω and for ~2 ns. The NIM pulses are counted using a Canberra Dual Counter/Timer 512 for a set time duration. A second NIM signal is generated in parallel for monitoring or timing information of the breakdown events. If there is a falling or rising trend, the SPAD is possibly not thermally stable and is heating up or cooling down, respectively.

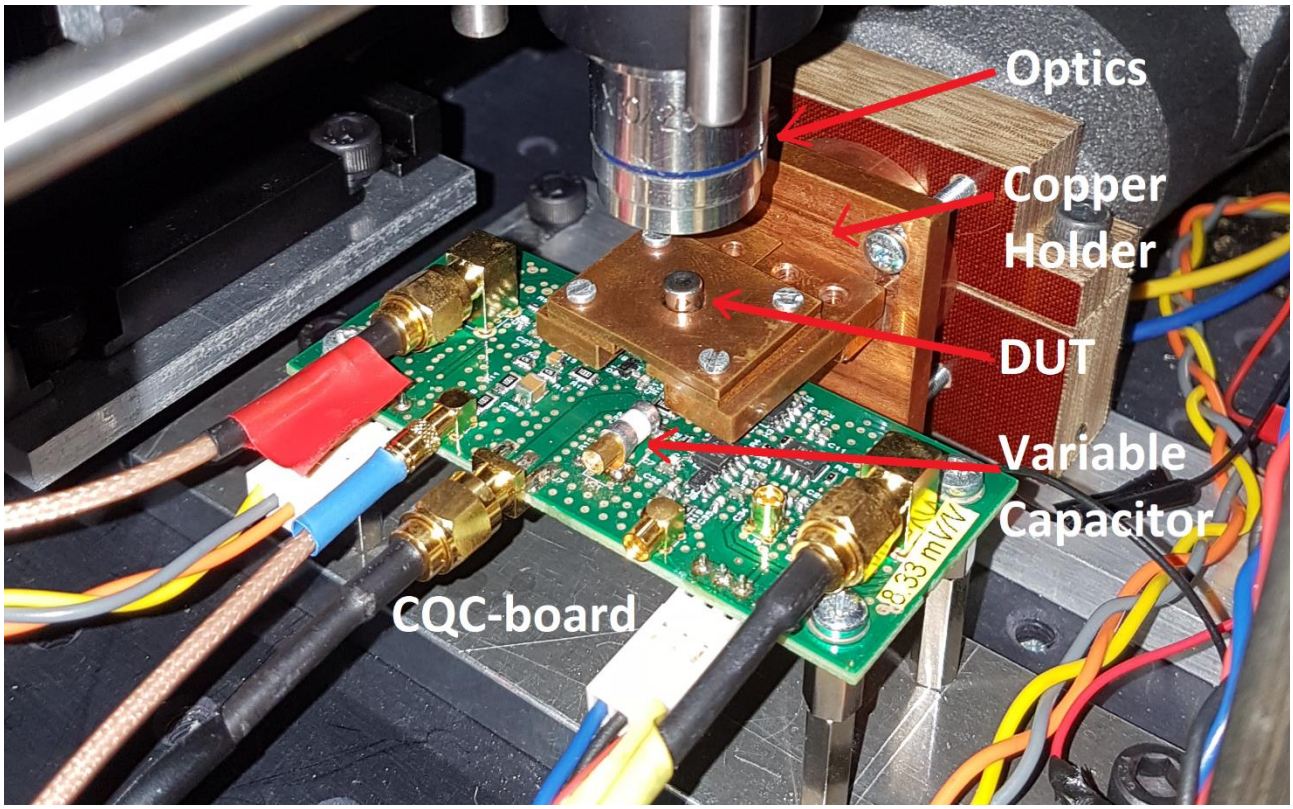

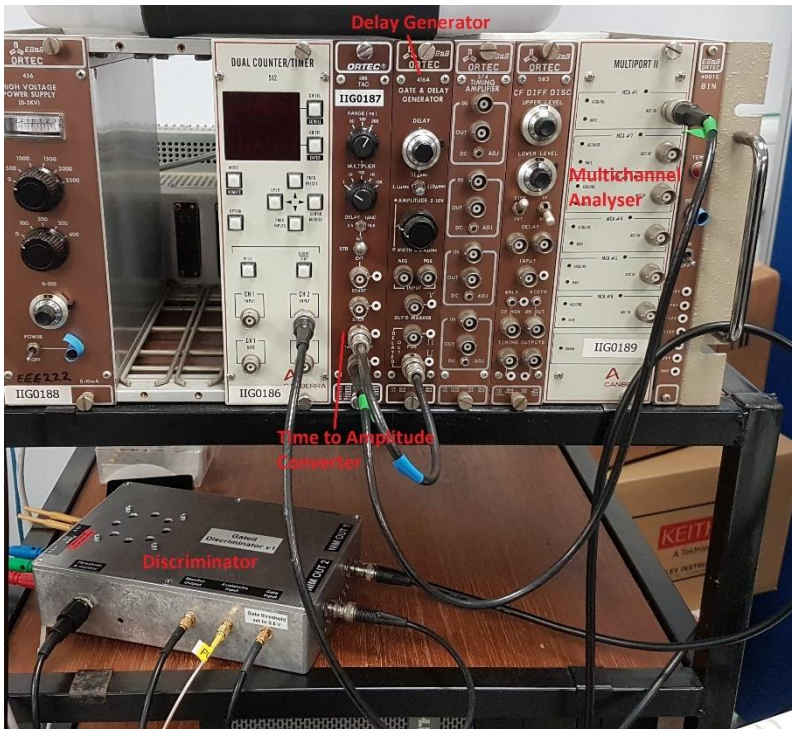

Fig. 3.11 SPAD setup CQC-board and DUT (top), Discriminator and counter (bottom)

For passively quenched devices in the cryogenic setup, a single DC voltage source is used to overbias the SPAD. A ballast resistor, typically in the order of 100 kΩ to MΩ, is connected in series with the SPAD to quench the avalanche current. The diode is then connected to the discriminator. When a breakdown event occurs, the increase in current causes an increase in voltage across the ballast resistor. Since the supply voltage is fixed, the bias across the SPAD reduces to approximately its breakdown voltage. At this condition, the avalanche current collapse and the SPAD is quenched. The SPAD is again overbiased due to a reduced voltage drop across the ballasted resistor. This method is one of the simplest to operate, but there is little user control. It is generally unsuitable for novel III-V material(s) characterisation due to the associated high dark count rate and lack of user control.

3.4.1) Dark Count Rate

Dark Count Rate (DCR) is the rate of dark events that occur per second. For gated measurements, DCR is calculated by measuring the mean number of dark counts per second and normalising for the duty cycle. Once a full bias sweep of results has been recorded, the counts per second (CPS) is used to calculate the DCR by $DCR = {}^{CPS}/_{\delta} W$here δ is the duty. Duty is a product of the frequency of the pulse generator (reptation rate, R_p) and on-time (T_{on}) of the ac pulse. The dark count probability may also be found by diving the CPS by the repetition rate.

3.4.2) Photon detection efficiency

Photon detection efficiency uses the same procedure from the dark count rate with the addition of a pulsed laser source attenuated to a single photon level. A pulsed laser ALPHALAS PICOPOWER^{TM} – LD, whose key parameters for its three emission wavelengths, 488, 635, and 1550 nm, are listed in Table 3.3. The pulse laser consists of a universal driver and three laser sources. A potentiometer is used to limit the driver power as each laser source has a different operating power. The optical path for the SPAD setup consists of the pulse laser, single-mode fibre coupler and splitter, electronically controlled Variable Optical Attenuators (eVOAs) and optomechanical components to focus the light on the optical window of the DUT.

Table 3.3. ALPHALAS pulsed laser specifications

Wavelength (nm)	Peak pulse power (mW)	Pulse width (ps)	Max potentiometer position at 1 MHz
488	115	71.0	4.5
635	453	56.9	7.1
1550	39	23.3	1.6

A simplified diagram of the SPAD setup for 633 nm optical measurements is shown in Fig. 3.12. The pulse generator, which is used to supply the ac pulse to the DUT, is also used to trigger the pulse laser driver, using the second output. The two outputs are temporally offset so that the optical pulse arrives when the DUT is overbias. This offset is required as there is a 45 ns delay between the pulse laser trigger and the laser firing.

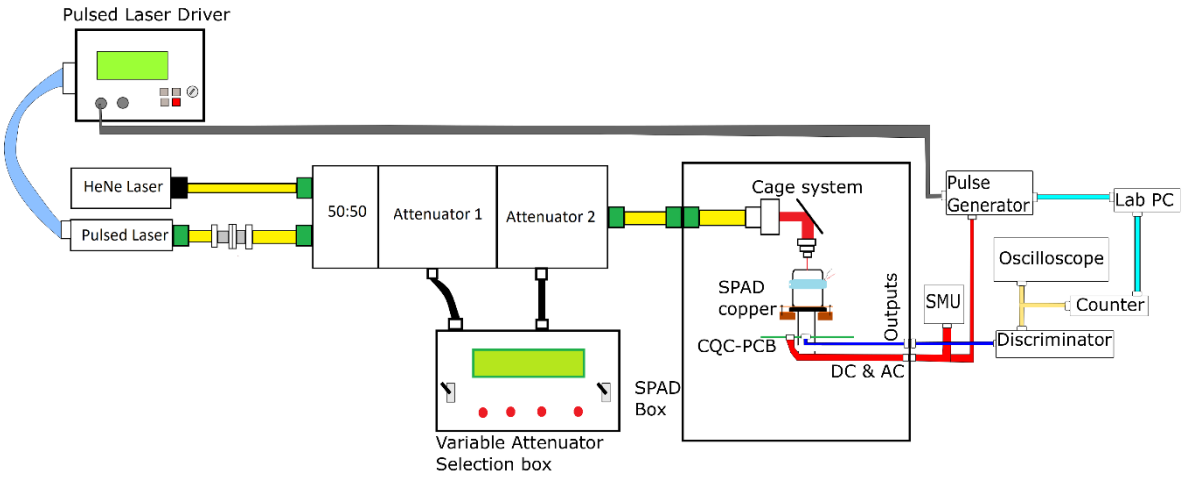

Fig. 3.12. Block diagram of the SPAD setup for 633 nm photon injection

The optical power of each source is attenuated to the single-photon level. The 1550 nm pulses are attenuated using a commercial variable attenuator is used. For 633 nm, two eVOAs are connected in series to provide enough dynamic range for single-photon attenuation levels.

The 1550 nm laser pulse is attenuated with a combination of single-mode fixed fibre optical attenuators and a variable optical attenuator, EXFO FVA-3100 (1 dB to 70 dB), whose attenuation calibration is given in Table 3.4. The fixed fibre optical attenuators are used to limit the peak optical power to avoid damage and to ensure the variable optical attenuator is kept within the calibrated range. The setup exhibits a static attenuation of 9.19 dB, which arises from coupling losses between the fibre coupler and the 50:50 optical splitter.

Table 3.4. Calibrated variable attenuation at 1550 nm for the EXFO FVA-3100.

Attenuation setting (dB)	Measured attenuation (dB)
10	10.05
20	20.02
30	29.96
40	39.78
50	48.77

The 633 nm laser pulse is attenuated with two ThorLabs V600A eVOAs and several FC/PC port savers used as fixed fibre optical attenuators. The port savers are required to reduce the peak power of the pulse laser to below 300 mW to avoid damage to the variable attenuators, fibre coupler, and splitter. The eVOAs are controlled by a dual variable 5 V source. The optical attenuation calibration of the 633 nm setup is shown in Table 3.5. The valid voltage range of the calibration fitting is between 0 V and 3.8 V

Table 3.5 eVOA attenuation SPAD box fitting

Static attenuation (dB)	eVOA A (dB)	eVOA B (dB)
17.1486	-0.9814 V^3 + 1.012 V^2 + 0.0898 V – 0.1927	-1.273 V^3 + 2.783 V^2 – 1.304 V -0.1515

The photon detection probability of the DUT cannot be directly measured but deduced from the total event probability less the dark event probability. The Single Photon detection efficiency is calculated by;

$$SPDE = \frac{P_t - P_d}{1 - e^{-\bar{n}}}, \tag{3.17}$$

where P_t is the probability of an event during optical measurement, P_d is the probability of an event during dark measurements. $\bar{n}$ is the average number of injected photons per pulse and $\bar{n} < 1$ and $P_{t(d)} = \frac{CPS}{R_p}$. SPDE can also be calculated from the gated experimental results as

$$\frac{CPS_{total} - CPS_{dark}}{R_p \bar{n}}. \tag{3.18}$$

3.4.3) Multichannel analyser

The multichannel analyser (MCA) measures when breakdown events occur during the overbias period. The timing data is measured using the variable delay generator, a Time to Amplitude Converter (TAC) and the MCA. The TAC output is varied between 0 and 10 V depending on the time difference between the start and stop inputs. The two inputs of the TAC are connected to the discriminator output and delay generator, respectively. The MCA bins the voltage from the TAC where the bin value can be referenced back to a time.

The variable delay generator (Ortec 416A) can delay a signal from 0.1 to 110 µs in three ranges, 1.1 µs, 11 µs, and 110 µs. The jitter of the delay is ≤ 0.02 % of the range, 220 ps, 2.2 ns, and 22 ns, respectively. The TAC (Ortect 566) ranges 50, 100, and 200 ns with a decade multiplier from 1 to 10 k. The MCA (Canberra Multiport II Multi channel analyser) has 16385 bins evenly distributed between 0 and 10 V. This gives a bin width of 3.05 ps and 12.2 ps, where the TAC is set to 50 ns and 200 ns, respectively. The jitter of the MCA and TAC was measured to be 9.15 and 24.4 ps for a TAC setting of 50 ns and 200 ns, respectively. The discriminator was measured with a jitter of 42.3 ps, and the delay generator, using TTL input, was measured with a jitter of 204.2 ps. The MCA requires a stable input of 1 µs, making it unsuitable for use with measurements of a repetition rate of over 100 kHz.

An example of the MCA results is shown in Fig. 3.13. A thin Si SPAD [2] was measured in the cryogenic probe station, using the setup as described previously. The waveform seen by the discriminator showed minimal transience after the differential amplifier, which allowed for accurate counting. However, the MCA results show the SPAD did not see a square overbias pulse, indicated by the change in counts over the gate period. This causes uncertainty in the recorded CPS as the voltage applied to the SPAD during the gate period is non-uniform. For a well-behaved SPAD, a dark carrier event will occur randomly for a single overbias. Since the SPAD is gated, the events will only occur during this time and the probability of the event occurring at a particular time will be proportional to the overbias voltage. Using the MCA, a record of when a dark event(s) occur and the suitability of the measurement conditions may be determined. The transient voltage can be estimated by relating the counts during the stable overbias period to a voltage, which can then be used for LCR analysis and extraction of breakdown probability.

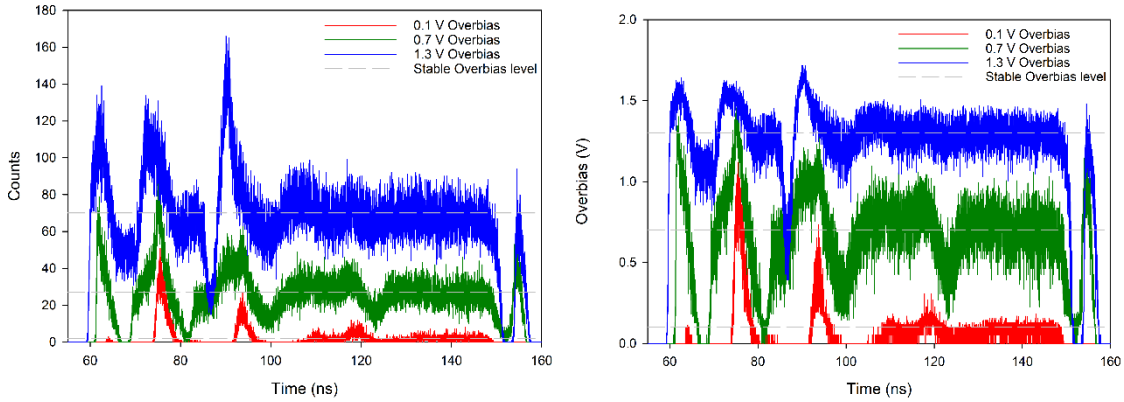

Fig. 3.13 Thin Si SPAD, Overbias vs time using Cryogenic setup

3.5) Modelling

3.5.1) light absorption profile model

This simple model uses the Beer-Lambert equation and published photon absorption coefficients to calculate photon absorption efficiency at a given wavelength by a given material. The model includes the following materials: $In_{0.53}Ga_{0.47}As$, $In_{0.52}Al_{0.48}As$, InP, $Al_{0.85}Ga_{0.15}As_{0.56}Sb_{0.44}$, $GaAs_{0.52}Sb_{0.48}$, and Si. Reflection loss at the air/semiconductor surface is included in the calculations of absorption efficiency in a single layer of the structure and the absorption and responsivity versus depth profile in the total structure.

3.5.2) Simple Monte Carlo Model

The SMC code reported by Petticrew *et al* [5] was modified to include alloy scattering for AlGaAsSb and simulating two scatter rates depending on an energy level. Alloy scattering rates were included for $Al_{0.85}Ga_{0.15}As_{0.56}Sb_{0.44}$ modelling. For $In_{0.53}Ga_{0.47}As$ a special case condition was written to fit the two distinct trends for electron impact ionisation rate [6]. The SMC requires two input files, a doping profile to calculate the electric field at a particular location in the depletion width and applied bias. For Geiger mode modelling, the breakdown condition is defined as 100 µA and is calculated using Ramo's theorem [7]

$$i_{br} = \frac{n_{br}\, q\, v}{w}, \tag{3.19}$$

where n_{br} is the number of carriers for breakdown, q is the electron charge, v is the velocity, and w is the device's width. The SMC models drift velocity by recording the time taken and distance travelled for 1 million drift events to occur. In the impact ionisation coefficients, the model simulates an infinite-length electric field and records the distance between impact ionisation events. The SMC model runs each carrier synchronous in

time steps. A trial is stopped when all active carriers leave the device, the breakdown condition is met, or the carriers are generated outside the simulation time limit.

3.5.3) Random Path Length Model

In Random Path Length (RPL) Model, $M(V)$ and $F(M)$ are modelled using the probability density function to weight a random distance a carrier travels. If the distance travelled is such that the carrier is still within the device from the initial position, an impact ionisation event is said to of occurred. The gain of each trial ($\bar{M}$) is averaged to calculate $M(V)$, and F(M) is calculated by $\frac{\langle \bar{M}^2 \rangle}{\langle \bar{M} \rangle^2}$. For Geiger mode modelling, the breakdown condition is also defined as 100 µA and is calculated using Eqn.(3.19). The RPL model assumes both carrier types have a single constant velocity, typically saturation velocity.

The RPL used in this work is written in C and runs each carrier asynchronous. Carriers are run in the order generated by the model, which is not necessarily the same as the order of time generated. This reduces the code's complexity and runtime but gives rise to uncertainty for breakdown conditions. Once the breakdown condition is reached, the trial is stopped and time recorded. This could result in some generated carriers not being run but could shorten the breakdown time. The trail stop condition is changed to be twice the breakdown condition before the breakdown time is recorded. Similarly to the SMC, the RPL trial is stopped by one of three conditions. When all active carriers have left the device region, when the breakdown condition is met or when the generated carriers are outside the user-define measurement period, the temporal results are not recorded.

References: Chapter 3

[1] B. K. Ng, 'Impact Ionization In Wide Band Gap Semiconductors: $Al_xGa_{1-x}As$ and 4H-SiC', PhD Thesis, The University of Sheffield, Department of Electronic and Electrical Engineering, 2002.

[2] J. D. Petticrew, 'Design and Device fabrication of Silicon Single Photon Avalanche Diodes', PhD Thesis, The University of Sheffield, Department of Electronic and Electrical Engineering, 2019.

[3] K. F. Li, 'Avalanche Noise in Submicron GaAs and InP Structures', PhD Thesis, University of Sheffield, Department of Electronic and Electrical Engineering, 1999.

[4] S. J. Dimler, J. S. Ng, R. C. Tozer, G. J. Rees, and J. P. R. David, 'Capacitive Quenching Measurement Circuit for Geiger-Mode Avalanche Photodiodes', *Sel. Top. Quantum Electron. IEEE J. Of*, vol. 13, no. 4, pp. 919–925, Aug. 2007, doi: 10.1109/JSTQE.2007.903595.

[5] J. D. Petticrew, S. J. Dimler, and J. S. Ng, 'Simple Monte Carlo Simulator for Modelling Linear Mode and Geiger Mode Avalanche Photodiodes in C++', *J. Open Res. Softw.*, vol. 6, May 2018, doi: 10.5334/jors.212.

[6] C. H. Tan, G. J. Rees, P. A. Houston, J. S. Ng, W. K. Ng, and J. P. R. David, 'Temperature dependence of electron impact ionisation in $In0._{0.53}Ga_{0.47}As$', *Appl. Phys. Lett.*, vol. 84, no. 13, p. 2322, 2004, doi: 10.1063/1.1691192.

[7] S. Ramo, 'Currents Induced by Electron Motion', *Proc. IRE*, vol. 27, no. 9, pp. 584–585, Sep. 1939, doi: 10.1109/JRPROC.1939.228757.

[8] C. H. Tan, J. S. Ng, G. J. Rees, and J. P. R. David, 'Statistics of Avalanche Current Buildup Time in Single-Photon Avalanche Diodes', *IEEE J. Sel. Top. Quantum Electron.*, vol. 13, no. 4, pp. 906–910, 2007, doi: 10.1109/JSTQE.2007.903843.
[9] J. D. Petticrew, S. J. Dimler, X. Zhou, A. P. Morrison, C. H. Tan, and J. S. Ng, 'Avalanche Breakdown Timing Statistics for Silicon Single Photon Avalanche Diodes', *IEEE J. Sel. Top. Quantum Electron.*, vol. 24, no. 2, 2018, doi: 10.1109/JSTQE.2017.2779834.
[10] P. J. Hambleton, J. P. R. David, and G. J. Rees, 'Enhanced carrier velocity to early impact ionisation', *J. Appl. Phys.*, vol. 95, no. 7, pp. 3561–3564, Apr. 2004, doi: 10.1063/1.1646434.

Chapter 4

$Al_{0.85}Ga_{0.15}As_{0.56}Sb_{0.44}$ avalanche characteristics and simulation

This chapter presents experimental results from a w = 600 nm $Al_{0.85}Ga_{0.15}As_{0.56}Sb_{0.44}$ (hereafter AlGaAsSb) p-i-n diode, an AlGaAsSb SMC model, and effective ionisation coefficients of AlGaAsSb for use in simpler simulation models. Experimental results from the 600 nm thick p-i-n diode included $M(V)$ and $F(M)$ characteristics from three optical injection profiles (pure electron and two mixed injection profiles). These and earlier data formed the verification data for an AlGaAsSb SMC model. Using the SMC model, effective impact ionisation coefficients and threshold energies valid for electric fields between 400 and 1200 kV.cm^{-1} were obtained.

The work presented in this chapter has been published [1], [2]

4.1) Experimental results (w = 600 nm AlGaAsSb p-i-n diode)

The AlGaAsSb p-i-n wafer, designed and commissioned by Phlux Technology Ltd, were grown using Molecular Beam Epitaxy (MBE) on a semi-insulating InP substrate by a wafer foundry. Layers of AlGaAsSb were grown as random alloys and X-ray diffraction was used to confirm the composition of the AlGaAsSb layers. The wafer structure is summarised in Table 4.1. The p-, i-, and n- AlGaAsSb layers are sandwiched between p^+-$In_{0.53}Ga_{0.47}As$ and n^+-$In_{0.53}Ga_{0.47}As$ (hereafter InGaAs) layers, which facilitate good ohmic contacts. The top InGaAs layer also acts as a barrier to prevent the AlGaAsSb from oxidising. The i-AlGaAsSb layer is sandwiched between highly doped p, and n AlGaAsSb layers. This is to facilitate a well-defined high electric field in the i-layer with minimal change to the depletion width as the reverse bias is increased.

Table 4.1. Nominal wafer structure

Material	Doping type	Nominal doping density (cm^{-3})	Nominal thickness (nm)	Notes
$In_{0.53}Ga_{0.47}As$	p^+	2×10^{19}	50	Capping and p-contact layer
$Al_{0.85}Ga_{0.15}As_{0.56}Sb_{0.44}$	p	1×10^{18}	300	
	i	-	600	High electric field region
	n	1×10^{18}	200	
$In_{0.53}Ga_{0.47}As$	n^+	2×10^{19}	500	n-contact layer
InP substrate (semi-insulating)				

4.1.1) Device fabrication details

Device fabrication using NEWPIN photolithography masks was carried out by Dr V. Shulyak. Circular mesa devices were fabricated from wafer pieces using standard photolithography and wet chemical etch with two etchants. The first etchant was a solution of Sulphuric acid (H_2SO_4): Hydrogen peroxide (H_2O_2): de-ionised water (H_2O) in a ratio of 1:8:80 to remove the top InGaAs layer. This was followed by a solution of Hydrochloric acid (HCl): Hydrogen peroxide (H_2O_2): de-ionised water in a ratio of 5:1:60 to etch the AlGaAsSb layers. The NEWPIN mask forms devices with a radii of 210, 110, 60 and 35 µm. Metal contacts were formed by evaporating Ti/Au (20/200nm) on top of the devices (for p-contact) and on the n^+-InGaAs layer (for n-contact). The Ti aids the Au in adhering to the semiconductor to form robust contacts. The devices were passivated using silicon nitride before a layer of Ti/Au was deposited to act as an optical mask. The metal is disposited on the mesa floor and sidewall, and are left floating. This prevented undesirable injection of incoming illumination to the sides of the devices during avalanche gain and excess noise measurements and limited any coupling capacitance effects.

Deposition of the SiN was carried at 300 °C, which may have resulted in I-V degradation (see data in later sections). To avoid fabrication tolerances causing the metal mask to influence C-V characteristics, all C-V measurements were performed prior to the deposition of the metal mask. SiN was used in this instance as it can be used as an anti-reflection coating for 420 nm illumination to maximise the photo response.

4.1.2) Experimental results

Room temperature forward I-V characteristics were obtained for three device sizes. Data and fittings using Equation (3.5) are shown in Fig. 4.1. The fittings yield ideality factor of 1.7-1.85 and series resistance of 60 – 200 Ω. Hence the devices have sufficiently good ohmic contact and should not compromise measurements of avalanche multiplication.

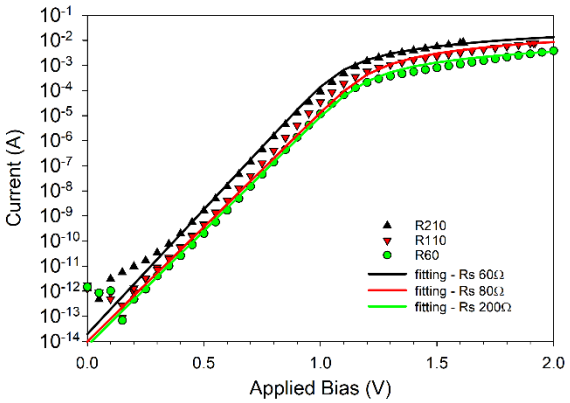

Fig. 4.1 Forward I-V data and fitting for three device sizes at room temperature. The fittings used ideality factor of 1.7-1.85 and the series resistance values in the legends.

Reverse dark I-V characteristics at room temperature were obtained from 4 - 6 devices for each size. The mean dark I-V and standard deviations for each radius of the devices are presented in Fig. 4.2(top). All devices exhibit an abrupt increase in dark current at ~ -37 V. Dark current densities from different sized devices, shown in Fig. 4.2(middle), are in disagreement, indicating that the surface-related dark current mechanism(s) dominate. The reverse I-V characteristics of the two smaller sizes scale with device perimeter, as shown in Fig. 4.2(bottom), indicating dark current is dominated by surface leakage for these sizes.

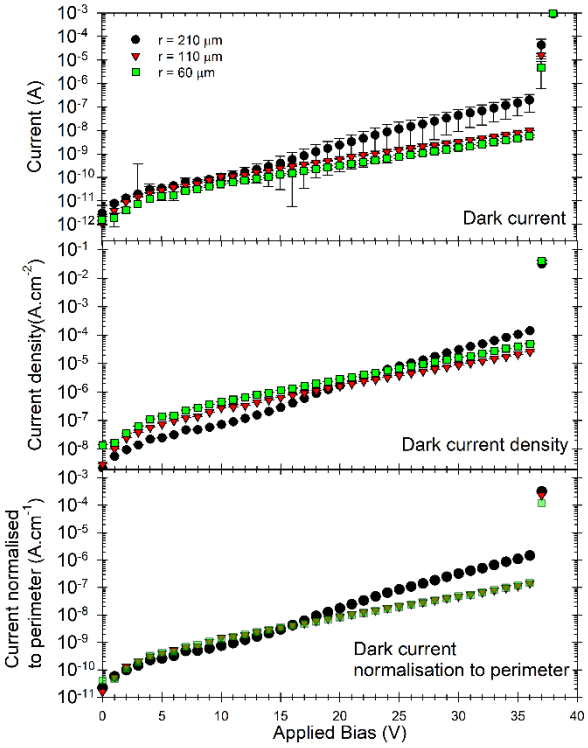

Fig. 4.2 Mean reverse dark I-V data with standard deviations of 210, 110 and 60 µm radii diodes at room temperature. The data are presented as dark current (top), current density (middle), and current normalised to the perimeter (bottom).

C-V data of the different-sized devices are shown in Fig. 4.3. A comparison of C/A data from different-sized devices indicated a mesa radial reduction of ~ 2 µm. Using the corrected radii, the depletion width as a function of reverse bias was obtained and shown in the right axis of Fig. 4.3. The depletion width was ~610 nm at 0 V and increased to 720 nm at the highest reverse bias used.

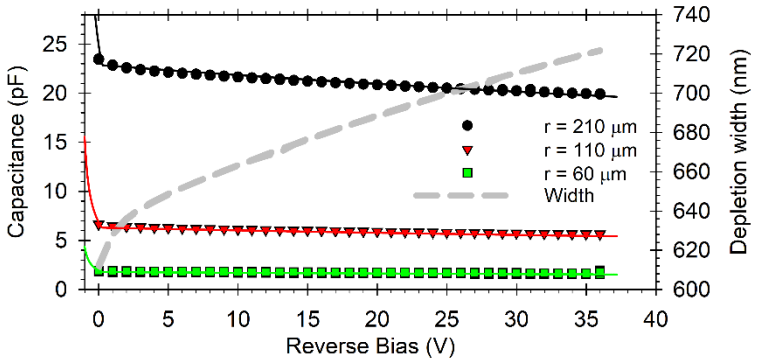

Fig. 4.3 Mean capacitance-voltage data (symbols) and fitting (solid) for 210, 110 and 60 µm radii diodes. and depletion width (dash)

Using 3-region C-V fitting (shown in Fig. 4.3), assuming constant doping in each of the p-, i-, and n layers, a dielectric constant of 11.41 [3] and corrected radii, it was found that the i-AlGaAsSb region width was ~608 nm with a background doping of 5 $\times 10^{15}$ cm^{-3}. The p-AlGaAsSb and n-AlGaAsSb were both fitted with a doping concentration of $\pm 7 \times 10^{17}$ cm^{-3}. Electric field profiles simulated using the extracted doping profile are shown in Fig. 4.4 for several reverse biases. C-V data were also used to extract noise power from raw noise measurement data.

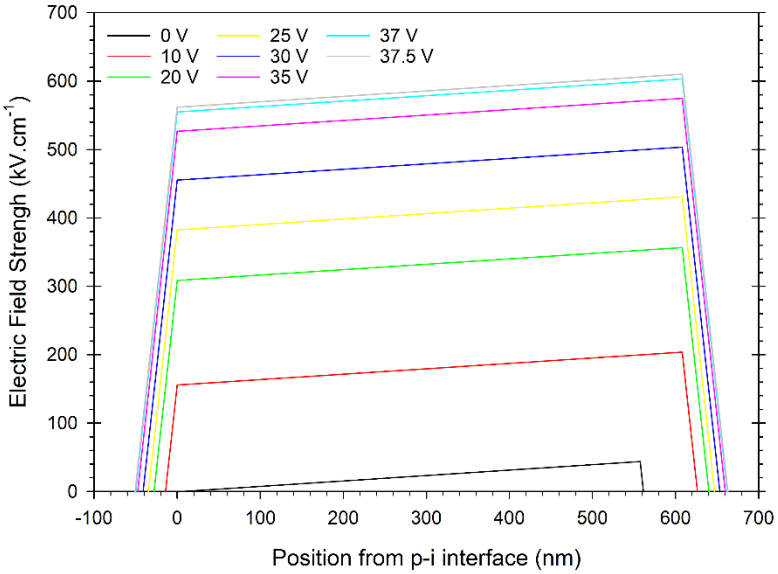

Fig. 4.4 Electric field profiles simulated using the extracted doping profiles at different reverse biases.

The main $M(V)$ and $F(M)$ data were obtained using a LED with a centre emission wavelength of 420 nm as the light source with a FWHM of ~15nm [4]. This wavelength choice ensured pure electron injection (as in [5]), with > 99.99% of the incoming light absorbed by the point of the p-AlGaAsSb/i-AlGaAsSb junction. The estimate was obtained using Beer-Lambert's Law and absorption coefficients (6.4×10^5 cm^{-1} for

$In_{0.53}Ga_{0.47}As$ [6] and 3.0×10^5 cm^{-1} for AlGaAsSb [5]), as summarised in Table 4.2. The absorption coefficients for AlGaAsSb were calculated using linear interpolation between the binary materials [6]–[9]. They are similar to those reported recently for AlGaAsSb [10], which was based on optical absorption data measured from 400 to 850 nm wavelengths for a 1 µm thick AlGaAsSb grown as a digital alloy.

Table 4.2. Calculated absorption coefficients for $In_{0.53}Ga_{0.47}As$ and $Al_{0.85}Ga_{0.15}As_{0.56}Sb_{0.44}$

Wavelength (nm)	**$In_{0.53}Ga_{0.47}As$ (cm^{-1})**	**$Al_{0.85}Ga_{0.15}As_{0.56}Sb_{0.44}$ (cm^{-1})**	
		Linear interpolation [6]–[9]	Ref. [10]
420	6.4×10^5	3.0×10^5	2.3×10^5
543	2.3×10^5	5.3×10^4	3.0×10^4
633	1.2×10^5	1.9×10^4	9.6×10^3

The light transmittance profiles within the device (using the linear interpolated values) for the three wavelengths is shown in Fig. 4.5. Electric field profiles at 0, and -37.2 V are included to indicate the expected depletion region's location. The optical absorption in each layer is tabulated in Table 4.3 for both the linear and Ref. [10] absorption coefficients.

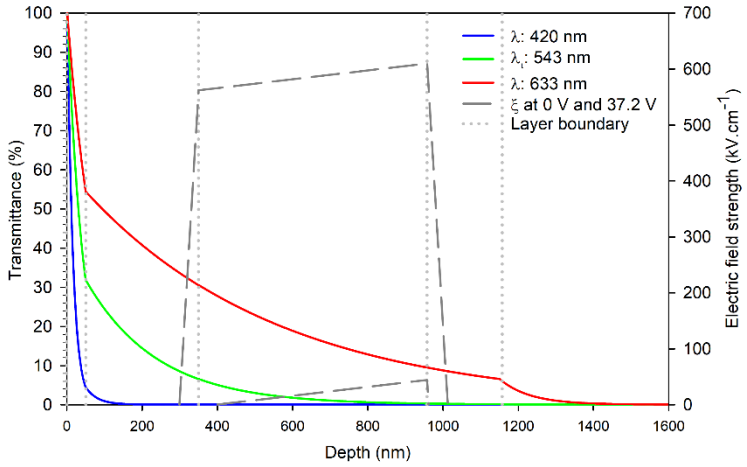

Fig. 4.5. The transmittance of a mesa for three different wavelengths with minimum and maximum electric field

Table 4.3. Calculated absorption of light in each layer of the device

Layer	Depth (nm)	doping	Amount of light absorbed (%)					
			Ref. [10]			Linear interpolation		
			420 nm	543 nm	633 nm	420 nm	543 nm	633 nm
$In_{0.53}Ga_{0.47}As$	50	p+	95.7	68.3	45.7	95.7	68.3	45.7
$Al_{0.85}Ga_{0.15}As_{0.56}Sb_{0.44}$	300	p	4.3	25.2	23.8	4.3	18.6	13.5
$Al_{0.85}Ga_{0.15}As_{0.56}Sb_{0.44}$	600	i	-	6.3	20.9	-	10.8	17.8
$Al_{0.85}Ga_{0.15}As_{0.56}Sb_{0.44}$	200	n	-	0.2	3.1	-	1.1	4.0
$In_{0.53}Ga_{0.47}As$	500	n+	-	-	6.5	-	1.2	19.0

A significant proportion of the injected light is absorbed in the InGaAs capping layer, which will reduce responsivity. The 420 nm wavelength light (meant to produce pure electron injection) is strongly absorbed before reaching the depletion region. A proportion of photo-generated carriers will be lost through recombination when diffusing towards the depletion region, resulting in low responsivity. Hence phase-sensitive measurements are essential in obtaining accurate $M(V)$ and $F(M)$ data. Additional measurements were taken using stablised He-Ne lasers emitting at 543 and 633 nm wavelengths. The percentage of light absorbed by the point of the p-AlGaAsSb/i-AlGaAsSb junction is 86.9-93.5 and 59.2-69.5 %, resulting in mixed carrier injections (since each absorbed photon will generate an electron-hole pair).

The $M(V)$ and $F(M)$ characteristics at room temperature were obtained from 5 – 15 devices of various sizes, with the results presented as an average and standard deviation for each optical injection profile. $M(V)$ data obtained using different wavelengths are compared in Fig. 4.6. Small increases in collection efficiency of photo-generated carriers with V were taken into account (using linear baseline correction from chapter 3) when extracting $M(V)$. For a given reverse bias, avalanche gain decreases as wavelength increases which is expected as more holes are injected into the avalanche region and $\alpha >> \beta$ in this material [5], [11], [12]. Data of inverse gain (right axis) in Fig. 4.6 has been extrapolated and shows the inverse gain, converging and intercepting the axis at a voltage of -37.2 V, confirming the avalanche breakdown voltage.

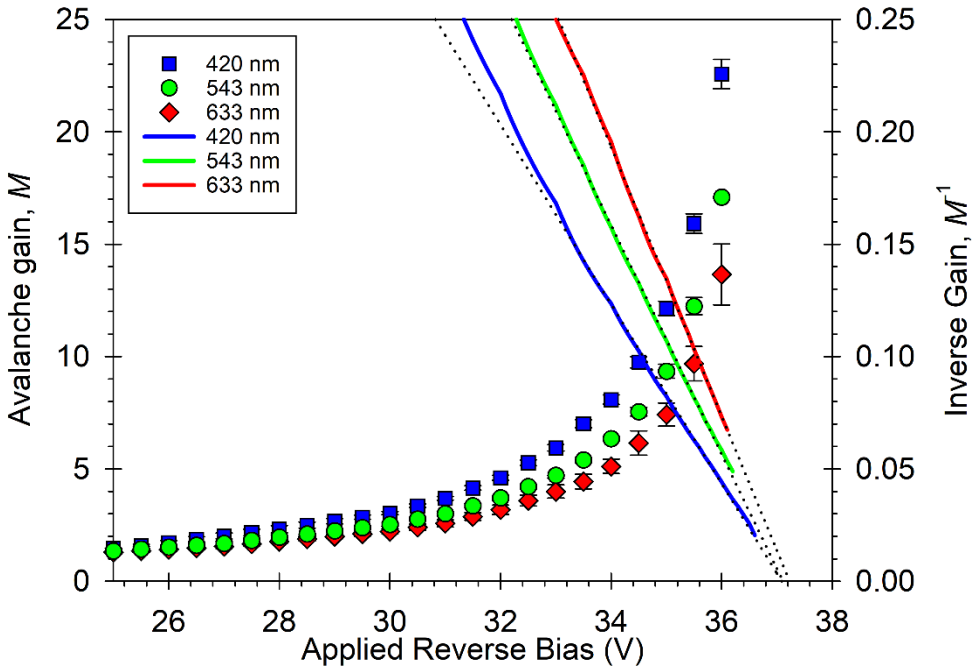

Fig. 4.6 M(V) of the sample under 420, 543, and 633 nm illumination (symbols), The inverse *M*(*V*) (lines) is used for indicating the breakdown voltage.

The corresponding *F*(*M*) data are shown in Fig. 4.7 (left), along with lines of *F*(*M*) based on the McIntyre model [13] for k values. Pure electron injection using 420 nm light produced the lowest *F*(*M*) data. As the wavelength of light increases, there is a monotonic, significant increase in *F* for a given *M*, indicating the significant impact that carrier injection profile has on the noise performance in AlGaAsSb. Again, this is consistent with $\alpha >> \beta$ since excess noise is highly sensitive to changes in carrier injection profile. $F_e(M_e)$ results on a sample before applying the metal mask indicated the devices were highly sensitive to side injection. The larger devices with the optical spot being many times smaller than the device had an *F*(*M*) result comparable to the pure electron injection presented in Fig. 4.7 (left). The smaller radius devices had an *F*(*M*) result comparable to the 543 nm injection profile. The side injection effect was not observed with the optical metal mask applied. In Fig. 4.7 (left), the data set with larger mean *F* values have larger standard deviations, consistent with the data reported in [5]. This may be due to a combination of greater optical power fluctuation of the light source and/or fewer devices in the data set._Comparison of *F*(*M*) data from different APDs or reports can be made by comparing their effective *k* values, which are deduced from the *F*(*M*) characteristics expected from the Local Model (section 2.4.1). The 420 nm illuminated $F_e(M_e)$ presented in Fig. 4.7 has a $k_{eff} < 0$ for $M<25$. This may be due to a combination of $\alpha >> \beta$ and the effects of carriers' deadspace. Previously reported AlGaAsSb *F*(*M*) and this work are compared between various avalanche widths in Fig. 4.7 (right). These include w = 100 and 200 nm devices [5] by Pinel *et al.* as well as w = 1000 nm DA (mixed) [11] and w = 910 nm RA [12] by Lee *et al*. Differences could be due to the characterisation method and analysis method. For example, ref [12] used an Agilent 8973 noise figure analyser, which does not utilise phase-sensitive

detection techniques as in this work. Both 1 µm and 910 nm devices follow a McIntyre local excess noise model [13], where k is ~0.01.

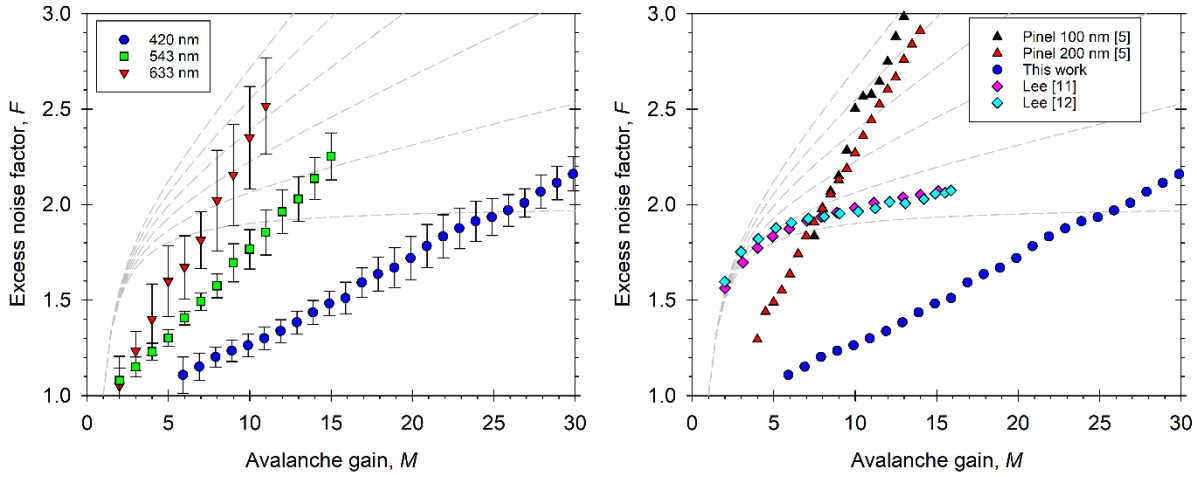

Fig. 4.7 F(M) data using 420, 543, and 633 nm illumination, with error bars indicate standard deviation (L). Comparison of *F(M)* with other reports, including L.Pinel (100 and 200 nm) *[5]*, S.Lee (1000 nm and 910 nm) *[11], [12]* (R). McIntyre's local model *[13]* for fixed *k* values (0 to 0.1 in 0.02 steps, grey dash) is included for comparison

4.2) AlGaAsSb Simple Monte Carlo modelling

A Simple Monte Carlo model for $Al_{0.85}Ga_{0.15}As_{0.56}Sb_{0.44}$ was developed and validated using reported experimental results of *C-V*, *M*(*V*), and *F*(*M*) from five AlGaAsSb APDs. The verified model was then used to extract the effective ionisation coefficients and threshold energies between 400–1200 kV.cm^{-1} at room temperature. These are suitable for use with less complex APD simulation models.

Extracting impact ionisation coefficients from experimental *M*(*V*) and *F*(*M*) results usually requires experimental samples with uniform electric fields across the avalanche regions. The AlGaAsSb diodes in Ref. [5] and in this work, possess relatively graded doping profiles, producing a highly non-uniform electric field profile, as illustrated in the comparison between the intended doping profile and SIMS analysis in Fig. 4.8. Commonly used APD simulation models, such as the local model [13], the recurrence model [14], and the RPL model [15], are unsuitable for non-uniform electric field profiles [16]. Therefore, obtaining the electric field dependences of α and β for AlGaAsSb requires a more complex method and APD simulation model. In this work, a Simple Monte Carlo (SMC) simulation model for AlGaAsSb APDs, validated with published room temperature data of *M*(*V*) and F(*M*) from Ref [5] and Section 4.1, is presented. The AlGaAsSb SMC model can then be used to extract the electric field dependencies of effective impact ionisation coefficients and threshold energies. These could be used with simpler, more accessible simulation models, such as the recurrence model and RPL model, provided the APD designs have well-defined doping profiles.

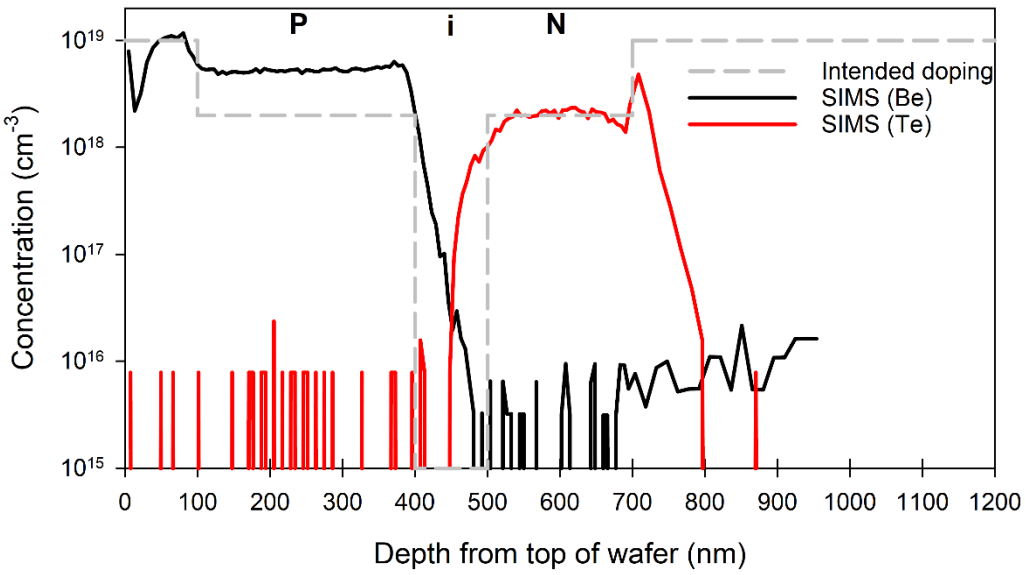

Fig. 4.8 Comparison between the intended doping profile (dash) and the SIMS P and N dopants for SF0921

4.2.1) Verification device details

The experimental data used in the AlGaAsSb SMC model validation were from three p-i-n wafers (A, C, and E) and two n-i-p wafers (B and D) of various avalanche widths from Refs. [5] and Section 4.1. Nominal w values, V_{bd} values, and data types of the wafers are summarised in Table 4.4. The p-i-n wafers provided validation data for electron-initiated avalanche multiplication and excess noise factor, $M_e(V)$ and $F_e(M_e)$, respectively. Similarly, the n-i-p wafers provided hole-initiated avalanche multiplication and excess noise factor $M_h(V)$ and $F_h(M_h)$. The wafer structure of these p-i-n (or n-i-p) diodes [5] are as follows: 100 nm of p^+ (or n^+) InGaAs (1×10^{19} cm^{-3}), 300 nm of p^+ (or n^+) AlGaAsSb (2×10^{18} cm^{-3}), 100-200 nm unintentionally doped AlGaAsSb, 200 nm of n^+ (or p^+) AlGaAsSb (2×10^{18} cm^{-3}), and 1000 nm of n^+(or p^+) InGaAs (1×10^{19} cm^{-3}).

Table 4.4. AlGaAsSb device details for modelling

Device	Wafer number	Nominal (fitted) i-region (nm)	Layer structure	Breakdown Voltage (V)	Impact ionisation data	Electric field range ($kV.cm^{-1}$)
A	SF0921	100 (80)	*p-i-n*	11.0	$M_e(V)$, $F_e(M_e)$	800-1200
B	SF0926	100 (98)	*n-i-p*	10.6	$M_h(V)$, $F_h(M_h)$	800-1050
C	SF0922	200 (160)	*p-i-n*	15.9	$M_e(V)$, $F_e(M_e)$	600-850
D	SF0929	200 (193)	*n-i-p*	15.9	$M_h(V)$, $F_h(M_h)$	700-810
E	IE-01	600 (608)	*p-i-n*	37.2	$M_e(V)$, $F_e(M_e)$	400 - 580

The doping profiles for wafer A-D used were estimated by fitting C-V data to Secondary Ion Mass Spectroscopy. For each of the five wafers, the C-V data used, covers multiple devices with at least three device diameters. In addition, C-V data analyses included slight radial reductions in the device area to account for device fabrication tolerances. The SIMS results for Device A -D are shown in Fig. 4.9 (L); the C-V data and fitting using the 1-D Poisson's field solver are shown in Fig. 4.9 (R).

The SIMS results have a noise floor of ~ 10^{15} cm^{-3}, and the calibration sample for the SIMS measurements was GaAs due to the lack of reliable AlGaAsSb reference samples (at the time of the analysis). C-V data of wafer E was fitted satisfactorily using a three-region fitting; hence SIMS analysis was not required. The SIMS profiles for devices B and D indicate the N-type dopant (Te) were less confined the p-type dopant (Be). For devices A and C, the SIMS profile indicate that both dopants were not well confined. To fit to the C-V data, approximately 75, 95, 60 and 95 % of the dopants in the SIMS data were assumed as electrically active dopants for wafers A, B, C and D, respectively.

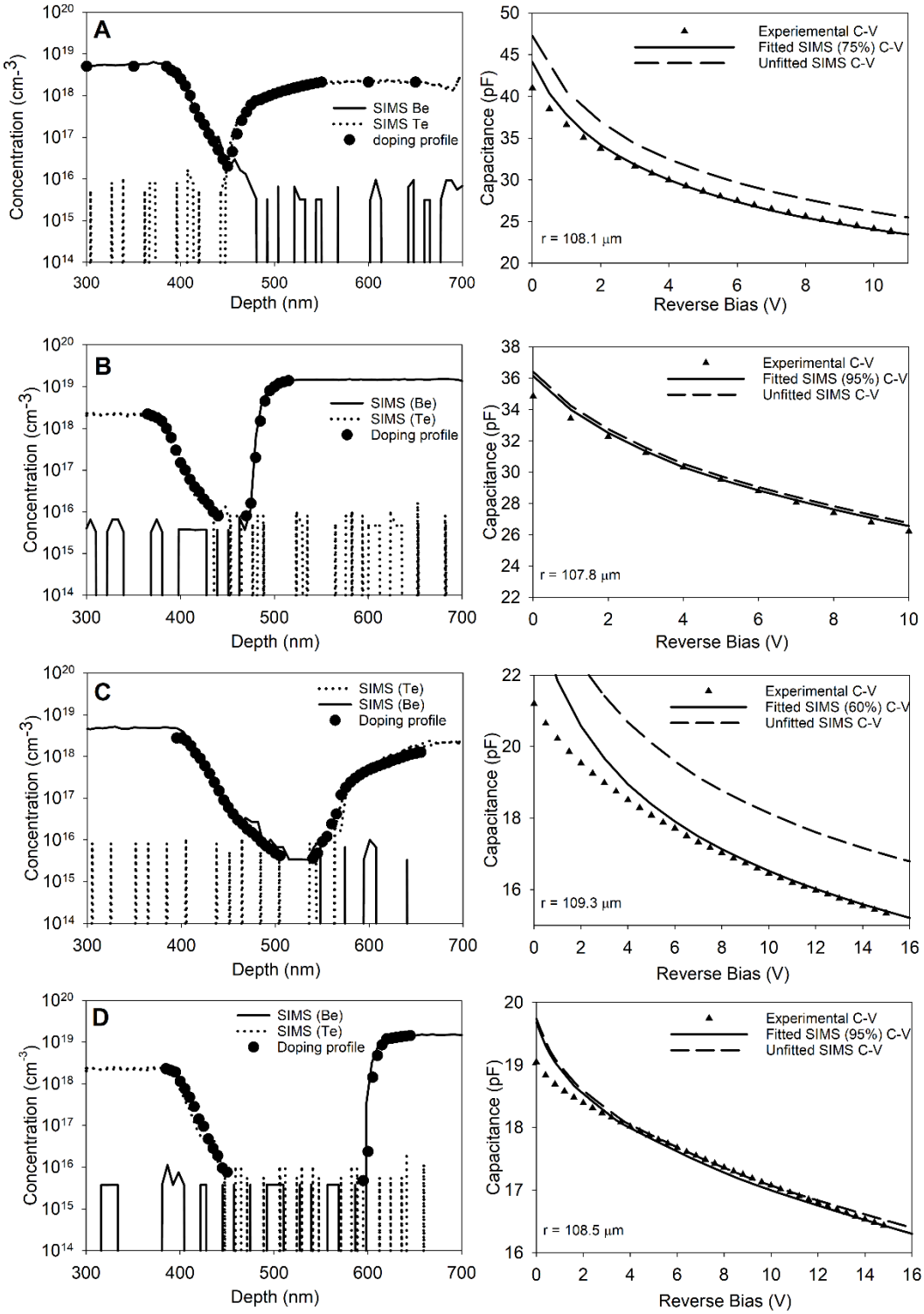

Fig. 4.9 SIMS and activated doping profile for Device A-D (L) and experimental Capacitance-Voltage (symbols) compared with 100 % dopant activation and fitted dopant activation (R)

The electric field of each wafer near breakdown versus a ratio of depletion width to intended i-region width is presented in Fig. 4.10. Wafers A and B have their depletion width 40% wider than the intended widths, with other samples wider by ≤ 20 %. Wafer A has a highly non-uniform electric field.

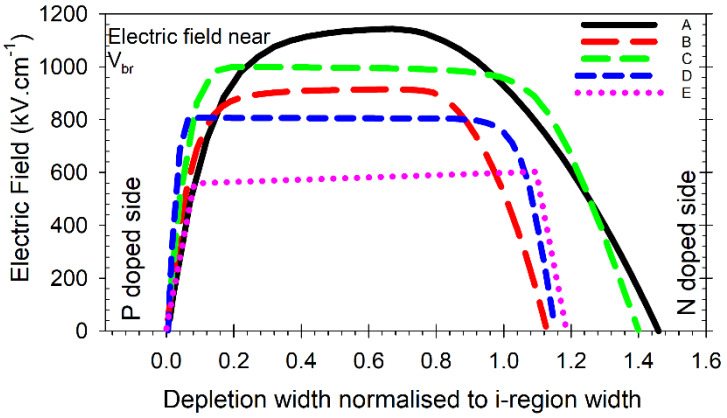

Fig. 4.10 Electric field strength for the five devices, near breakdown. The X-axis ratio of depletion width to i-region.

4.2.2) SMC parameter set

In the SMC model simulations, each carrier drifts across an avalanche region, under an electric field, for a random distance before undergoing one of four possible scattering mechanisms: intervalley phonon emission (R_{em}), intervalley phonon absorption (R_{ab}), impact ionisation (R_{ii}), and alloy scatting rate (R_{alloy}). The scattering rates are given by

$$R_{em} = \frac{N(T)+1}{\lambda\,(2N(T)+1)}\sqrt{\frac{2(E_c-\hbar\omega)}{m^*}} \qquad \text{(2.22 repeated)}$$

$$R_{ab} = \frac{N(T)}{\lambda\,(2N(T)+1)}\sqrt{\frac{2(E_c+\hbar\omega)}{m^*}} \qquad \text{(2.23 repeated)}$$

$$R_{ii} = C_{ii}\left(\frac{E_c - E_{th}}{E_{th}}\right)^{\gamma} \qquad \text{(2.25 repeated)}$$

$$R_{alloy} = C_{alloy}\,(m^*)^{\frac{3}{2}}\sqrt{E_c} \qquad \text{(2.27 repeated)}$$

When simulating an APD at a given reverse bias, the electric field profile was calculated using a 1-D Poisson's field solver with the C-V fitted doping profile. Typically, the rate equations are fitted to scattering rate data from literature and then modified to fit experimental impact ionisation results to obtain a verified parameter set. Due to a lack of published carrier scattering rates for AlGaAsSb, this approach was not feasible. Hence reported GaAs [17] and AlGaAs [18] [19] SMC parameter sets were used as an initial reference. The value of $\hbar\omega$ was obtained by linear interpolation of values from the binary materials [20]–[22]. The value of E_{th} was

similarly obtained. The value of the binary material's threshold energy was given by the weighted average [23] $E_{th} = (E_0 + 3E_x + 4E_L)/8$, where E_0, E_x, and E_L [20], [24]–[27] are the energy bandgap for Γ, X and L valleys, respectively. The drift velocities for electrons and holes were set to closely match GaAs and $Al_{0.8}Ga_{0.2}As$ due to the lack of experimental drift velocity data for AlGaAsSb. Values of C_{ii}, λ, γ, and C_{alloy} were adjusted so that the SMC results agree with published $M(V)$ and $F(M)$ results. The relative permittivity of the material [28] and built-in voltage were extracted from C-V data. The AlGaAsSb SMC model parameter set is summarised in Table 4.5.

Table 4.5 AlGaAsSb SMC model parameter set

	Electrons	Holes
Phonon energy, $\hbar\omega$ (meV)	44	
Threshold energy, E_{th} (eV)	2	
Mean free path, λ (Å)	50	33
Effective mass, m^*	0.6 m_0	0.65 m_0
Impact ionisation rate prefactor, C_{ii} ($\times 10^{12}$ s^{-1})	60	
Softness factor, γ	2	
Alloy scatting constant ($\times 10^{68}$)	1	3
Max energy (eV)	9	
Relative permittivity, ε_r	11.41	
Built-in voltage (V)	1.24	

Using our SMC model, $M(V)$ and $F(M)$ characteristics were simulated for wafers A, C and E (electron-initiated) as well as wafers B and D (hole-initiated). The simulated results are in agreement with the experimental validation data, as shown in Fig. 4.11. $F(M)$ for all devices show good agreement, with the *n-i-p* devices having a slightly higher $F(M)$ than the experimental. For wafer E, the agreement in $M(V)$ worsens as the gain increases, which may be due to the 3-layer abrupt doping profile approximation used.

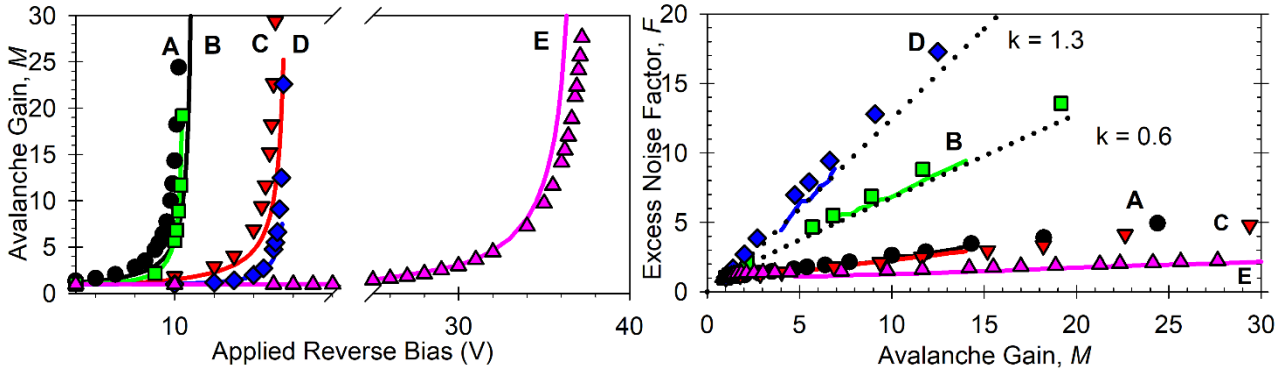

Fig. 4.11 M(V) for the five verification devices (lines) and the SMC model (symbols). F(M) for the five verification devices (lines) and SMC model (symbols)

4.2.3) Saturation velocity

The SMC's drift velocity for this parameter set is shown in Fig. 4.12. The saturation velocity values (between 100 and 400 kV.cm^{-1}) are 7.6×10^4 and 6.6×10^4 m.s^{-1} for electrons and holes respectively. They are similar to those of GaAs and $Al_{0.8}Ga_{0.2}As$. Beyond 400 kV.cm^{-1}, the SMC predicts that the drift velocity will increase as impact ionisation becomes significant. However, due to a lack of published experimental data for this material, the AlGaAsSb SMC model's drift velocity is unverified. This should be noted if the SMC model is applied to the time-domain simulations, such as time to breakdown simulation for Geiger-mode devices.

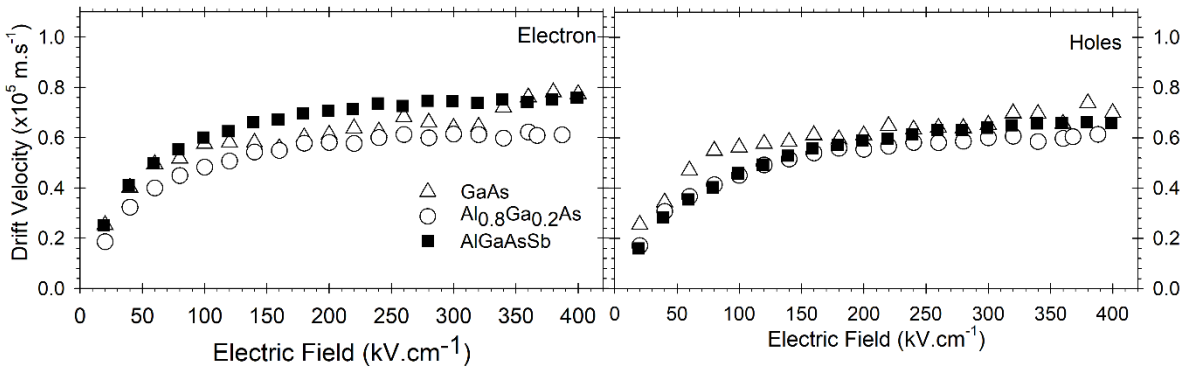

Fig. 4.12 Drift velocity calculated using the AlGaAsSb SMC parameter set for electrons (L) and holes (R). GaAs and $Al_{0.8}Ga_{0.2}As$ drift velocity produced by SMC are also plotted for comparison.

4.2.4) Probability density function fitting

Using the AlGaAsSb SMC model, another series of simulations were carried out to extract impact ionisation coefficients as functions of electric field (ξ) from 400 to 1200 kV.cm^{-1}. For this, each simulation tracked a single carrier (electron or hole) under a constant electric field of infinite length and recorded distances between each consecutive impact ionisation event (i.e. ionisation path lengths). These statistics yielded

probability density functions (PDFs) of the ionisation path lengths for electrons and holes, $h_e(x)$ and $h_h(x)$ [29]. The effective ionisation coefficient (α^* and β^*) and deadspace (d_e and d_h) for electrons and holes were obtained from fittings to these PDFs, using the hard deadspace assumption [14], where

$$h_{e(h)}(x) = \begin{cases} 0, & x \leq d_{e(h)} \\ \alpha^*(\beta^*) exp\left[-\alpha^*(\beta^*)\left(x - d_{e(h)}\right)\right] & x > d_{e(h)}. \end{cases} \tag{4.1}$$

Example $h_e(x)$ and $h_h(x)$ as well as their fittings at $\xi = 800$ kV.cm^{-1} are shown in Fig. 4.13 (L). Full PDFs fittings are shown in the appendix. For each electric field, values of α^* (or β^*) and d_e (or d_h) were extracted by fitting to the gradient of $h_e(x)$ at large x and the $h_e(x)$ region before the peak, respectively. The deadspaces were given by Eqn. (4.1), and the values obtained from the fittings were usually PDFs from the SMC model showing a soft dead space value. To represent this effect with the hard dead space approximation, a value less than the peak is chosen and modified to obtain good agreement. An example of this is shown in Fig. 4.13 (R) for electron $\xi = 800$ kV.cm^{-1}.

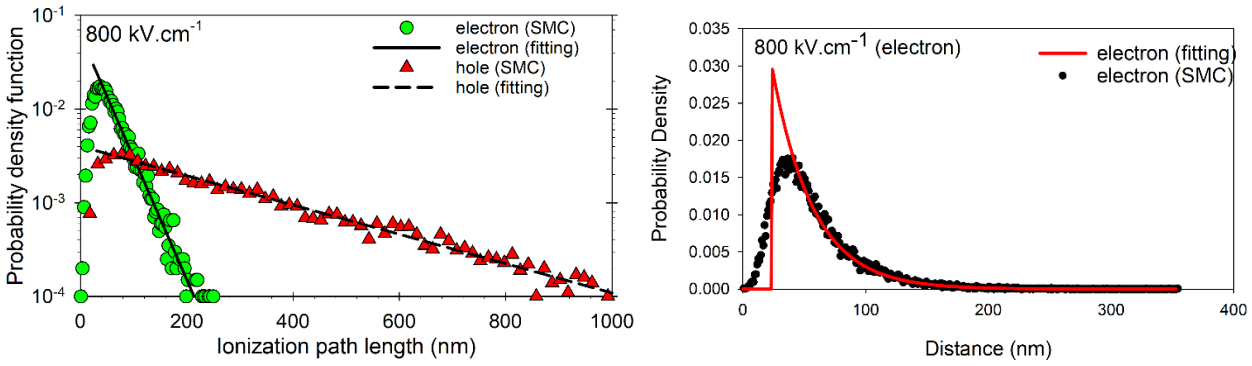

Fig. 4.13 *Example of PDF fitting for electrons and holes for AlGaAsSb at 800 kV.cm^{-1}(L). Example of PDF fitting for electron for AlGaAsSb at 800 kV.cm^{-1} (R).*

4.2.5) Ionisation coefficients and threshold energies

The values for E_{the} and E_{thh} are 3.6 eV. The extracted electric field dependence of α^* and β^* are plotted versus the electric field and inverse electric field in Fig. 4.14. They can be parametrised using

$$\alpha^*(\xi) = 5.2 \times 10^6 \exp\left[-\left(\frac{1.8 \times 10^6}{\xi}\right)^{1.27}\right] \text{cm}^{-1} \tag{4.2}$$

$$\beta^*(\xi) = 3.2 \times 10^6 \exp\left[-\left(\frac{2.1 \times 10^6}{\xi}\right)^{1.53}\right] \text{cm}^{-1}, \tag{4.3}$$

which are also included in Fig. 4.14.

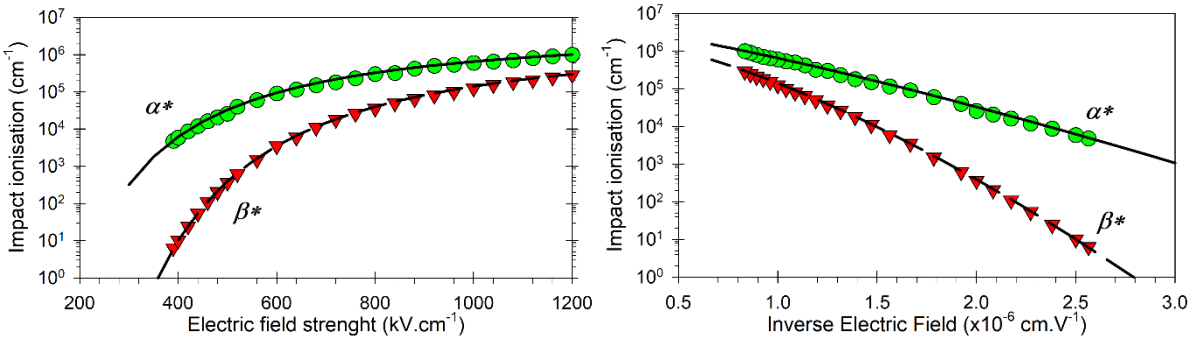

Fig. 4.14 Effective impact ionisation coefficient for ξ and ξ^{-1} from PDF fitting (symbols) and parametrised fitting (lines).

The extracted effective impact ionisation coefficients of AlGaAsSb are compared to those of AlAsSb [30], InAlAs [16], and InP [31] in Fig. 4.15 (right). α and β of AlGaAsSb are much more dissimilar, compared to those of InP and InAlAs. The α and β of AlGaAsSb and AlAsSb show a similar value for low electric fields. In addition, recently published AlGaAsSb [32] coefficients extracted using a local impact ionisation model (i.e. assuming zero deadspace) are compared to ionisation coefficients of this work in Fig. 4.15 (left). However, it is difficult to make direct comparison given the assumption made in ref [32].

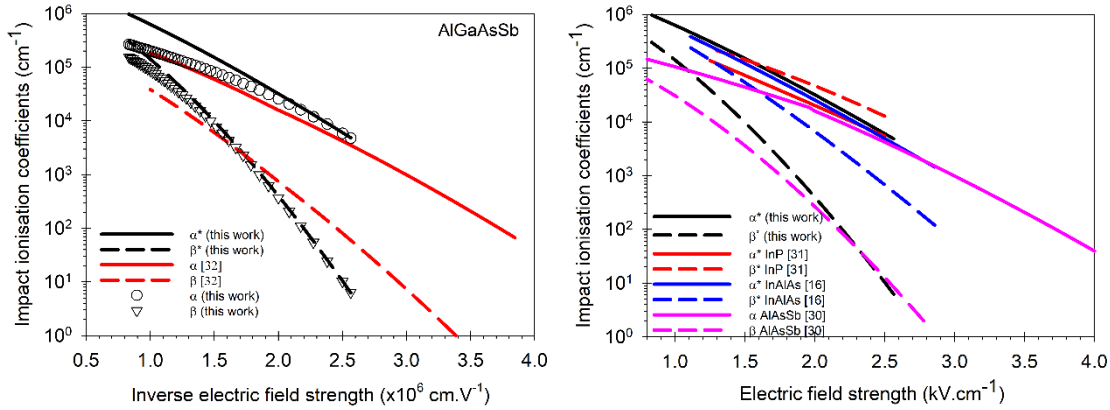

Fig. 4.15 Impact ionisation coefficient for AlGaAsSb for this work and reported [32] (L). Impact ionisation coefficients for AlGaAsSb, InP [31], InAlAs [16] and AlAsSb [30], lattices-matched to InP (R).

To confirm the validity of Eqn. (4.2) and (4.3), avalanche multiplication and excess noise factors of a series of AlGaAsSb ideal p-i-n diodes were simulated using both the AlGaAsSb SMC model and an RPL model. Inputs to the latter are Eqn. (4.2) and (4.3) as well as $E_{the} = E_{thh} = 3.6$ eV. The ideal p-i-n diodes, labelled as D1, D2, D3, D4, D5, and D6, have w of 100, 200, 500, 800, 1000, and 1500 nm, respectively. Avalanche gain results from SMC and RPL simulations are in good agreement, as shown in Fig. 4.16. Similar comparisons are made for excess noise factors due to pure electron or pure hole injection are also in good agreement, as shown in Fig. 4.17. These confirm the validity of the $\alpha^*(\xi)$, $\beta^*(\xi)$, E_{the}, and E_{thh} of this work.

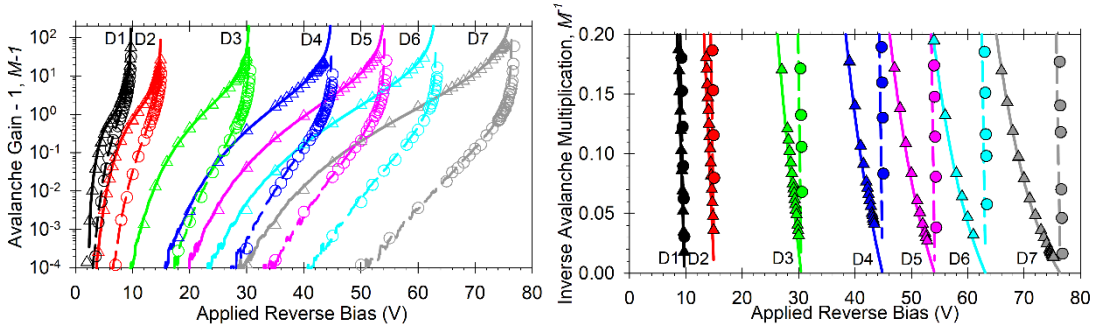

Fig. 4.16 Avalanche multiplication and inverse for the electron (triangle and solid) and hole (circle and dash) initialled impact ionisation for various widths compared between SMC (symbols) and RPL (lines)

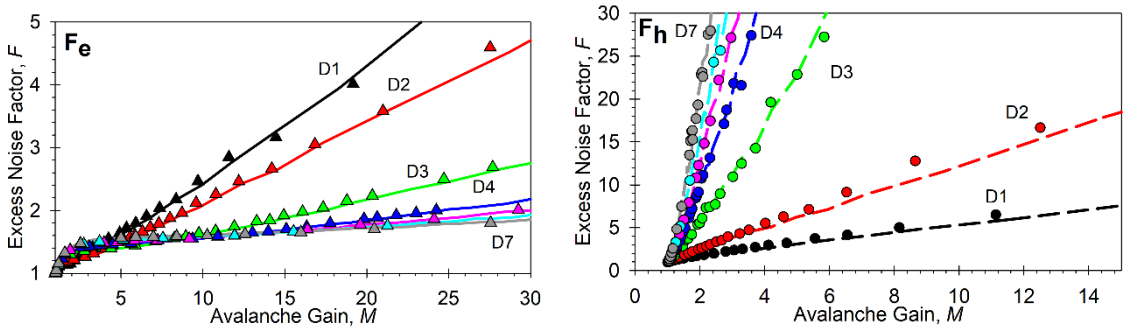

Fig. 4.17 Excess noise factor for the electron (triangle and solid) and hole (circle and dash) initialled impact ionisation for various widths compared between SMC (symbols) and RPL (lines)

A comparison of breakdown voltage extracted from $M^{-1}(V)$ for device width from the SMC and reported experimental [5], [11], [12] is presented in Fig. 4.18 (L). The breakdown voltage is fitted to the linear regression $V_{br} = 0.0478(width[nm]) + 5.8$. The $F_e(M_e)$ for M_e of 10, 20 and 30 is presented in Fig. 4.18 (R).

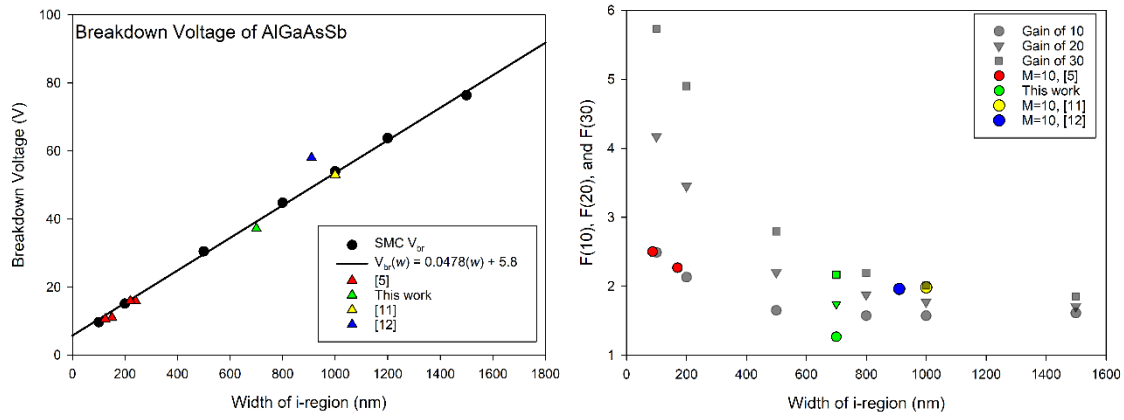

Fig. 4.18 Breakdown voltage compared to device-width from SMC fitting and experimental results (left). Excess noise factor for a particular gain compared to the width of the device for SMC fitting and experimental results (right).

4.3) Conclusion

A 600 nm AlGaAsSb mesa *p-i-n* diode has been experimentally characterised for avalanche gain and excess noise factor for pure electron injection and two mixed injection profiles. At an avalanche multiplication of 10 and 20, the excess noise factor was measured at 1.27 and 1.74 for pure electron injection, significantly lower than previously reported, narrower device based on $Al_{0.85}Ga_{0.15}As_{0.56}Sb_{0.44}$, as well as comparable devices based on relevant avalanche materials such as InP and $In_{0.52}Al_{0.48}As$. The importance of using pure electron injection is confirmed by the worsening excess noise performance when relatively low mixed carrier injection profiles were characterised. The pure electron injection impact ionisation results demonstrate the potential for this material system for a new generation of extremely low noise SAM APDs for 1.31 and 1.55 μm detection.

A Simple Monte Carlo model parameter set has been verified for avalanche multiplication and excess noise factor using this work's experimental capacitance-voltage, avalanche multiplication and excess noise factor, and those earlier reported in the literature. Using the validated parameter set, the electric field dependant effective impact ionisation coefficients and threshold energies of $Al_{0.85}Ga_{0.15}As_{0.56}Sb_{0.44}$ at room temperature has been extracted from the simulations. The impact ionisation coefficients have been parameterised between the electric field range of 400-1200 $kV.cm^{-1}$. These parameters were verified by simulating a range of p-i-n and n-i-p devices using the verified Simple Monte Carlo Model and the parameterised impact ionisation coefficients with a random path length model.

4.4) References: Chapter 4

[1] J. Taylor-Mew, V. Shulyak, B. White, C. H. Tan, and J. S. Ng, 'Low Excess Noise of $Al_{0.85}Ga_{0.15}As_{0.56}Sb_{0.44}$ Avalanche Photodiode From Pure Electron Injection', *IEEE Photonics Technol. Lett.*, vol. 33, no. 20, pp. 1155–1158, Oct. 2021, doi: 10.1109/LPT.2021.3110123.

[2] J. D. Taylor-Mew, J. D. Petticrew, C. H. Tan, and J. S. Ng, 'Simulation of $Al_{0.85}Ga_{0.15}As_{0.56}Sb_{0.44}$ avalanche photodiodes', *Opt. Express*, vol. 30, no. 11, p. 17946, May 2022, doi: 10.1364/OE.458922.

[3] X. Zhou, L. L. Pinel, S. J. Dimler, S. Zhang, J. S. Ng, and C. H. Tan, 'Thin Al1-xGaxAs0.56Sb0.44 Diodes With Low Excess Noise', *IEEE J. Sel. Top. Quantum Electron.*, vol. 24, no. 2, pp. 1–5, 2018.

[4] 'Thorlabs - M420F2 420 nm, 8.90 mW (Min) Fiber-Coupled LED, 1000 mA, SMA'. https://www.thorlabs.com/thorproduct.cfm?partnumber=M420F2&pn=M420F2#7108 (accessed Nov. 15, 2018).

[5] L. L. G. Pinel *et al.*, 'Effects of carrier injection profile on low noise thin $Al_{0.85}Ga_{0.15}As_{0.56}Sb_{0.44}$ avalanche photodiodes', *Opt. Express*, vol. 26, no. 3, p. 3568, Feb. 2018, doi: 10.1364/OE.26.003568.

[6] S. Adachi, 'Optical dispersion relations for GaP, GaAs, GaSb, InP, InAs, InSb, $Al_xGa_{1-x}As$, and $In_{1-x}Ga_xAs_yP_{1-y}$', *J. Appl. Phys.*, vol. 66, no. 12, pp. 6030–6040, Dec. 1989, doi: 10.1063/1.343580.

[7] D. E. Aspnes and A. A. Studna, 'Dielectric functions and optical parameters of Si, Ge, GaP, GaAs, GaSb, InP, InAs, and InSb from 1.5 to 6.0 eV', *Phys. Rev. B*, vol. 27, no. 2, pp. 985–1009, Jan. 1983, doi: 10.1103/PhysRevB.27.985.

[8] A. D. Rakić and M. L. Majewski, 'Modeling the optical dielectric function of GaAs and AlAs: Extension of Adachi's model', *J. Appl. Phys.*, vol. 80, no. 10, pp. 5909–5914, Nov. 1996, doi: 10.1063/1.363586.

[9] S. Zollner, C. Lin, E. Schönherr, A. Böhringer, and M. Cardona, 'The dielectric function of AlSb from 1.4 to 5.8 eV determined by spectroscopic ellipsometry', *J. Appl. Phys.*, vol. 66, no. 1, pp. 383–387, Jul. 1989, doi: 10.1063/1.343888.
[10] B. Guo *et al.*, 'Optical constants of $Al_{0.85}Ga_{0.15}As_{0.56}Sb_{0.44}$ and $Al_{0.79}In_{0.21}As_{0.74}Sb_{0.26}$', *Appl. Phys. Lett.*, vol. 119, no. 17, p. 171109, Oct. 2021, doi: 10.1063/5.0062035.
[11] S. Lee *et al.*, 'Low noise $Al_{0.85}Ga_{0.15}As_{0.56}Sb_{0.44}$ avalanche photodiodes on InP substrates', *Appl. Phys. Lett.*, vol. 118, no. 8, p. 081106, Feb. 2021, doi: 10.1063/5.0035571.
[12] S. Lee *et al.*, 'Random alloy thick AlGaAsSb avalanche photodiodes on InP substrates', *Appl. Phys. Lett.*, vol. 120, no. 7, p. 071101, Feb. 2022, doi: 10.1063/5.0067408.
[13] R. J. McIntyre, 'Multiplication noise in uniform avalanche diodes', *IEEE Trans. Electron Devices*, vol. ED-13, no. 1, pp. 164–168, Jan. 1966, doi: 10.1109/T-ED.1966.15651.
[14] M. M. Hayat, B. E. A. Saleh, and M. C. Teich, 'Effect of dead space on gain and noise of double-carrier-multiplication avalanche photodiodes', *IEEE Trans. Electron Devices*, vol. 39, no. 3, pp. 546–552, Mar. 1992, doi: 10.1109/16.123476.
[15] D. S. Ong, K. F. Li, G. J. Rees, J. P. R. David, and P. N. Robson, 'A simple model to determine multiplication and noise in avalanche photodiodes', *J. Appl. Phys.*, vol. 83, no. 6, pp. 3426–3428, 1998, doi: 10.1063/1.367111.
[16] S. C. Liew Tat Mun, C. H. Tan, Y. L. Goh, A. R. J. Marshall, and J. P. R. David, 'Modeling of avalanche multiplication and excess noise factor in $In_{0.52}Al_{0.48}As$ avalanche photodiodes using a simple Monte Carlo model', *J Appl Phys*, vol. 104, p. 7, 2008, doi: 10.1063/1.2952003.
[17] S. A. Plimmer, J. P. R. David, D. S. Ong, and K. F. Li, 'A simple model for avalanche multiplication including deadspace effects', *IEEE Trans. Electron Devices*, vol. 46, no. 4, pp. 769–775, Apr. 1999, doi: 10.1109/16.753712.
[18] S. A. Plimmer, 'Avalanche multiplication in $Al_xGa_{1-x}As$', Ph.D dissertation, University of Sheffield, Department of Electronic and Electrical Engineering, 1997.
[19] C. K. Chia and G. K. Dalapati, 'Monte Carlo Simulation of Hot Carrier Transport in Heterogeneous Ge/Al_xGa_{1-x} As ($0<x<0.8$) Multilayer Avalanche Photodiodes', *IEEE Trans. Electron Devices*, vol. 60, no. 10, pp. 3435–3441, Oct. 2013, doi: 10.1109/TED.2013.2275970.
[20] S. Adachi, *Properties of semiconductor alloys: group-IV, III-V and II-VI semiconductors*. in Wiley series in materials for electronic & optoelectronic applications. Chichester, U.K: Wiley, 2009.
[21] Z. C. Feng, S. Perkowitz, R. Rousina, and J. B. Webb, 'Raman and infrared spectroscopy of $In_{1-x}Ga_xSb$ films grown on GaAs by metal-organic magnetron sputtering', *Can. J. Phys.*, vol. 69, no. 3–4, pp. 386–389, Mar. 1991, doi: 10.1139/p91-064.
[22] R. Manor, O. Brafman, and R. F. Kopf, 'Charge transfer between In and Ga in InGaAs-based alloys', *Phys. Rev. B*, vol. 56, no. 7, pp. 3567–3570, Aug. 1997, doi: 10.1103/PhysRevB.56.3567.
[23] J. Allam, '"Universal" Dependence of Avalanche Breakdown on Bandstructure: Choosing Materials for High-Power Devices', *Jpn. J. Appl. Phys.*, vol. 36, no. Part 1, No. 3B, pp. 1529–1542, Mar. 1997, doi: 10.1143/JJAP.36.1529.
[24] J. L. Aubel, U. K. Reddy, S. Sundaram, W. T. Beard, and J. Comas, 'Interband transitions in molecular-beam-epitaxial $Al_xGa_{1-x}As$/GaAs', *J. Appl. Phys.*, vol. 58, no. 1, pp. 495–498, Jul. 1985, doi: 10.1063/1.335652.
[25] D. E. Aspnes, S. M. Kelso, R. A. Logan, and R. Bhat, 'Optical properties of $Al_xGa_{1-x}As$', *J. Appl. Phys.*, vol. 60, no. 2, pp. 754–767, Jul. 1986, doi: 10.1063/1.337426.
[26] A. K. Saxena, 'Non-Γ Deep Levels and the Conduction Band Structure of $Ga_{1-x}Al_xAs$ Alloys', *Phys. Status Solidi B*, vol. 105, no. 2, pp. 777–787, Jun. 1981, doi: 10.1002/pssb.2221050240.
[27] C. Alibert, A. Joullié, A. M. Joullié, and C. Ance, 'Modulation-spectroscopy study of the $Ga_{1-x}Al_xSb$ band structure', *Phys. Rev. B*, vol. 27, no. 8, pp. 4946–4954, Apr. 1983, doi: 10.1103/PhysRevB.27.4946.
[28] X. Zhou, S. Zhang, J. P. R. David, J. S. Ng, and C. H. Tan, 'Avalanche Breakdown Characteristics of Al_{1-x} Ga_xAs $_{0.56}Sb_{0.44}$ Quaternary Alloys', *IEEE Photonics Technol. Lett.*, vol. 28, no. 22, pp. 2495–2498, Nov. 2016, doi: 10.1109/LPT.2016.2601651.
[29] S. A. Plimmer, J. P. R. David, and D. S. Ong, 'The merits and limitations of local impact ionization theory [APDs]', *IEEE Trans. Electron Devices*, vol. 47, no. 5, pp. 1080–1088, May 2000, doi: 10.1109/16.841244.

[30] J. Xie, S. Xie, R. C. Tozer, and C. H. Tan, 'Excess Noise Characteristics of Thin AlAsSb APDs', *IEEE Trans. Electron Devices*, vol. 59, no. 5, pp. 1475–1479, May 2012, doi: 10.1109/TED.2012.2187211.
[31] J. D. Petticrew, S. J. Dimler, C. H. Tan, and J. S. Ng, 'Modeling Temperature-Dependent Avalanche Characteristics of InP', *J. Light. Technol.*, vol. 38, no. 4, pp. 961–965, Feb. 2020, doi: 10.1109/JLT.2019.2948072.
[32] B. Guo *et al.*, 'Impact ionization coefficients of digital alloy and random alloy Al0.85Ga0.15As0.56Sb0.44 in a wide electric field range', *Light. Technol.*, p. 8, doi: 10.1109/JLT.2022.3169008.

Chapter 5

Geiger-mode APD simulations using Simple Monte Carlo Models and Random Path Length Models

5.1) Geiger mode modelling

Simulations of SPADs are crucial in designing novel SPADs and analysing experimental device performance. The breakdown probability of SPADs has been simulated using models with varying complexity, e.g. Recurrence [1], Random Path Length (RPL) [2], Simple Monte Carlo (SMC) [3], and Full Band Monte Carlo (FBMC) [4] models. There are fewer studies on simulations of SPAD's temporal parameters, such as time to breakdown (t_b) and jitter, compared to breakdown probability. t_b influences system performance for applications such as LIDAR and high-speed data transfer.

There are as yet no equations of SPAD's instantaneous current or t_b developed for the Recurrence model, even though it can simulate APD instantaneous current [5]. Values of t_b can be obtained from RPL, SMC and FBMC models, which simulate the instantaneous SPAD current using Ramo's Theorem [6]

$$i = \frac{n\,q\,v}{w}. \tag{5.1}$$

A breakdown event occurs when the current exceeds a predefined breakdown threshold, typically 100 µA.

The RPL model is a simplistic Monte Carlo-based model compared to the SMC and FBMC models. Since simulation run times typically increase with the model's complexity, it is preferable to use the simplest possible simulation model for the desired outputs. The simpler computations allow the RPL model to perform simulations significantly quicker. For statistically significant temporal results, tens of thousands of trials for each simulation condition are required from Monte Carlo-based models. If an RPL model could be used, this would represent a significant reduction in simulation run time.

Carriers with a short ionisation path length have significantly fewer scattering events, resulting in a higher carrier velocity. However, the RPL model uses a saturation velocity (v_{sat}) assumption that consistently overestimates values of t_b [3], [7]. Using an SMC model to simulate a thin GaAs APD, the average ionising carrier velocity was found to be three times greater than the saturation velocity (7.4×10^4 m.s^{-1}) [8]. It may be

possible to rectify this deficiency in the RPL model by appropriately scaling the saturation velocity as a function of the electric field in the RPL model.

In this work, we report saturation velocity used in the RPL model as functions of electric field and avalanche material for replicating values of breakdown probability, t_b and jitter from the SMC model. Our simulations include p-i-n and n-i-p APDs of varying avalanche width and three avalanche materials, namely Si, InP and $Al_{0.85}Ga_{0.15}As_{0.56}Sb_{0.44}$. Si and InP have established avalanche materials used in commercial SPADs for visible and near-IR light, respectively. AlGaAsSb, as shown in chapter 4, is an exceptionally low noise avalanche material. Its large α / β ratio promises a steep rise in $P_{be}(V)$, which could result in a high SPDE for SPADs.

5.1.1) SMC model details

The SMC model used in this work was developed by Petticrew *et al.* [8] and modified to include the additional scattering mechanism for AlGaAsSb (Chapters 4 and [9]). The SMC model parameter set for the three avalanche materials used are presented in Table 5.1.

Table 5.1 Si, InP and AlGaAsSb SMC model parameter set used in this work

	Si [10]		InP [11]		AlGaAsSb (as in Table 4.5)	
	Electrons	Holes	Electrons	Holes	Electrons	Holes
Phonon energy, $\hbar\omega$ (meV)	63		42		44	
Threshold energy, E_{th} (eV)	1.2	1.5	1.55		2	
Mean free path, λ (Å)	98	68	41	42	50	33
Effective mass, m^*	0.6 m_0	0.9 m_0	0.62 m_0	0.63 m_0	0.6 m_0	0.65 m_0
Impact ionisation rate prefactor, C_{ii} ($\times 10^{12}$ s^{-1})	2.0	4.4	3.5	8.8	60	
Softness factor, γ	3.5		0.7		2	
Alloy scattering constant ($\times 10^{68}$)	-	-	-	-	1	3
Max energy (eV)	6		6		9	
Relative permittivity, ε_r	11.90		12.5		11.41	
Built-in voltage (V)	1.0		1.2		1.24	

5.1.2) RPL model details

The RPL model (described in chapter 2) uses effective impact ionisation coefficients given by,

$$\alpha^*(\xi) = A \exp\left[-\left(\frac{B}{\xi}\right)^C\right] \text{cm}^{-1}. \tag{5.2}$$

Values of *A*, *B* and *C*, as well as ionisation threshold energies for Si, InP and AlGaAsSb, are presented in Table 5.2. There are two sets for Si because set Si(a) were not validated for ξ > 800 kV.cm^{-1} [3]. Therefore an additional set, Si(b), were obtained for 350 < ξ < 1200 kV.cm^{-1}. It was extracted from ionisation path length PDFs simulated using an existing Si SMC model [10]. The PDFs range was selected to cover the ξ range that will be simulated with the SMC model.

Table 5.2. Effective impact ionisation coefficient and threshold energies used in the RPL model simulation.

		A (cm^{-1})	B (cm^{-1})	C	E_{the} (eV)	E_{thh} (eV)
Si(a) [3]	α*	5.0×10^5	8.0×10^5	1.28	2.18	3.41
	β*	4.4×10^5	9.4×10^5	1.65		
Si(b)	α*	9.0×10^6	2.1×10^6	0.95	3.4	3.5
	β*	6.0×10^6	2.1×10^6	1.44		
InP [11]	α*	2.55×10^6	2.15×10^6	1.08	2.8	3.0
	β*	9.80×10^6	1.00×10^6	1.60		
AlGaAsSb	α*	5.2×10^6	1.8×10^6	1.27	3.6	3.6
	β*	3.2×10^6	2.1×10^6	1.53		

The SMC models were used to adjust saturation velocity values as functions of electric field (0 - 1000 $kV.cm^{-1}$) for the RPL model. Although SMC models cannot accurately simulate drift velocity at low electric fields, they can do so at higher electric fields, where impact ionisation occurs. The drift velocity of Si, InP and AlGaAsSb from the SMC models are shown in Fig. 5.1(a), (b), and (c), respectively. Values of electron and hole saturation velocity are: 1×10^5 and 8×10^4 $m.s^{-1}$ for Si, 6.8×10^4 $m.s^{-1}$ and 7.0×10^4 $m.s^{-1}$ for InP, and 7.6×10^4 $m.s^{-1}$ and 6.6×10^4 $m.s^{-1}$ for AlGaAsSb, respectively.

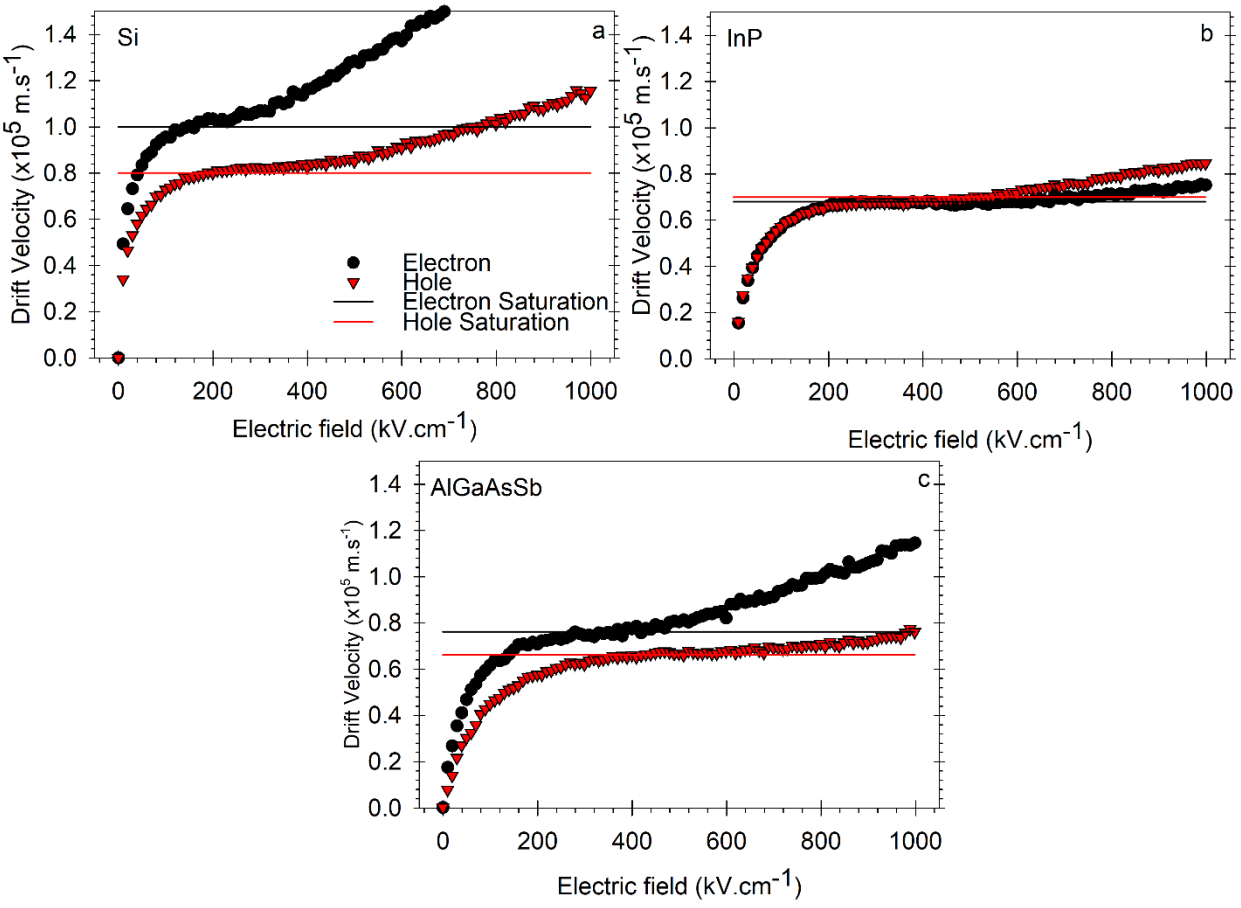

Fig. 5.1 Drift velocity (symbols) and Saturation velocity (lines) for electrons and holes for Si (a), InP (b), and AlGaAsSb (c).

The RPL model used simulates carriers asynchronously, meaning successive simulated carriers may occur at significantly different simulation times. This can lead to a later breakdown time being recorded as some carriers with an earlier simulation time are left unrun. To mitigate this, the simulations are ended using a threshold value higher than the predefined breakdown threshold, termed Overdrive multiplier (M_{od}). An AlGaAsSb APD (1.5 µm avalanche width) was simulated using overdrive factor of 1 to 5 to determine an appropriate M_{od}. The results are compared in Fig. 5.2. The M_{od} does not affect the simulated breakdown probability, but t_b and jitter are. The t_b values decrease as the overdrive factor increases, with the values saturating when the overdrive factor > 1.5. t_b was found to decrease by 5% as M_{od} increased. Increasing the M_{od}, however, increases the model simulation runtime (details in Appendix F). Hence a compromise of M_{od} = 1.5 was chosen for the remaining simulations.

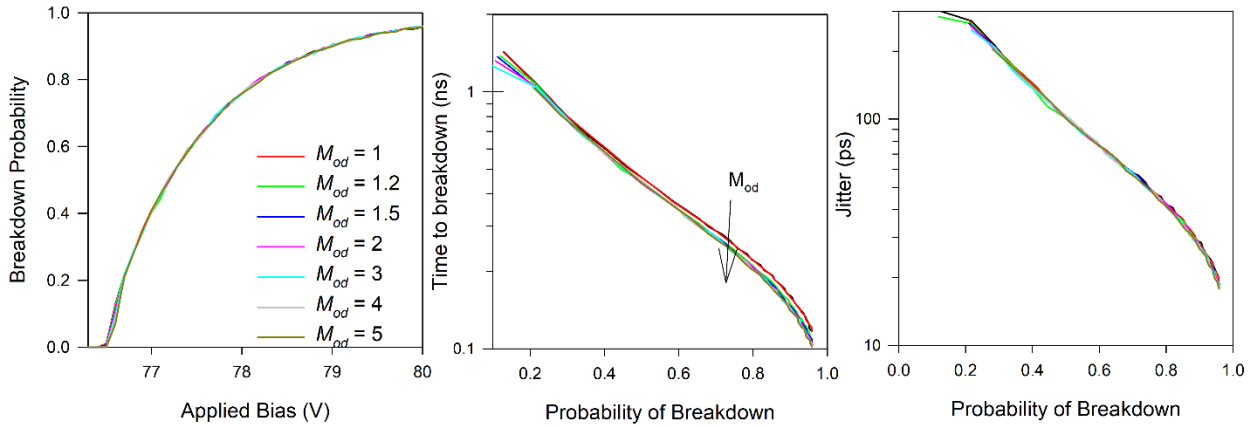

Fig. 5.2 Simulation results from RPL model for a 1.5 um AlGaAsSb APD using different overdrive values. The parameters simulated are Breakdown Probability - Voltage (left), time to breakdown (middle), and jitter (right)

5.2) Simulation results using saturated velocities

The RPL model was used to simulate pairs of p-i-n and n-i-p APDs with i-region thickness of 100, 200, 500, 800, 1000, 1200, and 1500 nm. Abrupt three-layer doping profiles were assumed so the APDs had uniform electric fields within the i-regions. For each voltage point, a total of 20,000 simulation trials were used and statistics were collected to yield breakdown probability, t_b and jitter of the breakdown time. The breakdown condition was defined as 100 µA.

For Si APDs, using the impact ionisation coefficient from [ref], Si(a) in Table 5.2, there is a poor agreement between the results from RPL model and the SMC model for the breakdown probability of the narrow devices, as shown in Fig. 5.3. This may be caused by using the ionisation coefficients beyond their validated electric field range of 350 to 800 kV.cm^{-1} [3]. Therefore, a new set of ionisation coefficients and threshold energies, Si(b) in Table 5.2, were extracted from the ionisation path length PDFs generated by the Si SMC model, focusing on the higher electric fields (upto 1200 kV.cm^{-1}). The detailed process for this were outlined in

Chapter 4, with data and fittings shown in Appendix D. For InP and AlGaAsSb, the reported ionisation coefficients and threshold energies were used as they were and without adjustments.

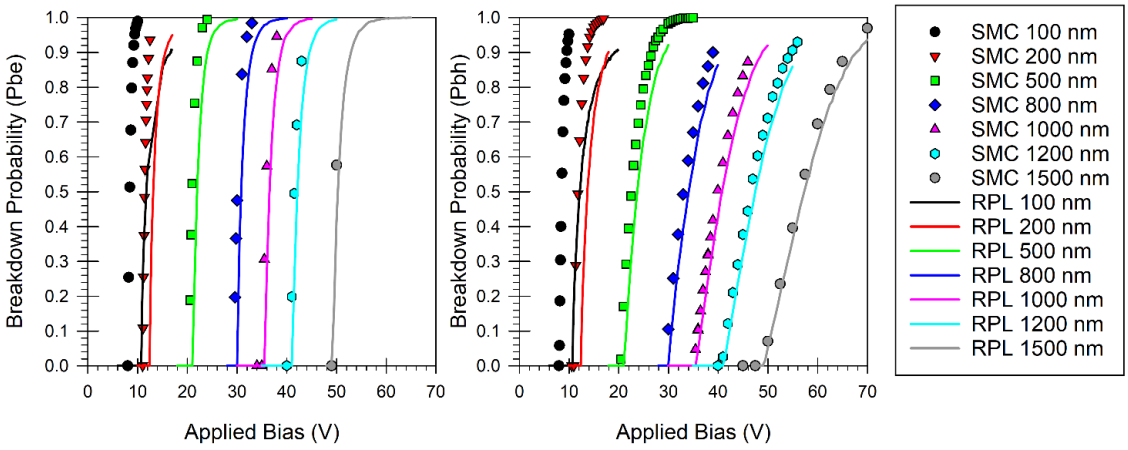

*Fig. 5.3 Comparison of breakdown probability simulated using SMC model and RPL model for **Si** SPADs using saturation velocities of 1×10^5 and 8×10^4 $m.s^{-1}$. Results include pure electron (L) and pure hole (R) injection conditions. The values of $\alpha^*(\xi)$, $\beta^*(\xi)$, E_{the}, and E_{thh} are given in Table 5.2 as Si(a).*

The SMC and RPL results for Si (using Si(b)), InP and AlGaAsSb using standard v_{sat} values are compared in in Fig. 5.4, Fig. 5.5, and Fig. 5.6, respectively. are in good agreement for $P_{be(h)}(V)$ for both electron and hole-initiated breakdown, as shown in Fig. 5.4 (top). Results from the two models are in good agreement for $P_{be}(V)$ and $P_{bh}(V)$ for each material over the full range of devices simulated. However mean t_b and jitter results show poor agreement, with the RPL results higher than the SMC results. The disagreement is more significant for the narrower SPADs, which operate at higher electric fields. This is expected because the assumption of saturation velocity for ionising carriers is less valid for narrow SPADs than thick SPADs [12]. However, for the three material systems simulated, no device simulated upto 1.5 µm showed good agreement between the SMC and RPL model for time to breakdown and jitter. The 100 nm devices typically exhibited a difference of ×2.3-2.9 times difference, and the 1.5 µm devices exhibited a difference of ×1.3 times difference between the SMC and RPL simulations.

For AlGaAsSb, the effect of the large ratio between α and β can be seen when comparing the voltage requirement for $P_b > 0.95$ between the two carrier types. To achieve P_b ~0.95 in a 1.5 µm device, the over bias required is 4.4 V (5.5%) and 53.5 V (41%) for electrons and holes, respectively. This would indicate a reduction in the theoretical dark count rate compared to both InP and InAlAs [13]. To realise a 1.5 µm thick AlGaAsSb avalanche layer in practical SPADs, there may be challenges related to wafer growth of thick, high-quality AlGaAsSb needed because the AlGaAsSb APDs reported to date have avalanche layers thickness below 1.0 µm.

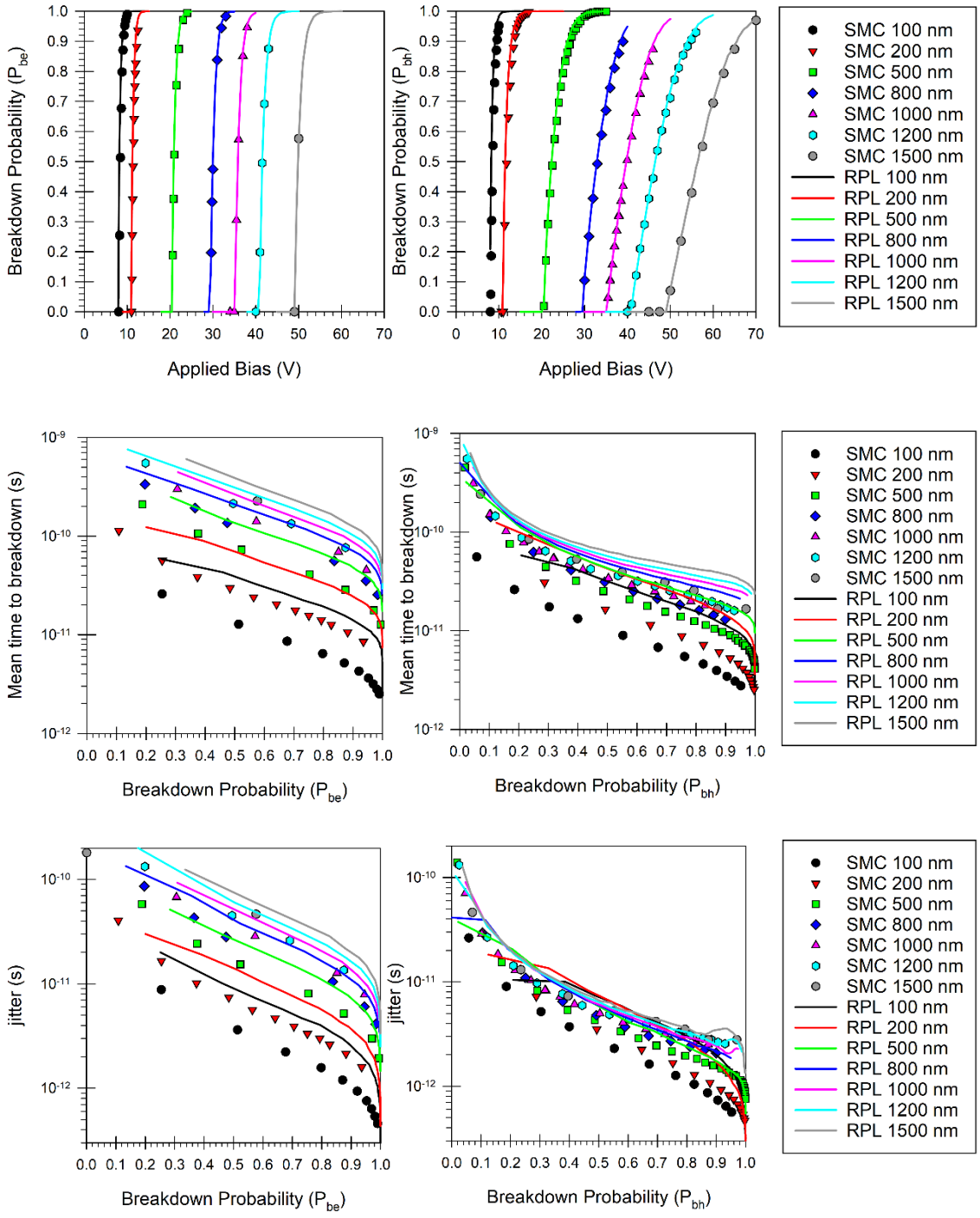

*Fig. 5.4 Comparison of breakdown probability (top), time to breakdown (middle) and jitter (bottom) simulated using SMC model and RPL model for **Si** SPADs using saturation velocities of 1×10^5 and 8×10^4 m.s^{-1}. Results include pure electron (L) and pure hole (R) injection conditions. The values of $\alpha^*(\xi)$, $\beta^*(\xi)$, E_{the}, and E_{thh} are given in Table 5.2 as Si(b).*

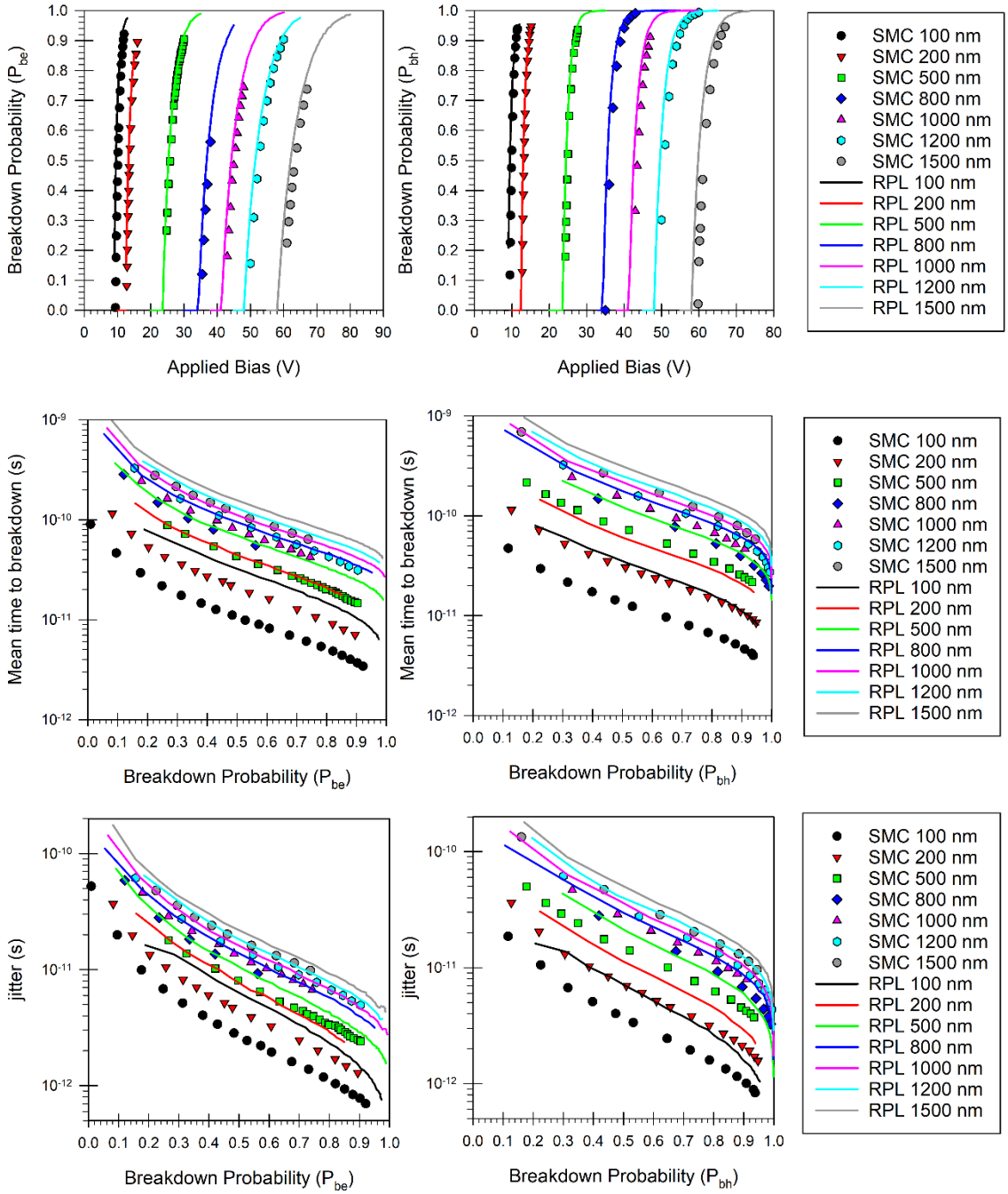

*Fig. 5.5 Comparison of breakdown probability (top), time to breakdown (middle) and jitter (bottom) simulated using SMC model and RPL model for **InP** SPADs using saturation velocities of 6.8×10^4 and 7×10^4 m.s^{-1}. Results include pure electron (L) and pure hole (R) injection conditions.*

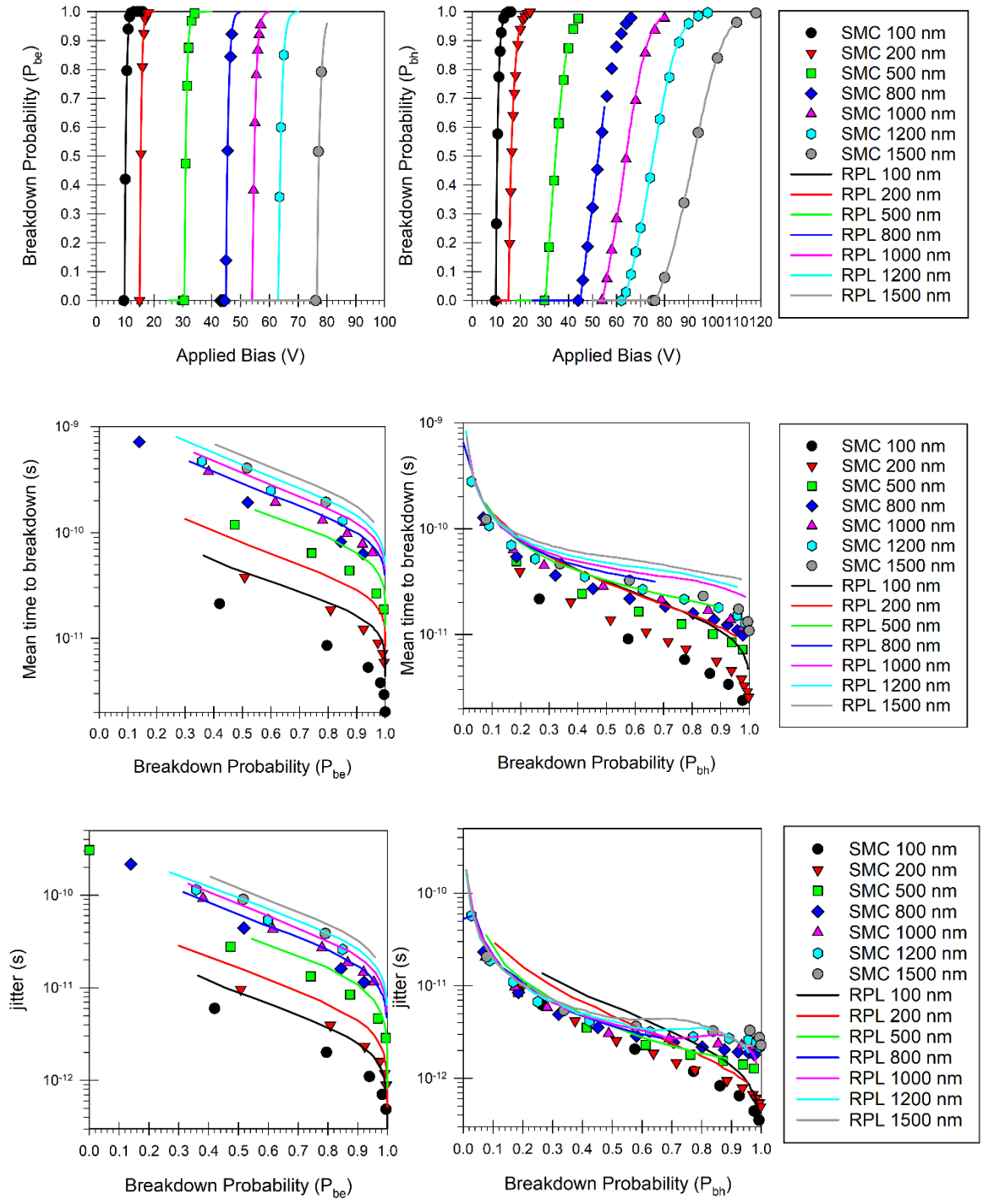

*Fig. 5.6 Comparison of breakdown probability (top), time to breakdown (middle) and jitter (bottom) simulated using SMC model and RPL model for **AlGaAsSb** SPADs using saturation velocities of 7.6×10^4 and 6.6×10^4 m.s^{-1}. Results include pure electron (L) and pure hole (R) injection conditions.*

5.3) Simulation results using enhanced velocities

To rectify the disagreements observed in the previous section, an enhanced velocity (v_{en})(ξ) is introduced to ensure the RPL results fit to the SMC results. $v_{en}(\xi)$ is a sigmoid equation,

$$v_{en} = \left(1 + \frac{a}{\left[1 + \exp\left(-\left(\frac{\xi - b}{c}\right)\right)\right]^{d}}\right) v_{sat}, \tag{5.3}$$

where a, b, c, and d are unitless constants, which are adjusted as fitting parameters. Their values for Si, InP and AlGaAsSb are summarised in Table 5.3. RPL results for P_b, t_b and jitter obtained using the enhanced velocity values are compared to the SMC results. All other conditions were the same as earlier simulations using saturated velocity values. v_{en} versus electric field are shown in Fig. 5.7 for Si, InP and AlGaAsSb, with dashed lines indicating the valid range of v_{en} of this work. The lower limit corresponds to the breakdown electric field for w = 1500 nm devices. The upper limit is the electric field for w = 100 nm SPAD at P_b > 0.95.

Table 5.3 fitting parameters for v_{en} for Si, InP, and AlGaAsSb, with validated electric field range

Material	a	b	c	d	Valid ξ range (kV.cm^{-1})
Si	1.4296	5.9e7	4.8e6	0.2922	330 - 1000
InP	1.73	7.4e7	2.5e7	1	400 - 1100
AlGaAsSb	0.997	-1.2e7	1.4e7	174	500 - 1250

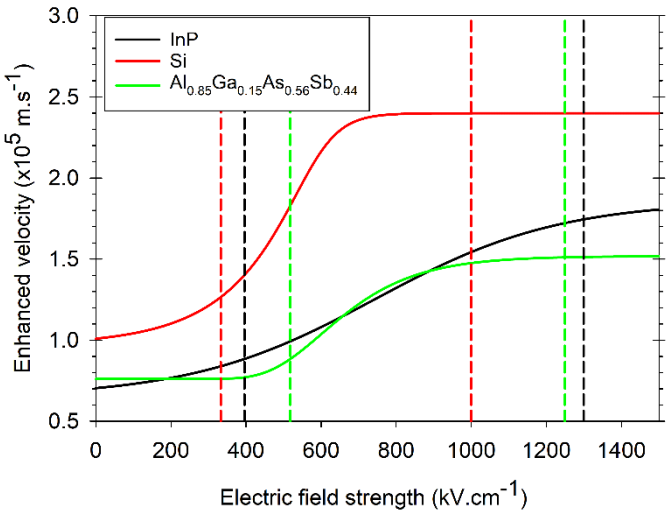

Fig. 5.7 v_{en} for InP, Si and AlGaAsSb (solid lines). The valid electric field range for each material is indicated by dashed lines.

Simulation results from the RPL (enhanced velocity) and SMC models are compared in Fig. 5.8, Fig. 5.9, and Fig. 5.10, for Si, InP, and AlGaAsSb, respectively. Good agreement between the two models can be observed for $P_b(V)$ of all materials and SPAD widths simulated. For t_b and jitter, agreement between the two

models is also good, except for slight disagreement in Si and AlGaAsSb jitter results for hole injection when $P_{b(h)} > 0.5$. The disagreement may have been caused by uncertainty in reported values of β^* and E_{thh} for these materials.

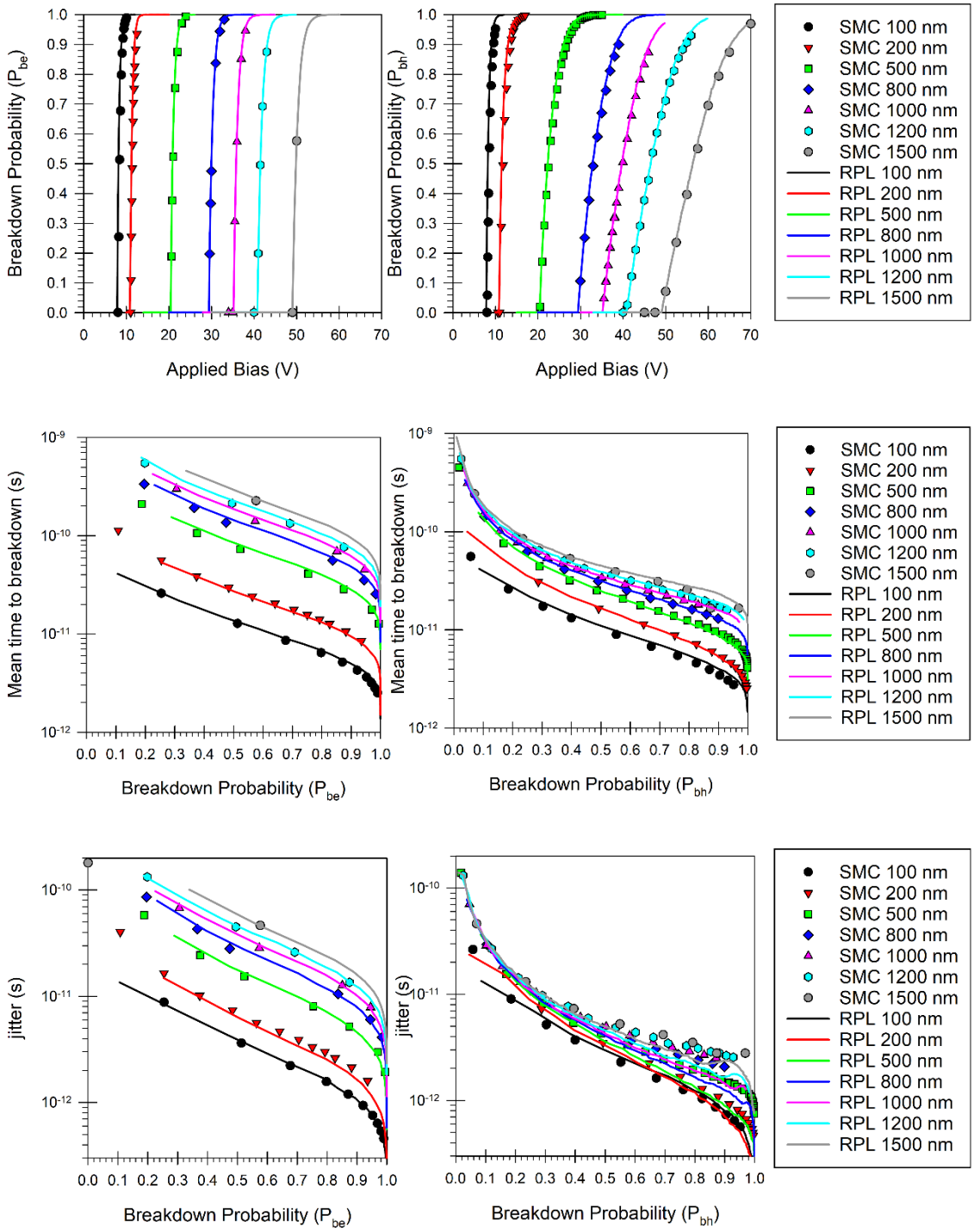

*Fig. 5.8 Comparison of breakdown probability (top), time to breakdown (middle) and jitter (bottom) simulated using SMC model and RPL model for **Si** SPADs using the enhanced carrier velocity fitting from Table 5.3. Results include pure electron (L) and pure hole (R) injection conditions. The values of $\alpha^*(\xi)$, $\beta^*(\xi)$, E_{the}, and E_{thh} are given in Table 5.2 as Si(b).*

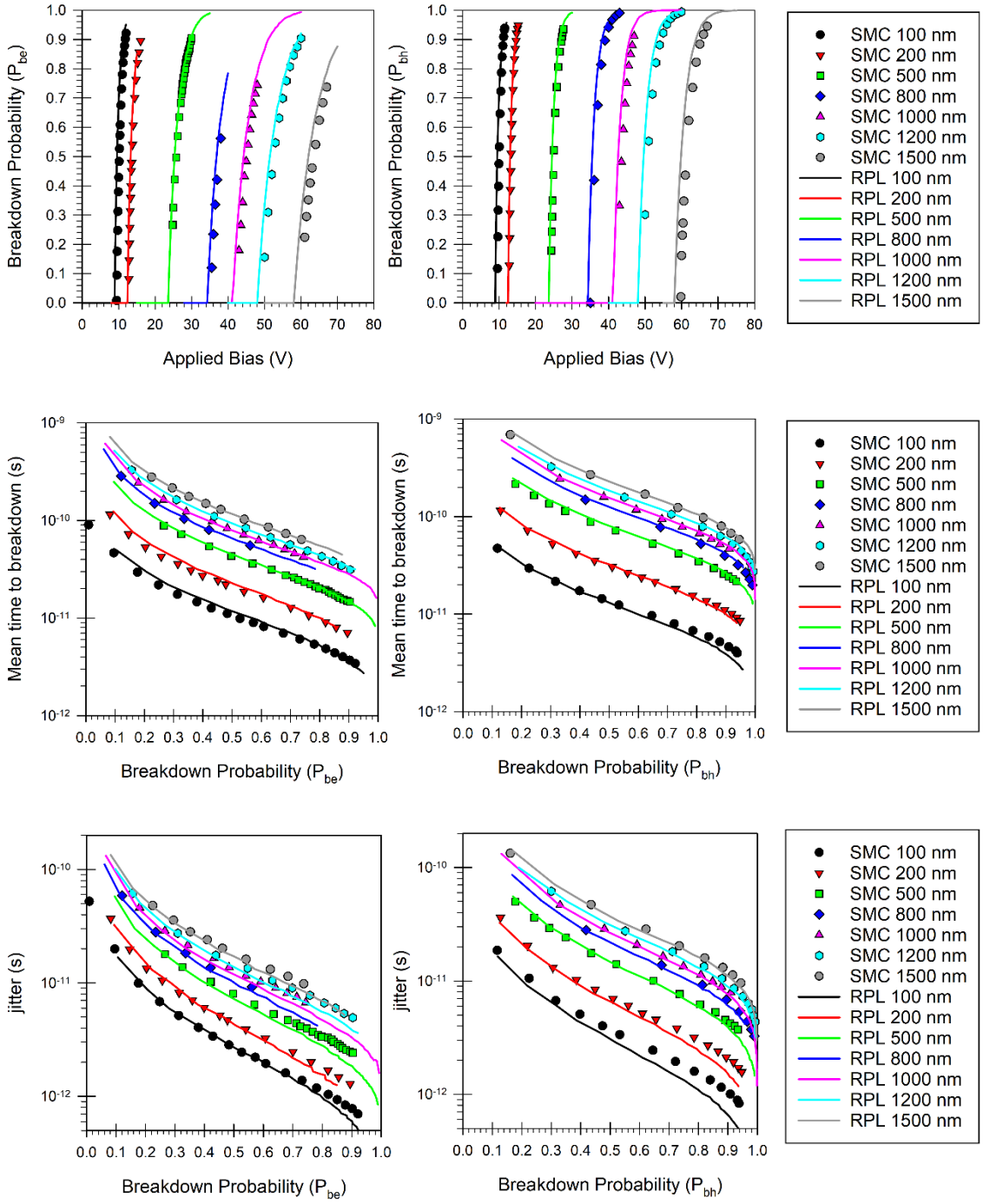

*Fig. 5.9 Comparison of breakdown probability (top), time to breakdown (middle) and jitter (bottom) simulated using SMC model and RPL model for **InP** SPADs using the enhanced carrier velocity fitting from Table 5.3. Results include pure electron (L) and pure hole (R) injection conditions.*

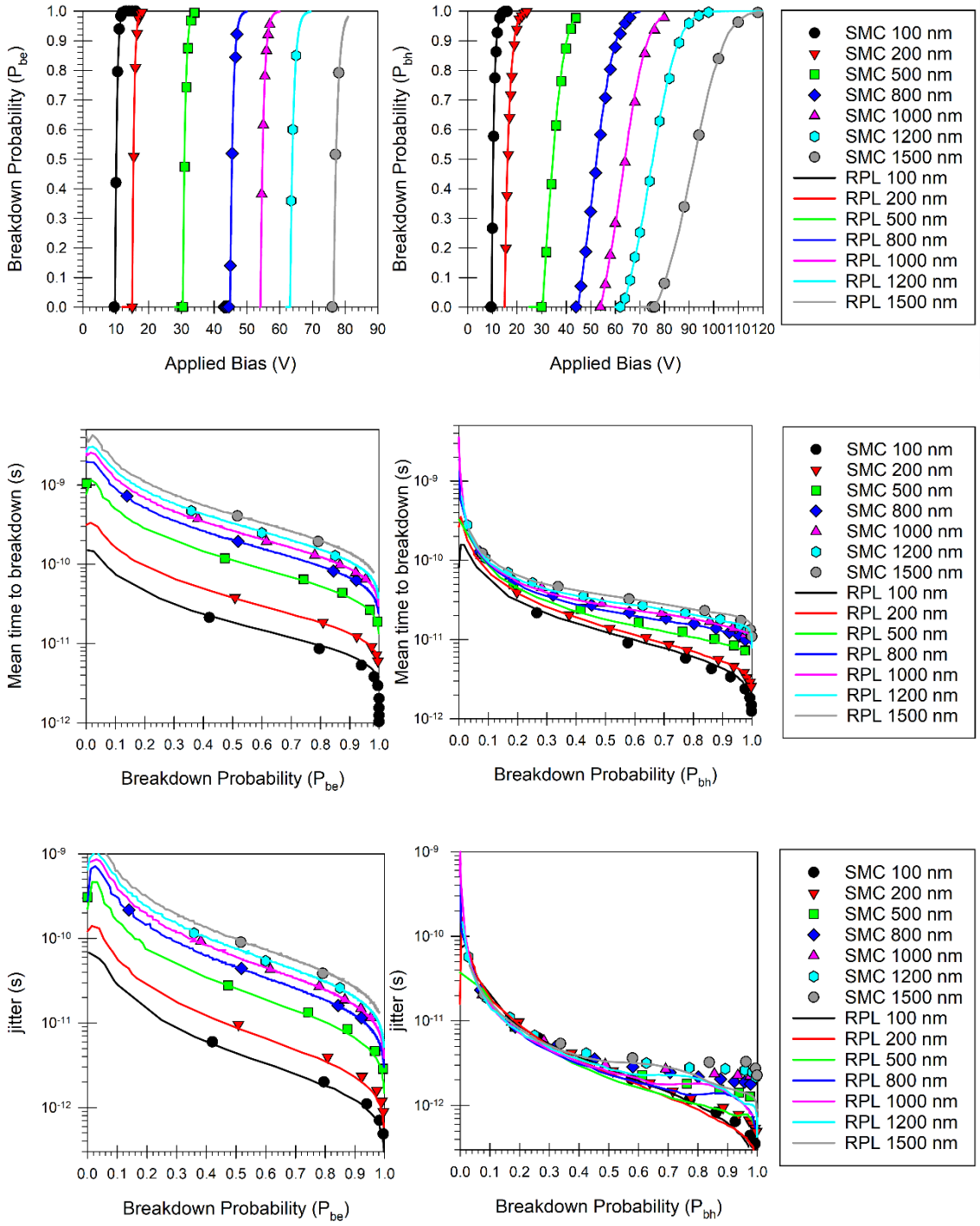

*Fig. 5.10 Comparison of breakdown probability (top), time to breakdown (middle) and jitter (bottom) simulated using SMC model and RPL model for **AlGaAsSb** SPADs using the enhanced carrier velocity fitting from Table 5.3. Results include pure electron (L) and pure hole (R) injection conditions.*

5.3) Comparison

Observing Fig. 5.10, AlGaAsSb results of P_{be} and P_{bh} for a given bias differ significantly, as expected from the large ratio of α^* to β^*. If using electron injection, a thick AlGaAsSb SPAD could exhibit abruptly increasing P_{be} versus overbias characteristics, which is an attractive attribute for SPADs [13]. From the literature, simulated InAlAs has a lower DCR compared to InP and a higher t_b at the same overbias. This was attributed to InAlAs having a more dissimilar impact ionisation coefficient compared to InP and a lower band-to-band tunnelling current for a given ξ. AlGaAsSb will be of interest for novel SPAD design due to a more dissimilar α^* β^* compared to InAlAs, resulting in a lower DCR potential.

A comparison of InP, Si and AlGaAsSb is presented in Fig. 5.11 for P_b (left) and t_b (right). InP requires the highest overbias to achieve the same P_b as Si and AlGaAsSb. Although Si has a more dissimilar impact ionisation coefficient, it displays a comparable t_b compared to InP. This is maybe due to Si having a higher carrier velocity compared to InP. Compared to Si, AlGaAsSb gives a higher P_{be} (which is desirable) for a given overbias but its t_b values are also higher (undesirable).

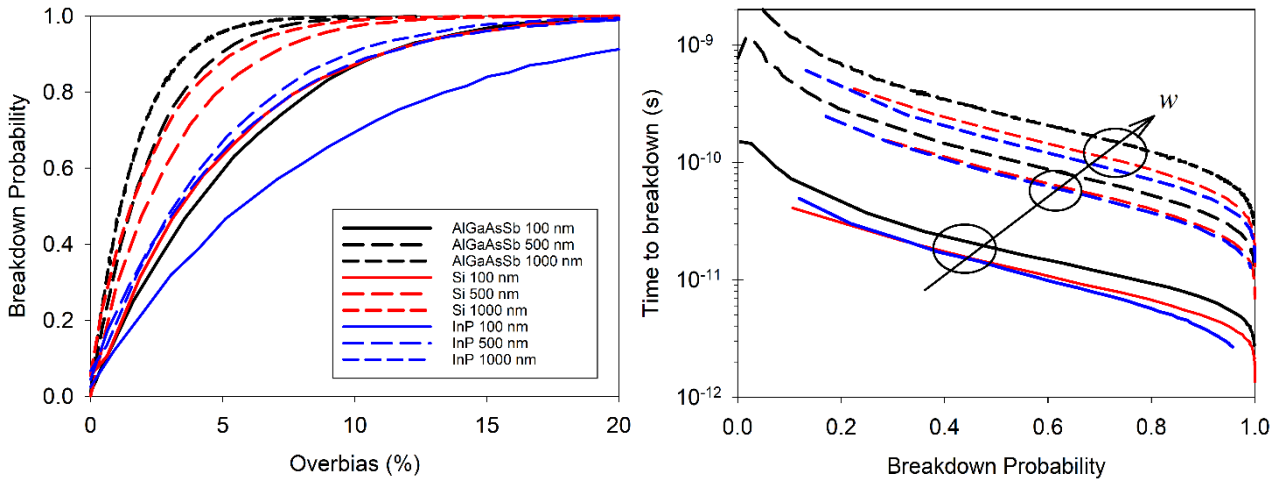

Fig. 5.11. Overbias - Pb for InP, Si, and AlGaAsSb for w = 100, 500, and 1000 nm (L). Pb-tb for InP, Si, and AlGaAsSb for w = 100, 500, and 1000 nm (R)

RPL results of AlGaAsSb SPADs are also compared to results from a recent simulation study of Geiger-mode $AlAs_{0.56}Sb_{0.44}$ [14]. Ref [14] work used a commercial software (Silvaco Atlas), reported impact ionisation coefficients [15] and their own ionisation threshold energies [14] to calculate P_{be}. To validate a comparison, the RPL model was used to replicates the $P_{be(h)}$ presented in [14]. A good agreement was achieved and is presented in appendix F. A comparison between P_{be} versus overbias for AlAsSb and AlGaAsSb SPADs for a range of w is shown in Fig. 5.12. AlGaAsSb shows a higher P_{be} for a given overbias, compared to AlAsSb for all w values.

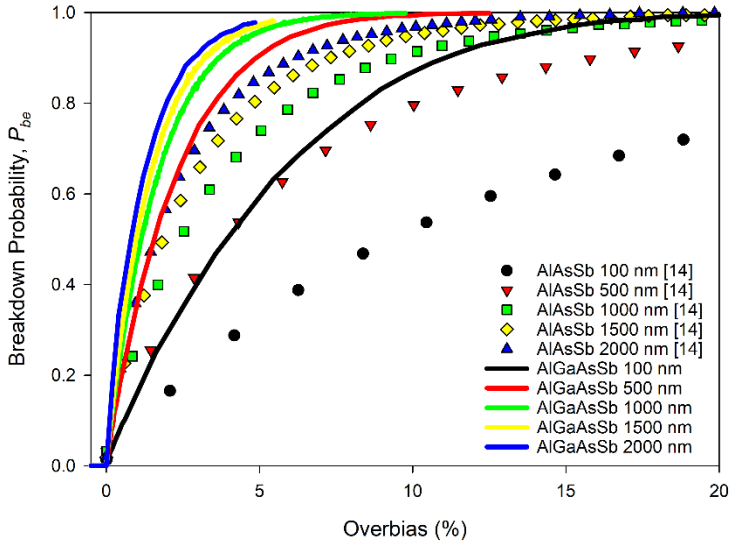

Fig. 5.12. Comparison of simulated P_{be} versus Overbias for AlAsSb [14](symbols) and AlGaAsSb (lines) SPADs with 100 - 2000 nm avalanche region width

5.4) Conclusions

Devices with an i-region of 100 nm to 1500nm have been simulated using the Simple Monte Carlo model for breakdown probability, time to breakdown and jitter of the breakdown time. InP and Si represent common avalanche materials used in SPADs which are commercially available. AlGaAsSb is a novel material which could not be simulated previously due to the lack of validated models for the material. Using the SMC from chapter 4, AlGaAsSb has been simulated for the breakdown probability for electrons and holes, time to breakdown and the jitter. It was found that AlGaAsSb has a very favourable breakdown probability compared to InP and Si, which can be attributed in part to the large difference in the impact ionisation coefficient, as shown in chapter 4. However, the $t_b(P_b)$ were worse compared to InP and Si for the same device widths. The $P_b(V)$ of AlGaAsSb was also compared to published AlAsSb, which suggests AlGaAsSb has a more favourable P_b for a wide range of devices and a promising avalanche material for the next generation of single photon avalanche photodiodes.

A Random path length model has been modified to replicate the SMC's t_b and jitter simulated results. The RPL model is a very simplistic model and, due to the saturation velocity assumption, would simulate higher $t_b(P_b)$ than the SMC. However, due to the RPL model's simplicity, it is significantly faster running, making it desirable to use for ideal device structures in SPAD designs. Instead, the enhanced velocity as a function of the electric field was used and validated against the SMC simulated results. Good agreement was achieved for Si, InP, and AlGaAsSb for all device widths with a significant reduction in simulation runtime.

5.5) References

[1] R. J. McIntyre, 'A new look at impact ionization-Part I: A theory of gain, noise, breakdown probability, and frequency response', *IEEE Trans. Electron Devices*, vol. 46, no. 8, pp. 1623–1631, Aug. 1999, doi: 10.1109/16.777150.

[2] C. H. Tan, J. S. Ng, G. J. Rees, and J. P. R. David, 'Statistics of Avalanche Current Buildup Time in Single-Photon Avalanche Diodes', *IEEE J. Sel. Top. Quantum Electron.*, vol. 13, no. 4, pp. 906–910, 2007, doi: 10.1109/JSTQE.2007.903843.

[3] J. D. Petticrew, S. J. Dimler, X. Zhou, A. P. Morrison, C. H. Tan, and J. S. Ng, 'Avalanche Breakdown Timing Statistics for Silicon Single Photon Avalanche Diodes', *IEEE J. Sel. Top. Quantum Electron.*, vol. 24, no. 2, 2018, doi: 10.1109/JSTQE.2017.2779834.

[4] D. Dolgos, H. Meier, A. Schenk, and B. Witzigmann, 'Full-band Monte Carlo simulation of high-energy carrier transport in single photon avalanche diodes with multiplication layers made of InP, InAlAs, and GaAs', *J. Appl. Phys.*, vol. 111, no. 10, p. 104508, May 2012, doi: 10.1063/1.4717729.

[5] M. M. Hayat and B. E. A. Saleh, 'Statistical properties of the impulse response function of double-carrier multiplication avalanche photodiodes including the effect of dead space', *J. Light. Technol.*, vol. 10, no. 10, pp. 1415–1425, Oct. 1992, doi: 10.1109/50.166785.

[6] S. Ramo, 'Currents Induced by Electron Motion', *Proc. IRE*, vol. 27, no. 9, pp. 584–585, Sep. 1939, doi: 10.1109/JRPROC.1939.228757.

[7] P. J. Hambleton, S. A. Plimmer, J. P. R. David, and G. J. Rees, 'Time response modelling in submicron avalanche photodiodes', *IEE Proc. - Optoelectron.*, vol. 150, no. 2, pp. 167–170, Apr. 2003, doi: 10.1049/ip-opt:20030328.

[8] J. D. Petticrew, S. J. Dimler, and J. S. Ng, 'Simple Monte Carlo Simulator for Modelling Linear Mode and Geiger Mode Avalanche Photodiodes in C++', *J. Open Res. Softw.*, vol. 6, May 2018, doi: 10.5334/jors.212.

[9] J. D. Taylor-Mew, J. D. Petticrew, C. H. Tan, and J. S. Ng, 'Simulation of $Al_{0.85}Ga_{0.15}As_{0.56}Sb_{0.44}$ avalanche photodiodes', *Opt. Express*, vol. 30, no. 11, p. 17946, May 2022, doi: 10.1364/OE.458922.

[10] X. Zhou, J. S. Ng, and C. H. Tan, 'A simple Monte Carlo model for prediction of avalanche multiplication process in Silicon', *J. Instrum.*, vol. 7, no. 08, p. P08006, 2012, doi: 10.1088/1748-0221/7/08/P08006.

[11] J. D. Petticrew, S. J. Dimler, C. H. Tan, and J. S. Ng, 'Modeling Temperature-Dependent Avalanche Characteristics of InP', *J. Light. Technol.*, vol. 38, no. 4, pp. 961–965, Feb. 2020, doi: 10.1109/JLT.2019.2948072.

[12] P. J. Hambleton, J. P. R. David, and G. J. Rees, 'Enhanced carrier velocity to early impact ionization', *J. Appl. Phys.*, vol. 95, no. 7, pp. 3561–3564, Apr. 2004, doi: 10.1063/1.1646434.

[13] S. C. Liew Tat Mun *et al.*, 'A Theoretical Comparison of the Breakdown Behavior of $In_{0.52}Al_{0.48}As$ and InP Near-Infrared Single-Photon Avalanche Photodiodes', *IEEE J. Quantum Electron.*, vol. 45, no. 5, pp. 566–571, May 2009, doi: 10.1109/JQE.2009.2013094.

[14] J. Ahmed *et al.*, 'Theoretical Analysis of $AlAs_{0.56}Sb_{0.44}$ Single Photon Avalanche Diodes With High Breakdown Probability', *IEEE J. Quantum Electron.*, vol. 57, no. 2, pp. 1–6, Apr. 2021, doi: 10.1109/JQE.2021.3058356.

[15] X. Yi *et al.*, 'Demonstration of large ionization coefficient ratio in AlAs0.56Sb0.44 lattice matched to InP', *Sci. Rep.*, vol. 8, no. 1, p. 9107, Dec. 2018, doi: 10.1038/s41598-018-27507-w.

Chapter 6
$In_{0.53}Ga_{0.47}As$ Simple Monte Carlo Model

$In_{0.53}Ga_{0.47}As$ (InGaAs) is widely used for absorbing 1.3 and 1.55 µm wavelength light, in particular as the absorber material in a Separate Absorption Multiplication (SAM) APDs. In these SAM APDs, it is undesirable to have impact ionisation in the InGaAs absorber because this can worsen $F(M)$ performance [1]. However, when developing SAM APDs in research activities, the absorber may have a higher than intended electric field that is not constant (perhaps due to doping concentration tolerances in the charge sheet or dopants diffusing into the absorber). The SMC model has been shown previously [2] to handle highly graded fields; hence a validated InGaAs SMC model parameter set is useful for both design and analysis of SAM APDs with InGaAs absorber. In this work, an InGaAs SMC model is developed and validated using reported data over an electric field range of 80 to 340 $kV.cm^{-1}$. Which represents the onset of measured avalanche multiplication and the breakdown field of the widest and narrowest validation devices, respectively.

6.1) Validation data

The verification data used were from eight InGaAs p-i-n diodes, Device A to H, with w from 400 nm to 5 µm. These were grown lattice-matched to InP substrates by MBE or MOVPE. Their nominal w values and doping densities (using 3-layer approximation) are summarised in Table 6.1. Available impact ionisation data for each diode are also listed and they range from breakdown voltage only to complete sets $M_e(V)$ and $F_e(M_e)$. This is due to diodes with narrow i-regions exhibiting higher dark currents (band-to-band tunnelling current), which prevents certain types of measurements, such as avalanche multiplication and excess noise as highlighted in sections 3.3.1 and 3.3.2, respectively.

Table 6.1. InGaAs diodes and their data used to validate the SMC model

Device	P (N) doping concentration (cm^{-3})	I doping concentration (cm^{-3})	Nominal (fitted) i-region (nm)	Available impact ionisation data	Reference
A	2×10^{18} (-2×10^{18})	2×10^{16}	400 (330)	V_{br} only	[3]
B	2×10^{17} (-5×10^{17})	5×10^{15}	750(750)	$M_e(V)$	[4]
C	8×10^{17} (-5×10^{17})	1.5×10^{15}	1100 (1120)	$M_e(V)$	[3]
D	1.5×10^{17} (-2×10^{17})	1.5×10^{15}	1300 (1350)	$M_e(V)$	[3]
E	2×10^{17} (-2×10^{17})	1.5×10^{15}	2000 (2000)	$M_e(V)$ and $F_e(M_e)$	[3] [4]
F	2×10^{17} (-2×10^{17})	1.5×10^{15}	2450 (2350)	$M_e(V)$ and $F_e(M_e)$	[4]
G	1×10^{17} (-2×10^{18})	7×10^{14}	3500 (3500)	$M_e(V)$ and $F_e(M_e)$	[3] [4]
H	1×10^{17} (-2×10^{17})	4×10^{14}	4800 (5000)	$M_e(V)$ and $F_e(M_e)$	[3] [4]

The doping profiles for devices A-H were estimated from fittings to experimental C-V data using 1-D Poisson's field solver and assuming 3-layer abrupt doping profiles. Good agreement between the C-V data and the fitting was achieved for all devices at reverse biases greater than 5 V, as shown in Fig. 6.1. For lower biases, the agreement is not as good since the 3-layer abrupt doping profile assumption is less accurate in describing the doping profiles around the p/i and n/i junctions. All devices were assumed to have a radius of 200 µm, except for device A, which was 100 µm. The radial reduction was not carried out due to a lack of readily available C/A-V data.

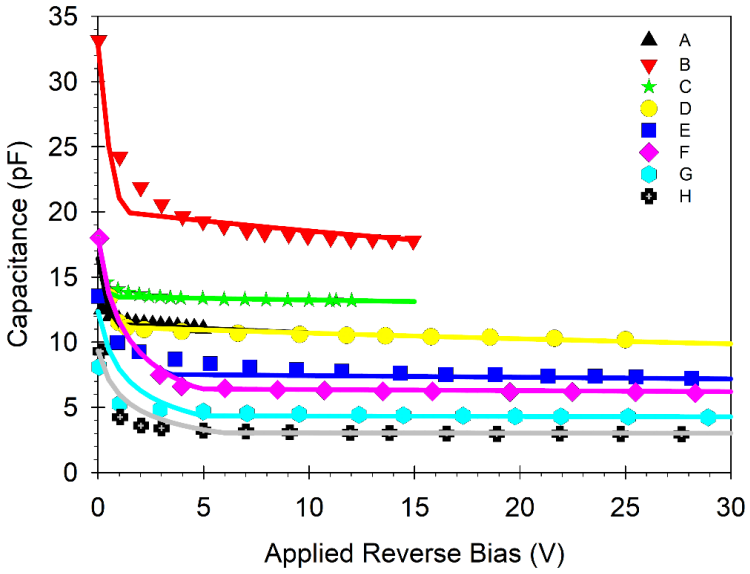

Fig. 6.1. Experimental C-V characteristics (symbols) and fitting (lines) using 1-D Poisson's field solver.

6.2) Simple Monte Carlo model

The SMC model used in this work is modified from [5] to include alloy scattering as one of the carrier scattering mechanisms. Since the reported electric field dependence of α in InGaAs is distinct from those of Si and InP [6], the SMC model was further modified to include two parameter sets for impact ionisation rates (for low and high carrier's energy range). As stated in chapter 2, in a SMC simulation, each carrier will drift across an avalanche region, under an electric field, for a random distance before undergoing one of four possible scattering mechanisms intervalley phonon emission (R_{em}), intervalley phonon absorption (R_{ab}), impact ionisation (R_{ii}), and alloy scatting rate (R_{alloy}). They are given by:

$$R_{em} = \frac{N(T)+1}{\lambda\,(2N(T)+1)}\sqrt{\frac{2(E_c-\hbar\omega)}{m^*}} \qquad \text{(2.22 repeated)}$$

$$R_{ab} = \frac{N(T)}{\lambda\,(2N(T)+1)}\sqrt{\frac{2(E_c+\hbar\omega)}{m^*}} \qquad \text{(2.23 repeated)}$$

$$R_{ii} = C_{ii}\left(\frac{E_c - E_{th}}{E_{th}}\right)^{\gamma} \quad \text{(2.25 repeated)}$$

$$R_{alloy} = C_{alloy}\,(m^*)^{\frac{3}{2}}\sqrt{E_c} \quad \text{(2.27 repeated)}$$

The electron's electron ionisation rate for the SMC model is similar to those of reported InGaAs Monte Carlo models [7]–[9], as shown in Fig. 6.2. Ref [7] and [10] have two components corresponding to the Γ-valley (E_{th} of 0.75 eV) and the weighted three-valley approximation (E_{th} of 1.46 eV), whereas ref [9] used only a single component. Ref [7] reported that all three rates produce alpha consistent with experimental report of ref [6] for fields above 220 $kV.cm^{-1}$, however rate from ref [9] resulted in significantly lower alpha values. Hence the electron ionisation rate used in this work was from [7]. The switchover point between the two impact ionisation rates is 1.8 eV. There is a single parameter set values for hole ionisation rate as in SMC models for other materials. Holes do not benefit from large energy separation between E_{Γ} and E_{χ}, which allows electrons to impact ionise in the Γ-valley [6] [8]. Hence $\beta(\xi)$ in InGaAs exhibited a conventional field dependence.

The full set of parameters used in the SMC model is summarised in Table 6.2. The value of $\hbar\omega$ was calculated from linear interpolation of the binaries [11]. The values of C_{alloy}, m^* and λ were adjusted so the SMC results agreed with the validation data. The relative permittivity and built-in voltage were set to be 13.6 and 0.7 V, respectively, where the latter is commonly extracted from experimental C-V.

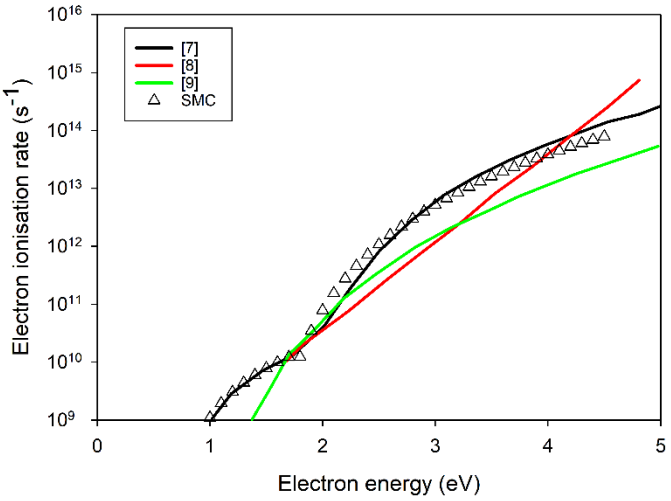

Fig. 6.2 Electron's impact ionisation rate used in the InGaAs SMC model (symbols) is similar to those reported by Tan et al [7], Bude and Hess [8], and Harrison et al [9].

Table 6.2 $In_{0.53}Ga_{0.47}As$ SMC model parameter set

	Electrons	Holes	E_c range (eV)
Effective mass, m^*	0.15	0.65	0 - 1.8
Mean free path, λ (Å)	220	55.3	
Threshold energy, E_{th} (eV)	0.75	1.46	
Impact ionisation rate prefactor, C_{ii} ($\times 10^{12}$ s^{-1})	0.006	4.0	
Softness factor, γ	2.0	4.0	
Alloy scatting constant ($\times 10^{68}$)	0.1	0.5	
Effective mass, m^*	0.35	0.65	1.8 - 4.5
Mean free path, λ (Å)	60.0	55.3	
Threshold energy, E_{th} (eV)	1.46	1.46	
Impact ionisation rate prefactor, C_{ii} ($\times 10^{12}$ s^{-1})	4.2	4.0	
Softness factor, γ	4.0	4.0	
Alloy scatting constant ($\times 10^{68}$)	110	0.5	
Phonon energy, $\hbar\omega$ (meV)	33		0 – 4.5
Max energy (eV)	4.5		
Relative permittivity, ε_r	13.6		
Built-in voltage (V)	0.7		

The SMC's drift velocity produced by this SMC model is shown in Fig. 6.3. The drift velocities for electrons and holes at 200 kV.cm^{-1} are 6.9 × 10^4 and 5.2 × 10^4 m.s^{-1}, respectively. These correspond to reported values of 6.8 × 10^4 [12] and 4.8 × 10^4 m.s^{-1} [13]. The drift velocity agreement between the InGaAs SMC model and the experimental reports is poor at low electric fields, because the SMC model does not contain sufficient band strucutre details near the band edge (which affects low field velocity). This is a known issue [14], [15], but it is necessary to ensure the SMC model is computationally efficient. This does not affect accuracy of simulated avalalnche multiplication and excess noise.

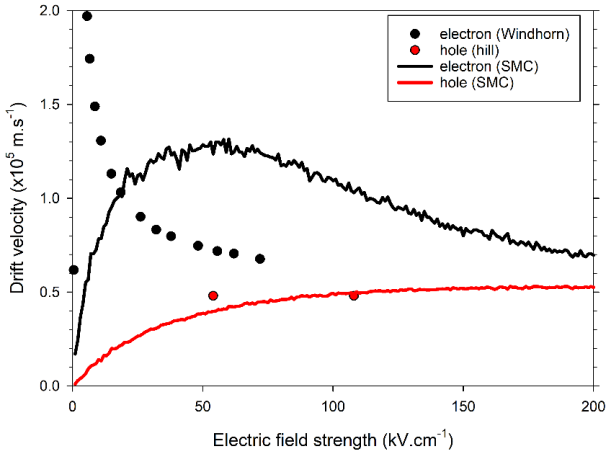

Fig. 6.3 drift velocity for electrons [12]and holes [13]and the SMC

6.3) Avalanche multiplication and Excess noise

Using the InGaAs parameter set with the SMC model, $M_e(V)$ and $F_e(M_e)$ were simulated for devices A-H and E-H, respectively. The SMC model results and the validation data are compared in Fig. 6.4. For $M_e(V)$ there is good agreement for both low and high electric fields. This is of particular importance for SAM APD simulations since electron's impact ionisation at low fields can adversely affect SAM APD performance. For $F_e(M_e)$, there is reasonable agreement, but deviations exist at higher multiplication. The deviations at higher multiplication factors may be due to the validation excess noise data being affected by high dark currents in the device, despite the use of a phase-sensitive detection technique. A simular tend of excess noise characteristics has been obseved in experiments when devices with high dark current were used (see section 3.3.2)

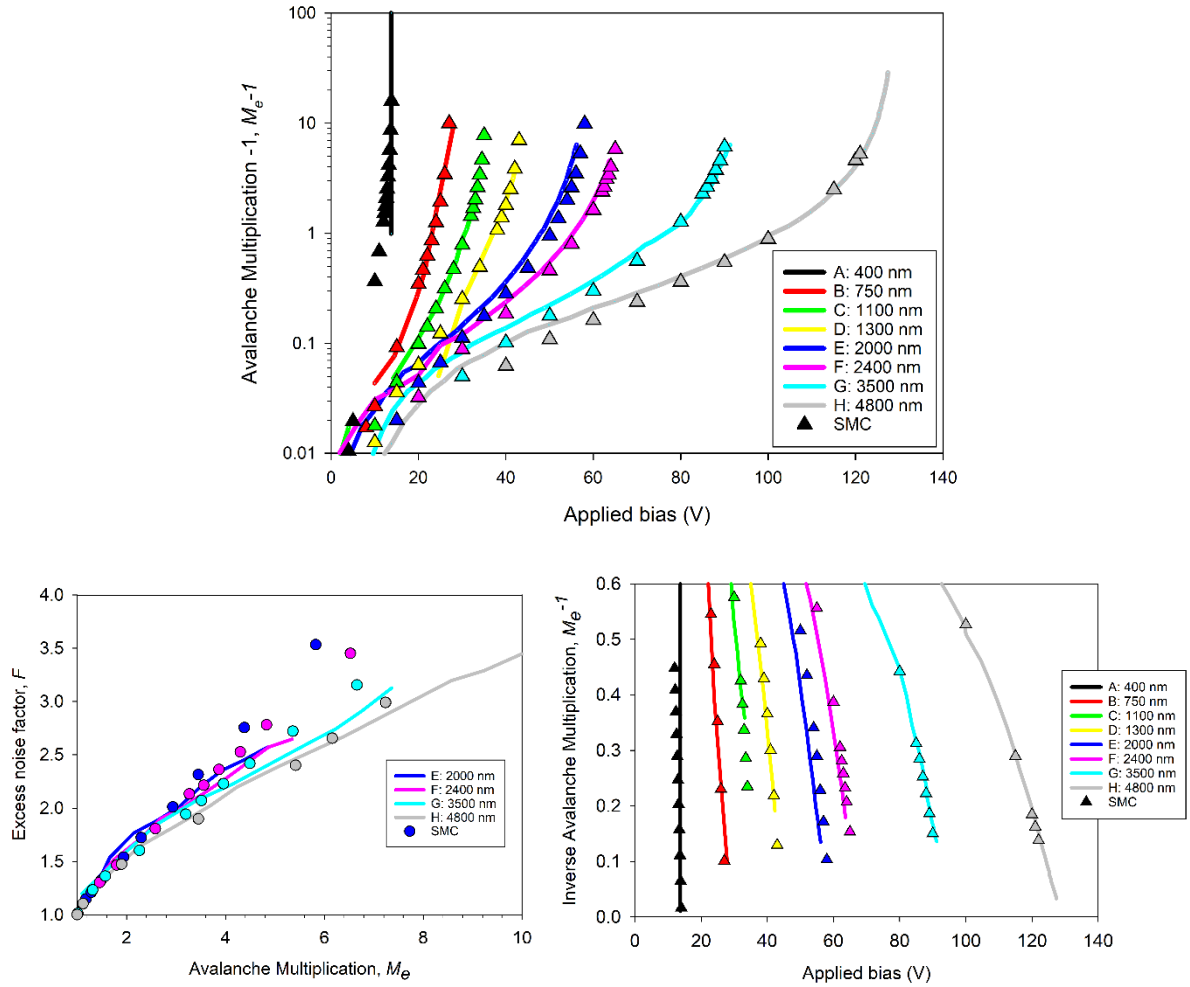

Fig. 6.4 $M_e(V)$ (top), $F_e(M_e)$ (bottom left) and $1/M_e(V)$ (bottom right) from the SMC model (symbols) and validation data (lines)

6.4) Ionisation coefficients

Using the InGaAs SMC model, statistics of the impact ionisation path lengths were obtained for electrons and holes as functions of electric field (as described in Chapters 3 and 4). The electric field ranges covered are 80 to 500 kV.cm^{-1} and 180 to 500 kV.cm^{-1}, for electron and holes respectively. The statistics were converted to PDFs for electrons and holes $h_e(x)$ and $h_h(x)$ [16]. Using the hard deadspace assumption [17], effective ionisation coefficients and deadspace values for electrons and holes were obtained by fitting the PDFs (see Appendix E).

The threshold energies extracted are E_{the} = 2.3 eV and E_{thh} = 2.6 eV. The extracted α^* and β^* can be parametrised by

$$\alpha^*(\xi) = \begin{cases} 2.1 \times 10^3 \exp\left[-\left(\frac{1.95 \times 10^5}{\xi}\right)^{1.15}\right] \mathrm{cm}^{-1}, (80\mathrm{kV.cm}^{-1} \leq \xi < 170\mathrm{kV.cm}^{-1}) \\ 1.1 \times 10^4 \exp\left[-\left(\frac{2.8 \times 10^5}{\xi}\right)^{2.10}\right] \mathrm{cm}^{-1}, (170\mathrm{kV.cm}^{-1} \leq \xi < 250\mathrm{kV.cm}^{-1}) \\ 3.0 \times 10^6 \exp\left[-\left(\frac{1.7 \times 10^6}{\xi}\right)^{1.00}\right] \mathrm{cm}^{-1}, (250\mathrm{kV.cm}^{-1} \leq \xi \leq 340\mathrm{kV.cm}^{-1}), \end{cases} \quad (6.1)$$

and

$$\beta^*(\xi) = 2.7 \times 10^6 \exp\left[-\left(\frac{1.14 \times 10^6}{\xi}\right)^{1.35}\right] \mathrm{cm}^{-1}, \quad (6.2)$$

where ξ is in V.cm^{-1}.

The values of α^* and β^* extracted from the PDFs, and Equations 6.1 -6.2 are compared in Fig. 6.5. They are in agreement. The avalanche multiplication that could be achieved in a practical device will, however be limited by the band-to-band tunnelling current. Where in a Geiger mode device, the electric field is typically below 150 kV.cm^{-1} and in a linear mode device, an electric field of ~300 kV.cm^{-1} yeilded a tunnelling current of 1 mA [3].The threshold energies are quite high compared to E_g; a possible cause for this could be due to the high non-impact ionising scattering rates in the material at higher energies resulting in a slower build up of carrier energy once the carrier is outside the Γ-valley. Practically the deadspace has a limited effect on $M(V)$ for devices with a width < 1µm, but it has a noticeable impact on $F(M)$ at that width.

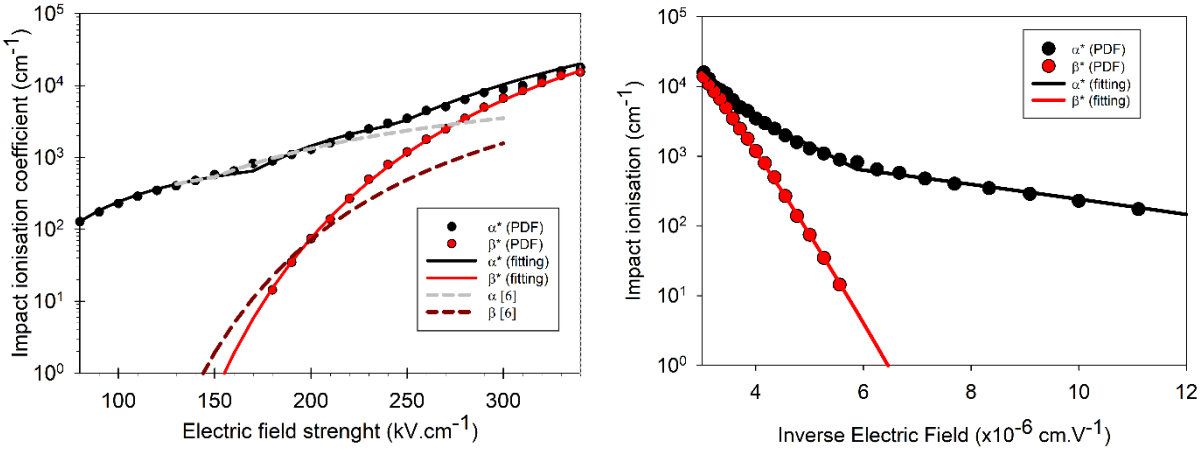

Fig. 6.5 Effective impact ionisation coefficients for ξ and $\xi^{-1}$from PDF fitting (symbols) and parameterised fitting (solid). Impact ionisation coefficients Ng [6] (dash)

6.5) Parametrised effective impact ionisation coefficients verification

To confirm the validity of the parametrised α^* and β^*, avalanche multiplication and excess noise factor for ideal InGaAs p-i-n were simulated using bother the SMC and the RPL models. The ideal p-i-n diodes, labelled D1 to D6, have w of 400 nm, 1 µm, 2 µm, 3 µm, 4 µm, and 5 µm, respectively. Results from the SMC and RPL model simulations are in agreement with $M(V)$, and $M^{-1}(V)$ between the two models, Fig. 6.6. For the RPL simulation, the change in the parametrised α^* fitting equation can be seen by the abrupt changes in gradient. The most prominent example is seen in the $M^{-1}(V)$ plot for D5 and D6 and is a consequence of using three distinct fitting regions for α^*. This aliasing effect is not seen in the SMC simulations, demonstrated by D6. Excess noise factor for electron and hole injection shows good agreement, Fig. 6.7, confirming the validity for $\alpha^*(\xi)$, $\beta^*(\xi)$, E_{the}, and E_{thh}.

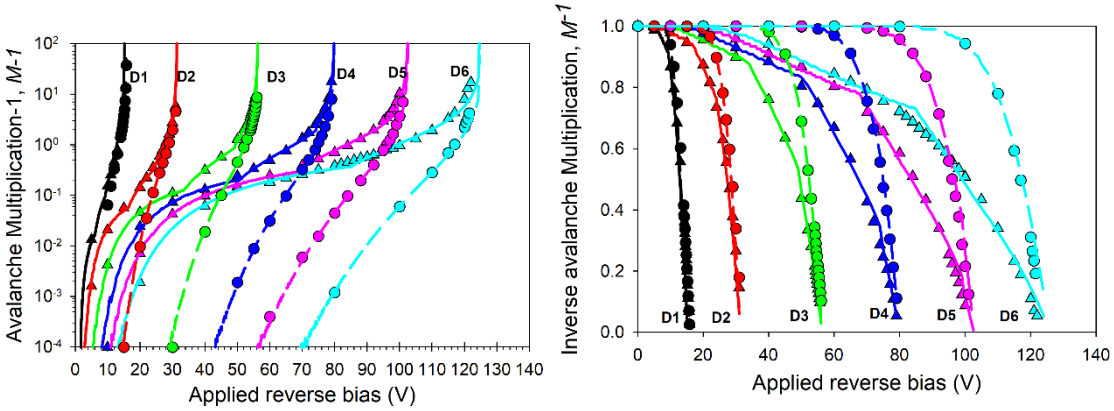

Fig. 6.6 Avalanche multiplication and inverse for the electron (triangle and solid) and hole (circle and dash) initialled impact ionisation for various widths compared between SMC (symbols) and RPL (lines)

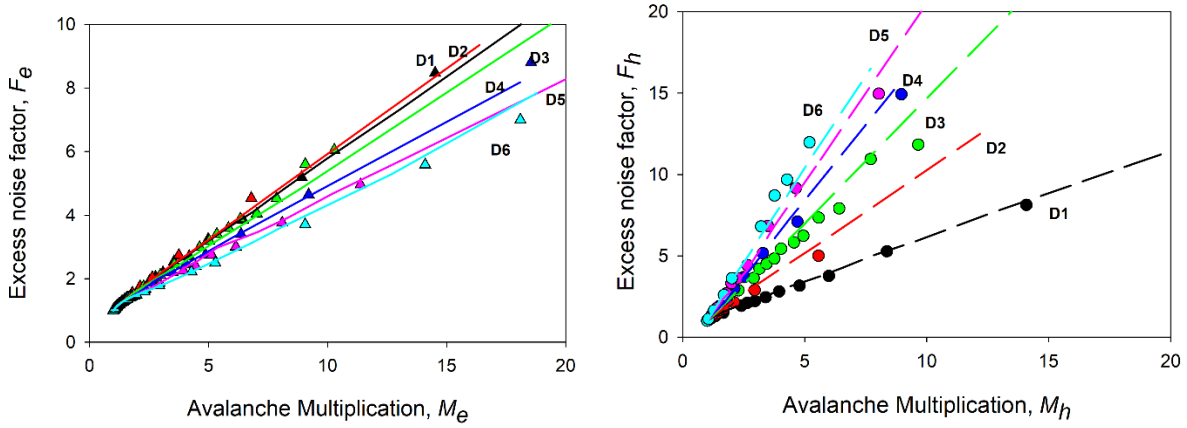

Fig. 6.7 Excess noise factor for the electron (triangle and solid) and hole (circle and dash) initialled impact ionisation for various widths compared between SMC (symbols) and RPL (lines)

6.6) Conclusions

An SMC parameter set was created to model InGaAs for both low and high electric field conditions. The SMC parameter set was then verified for $M_e(V)$ and $F_e(M_e)$ for an electric field range between 80 to 340 kV.cm^{-1}. The SMC parameter set is divided into two sections, 0-1.8 eV and 1.8-4.5 eV. This allows the SMC model to simulate the Γ-valley only avalanche multiplication as well as the avalanche multiplication at the higher energies. The model can then be used to simulate expected avalanche multiplication in a SAM device or verify the presents of avalanche multiplication in the absorber region of an experimental device.

The SMC was used to generate PDFs for electric fields between 80 and 500 kV.cm^{-1}, for electrons and holes. The PDFs were used to extract the effective impact ionisation coefficients and threshold energies for InGaAs. The effective impact ionisation coefficients were parameterised and verified using an RPL model by comparing $M(V)$, and $F(M)$ results to the verified SMC model.

The InGaAs SMC will allow for accurate simulation of the absorption layer of a SAM APD and the absorber's contribution to the avalanche multiplication and excess noise to the SAM APD.

6.7) References

[1] J. S. Ng, C. H. Tan, J. P. R. David, and G. J. Rees, 'Effect of impact ionization in the InGaAs absorber on excess noise of avalanche photodiodes', *IEEE J. Quantum Electron.*, vol. 41, no. 8, pp. 1092–1096, Aug. 2005, doi: 10.1109/JQE.2005.850700.

[2] S. C. Liew Tat Mun, C. H. Tan, Y. L. Goh, A. R. J. Marshall, and J. P. R. David, 'Modeling of avalanche multiplication and excess noise factor in $In_{0.52}Al_{0.48}As$ avalanche photodiodes using a simple Monte Carlo model', *J Appl Phys*, vol. 104, p. 7, 2008, doi: 10.1063/1.2952003.

[3] J. S. Ng, 'Impact ionisation measurement and modelling of long wavelength avalanche photodiodes', Ph.D dissertation, University of Sheffield, Department of Electronic and Electrical Engineering, 2003.

[4] Y. L. Goh, 'Impact Ionisation in InGaAs, InAlAs and InGaAs/GaAsSb Superlattices for Near Infrared Avalanche Photodetectors', Ph.D dissertation, University of Sheffield, Department of Electronic and Electrical Engineering, 2008.
[5] J. D. Petticrew, S. J. Dimler, and J. S. Ng, 'Simple Monte Carlo Simulator for Modelling Linear Mode and Geiger Mode Avalanche Photodiodes in C++', *J. Open Res. Softw.*, vol. 6, May 2018, doi: 10.5334/jors.212.
[6] J. S. Ng, C. H. Tan, J. P. R. David, G. Hill, and G. J. Rees, 'Field dependence of impact ionization coefficients in $In_{0.53}$ Ga $_{0.47}As$', *IEEE Trans. Electron Devices*, vol. 50, no. 4, pp. 901–905, Apr. 2003, doi: 10.1109/TED.2003.812492.
[7] C. H. Tan, G. J. Rees, P. A. Houston, J. S. Ng, W. K. Ng, and J. P. R. David, 'Temperature dependence of electron impact ionization in $In0._{0.53}Ga_{0.47}As$', *Appl. Phys. Lett.*, vol. 84, no. 13, p. 2322, 2004, doi: 10.1063/1.1691192.
[8] J. Bude and K. Hess, 'Thresholds of impact ionization in semiconductors', *J. Appl. Phys.*, vol. 72, no. 8, p. 3554, 1992, doi: 10.1063/1.351434.
[9] D. Harrison, R. A. Abram, and S. Brand, 'Characteristics of impact ionization rates in direct and indirect gap semiconductors', *J. Appl. Phys.*, vol. 85, no. 12, pp. 8186–8192, Jun. 1999, doi: 10.1063/1.370658.
[10] J. Allam, '"Universal" Dependence of Avalanche Breakdown on Bandstructure: Choosing Materials for High-Power Devices', *Jpn. J. Appl. Phys.*, vol. 36, no. Part 1, No. 3B, pp. 1529–1542, Mar. 1997, doi: 10.1143/JJAP.36.1529.
[11] S. Adachi, *Properties of semiconductor alloys: group-IV, III-V and II-VI semiconductors*. in Wiley series in materials for electronic & optoelectronic applications. Chichester, U.K: Wiley, 2009.
[12] T. H. Windhorn, L. W. Cook, and G. E. Stillman, 'The electron velocity-field characteristic for n-$In_{0.53}Ga_{0.47}As$ at 300 K', *IEEE Electron Device Lett.*, vol. 3, no. 1, pp. 18–20, Jan. 1982, doi: 10.1109/EDL.1982.25459.
[13] P. Hill, J. Schlafer, W. Powazinik, M. Urban, E. Eichen, and R. Olshansky, 'Measurement of hole velocity in *n* -type InGaAs', *Appl. Phys. Lett.*, vol. 50, no. 18, pp. 1260–1262, May 1987, doi: 10.1063/1.97877.
[14] M. V. Fischetti and S. E. Laux, 'Monte carlo analysis of electron transport in small semiconductor devices including band-structure and space-charge effects', *Phys. Rev. B*, vol. 38, no. 14, pp. 9721–9745, Nov. 1988, doi: 10.1103/PhysRevB.38.9721.
[15] S. A. Plimmer, 'Avalanche multiplication in $Al_xGa_{1-x}As$', Ph.D dissertation, University of Sheffield, Department of Electronic and Electrical Engineering, 1997.
[16] S. A. Plimmer, J. P. R. David, and D. S. Ong, 'The merits and limitations of local impact ionization theory [APDs]', *IEEE Trans. Electron Devices*, vol. 47, no. 5, pp. 1080–1088, May 2000, doi: 10.1109/16.841244.
[17] M. M. Hayat, B. E. A. Saleh, and M. C. Teich, 'Effect of dead space on gain and noise of double-carrier-multiplication avalanche photodiodes', *IEEE Trans. Electron Devices*, vol. 39, no. 3, pp. 546–552, Mar. 1992, doi: 10.1109/16.123476.

Chapter 7
Conclusion & Future Work

7.1) Conclusion

A 600 nm AlGaAsSb mesa p-i-n diode has been experimentally characterised for avalanche gain and excess noise factor for pure electron injection and two mixed injection profiles at room temperature. The importance of using pure electron injection is confirmed by the worsening excess noise performance when relatively low mixed carrier injection profiles were characterised. With pure electron injection $F(10) = 1.27$ and $F(20) = 1.74$ was measured, significantly lower than previously reported at $F(10) = 2.50$ and 200 nm pin $F(10) = 2.27$ for 100 nm and 200 nm pin device, respectively [1], $F(10) =1.99$ for a 1 μm[2], F(10) = 1.90 for a 910 nm [3], and a SAM APD with F(10) = 1.93 [4]. The experimental 600 nm p-i-n also exhibited lower excess noise than other III-V based materials, shown previously in Fig.1.2. The pure electron injection impact ionisation results demonstrate the potential for this material system for a new generation of extremely low noise SAM APDs for 1.31 and 1.55 μm detection.

Utilising the experimental data and data from earlier work, a Simple Monte Carlo model parameter set has been validated for avalanche multiplication and excess noise factor at room temperature using this work's experimental capacitance-voltage, avalanche multiplication and excess noise factor, and those of narrower devices, reported in the literature. Using the validated parameter set, the electric field dependant effective impact ionisation coefficients and threshold energies of $Al_{0.85}Ga_{0.15}As_{0.56}Sb_{0.44}$ at room temperature has been extracted from the simulations. The impact ionisation coefficients have been parameterised between the electric field range of 400-1200 $kV.cm^{-1}$. These parameters were verified by simulating a range of p-i-n and n-i-p devices using the verified simple monte carlo model and the parameterised impact ionisation coefficients with a random path length model. Comparing the impact ionisation coefficient ratio with InP and InAlAs, Fig. 1.1, AlGaAsSb has a significantly higher ratio, leading to very low excess noise for both narrow and thick devices.

With the AlGaAsSb SMC model validated, a simulation study was carried out to compare AlGaAsSb with InP and Si for breakdown probability, time to breakdown and jitter. Devices with an i-region of 100 nm, 200 nm, 500 nm, 800 nm, 1000 nm, 1200 nm, and 1500nm have been simulated using the Simple Monte Carlo model for breakdown probability, time to breakdown and jitter of the breakdown time, for three different materials. InP and Si represent common avalanche materials used in SPADs which are commercially available. AlGaAsSb, is a novel material which can now be simulated using the work in Chapter 4. AlGaAsSb has been shown to have a large impact ionisation coefficient ratio, indicating a promising replacement for InP in 1550

nm detection SPADs. AlGaAsSb's breakdown probability simulation indicated a very promising alternative to InP, with a small overbias required for electron-initiated breakdown events to occur compared to a significant overbias required for holes. The AlGaAsSb breakdown probability simulation also indicates a favourable comparison to the Si simulations.

The Simple Monte Carlo model for Geiger mode simulations was found to be computationally intensive and with long simulation runtimes. It is, therefore, desirable to utilise less complex simulation models where possible to reduce simulation runtimes. The Random Path Length model was able to accurately replicate the Simple Monte Carlo model's breakdown probability simulations in a significantly short simulation run time. However, the Random Path Length model could not replicate the time to breakdown and jitter simulations of the Simple Monte Carlo model for any material or device width. When calculating the instantaneous current using Ramo's theorem, the Random Path Length model assumes that all free carriers travel at saturation velocity. However, the saturation velocity assumption is not valid for hot carriers, as they can exceed the saturation velocity by 2-3 times. In this work, an effective enhanced velocity was determined for Si, InP, and AlGaAsSb and parameterised for the applied electric field across the device. Excellent agreement was achieved for all three materials across all devices for both time to breakdown and jitter of electron and hole initialised events, with an acceptable agreement for hole-initiated jitter for Si and AlGaAsSb. The enhanced velocity Random Path Length model represents a significant reduction in simulation time compared to the Simple Monte Carlo.

Finally, an $In_{0.53}Ga_{0.47}As$ Simple Monte Carlo parameter set was verified for M(V) and F(M) for for both low and high electric field conditions. The InGaAs Simple Monte Carlo model parameter set is divided into two sections, 0-1.8 eV and 1.8-4.5 eV. This allows the Simple Monte Carlo model to simulate the Γ-valley only avalanche multiplication as well as the avalanche multiplication at the higher energies. The model can then be used to simulate expected avalanche multiplication in a SAM device or verify the presents of avalanche multiplication in the absorber region of an experimental device. Using the Simple Monte Carlo parameter, set the probability density function for electric fields fitted between 80 and 500 $kV.cm^{-1}$, with the effective impact ionisation coefficients and threshold energies being parameterised between 80 ad 340 $kV.cm^{-1}$. Good agreement was achieved between the Simple Monte Carlo model and the Random Path Length model for M(V) and F(M) for a set of ideal p-i-n and n-i-p devices with an i-region of 0.4 μm, 1 μm, 2 μm, 3 μm, 4 μm, and 5 μm. The InGaAs Simple Monte Carlo model will allow for accurate simulation of the absorption layer of a SAM APD and any contribution to the avalanche multiplication and excess noise to the SAM APD

7.2) Future Work

With this work, InGaAs can now be modelled using the SMC model. It would be advantageous for designing and characterising the SMC model to be modified to simulate SAM device structures. This would allow 1) the designer to simulate the expected performance of an entire novel structure without the need to make assumptions about impact ionisation, temporal results and breakdown probability. 2) Allow the simulation of an experimental device to identify irregularities in an experimental SAM APD impact ionisation results.
Due to the nature of the work presented in Chapter 5, only three materials were verified for enhanced velocity simulations. Hence a general relationship between the enhanced velocity curve and the modelled material would be advantageous, especially for novel materials where little to no experimental results is available. Additionally, experimental determined P_b, t_b, and jitter for the materials would add to the validity of this work and Geiger-mode APD simulations in general.

In chapter 4, an AlGaAsSb p-i-n was experimentally characterised for excess noise. With very low $F(M)$ displayed in recent novel materials, experimental limitations are becoming a significant barrier to characterisation. With low $F(M)$, the noise due to variations in the impact ionisation rate is not much greater than the expected shot noise. By characterising both p-i-n and n-i-p devices, the low $F(M)$ can be confirmed with one device and the additionally high $F(M)$ can be used for verifying simulations. The non-prefered injection type typically shows more significant variation with w compared to the preferred injection type, as seen in chapter 4. This will add to the rigour for fitting the impact ionisation coefficients.

7.3) References

[1] L. L. G. Pinel *et al.*, 'Effects of carrier injection profile on low noise thin $Al_{0.85}Ga_{0.15}As_{0.56}Sb_{0.44}$ avalanche photodiodes', *Opt. Express*, vol. 26, no. 3, p. 3568, Feb. 2018, doi: 10.1364/OE.26.003568.
[2] S. Lee *et al.*, 'Low noise $Al_{0.85}Ga_{0.15}As_{0.56}Sb_{0.44}$ avalanche photodiodes on InP substrates', *Appl. Phys. Lett.*, vol. 118, no. 8, p. 081106, Feb. 2021, doi: 10.1063/5.0035571.
[3] S. Lee *et al.*, 'Random alloy thick AlGaAsSb avalanche photodiodes on InP substrates', *Appl. Phys. Lett.*, vol. 120, no. 7, p. 071101, Feb. 2022, doi: 10.1063/5.0067408.
[4] X. Collins *et al.*, 'Low-noise AlGaAsSb avalanche photodiodes for 1550nm light detection', in *Optical Components and Materials XIX*, M. J. Digonnet and S. Jiang, Eds., San Francisco, United States: SPIE, Mar. 2022, p. 16. doi: 10.1117/12.2608842.

Appendix A.

Excess noise setup Calibration

A.1) Shot Noise Calibration

Shot noise arises due to the photocurrent of the device under test; an accurate knowledge of the shot noise response of the system is required to calculate $F(M)$. A reference photodiode is used to calculate the shot noise power equivalent voltage. For viable wavelength, a Centronic BPX65 Si photodiode is used. For near Infrared, a Thorlabs FGA015 InGaAs photodiode is used. The reference diode is soldered to the input of

- Turn on the LIA, SMU, light source, chopper and oscilospce
- Solder the reference diode to the input of the TIA and the SMU
- Reverse bias the reference diode, typically 5 V to a known capacitance value
- Focus the light onto the active region of the reference diode
- Set the variable attenuator to no less than 20 dB
- Shine the light on the device and record the photocurrent and noise power equivalent voltage from the two LIAs
- Vary the optical power and record the photocurrent and noise power equivalent voltage and repeat for multiple optical powers.
- Plot photocurrent – noise power equivalent voltage
- Calculate the linear regression for that given light source.

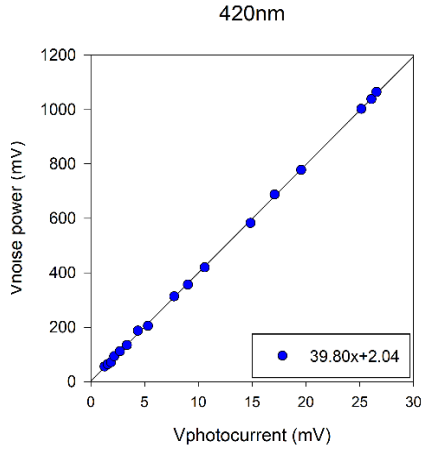

Fig. A.1 Example of shot noise and fitting calibration

Table A.1 Previous shot noise calibration results

Date	Wavelength (nm)	K	c	Reference device capacitance (pF)	Reference device
01/19	633	40.79	5.74	4.7	BPX65
01/19	543	41.54	1.48	4.7	BPX65
01/19	420	41.08	3.56	4.7	BPX65
03/20	633	47.51	-2.72	4.7	BPX65
03/20	543	47.65	1.83	4.7	BPX65
03/20	420	46.46	6.43	4.7	BPX65
11/20	633	39.89	4.59	4.7	BPX65
11/20	543	40.46	1.85	4.7	BPX65
11/20	420	41.40	-1.67	4.7	BPX65
01/21	1520	38.70	0.00	1.5	FGA015
03/21	1520	39.30	2.05	1.5	FGA015
03/21	633	39.37	4.84	4.7	BPX65
03/21	543	39.73	1.61	4.7	BPX65
03/21	420	38.55	2.70	4.7	BPX65
05/21	1520	42.10	0.80	1.5	FGA015
05/21	940	40.80	7.77	1.5	FGA015

A.2) Effective Noise Bandwidth

The Effective Noise Bandwidth (ENBW)

This calibration should be done every time the op-amp is replaced.

- Turn on the network analyser and excess noise setup power supply to warm up for at least 30 mins
- Turn on the PC associated with the network analyser and ensure the LabView program called **V0.5.1** connects to the network analyser via a GPIB cable and can retrieve the data successfully
    - Without the PC and labview, a floppy disk will be required to retrieve the data from the network analyser
- Equipment required
    - Four impedance match SMA cables of the same length
    - Impedance matched signal splitter PCB
    - Resistor block PCB
        - Resistor block PCB consists of a pair of 50 Ω impedance match connectors with three groups of 33 kΩ in parallel connected in series. The total impedance is 33 kΩ
- Change network analyser setting to desired power and frequency range. An example of possible settings for the HP4396B Network/Spectrum Analyser
    - Press start and on the number pad key in starting frequency 100 kHz
    - Press stop and on the number pay key in stopping frequency to 50 MHz
    - Change sweep type to log sweep
    - Change the number of points to the maximum of 801
    - Ensure IF frequency is set from 40 kHz to 1 kHz
        - Defines the frequency accuracy of the network analyser sweep

    - Change output reference power of the network analyser
        - -50dBm with 50dB through the valuable attenuator was found to avoid signal clipping
    - Turn on sweep averaging
- Solder an SMA jack to the resistor block and plug it into the network analyser
        - Signal out to splitter, splitter to reference and splitter to resistor block and resistor block to input A
    - Press Calibrate and select through and wait for the network analyser to finish – there should now be a letter C in the top left side indicating that it is calibrated.
    - De-solder resistor block and solder to the input of the TIA
- Disconnect the cable linking the variable attenuator to the power meter equivalent circuit input and connect this to Input A of the network analyser
- Press avg on the network analyser to start the sweep
- Retrieve the frequency response using the Labview code and label with the appropriate input capacitance value.
- Solder a capacitor between the input and earth on the TIA board (As close to the input of the TIA as possible is preferable) and repeat data acquisition for each capacitor value.
    - Calibration should only be required once, but changing frequency or power settings will cause the calibration to be lost
- To calculate the ENBW(cj) $\frac{1}{A_0^2}\int_0^\infty \left|A(f;C_j)\right|^2 df$:
    - Numerically integrate each waveform to find area
    - Multiply each by $\frac{1}{A_0^2}$Where A_0 is the gain at 10MHz for 0pF input
    - Plot ENBW again C_j and find the fitted quadratic equation (The current system cannot handle C_j in excess of around 30pF)
        - ENBW(Cj) = $x.C_j^2 + y.C_j + z$, where C_j is in pF

Table A.2 Previous calibration for ENBW

Date	x	y	z
12/18	562.31	73833	4309280
02/20	428.1	82610	4429000

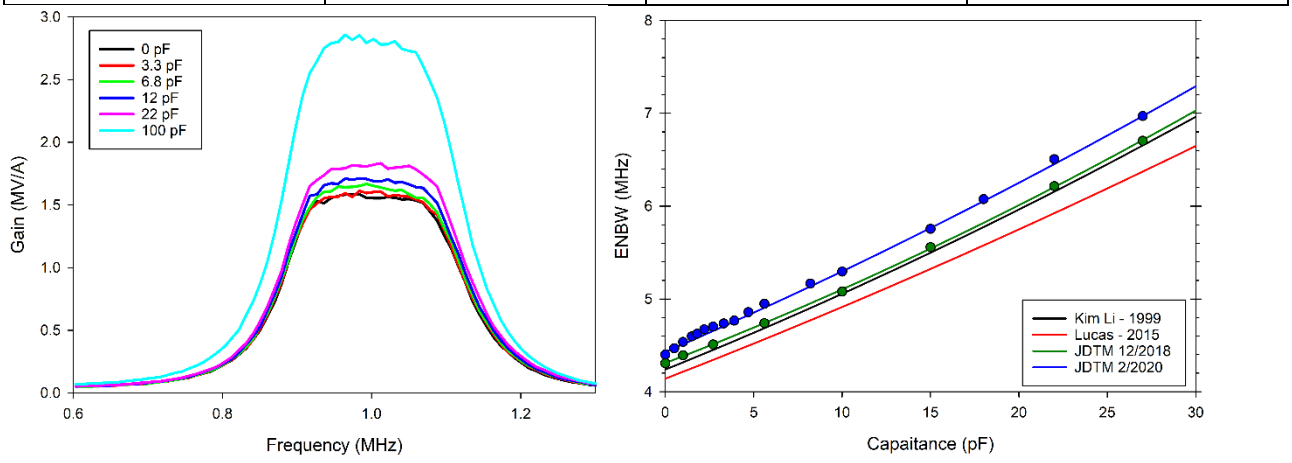

Fig. A.2 Example of expected frequency response of the excess noise setup, using a 1 MHz bandpass filter (L). Fitted ENBW for input capacitance compared with previous fitting (R).

Appendix B.

Single Photon Avalanche Photodiode setup Calibration

B.1) CQC-PCB Calibrations

1. Remove CQC-board from the SPAD setup
    a. move cage setup to one side (not require for calibration)
    b. Remove all copper blocks, device etc
2. Solder a 50Ω from the high voltage side of the component to ground
3. Solder the core of a BNC cable to the high voltage side and the shield braid to ground
4. Put the CQC-board back in to the SPAD box and connect the two DC power supplies and turn on
5. Connect the BNC cable to the Pulse generator
6. Connect the Pulse monitor to the Oscilloscope
7. Connect an oscilloscope probe to the BNC core
8. Vary the AC Pulse height and record the value of the oscilloscope probe and the pulse monitor
9. Plot pulse monitor voltage against oscilloscope probe voltage

B.2) Optical Calibration

Due to the High attenuation value possible of the 633 nm eVOAs it is recommended that the user only calibrates one attenuator at a time.
To calibrate the eVOA

1. Turn on 633nm HeNe laser (or other CW 633nm source) and wait for it to stabilise
2. Using the fibre mounted connected, place the optical power meter on the output of the eVOA and zero offset calibrate
3. Set both attenuator voltages to 0V
4. Connected laser source to input of eVOA.
5. Record optical power through eVOA at 0V input
    a. Data may need to be recorded over a period of time and averaged
    b. If a HeNe light souce is used, a single mode fibre connection, like that used with the eVOAs, can cause back reflections decreasing the stability of the laser source.
6. Ser input voltage to eVOA record optical power.
7. Repeat steps 5 and 6 until full range has been achieved for a single eVOA
8. Repeat steps 3-7 for the second eVOA.
9. Calculated optical attenuation as $10 * \log \frac{Average\ optical\ power\ (with\ voltage\ applied)}{Average\ optical\ power\ (0\ V)}$

Static Attenuation:

To measure the static attenuation of the eVOA

1. Measure optical power at the light source (using a single mode fibre)
2. Set eVOAs to 0V

3. Measure the optical power of light on the output of the eVOA setup.

To measure the static attenuation of the system:

1. Measure optical power from the light source through a single mode fibre
2. Place optical power meter on the CQC-board where the DUT would be placed
    a. Calibrate the power meter for the optical power offset
3. Place the light soure fibre on the input to the SPAD setup's black box
4. Record optical power through the fibres to the sensor on the CQC board
5. Calculate attenuation due to the fibres and optics inside the black box

The total attenuation of the eVOAs will be the sum of the static attenuation and the selected variable attenuation. The total attenuation of the system is the sum of the static attenuation of the system, static attenuation of the eVOAs and the variable attenuation selected.

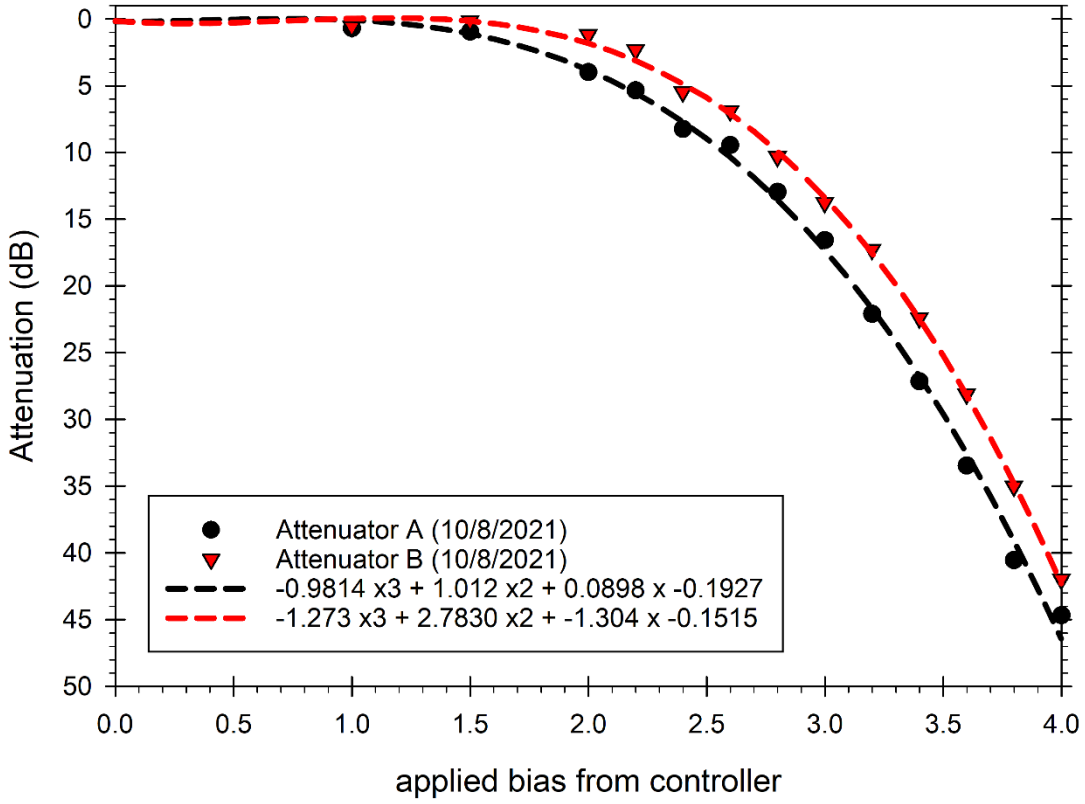

Fig. B.1 Example of eVOA calibration and fitting

Appendix C.

$Al_{0.85}Ga_{0.15}As_{0.56}Sb_{0.44}$ PDF fitting

This appendices shows the complete PDF fitting for the extraction of effective impact ionisation coefficients for electrons and holes. The fitting used the hard deadspace approximation,

$$h_{e(h)}(x) = \begin{cases} 0, & x \leq d_{e(h)} \\ \alpha^*(\beta^*)exp\left[-\alpha^*(\beta^*)\left(x - d_{e(h)}\right)\right] & x > d_{e(h)}. \end{cases}$$, where $h_e(x)$ is the probability density, α^* is the gradient of the decay function and d_e is the offset.

The impact ionisation path length was measured with 20,000 events for each carrier at each voltage level

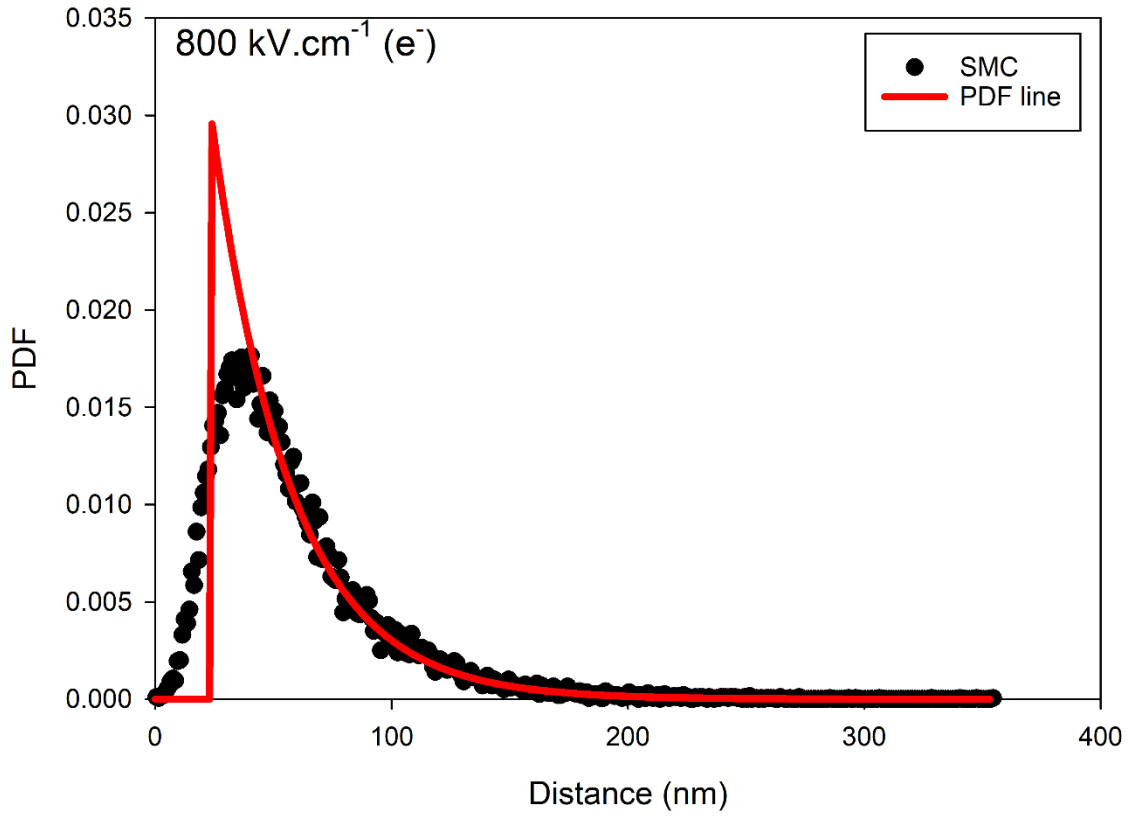

Fig. C.1 Example of electron PDF fitting for AlGaAsSb at an electric field of 800 kV.cm^{-1}

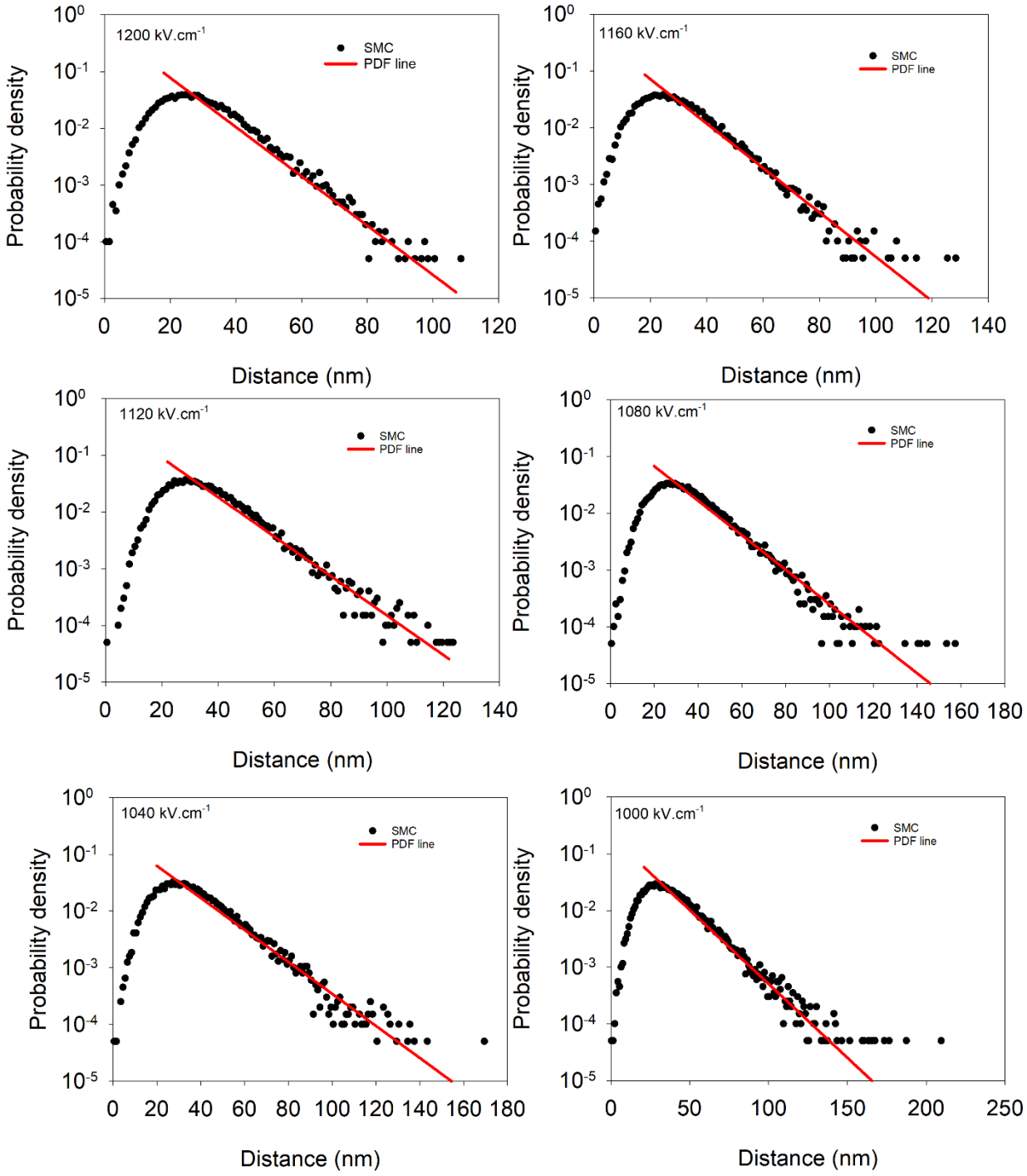

Fig. C.2 PDF fitting for AlGaAsSb using the SMC for electrons, between 1000 and 1200 kV.cm^{-1}

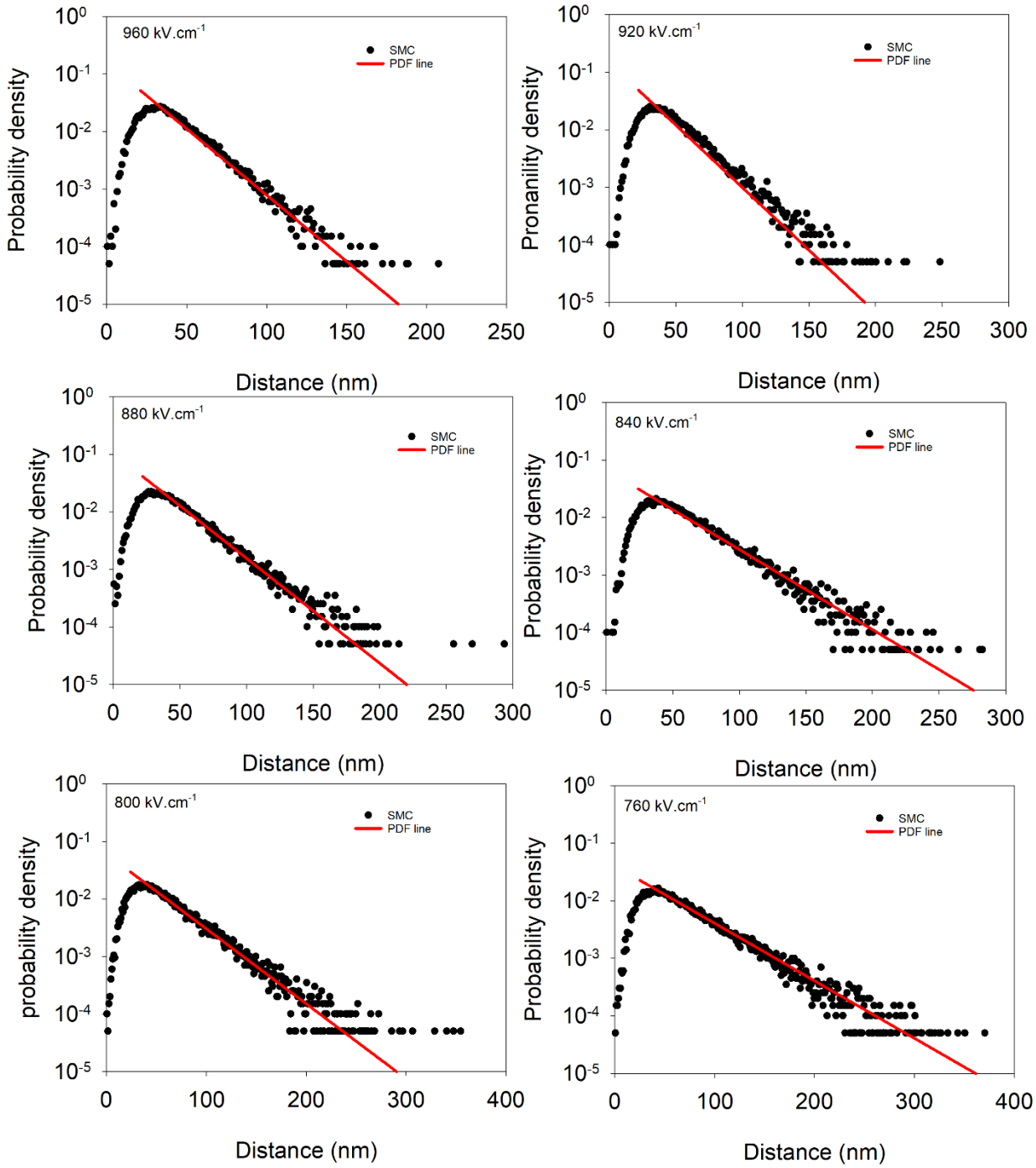

Fig. C.3 PDF fitting for AlGaAsSb using the SMC for electrons, between 760 and 960 kV.cm^{-1}

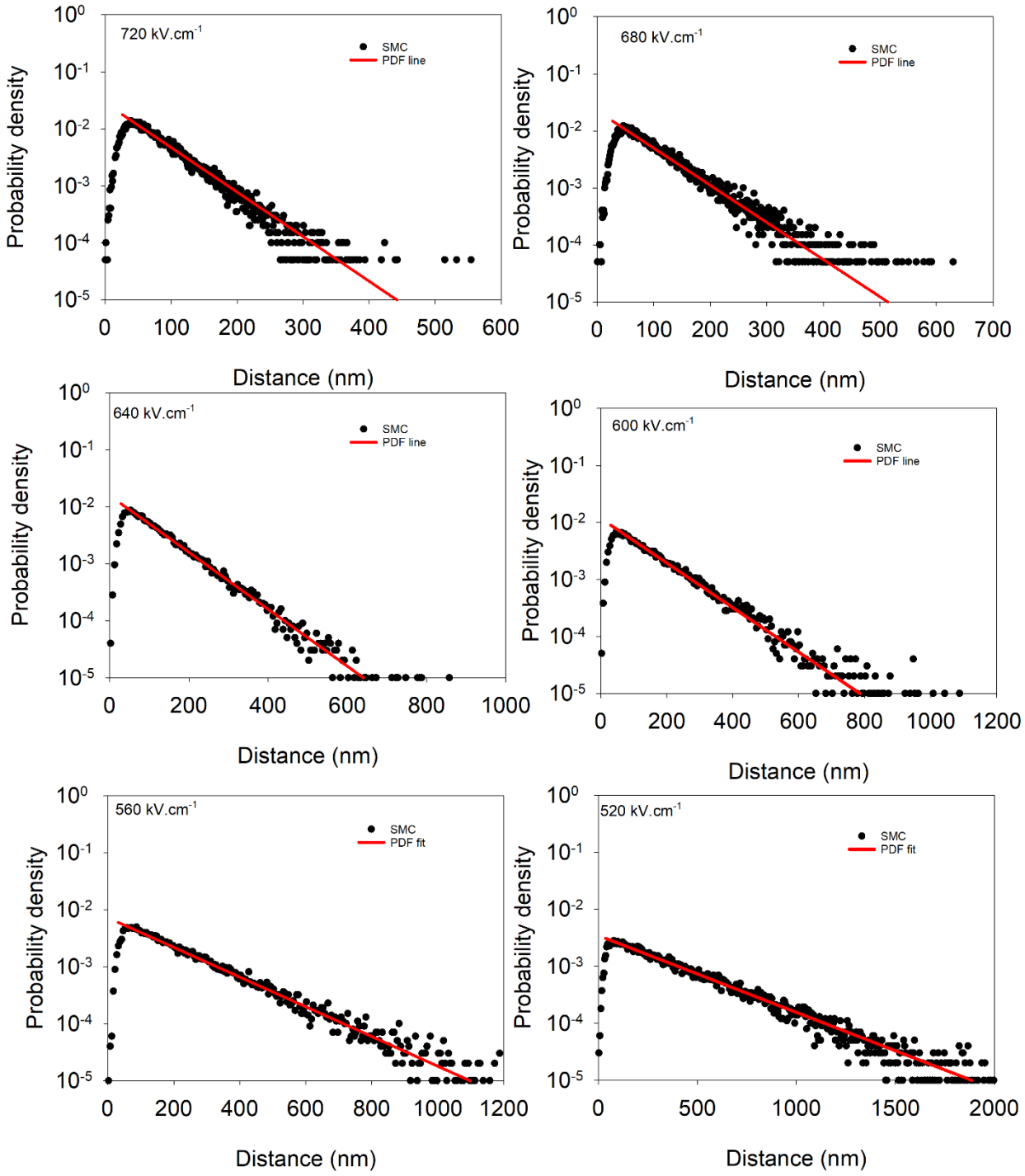

Fig. C.4 PDF fitting for AlGaAsSb using the SMC for electrons, between 520 and 720 kV.cm^{-1}

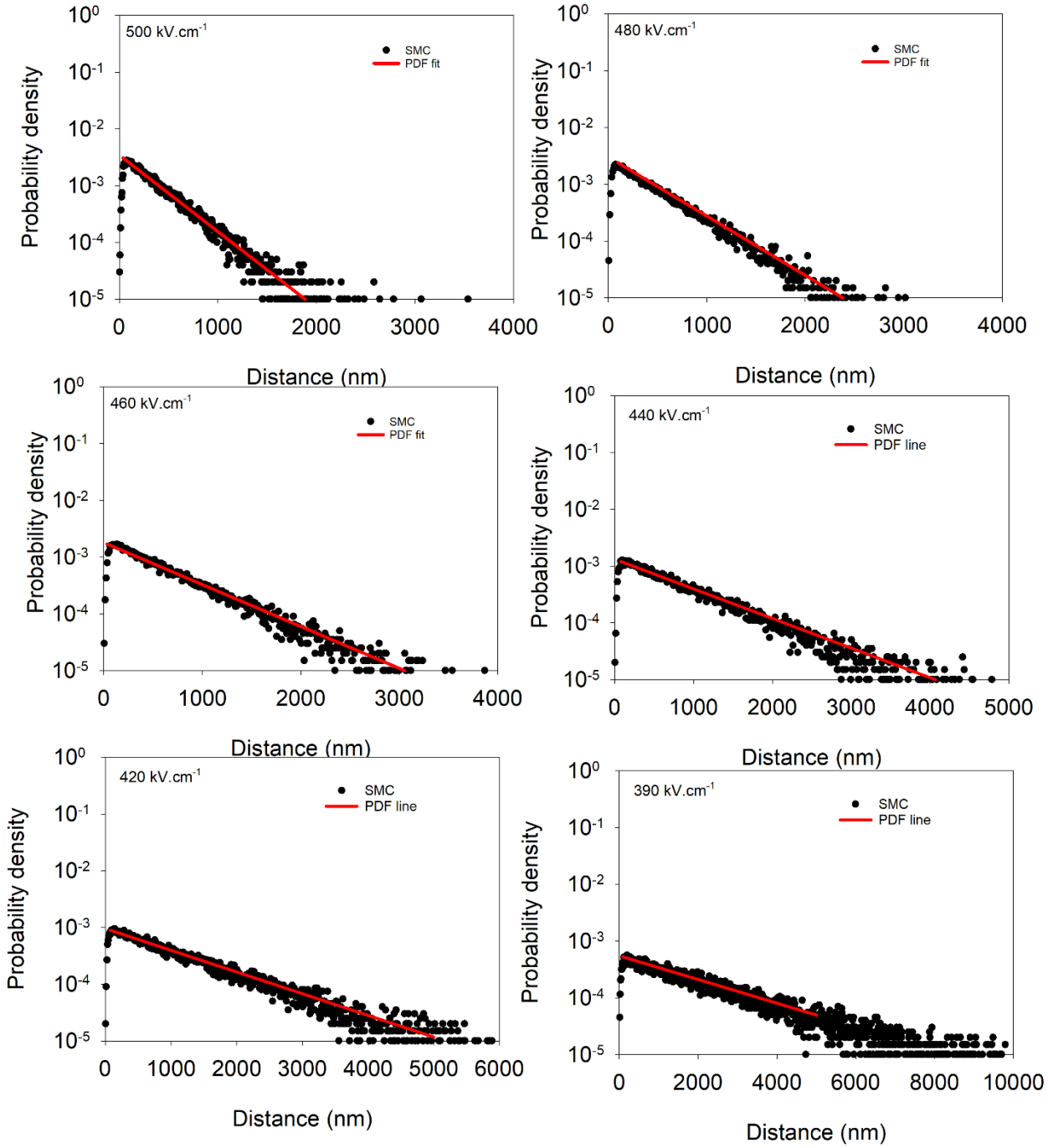

Fig. C.5 PDF fitting for AlGaAsSb using the SMC for electrons, between 500 and 390 kV.cm^{-1}

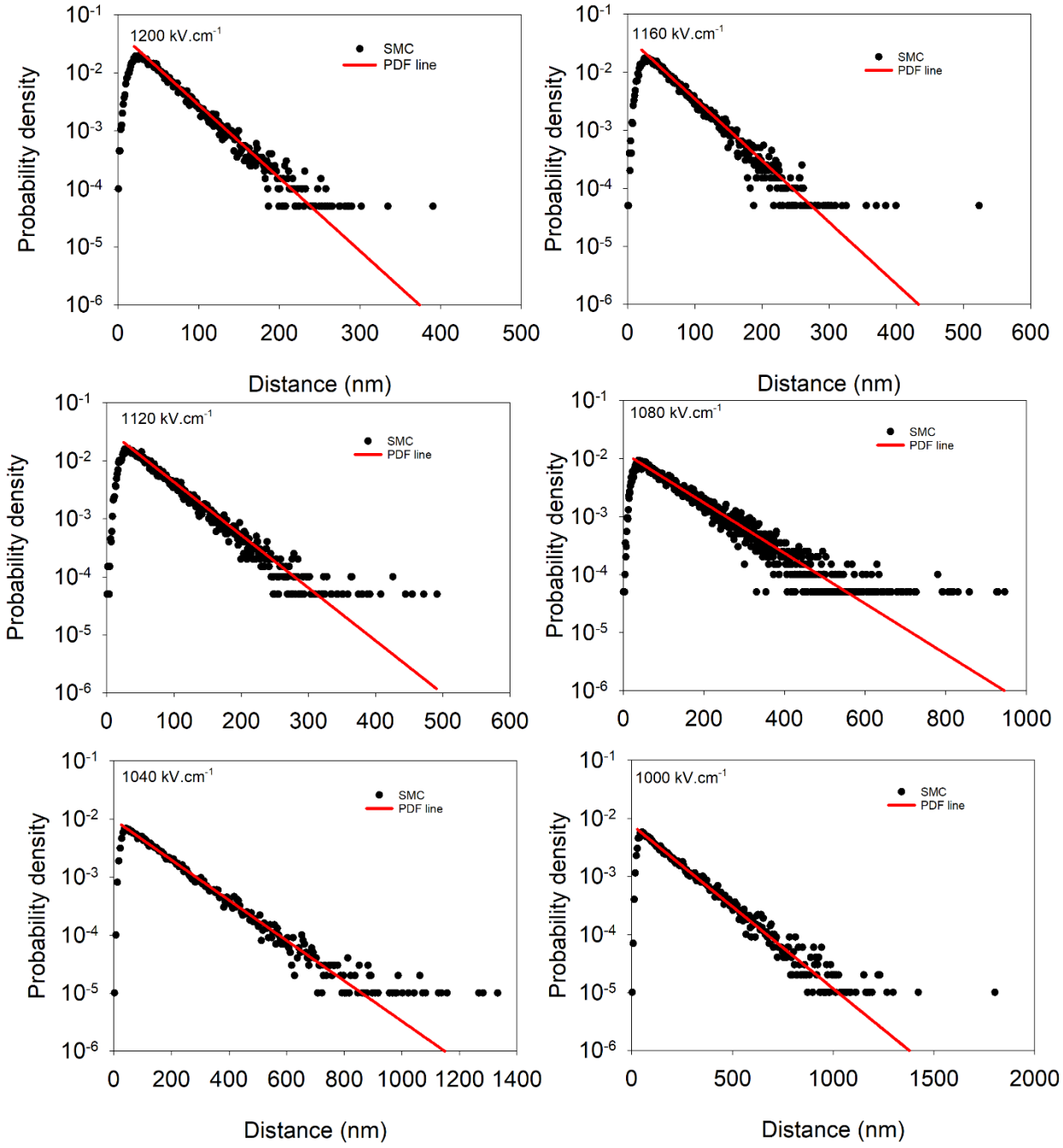

Fig. C.6 PDF fitting for AlGaAsSb using the SMC for holes, between 1000 and 1200 kV.cm^{-1}

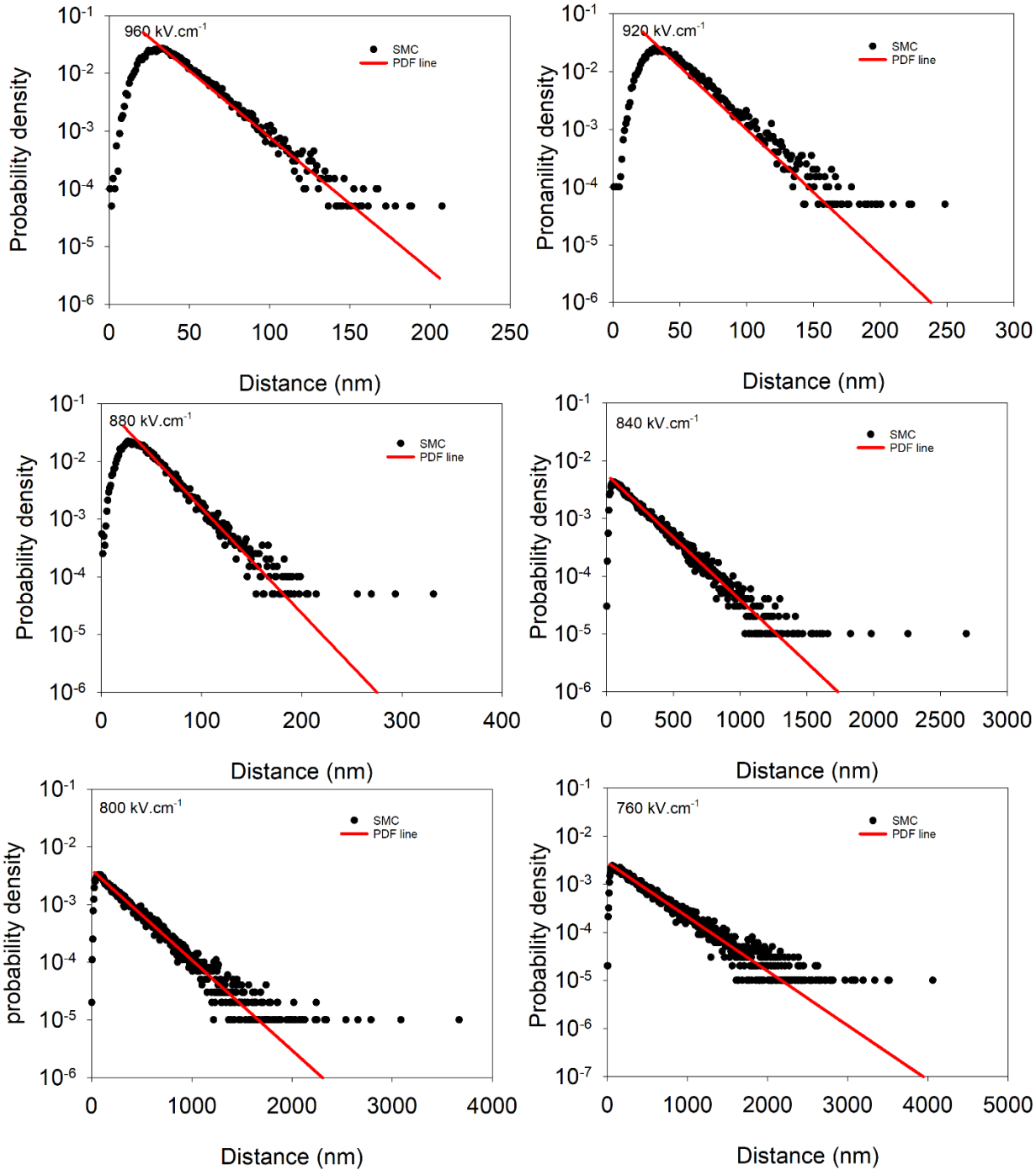

Fig. C.7 PDF fitting for AlGaAsSb using the SMC for holes, between 760 and 960 kV.cm^{-1}

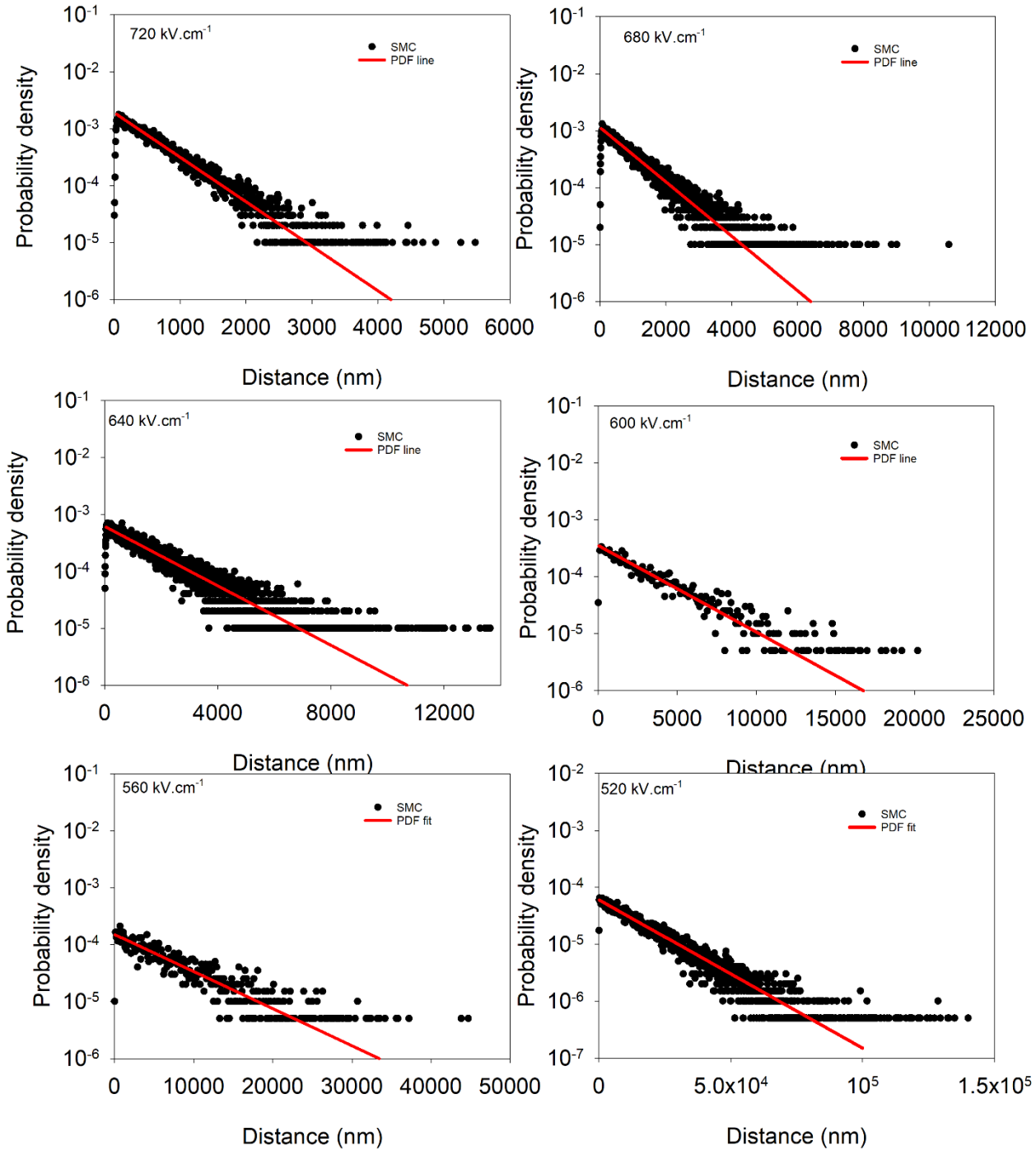

Fig. C.8 PDF fitting for AlGaAsSb using the SMC for holes, between 520 and 720 kV.cm^{-1}

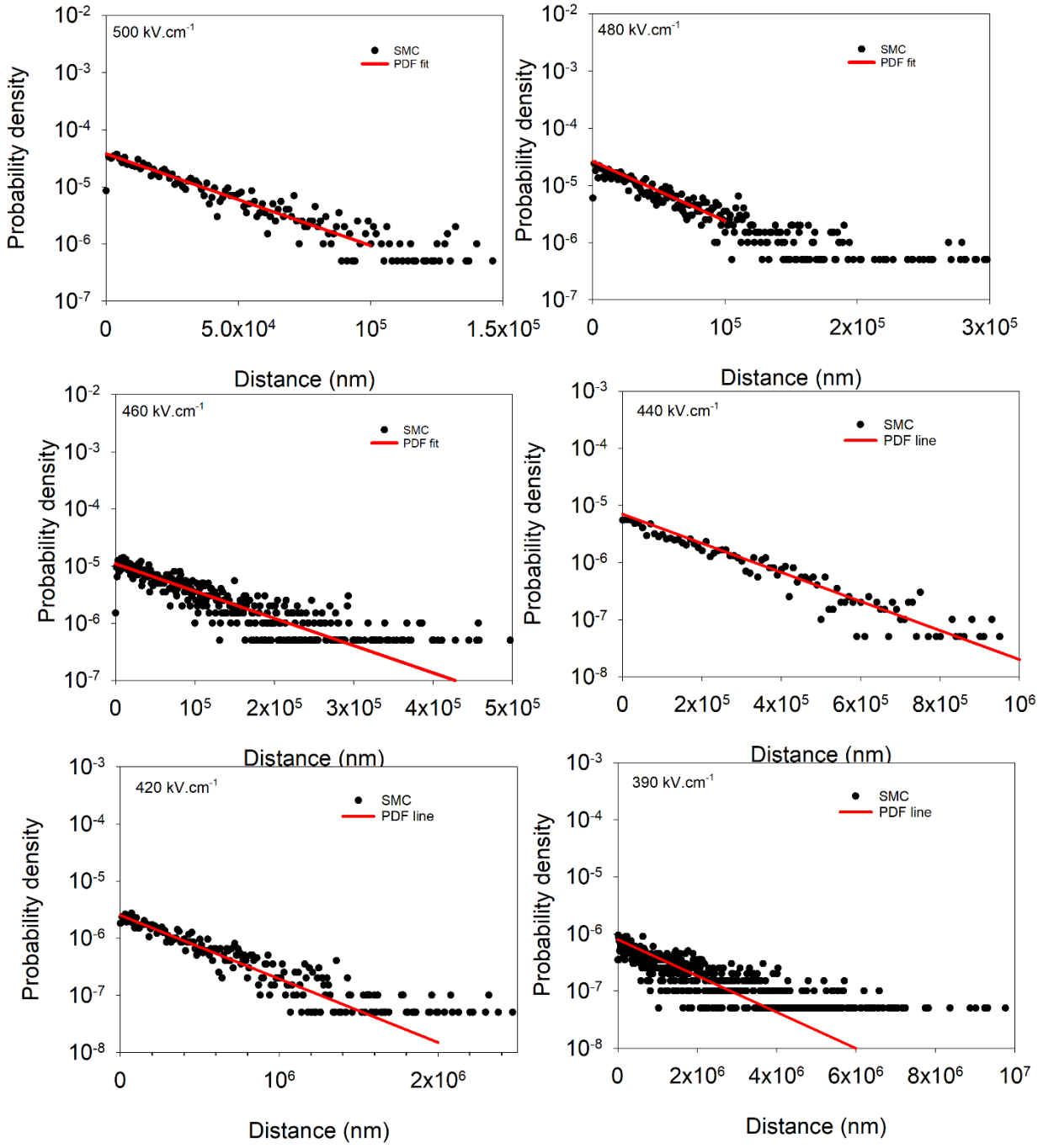

Fig. C.9 PDF fitting for AlGaAsSb using the SMC for holes, between 390 and 500 kV.cm^{-1}

Appendix C: $Al_{0.85}Ga_{0.15}As_{0.56}Sb_{0.44}$ PDF fitting

Appendix D.

Si PDF fitting

This appendix shows the complete PDF fitting for the extraction of effective impact ionisation coefficients for electrons and holes. The fitting used the hard deadspace approximation,

$$h_{e(h)}(x) = \begin{cases} 0, & x \leq d_{e(h)} \\ \alpha^*(\beta^*)exp\left[-\alpha^*(\beta^*)\left(x - d_{e(h)}\right)\right] & x > d_{e(h)}. \end{cases}$$, where $h_e(x)$ is the probability density, α^* is the gradient of the decay function and d_e is the offset.

The impact ionisation path length was measured with 20,000 events for each carrier at each voltage level

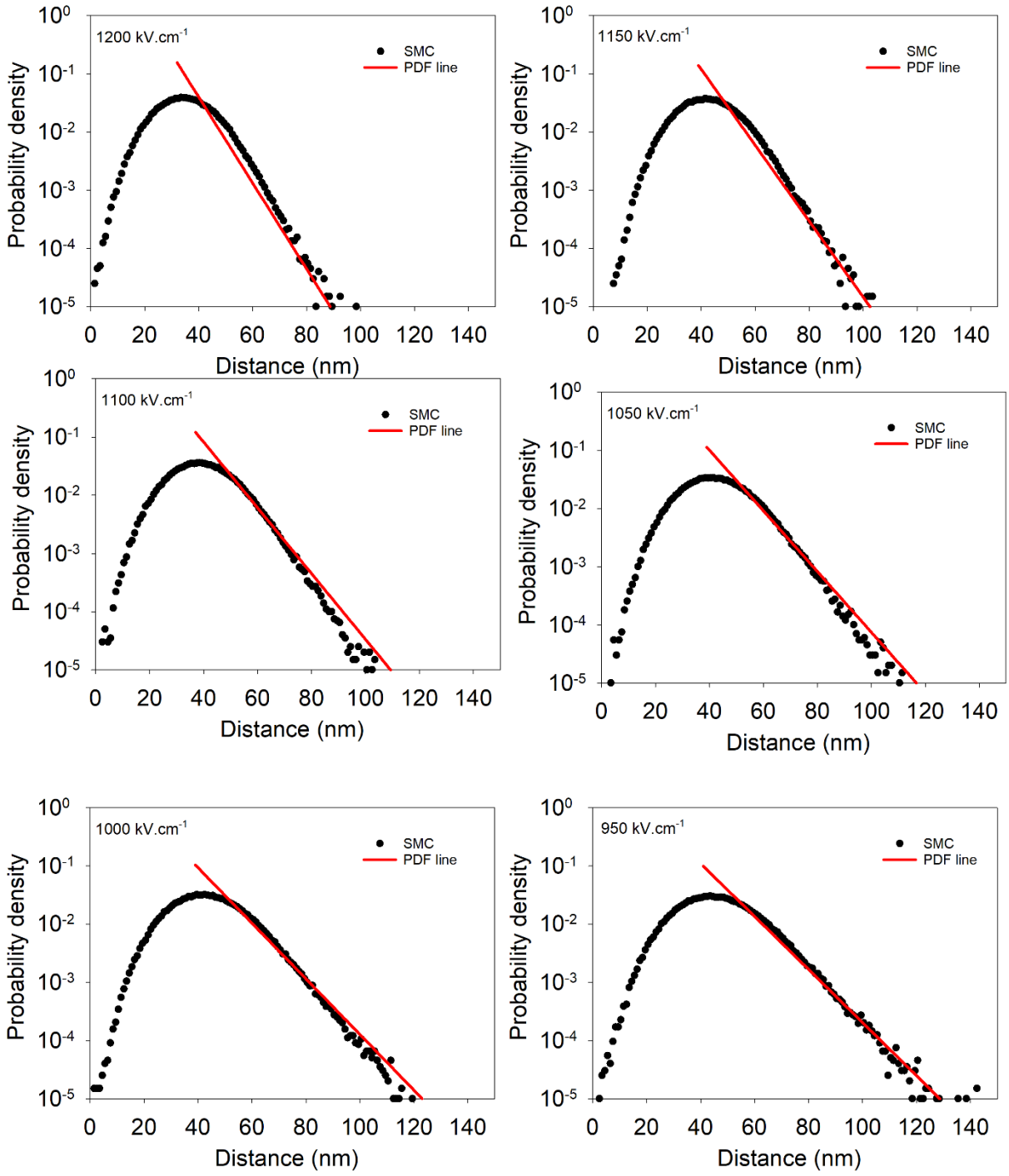

Fig. D.1 PDF fitting for Si using the SMC for electrons, between 950 and 1200 kV.cm^{-1}

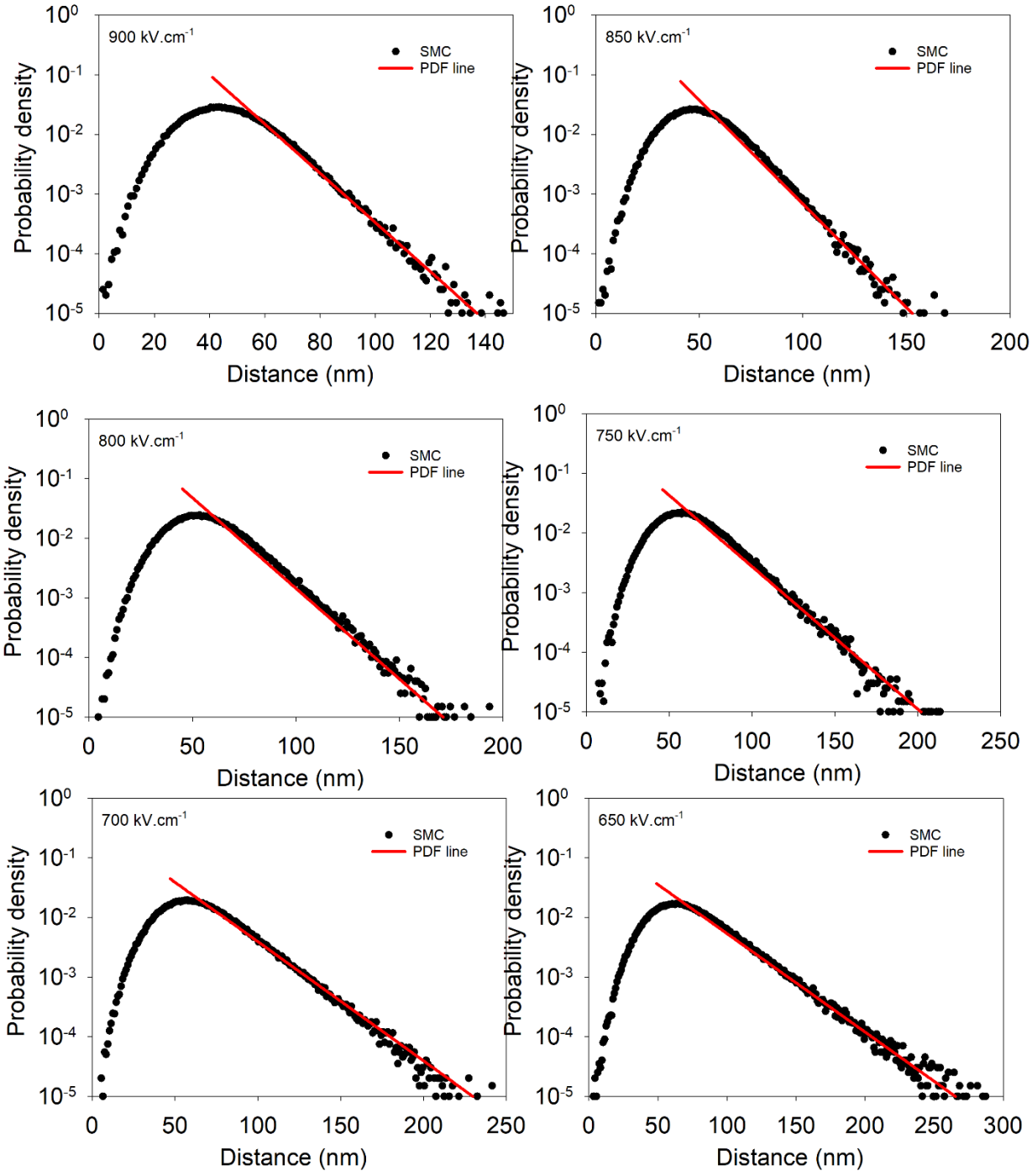

Fig. D.2 PDF fitting for Si using the SMC for electrons, between 650 and 900 kV.cm^{-1}

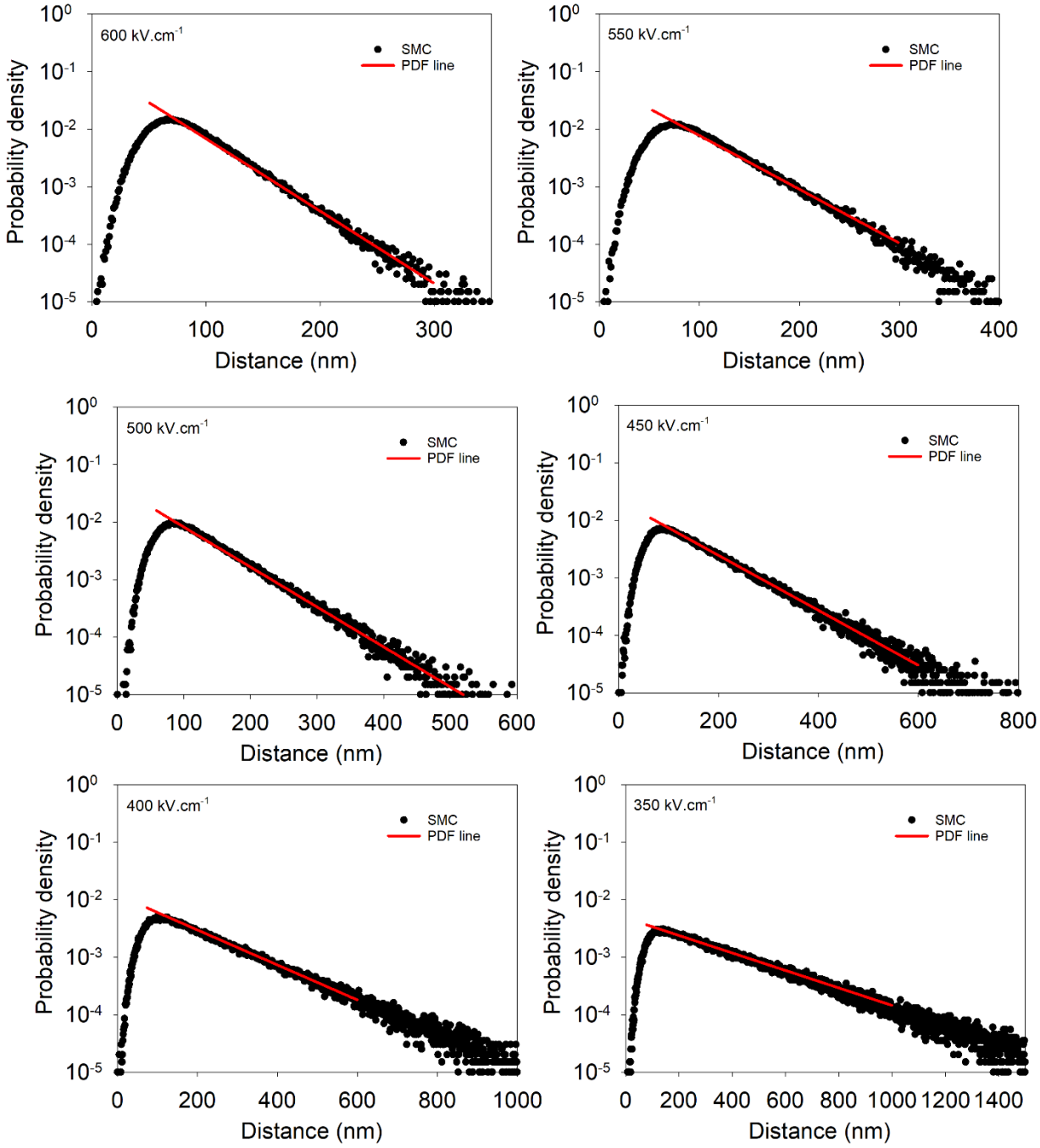

Fig. D.3 PDF fitting for Si using the SMC for electrons, between 350 and 600 kV.cm^{-1}

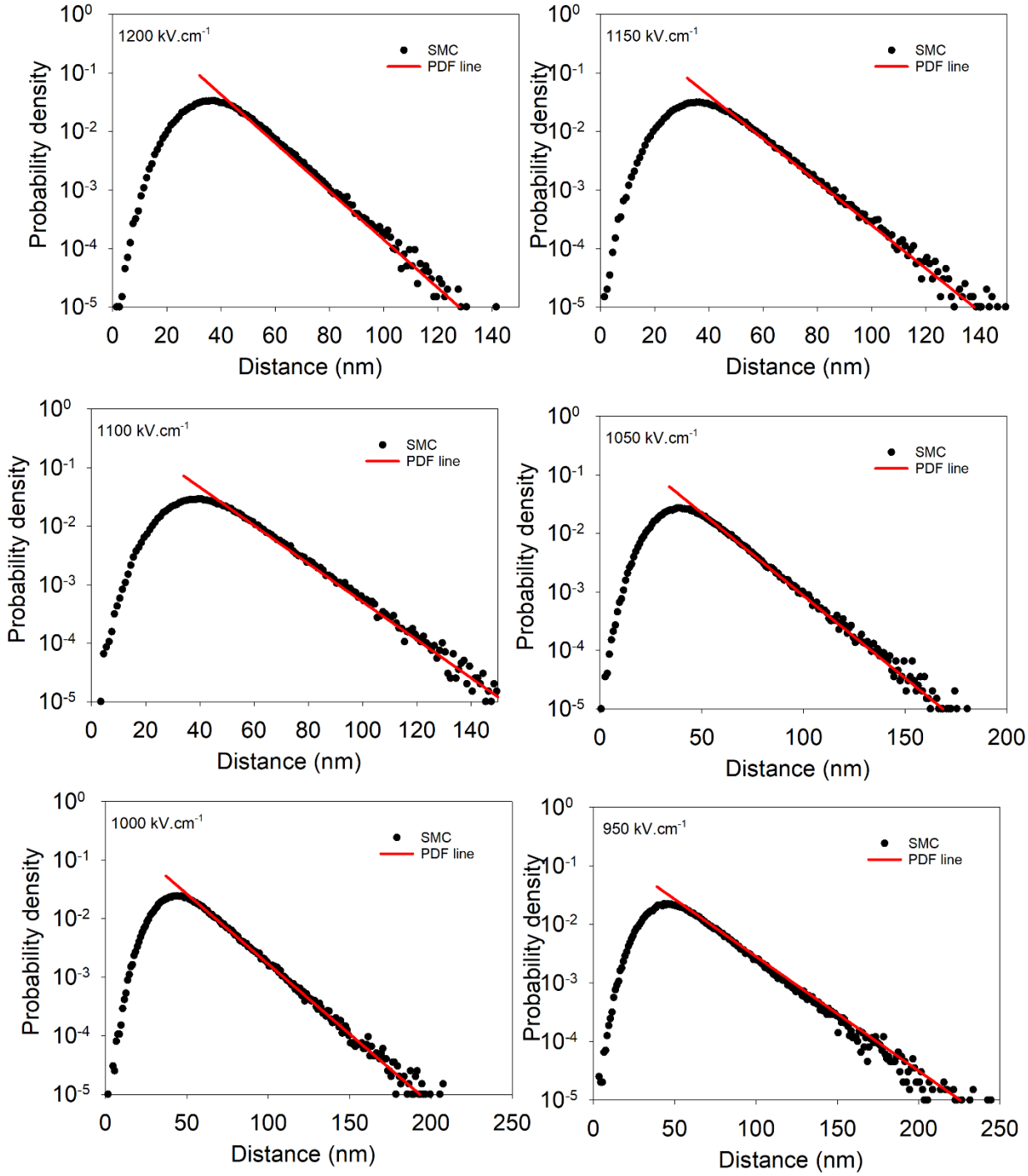

Fig. D.4 PDF fitting for Si using the SMC for holes, between 950 and 1200 kV.cm^{-1}

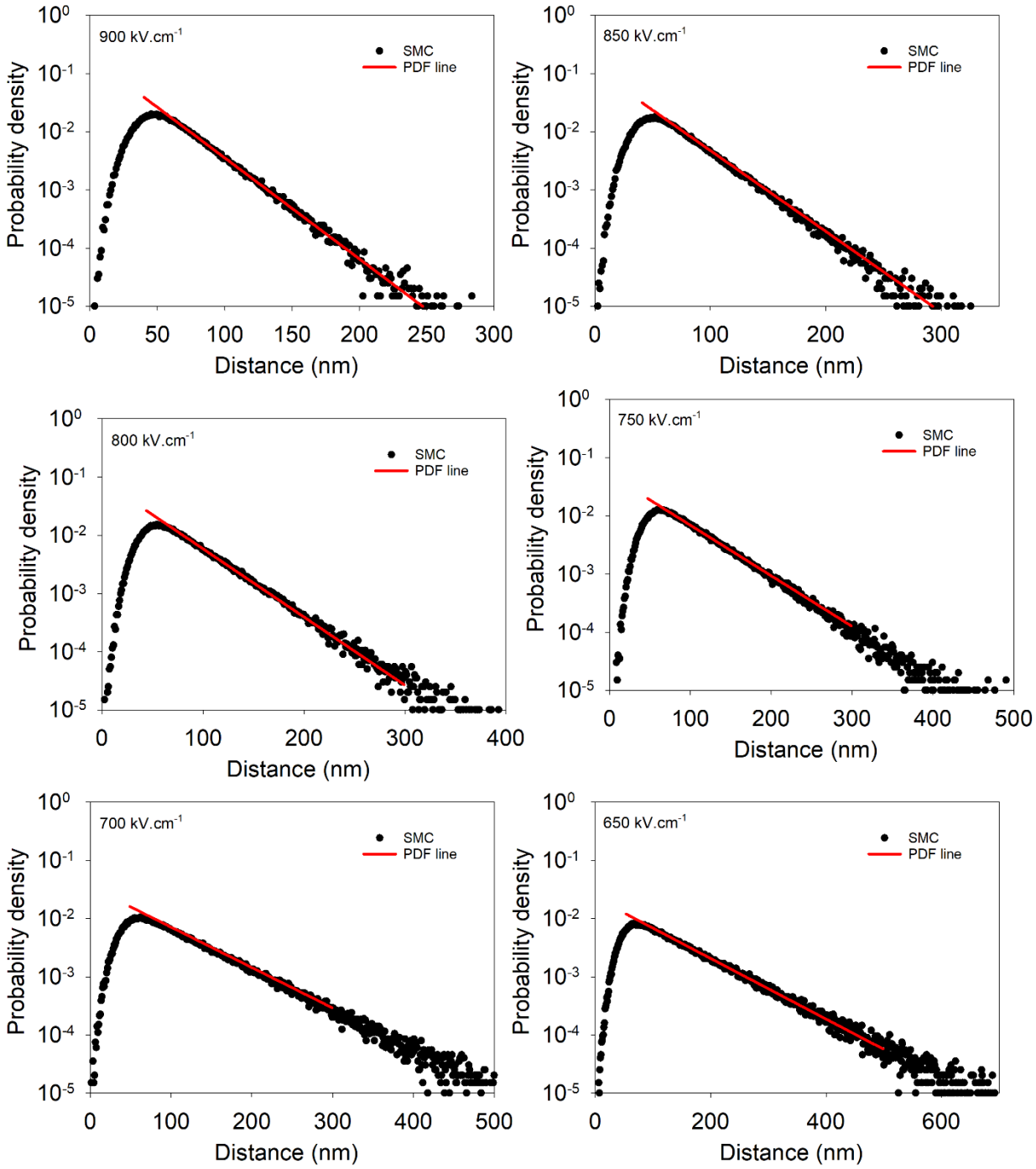

Fig. D.5 PDF fitting for Si using the SMC for electrons, between 650 and 900 kV.cm^{-1}

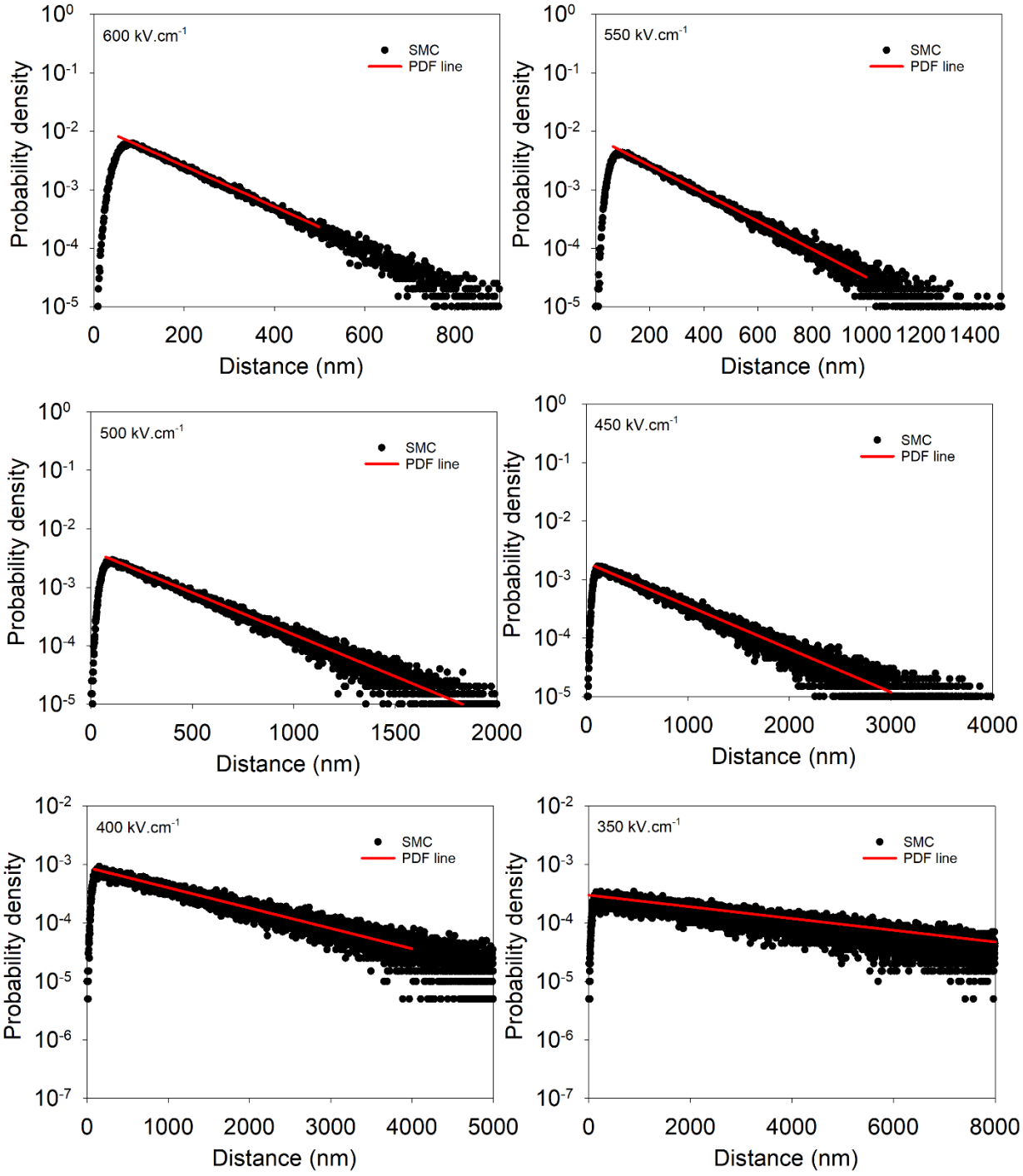

Fig. D.6 PDF fitting for Si using the SMC for electrons, between 350 and 600 kV.cm^{-1}

Appendix E.

$In_{0.53}Ga_{0.47}As$ PDF fitting

This appendix shows the complete PDF fitting for extracting effective impact ionisation coefficients for electrons and holes. The fitting used the hard deadspace approximation,

$$h_{e(h)}(x) = \begin{cases} 0, & x \leq d_{e(h)} \\ \alpha^*(\beta^*)exp\left[-\alpha^*(\beta^*)\left(x - d_{e(h)}\right)\right] & x > d_{e(h)}. \end{cases}$$ Where $h_e(x)$ is the probability density, α^* is the gradient of the decay function, and d_e is the offset.

The impact ionisation path length was measured with 20,000 events for each carrier at each voltage level

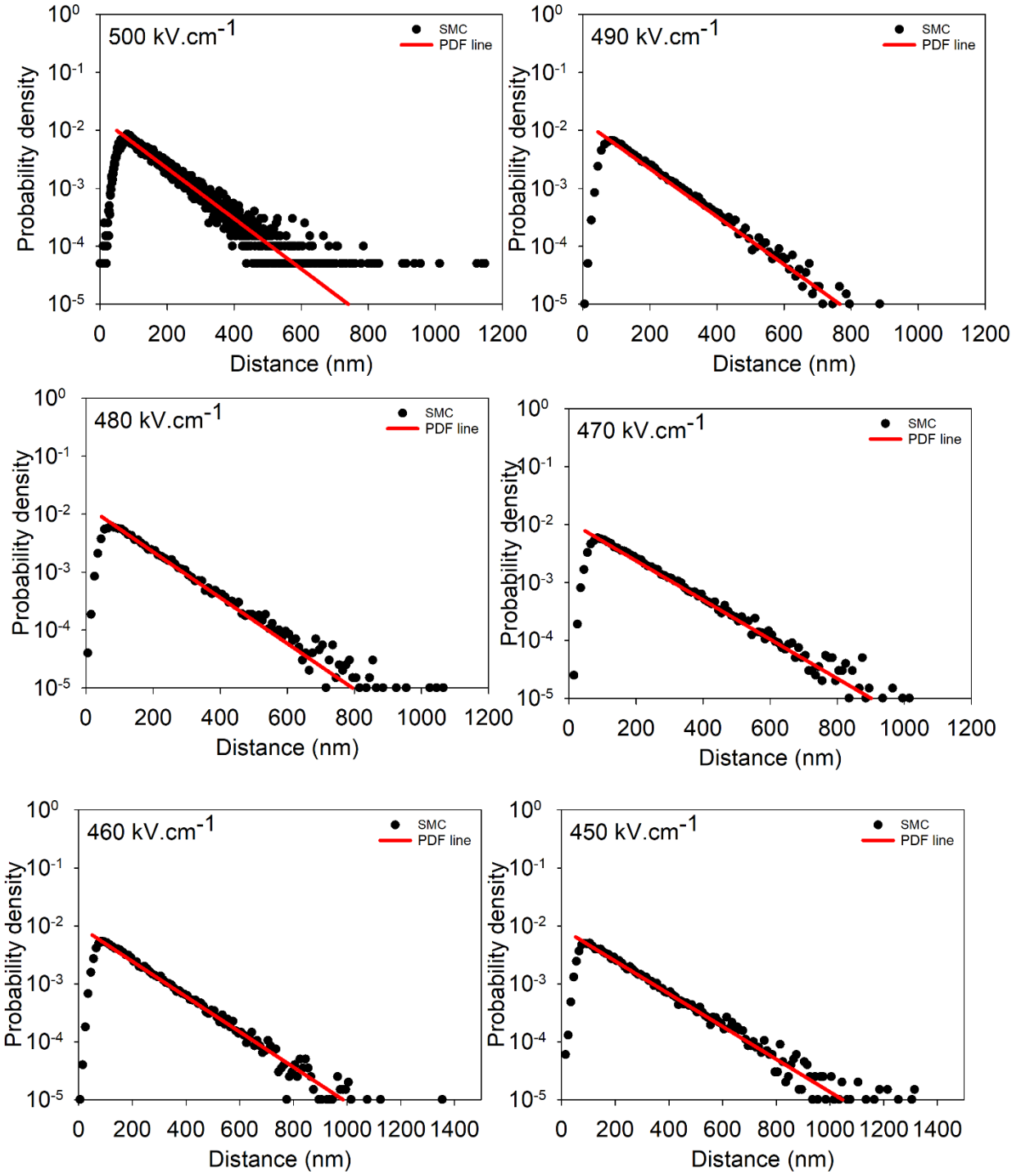

Fig. E.1 PDF fitting for InGaAs using the SMC for electrons, between 450 and 500 kV.cm^{-1}

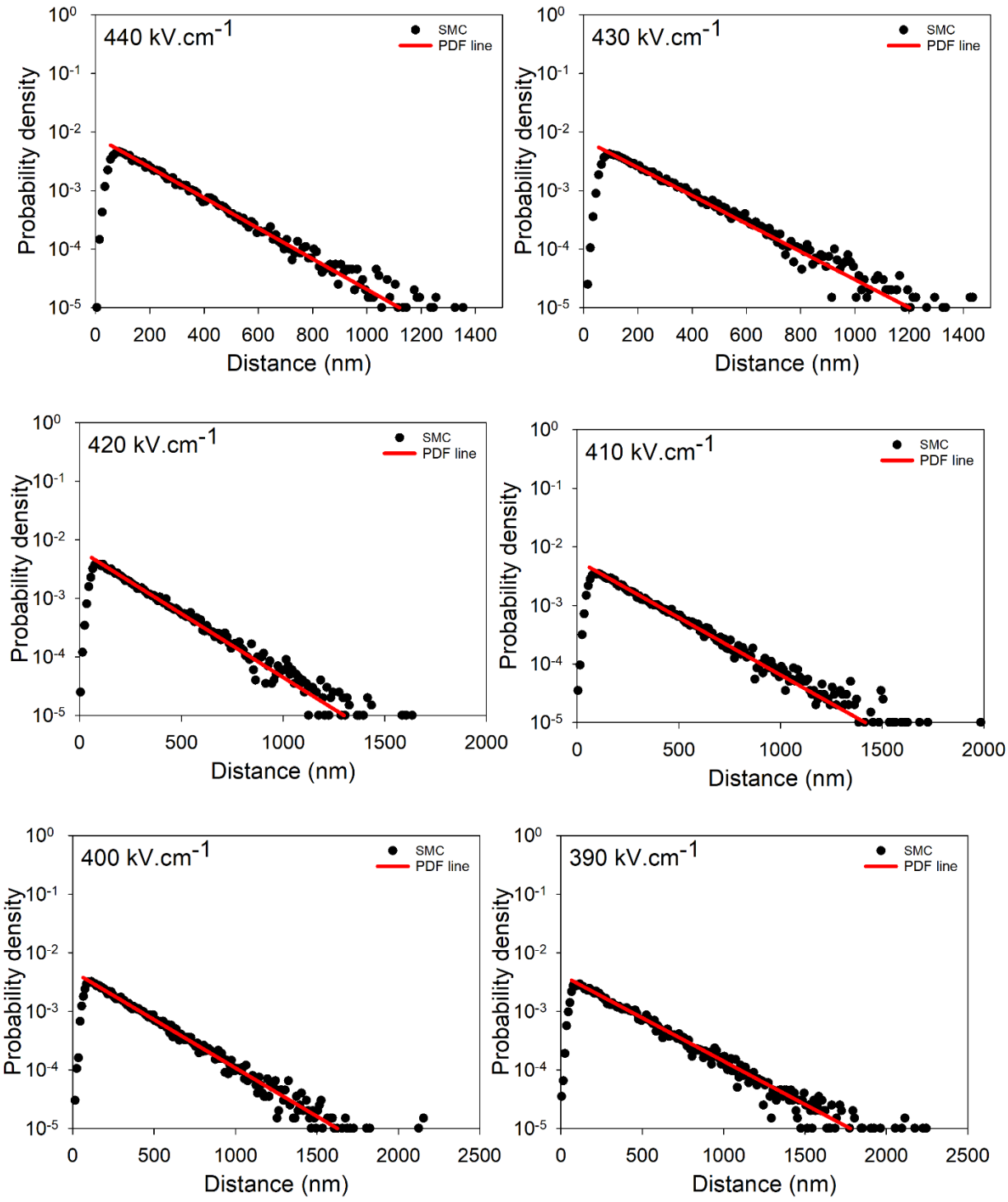

Fig. E.2 PDF fitting for InGaAs using the SMC for electrons, between 390 and 440 kV.cm^{-1}

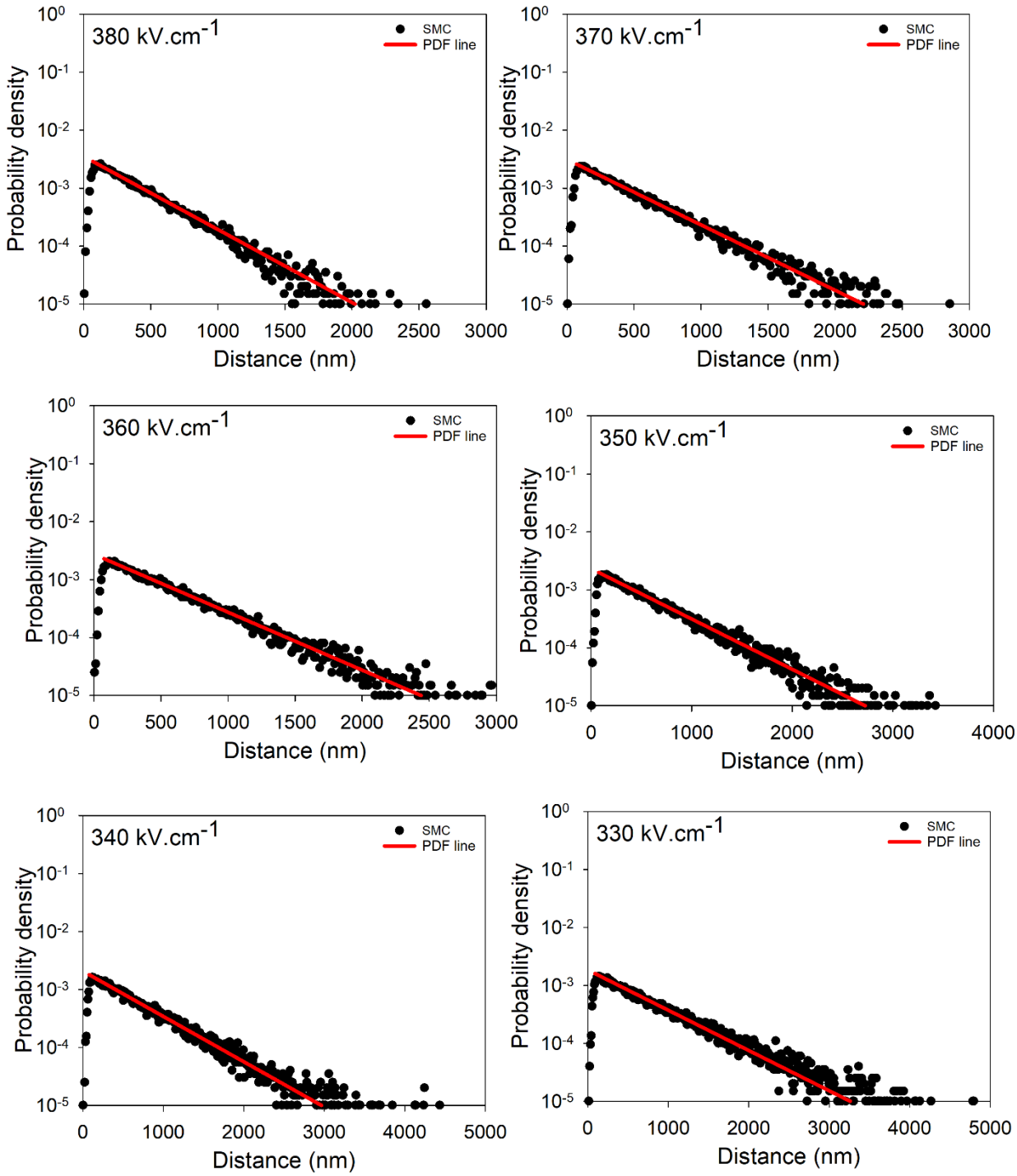

Fig. E.3 PDF fitting for InGaAs using the SMC for electrons, between 330 and 380 kV.cm^{-1}

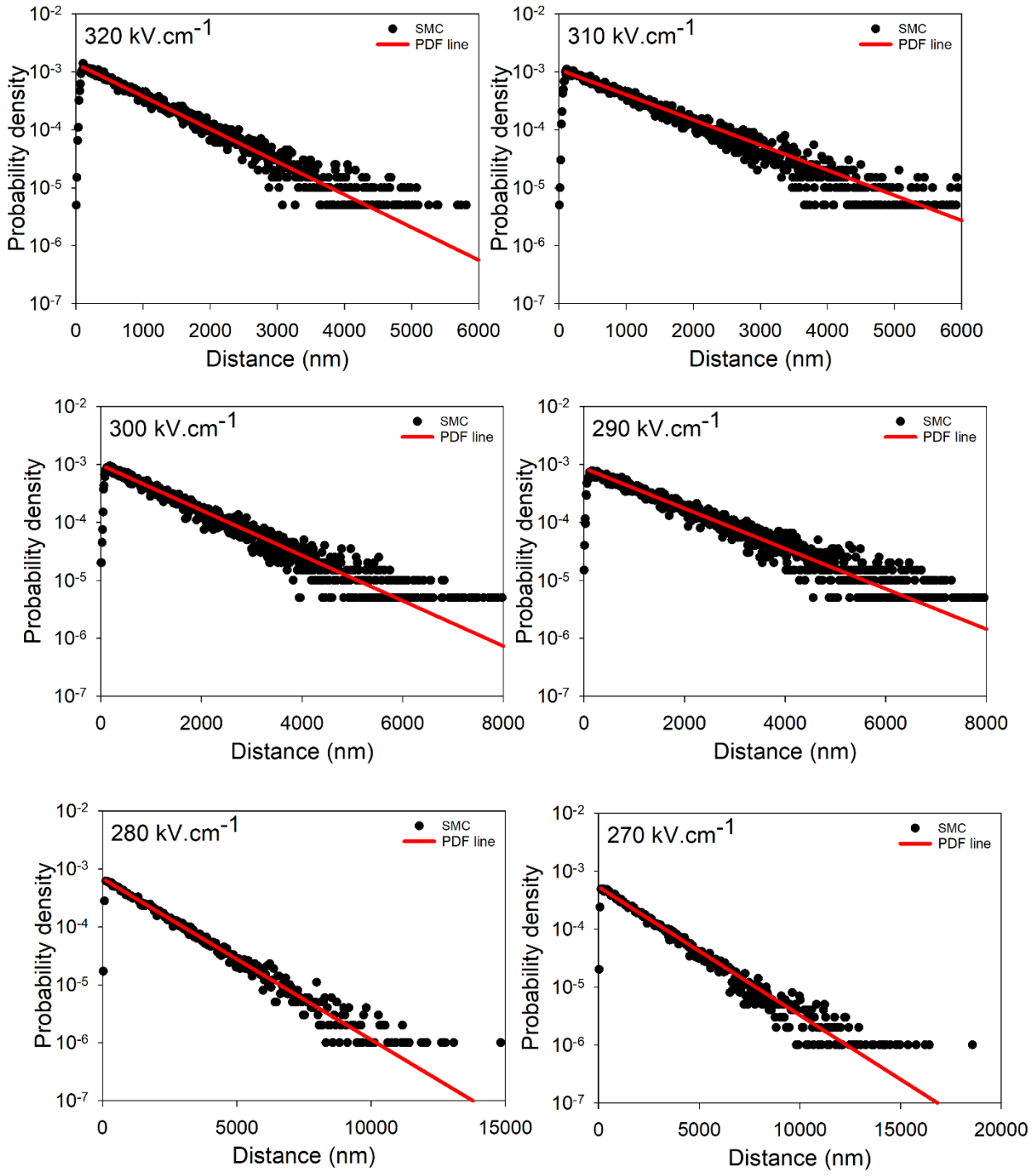

Fig. E.4 PDF fitting for InGaAs using the SMC for electrons, between 270 and 320 kV.cm^{-1}

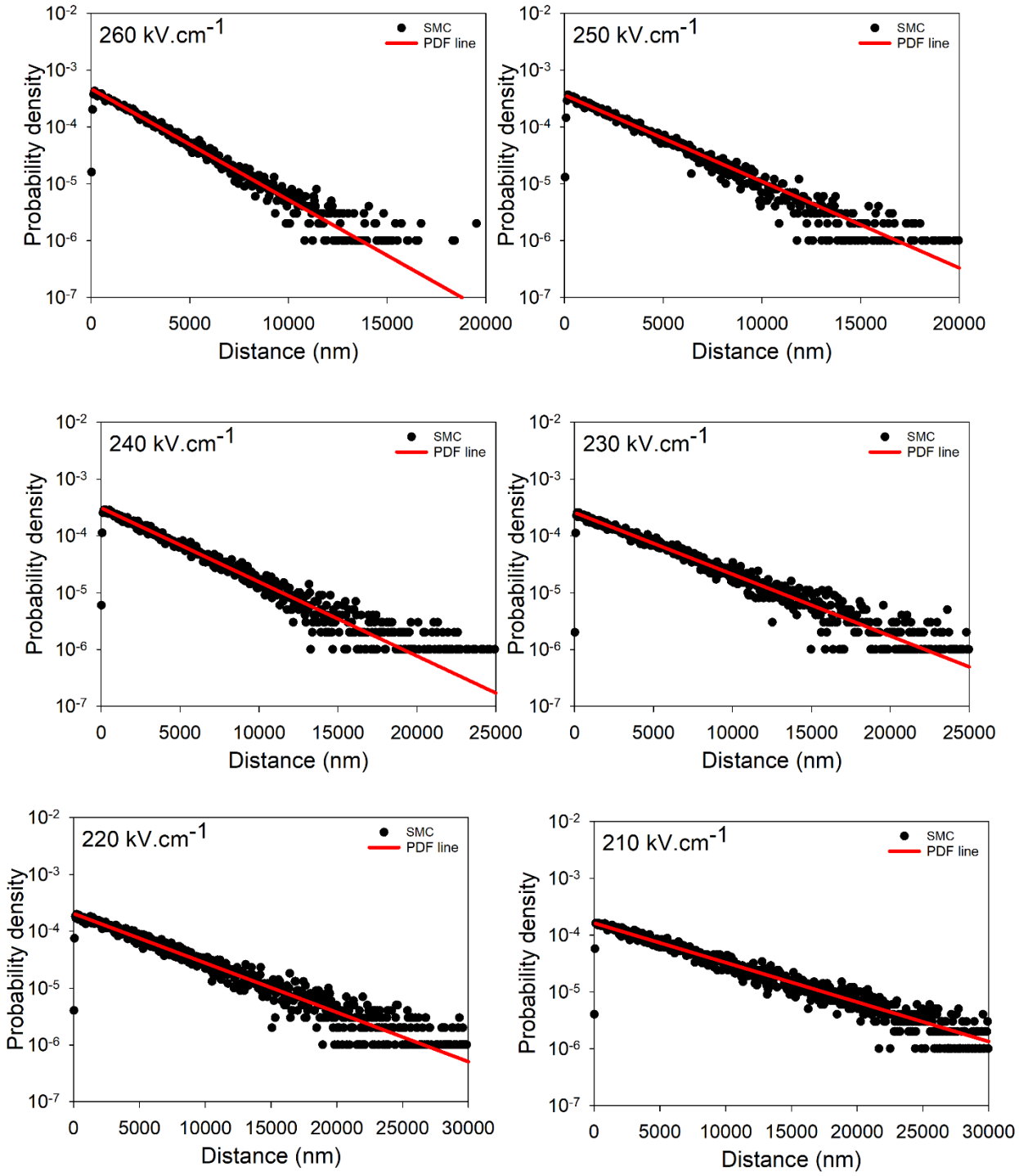

Fig. E.5 PDF fitting for InGaAs using the SMC for electrons, between 210 and 260 kV.cm^{-1}

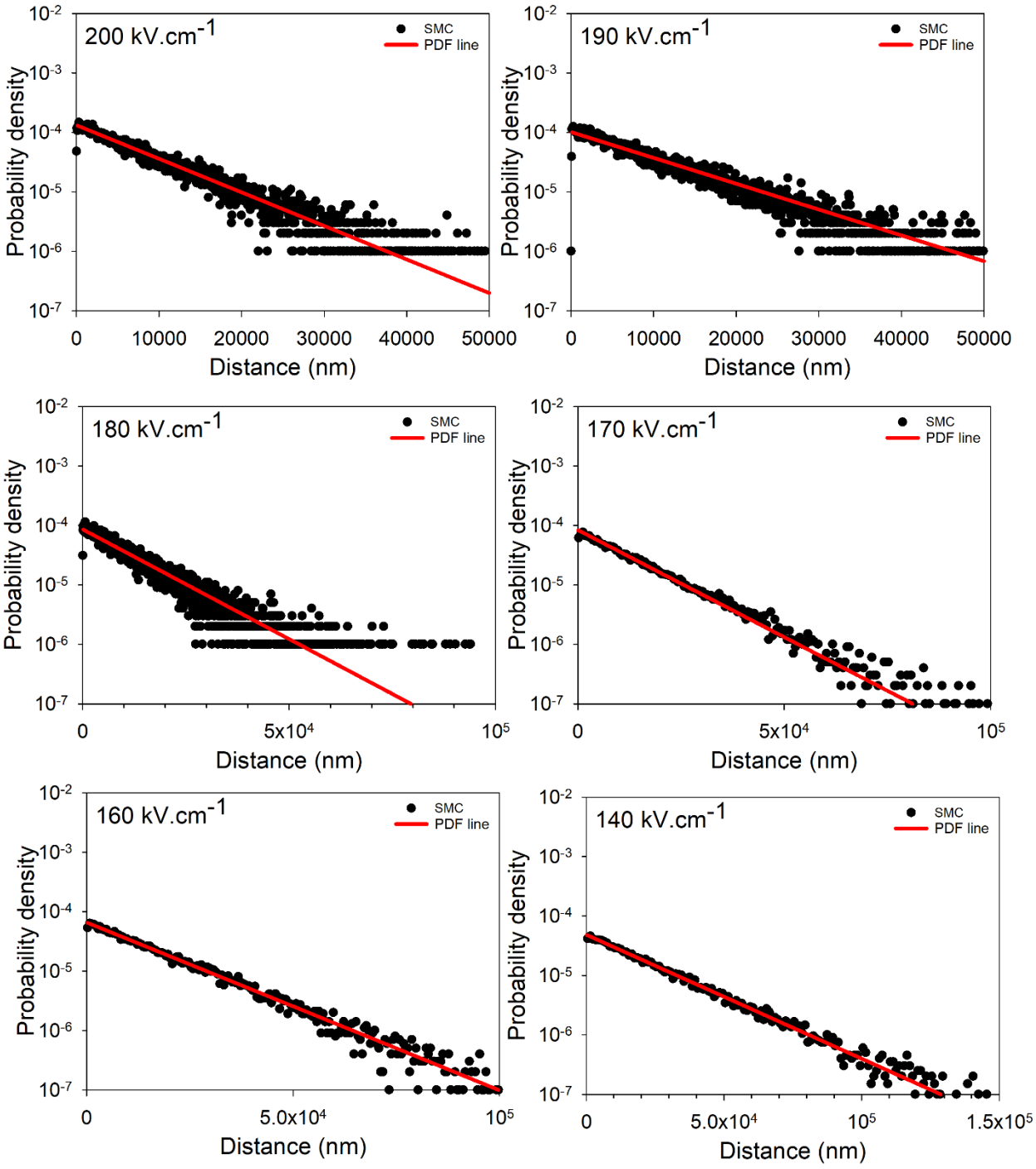

Fig. E.6 PDF fitting for InGaAs using the SMC for electrons, between 140 and 200 kV.cm^{-1}

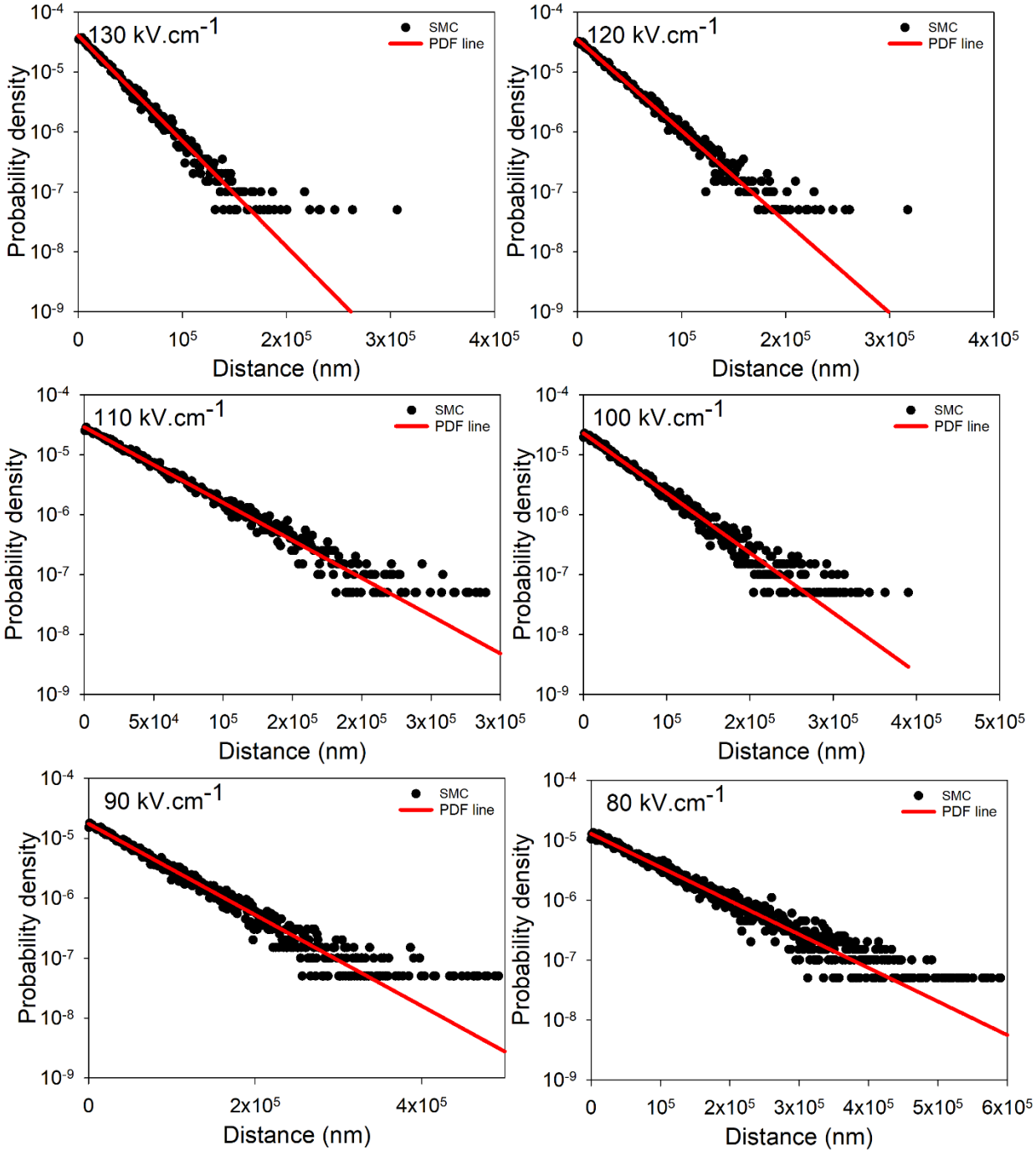

Fig. E.7 PDF fitting for InGaAs using the SMC for electrons, between 80 and 130 kV.cm^{-1}

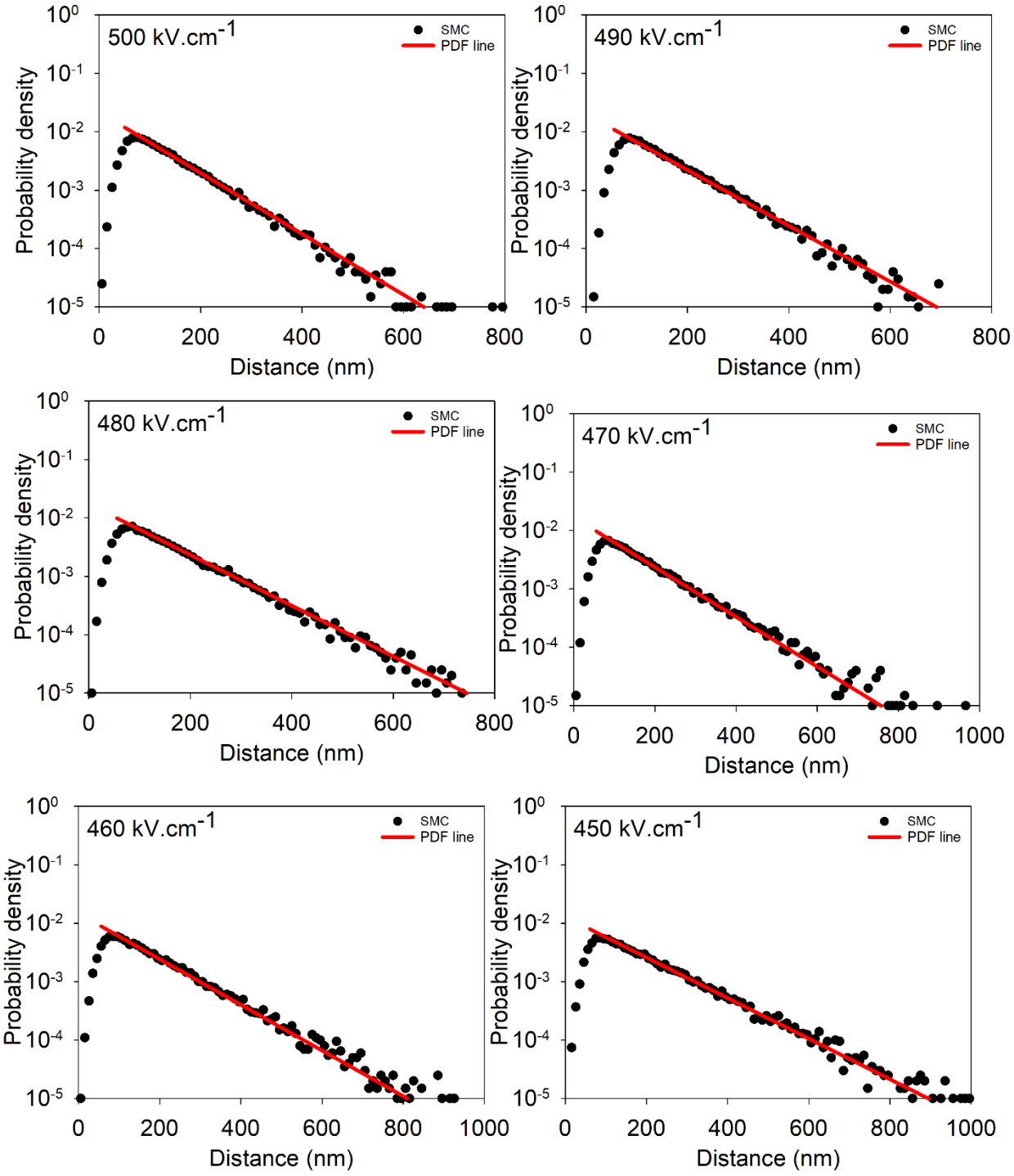

Fig. E.8 PDF fitting for InGaAs using the SMC for holes, between 450 and 500 kV.cm^{-1}

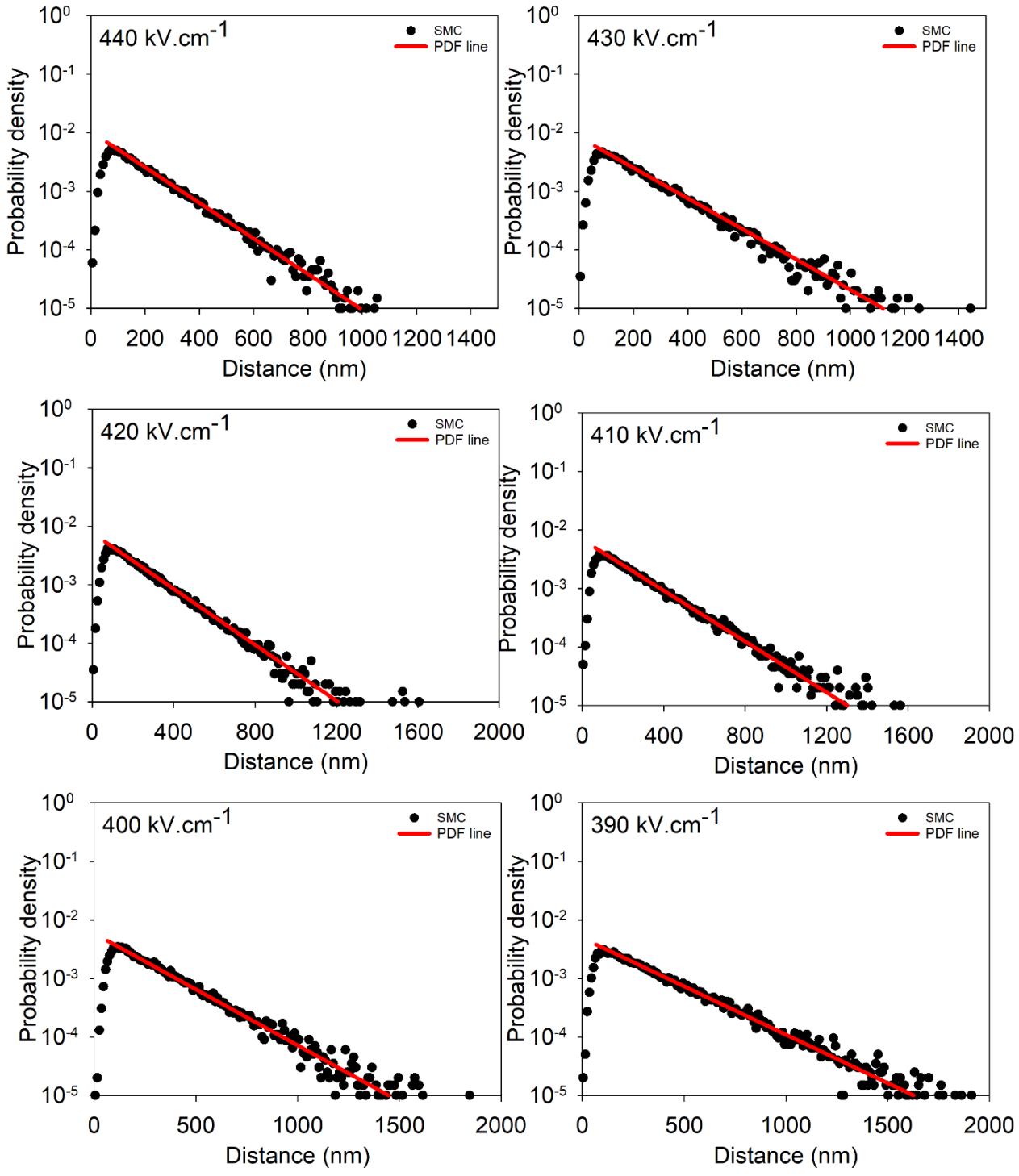

Fig. E.9 PDF fitting for InGaAs using the SMC for holes, between 390 and 440 kV.cm^{-1}

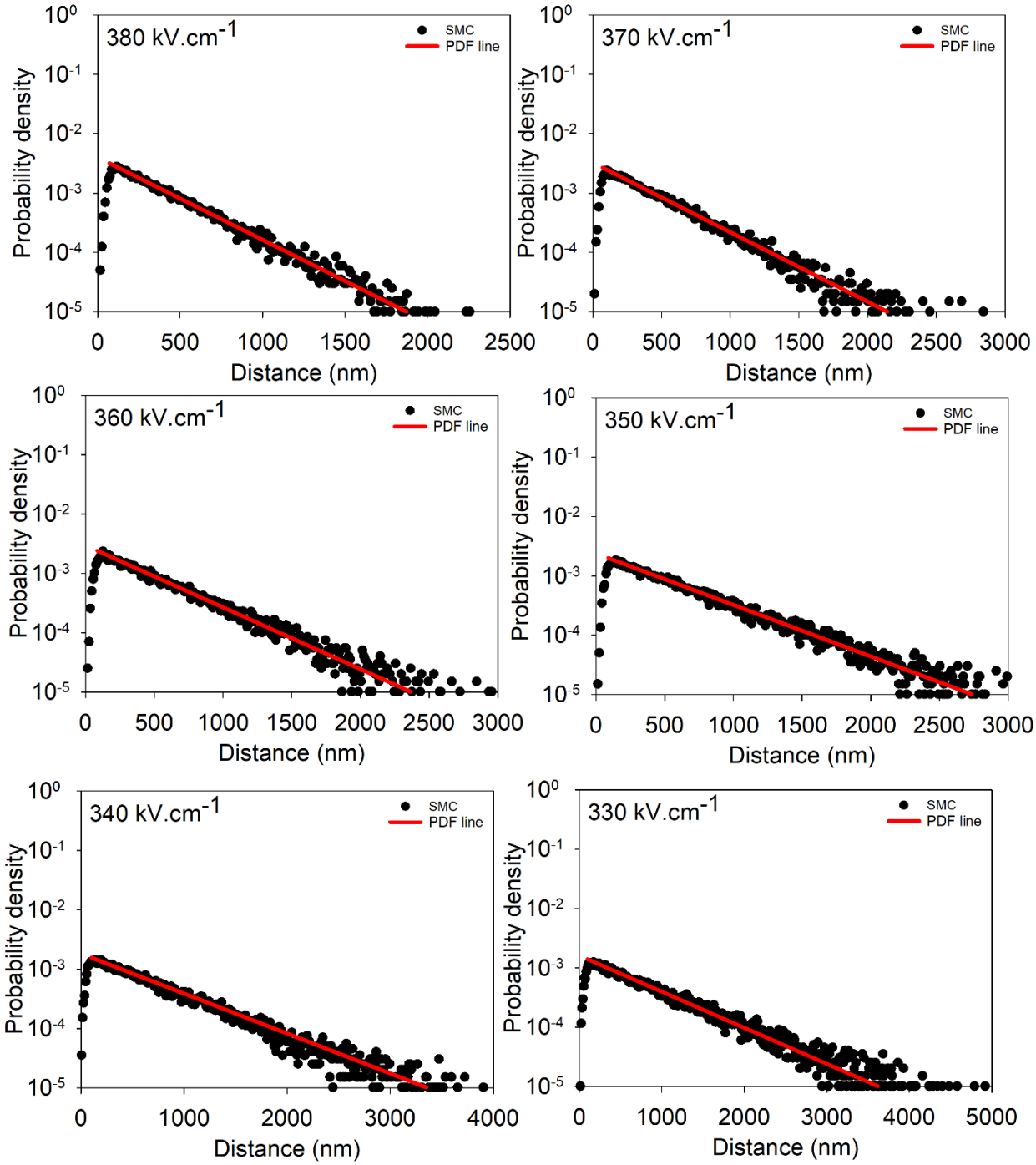

Fig. E.10 PDF fitting for InGaAs using the SMC for holes, between 330 and 380 kV.cm^{-1}

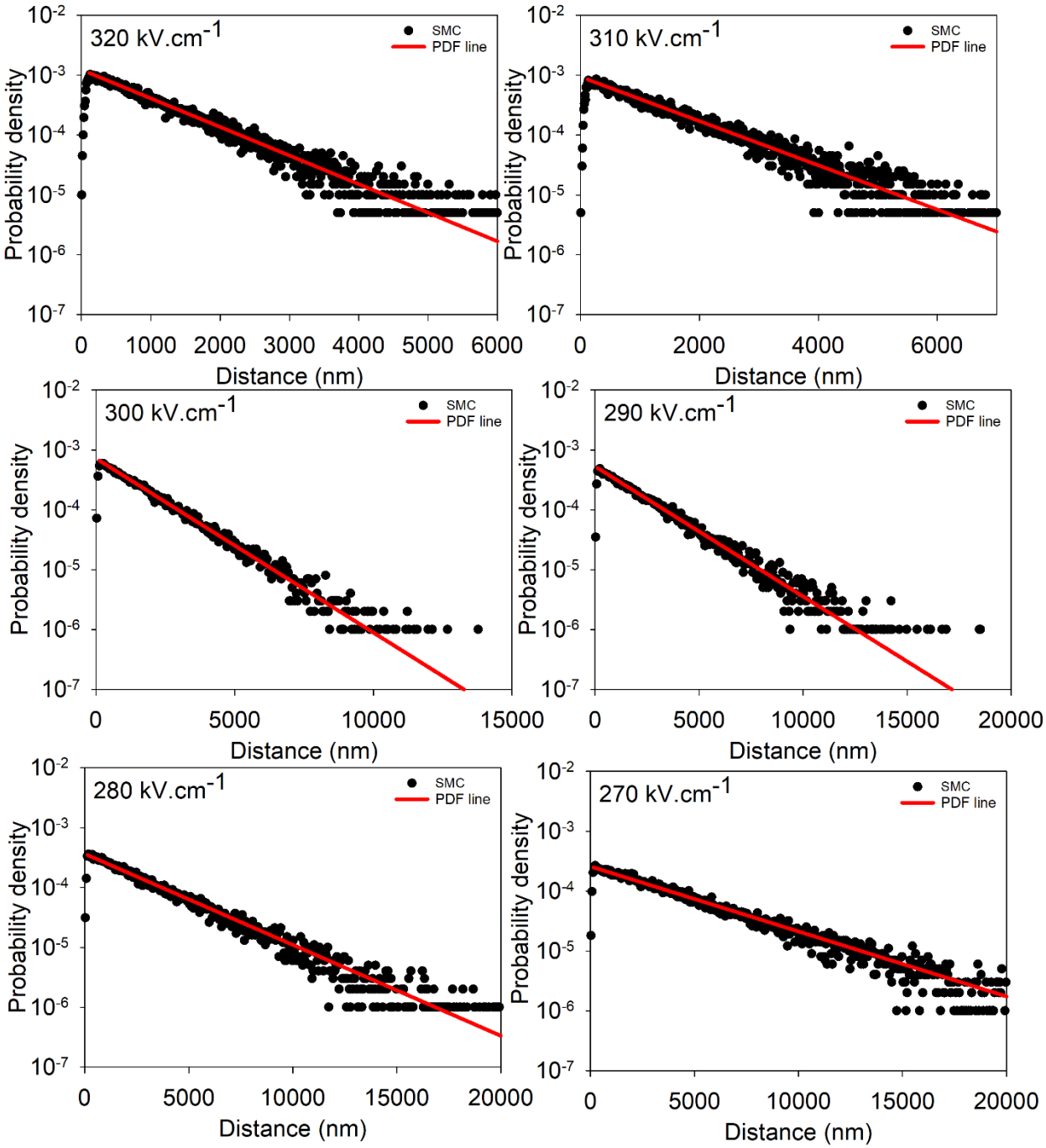

Fig. E.11 PDF fitting for InGaAs using the SMC for holes, between 270 and 320 kV.cm^{-1}

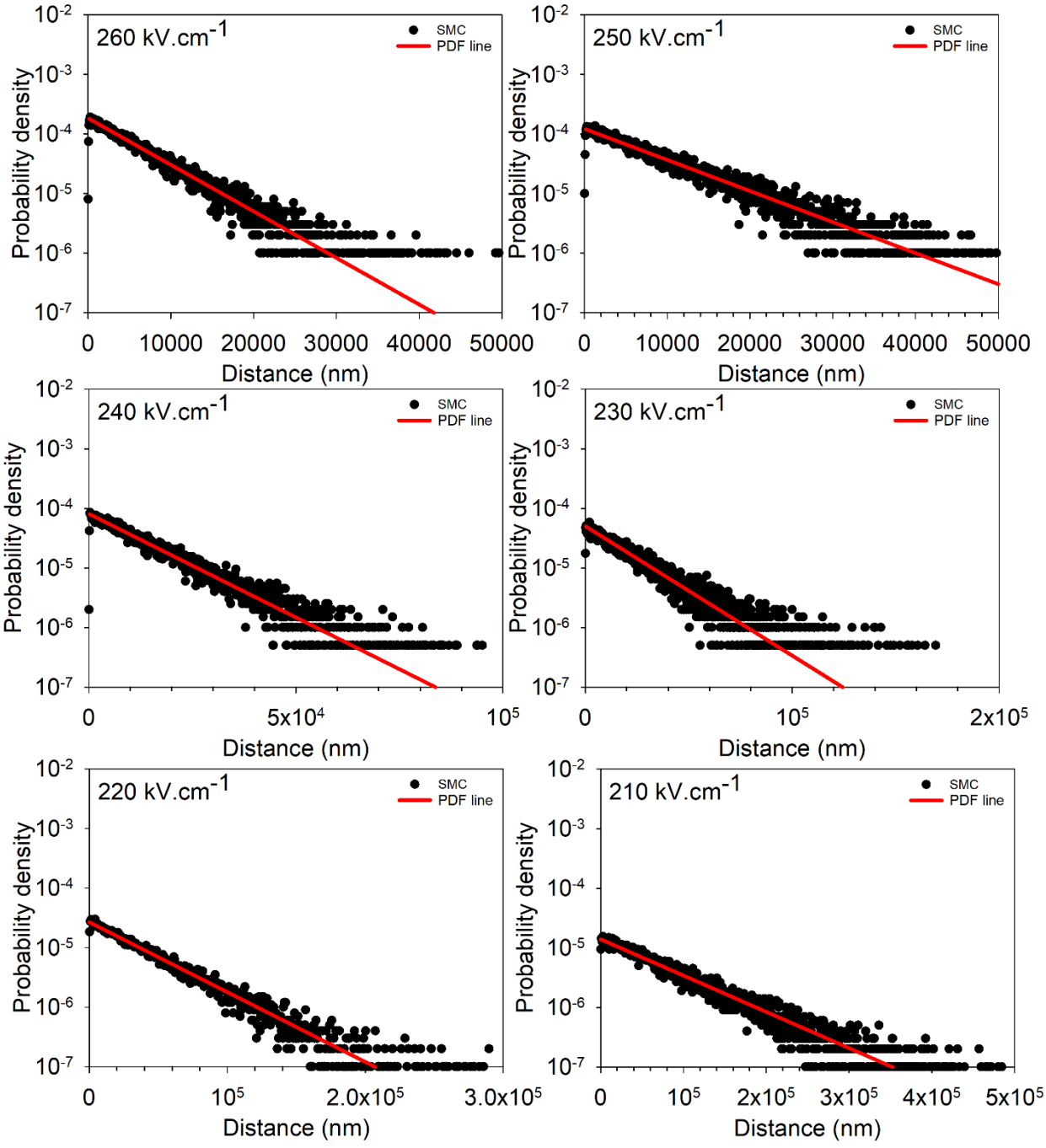

Fig. E.12 PDF fitting for InGaAs using the SMC for holes, between 210 and 260 kV.cm^{-1}

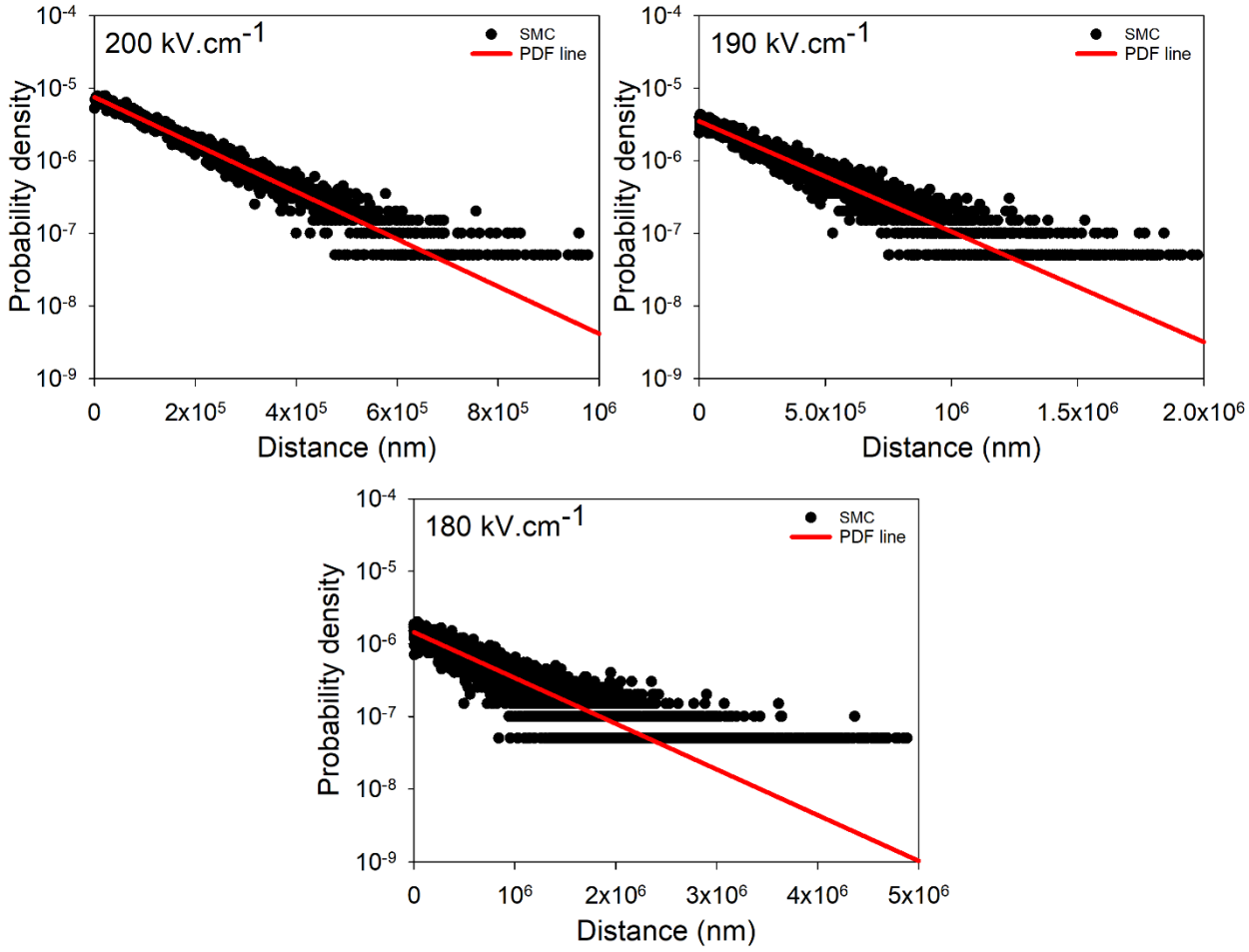

Fig. E.13 PDF fitting for InGaAs using the SMC for holes, between 180 and 200 kV.cm^{-1}

Appendix F.

Geiger-mode APD Simulation using the RPL Model

F.1) Simulation runtime comparison between the SMC and RPL models

A comparison of simulation runtimes, Table F.1, the simulation runtime between the SMC and RPL model for comparable inputs is shown. In these simulations, two InP p-i-n diodes with 100 and 1500 nm i-region widths were modelled using the SMC and the RPL models. Identical conditions were used: the number of trials per voltage point (500), voltage range, voltage step, breakdown condition (100 µA) and simulation cut-off time. A trial count of 500 is used for demonstration purposes for the simulation time difference. For Monte Carlo-based models like the SMC and RPL models, a trial count of 500 is not enough to yield a statistically significant result for $P_b(V)$, t_b or jitter.

Table F.1. Simulation runtime difference between the SMC and RPL model for a narrow and thick pin APD

W	Voltage range (V)	Voltage step (V)	SMC	RPL	Time difference
100 nm	8-12	0.5	45 mins	< 1 min	× 45
1500 nm	55-70	1	10 days, 3 hrs, 53 mins	17 mins	× 861

F.2) Overdrive effect on simulation results and runtime

A comparison of the time to breakdown (t_b) for three overdrive factor (M_{od}) conditions is presented in Fig. F.1. As the overdrive factor increases, the time to breakdown decreases. As the overdrive factor increased above 1.5, it was found the decrease seen in t_b started to become negligible. The simulation runtime difference can be seen in Table F.2. The control (no M_{od}) is the same as M_{od} = 1. This is a control to ensure the implementation of M_{od} was not having an unintended effect on $P_b(V)$ and t_b. The current array is checked at the end of each carrier trial. However, to avoid unnecessary checks slowing down the simulation, a flag is raised if the value exceeds $I_{br} \times M_{od}$ while the instantaneous current array has populated. The control represents the least efficient and slowest implementation of the RPL model.

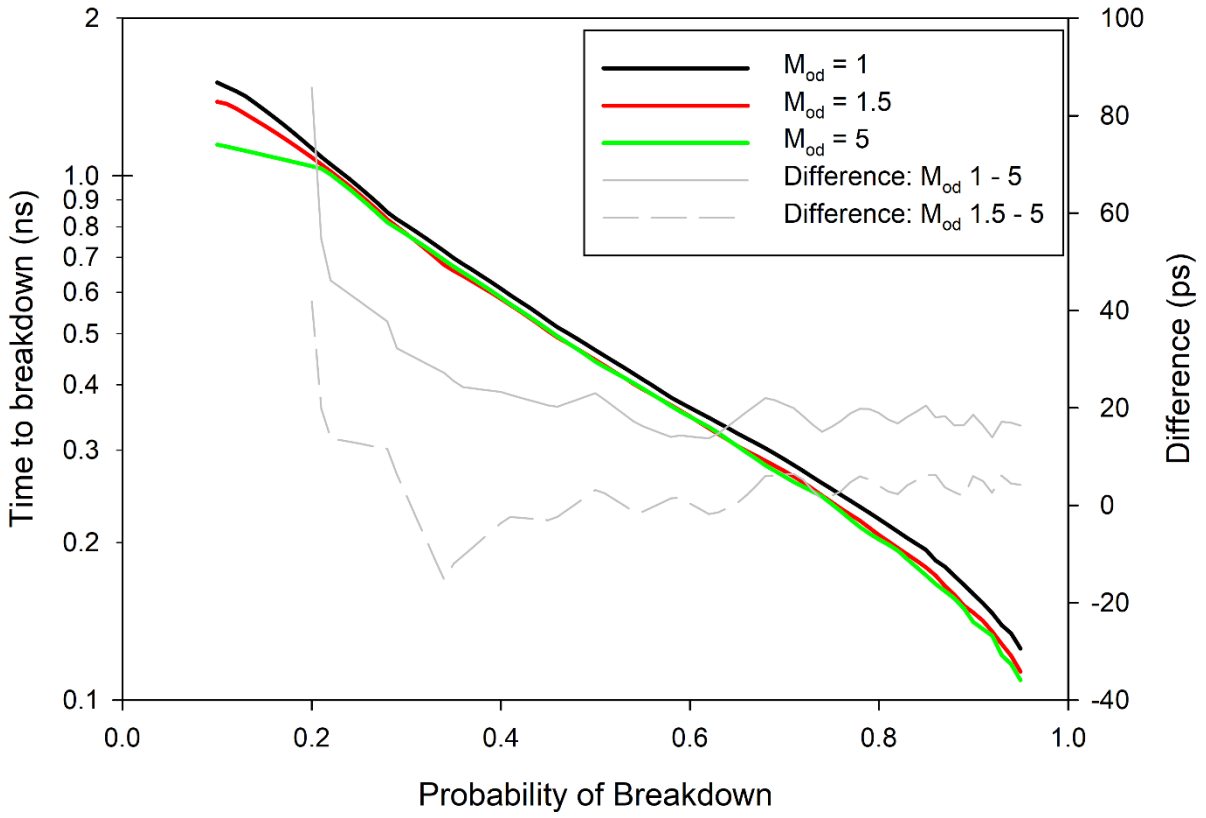

Fig. F.1 Time to breakdown for M_{od} = 1, 1.5, and 5. The difference in t_b between M_{od} 1-5 and 1.5-5 is presented in the grey lines

Table F.2. RPL runtime for 1.5 um AlGaAsSb pin, with 20k trials. for a voltage range between 76 and 80 V in 0.1 V steps

M_{od}	Model runtime	Simulation Δt from M_{od} = 1
Control (no M_{od})	155 hrs 53 mins	140 hrs 59 mins
1	14 hrs 15 mins	-
1.2	16 hrs 45 mins	2 hrs 30 mins
1.5	19 hrs 16 mins	5 hrs 1 mins
2	22 hrs 55 mins	8 hrs 40 mins
3	28 hrs 24 mins	14 hrs 9 mins
4	34 hrs 19 mins	20 hrs 4 mins
5	39 hrs 9 mins	24 hrs 54 mins

F.3) Simulation comparison check

In this work, the RPL model simulation results were validated against those published by Ahmed *et al.* [1] to ensure the comparison with AlAsSb to AlGaAsSb was valid. These checks can be seen in Fig. F.2. Where the ionisation coefficient used is the same as those quoted by Ahmed *et al.* InP [2], InAlAs [3], Si [4],

and AlAsSb [5]. All devices modelled used w = 1500 nm and electron initialisation except for InP where hole initialisation was used. Good agreement was achieved for all materials simulation

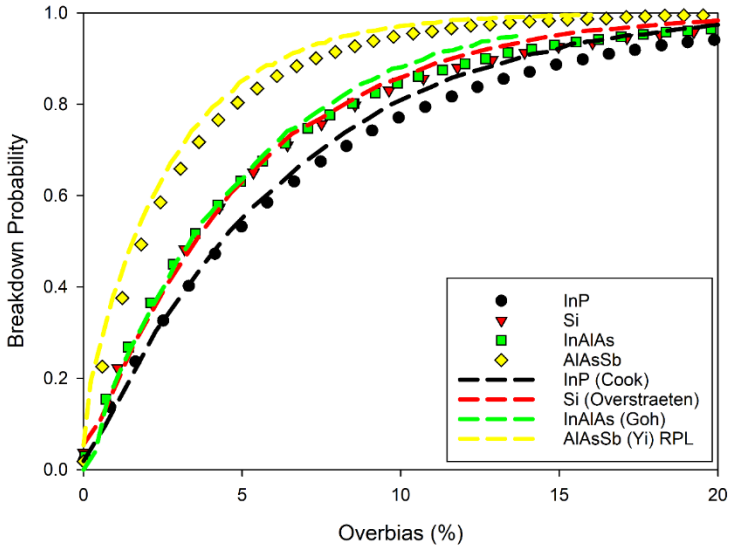

Fig. F.2 Comparison between results presented by Ahmed et al. (symbols) and those reproduced using the RPL model (lines)

F.4) References

[1] J. Ahmed *et al.*, 'Theoretical Analysis of $AlAs_{0.56}Sb_{0.44}$ Single Photon Avalanche Diodes With High Breakdown Probability', *IEEE J. Quantum Electron.*, vol. 57, no. 2, pp. 1–6, Apr. 2021, doi: 10.1109/JQE.2021.3058356.

[2] L. W. Cook, G. E. Bulman, and G. E. Stillman, 'Electron and hole impact ionisation coefficients in InP determined by photomultiplication measurements', *Appl. Phys. Lett.*, vol. 40, no. 7, pp. 589–591, Apr. 1982, doi: 10.1063/1.93190.

[3] Y. L. Goh *et al.*, 'Excess Avalanche Noise in $In_{0.52}Al_{0.48}As$', *IEEE J. Quantum Electron.*, vol. 43, no. 6, pp. 503–507, Jun. 2007, doi: 10.1109/JQE.2007.897900.

[4] R. Van Overstraeten and H. De Man, 'Measurement of the ionisation rates in diffused silicon p-n junctions', *Solid State Electron.*, vol. 13, no. 5, pp. 583–608, 1970.

[5] X. Yi *et al.*, 'Demonstration of large ionisation coefficient ratio in AlAs0.56Sb0.44 lattice matched to InP', *Sci. Rep.*, vol. 8, no. 1, p. 9107, Dec. 2018, doi: 10.1038/s41598-018-27507-w.

Appendix G.

$Al_{0.85}Ga_{0.15}As_{0.56}Sb_{0.44}$ tunnelling current fitting

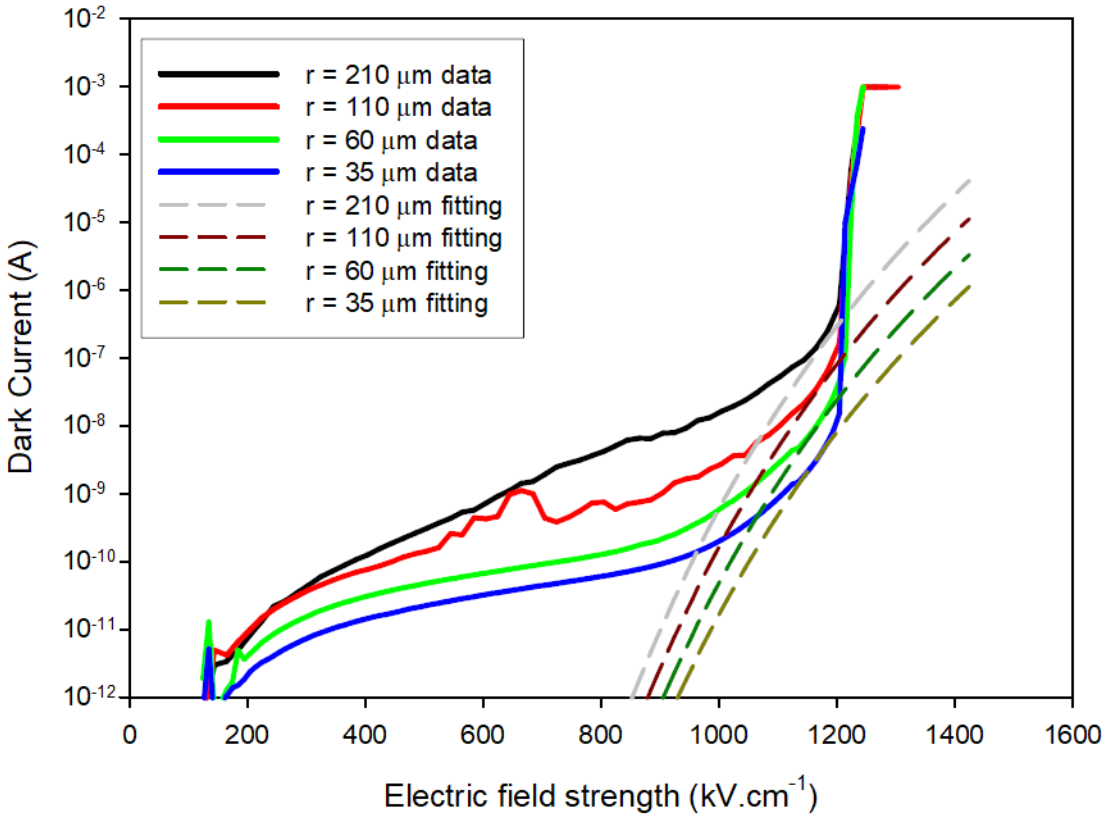

Fig. G.1. Dark current of 100 nm AlGaAsSb nip (solid)[1] and tunnelling current fitting using the fitting values in Table G.1

Table G.1. AlGaAsSb Tunnelling current fitting and equation (eq. G.1)

m_e*	0.076
E_g *(eV)*	1.56
σ_{tun}	1.8
V_{bi}	1.24
π	3.1416
h	6.6261×10^{-34}
m_0	9.11×10^{-31}
q	1.6×10^{-19}

$$I_{tun}(V) = \frac{(2m_e^*)^{0.5} q^3 \xi V A}{h^2 E_g^{0.5}} \exp\left(-\frac{2\pi\sigma_{tun} m^{*0.5}_e E_g^{1.5}}{qh\xi}\right), \quad \text{(G.1)}$$

Appendix H.

Simple Monte Carlo Model Parameter set reference

H.1) Simple Monte Carlo Model Parameter set references

Table H.1. Simple Monte Carlo Model Parameter set reference

	Si [1]		GaAs [2]		$Al_{0.3}Ga_{0.7}As$ [3]		$Al_{0.8}Ga_{0.2}As$ [3]		InGaP [4]		InP [5]		$In_{0.52}Al_{0.48}As$ [6]		$Al_{0.85}Ga_{0.15}As_{0.56}Sb_{0.44}$ [7]		$In_{0.53}Ga_{0.48}As$	
	e^-	h^+	e^-	h^+	e^-	h^+	e^-	h^+	e^-	h^+	e^-	h^+	e^-	h^+	e^-	h^+	e^-	h^+
Effective mass, m^*	0.6	0.9	0.5		0.64	0.60	0.69	0.71	0.7		0.62	0.63	0.2	0.4	0.6	0.65	0.15 0.35	0.65
Mean free path, λ, (Å)	98	68	50.4	47.6	43	41	39	34	55.7	58.2	41	42	37	34.5	50	33	240 60	55.3
Threshold energy, E_{th} (eV)	1.2	1.5	1.75		1.91		2.21		2.11		1.55		1.835		2		0.75 1.46	1.46
Impact ionisation rate prefactor, C_{ii} ($x10^{12}$)	2	4.4	40	30	13.0		16.5		8		3.5	8.8	21	14	60		0.006 4.2	4
Softness factor, γ	3.5		4		3		3		2.3		0.7		2	4	2		2 4	4
Alloy scattering prefactor ($x10^{68}$)	-		-		-		-		-		-		62.8	12.8	1	3	0.1 110	0.5
Phonon energy, $\hbar\omega$, (meV)	63		29		35		31		37		42		27		44		33	
Max Energy (eV)	6		8.75		9		9		6		6		12		9		4.5	
Built in voltage, (V)	1		1.2		1.2		1.2		1.8		1.2		1.2		1.24		13.6	
Relative permittivity, ε_r	11.9		12.9		12.3		10.6		11.8		12.5		12.44		11.41		0.7	

$Al_xGa_{1-x}As$ for x = 0,0.15,0.30,0.60, and 0.90 SMC model parameter sets were validated by Plimmer [8]. However, the scattering rate equation inputs used in this work are not compatible with the SMC model [9] and require modification and revalidation.

H.2) References

[1] X. Zhou, J. S. Ng, and C. H. Tan, 'A simple Monte Carlo model for prediction of avalanche multiplication process in Silicon', *J. Instrum.*, vol. 7, no. 08, p. P08006, 2012, doi: 10.1088/1748-0221/7/08/P08006.

[2] S. A. Plimmer, J. P. R. David, D. S. Ong, and K. F. Li, 'A simple model for avalanche multiplication including deadspace effects', *IEEE Trans. Electron Devices*, vol. 46, no. 4, pp. 769–775, Apr. 1999, doi: 10.1109/16.753712.

[3] C. K. Chia and G. K. Dalapati, 'Monte Carlo Simulation of Hot Carrier Transport in Heterogeneous Ge/Al_xGa_{1-x} As (0<x<0.8) Multilayer Avalanche Photodiodes', *IEEE Trans. Electron Devices*, vol. 60, no. 10, pp. 3435–3441, Oct. 2013, doi: 10.1109/TED.2013.2275970.

[4] C. H. Tan, R. Ghin, J. P. R. David, G. J. Rees, and M. Hopkinson, 'The effect of dead space on gain and excess noise in In $_{0.48}$ Ga $_{0.52}$ P p in diodes', *Semicond. Sci. Technol.*, vol. 18, no. 8, pp. 803–806, Aug. 2003, doi: 10.1088/0268-1242/18/8/314.

[5] J. D. Petticrew, S. J. Dimler, C. H. Tan, and J. S. Ng, 'Modeling Temperature-Dependent Avalanche Characteristics of InP', *J. Light. Technol.*, vol. 38, no. 4, pp. 961–965, Feb. 2020, doi: 10.1109/JLT.2019.2948072.

[6] S. C. Liew Tat Mun, C. H. Tan, Y. L. Goh, A. R. J. Marshall, and J. P. R. David, 'Modeling of avalanche multiplication and excess noise factor in $In_{0.52}Al_{0.48}As$ avalanche photodiodes using a simple Monte Carlo model', *J Appl Phys*, vol. 104, p. 7, 2008, doi: 10.1063/1.2952003.

[7] J. D. Taylor-Mew, J. D. Petticrew, C. H. Tan, and J. S. Ng, 'Simulation of $Al_{0.85}Ga_{0.15}As_{0.56}Sb_{0.44}$ avalanche photodiodes', *Opt. Express*, vol. 30, no. 11, p. 17946, May 2022, doi: 10.1364/OE.458922.

[8] S. A. Plimmer, 'Avalanche multiplication in $Al_xGa_{1-x}As$', Ph.D dissertation, University of Sheffield, Department of Electronic and Electrical Engineering, 1997.

[9] J. D. Petticrew, S. J. Dimler, and J. S. Ng, 'Simple Monte Carlo Simulator for Modelling Linear Mode and Geiger Mode Avalanche Photodiodes in C++', *J. Open Res. Softw.*, vol. 6, May 2018, doi: 10.5334/jors.212.